ESPOO 2008 VTT PUBLICATIONS 683

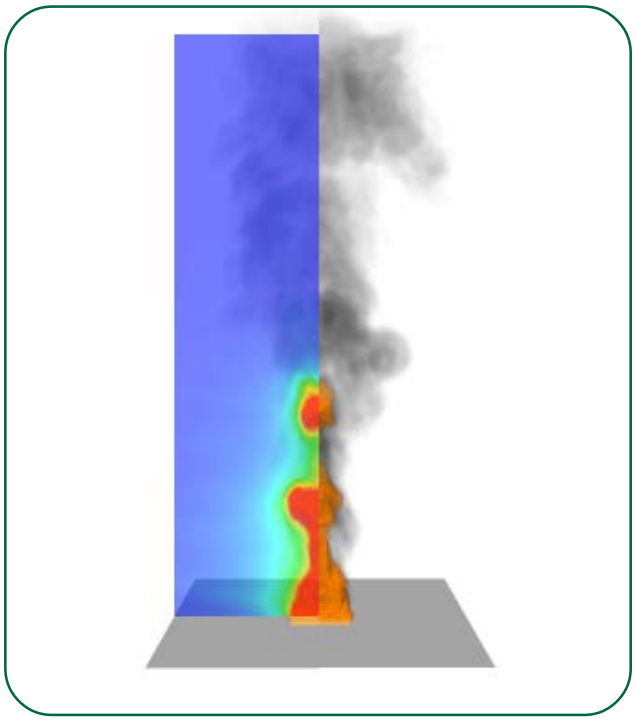

Simo Hostikka

# Development of fire simulation models for radiative heat transfer and probabilistic risk assessment

VTT PUBLICATIONS 683

# Development of fire simulation models for radiative heat transfer and probabilistic risk assessment

Simo Hostikka

*Thesis for the degree of Doctor of Technology to be presented with due permission for public examination and criticism in Lecture Room E at Helsinki University of Technology on the 6th of June, 2008, at 12 o'clock noon.*

ISBN 978-951-38-7099-7 (soft back ed.)
ISSN 1235-0621 (soft back ed.)

ISBN 978-951-38-7100-0 (URL: http://www.vtt.fi/publications/index.jsp)
ISSN 1455-0849 (URL: http://www.vtt.fi/publications/index.jsp)



JULKAISIJA – UTGIVARE – PUBLISHER

VTT, Vuorimiehentie 3, PL 1000, 02044 VTT
puh. vaihde 020 722 111, faksi 020 722 4374

VTT, Bergsmansvägen 3, PB 1000, 02044 VTT
tel. växel 020 722 111, fax 020 722 4374

VTT Technical Research Centre of Finland, Vuorimiehentie 3, P.O. Box 1000, FI-02044 VTT, Finland
phone internat. +358 20 722 111, fax + 358 20 722 4374

VTT, Kivimiehentie 4, PL 1000, 02044 VTT
puh. vaihde 020 722 111, faksi 020 722 4815

VTT, Stenkarlsvägen 4, PB 1000, 02044 VTT
tel. växel 020 722 111, fax 020 722 4815

VTT Technical Research Centre of Finland, Kivimiehentie 4, P.O. Box 1000, FI-02044 VTT, Finland
phone internat. +358 20 722 111, fax +358 20 722 4815

Edita Prima Oy, Helsinki 2008

Hostikka, Simo. Development of fire simulation models for radiative heat transfer and probabilistic risk assessment [Tulipalon simuloinnissa käytettävän säteilylämmönsiirtomallin ja riskianalyysimenetelmän kehittäminen]. Espoo 2008. VTT Publications 683. 103 p. + app. 82 p.

**Keywords** fire simulation, Monte Carlo simulation, probabilistic risk assessment, thermal radiation, verification, validation

# Abstract

An essential part of fire risk assessment is the analysis of fire hazards and fire propagation. In this work, models and tools for two different aspects of numerical fire simulation have been developed. The primary objectives have been firstly to investigate the possibility of exploiting state-of-the-art fire models within probabilistic fire risk assessments and secondly to develop a computationally efficient solver of thermal radiation for the Fire Dynamics Simulator (FDS) code.

In the first part of the work, an engineering tool for probabilistic fire risk assessment has been developed. The tool can be used to perform Monte Carlo simulations of fires and is called the Probabilistic Fire Simulator (PFS). In Monte Carlo simulation, the simulations are repeated multiple times, covering the whole range of variability of the input parameters and thus resulting in a distribution of results covering what can be expected in reality. In practical applications, advanced simulation techniques based on computational fluid dynamics (CFD) are needed because the simulations cover large and complicated geometries and must address the question of fire spreading. Due to the high computational cost associated with CFD-based fire simulation, specialized algorithms are needed to allow the use of CFD in Monte Carlo simulation. By the use of the Two-Model Monte Carlo (TMMC) technique, developed in this work, the computational cost can be reduced significantly by combining the results of two different models. In TMMC, the results of fast but approximate models are improved by using the results of more accurate, but computationally more demanding, models. The developed technique has been verified and validated by using different combinations of fire models, ranging from analytical formulas to CFD.

In the second part of the work, a numerical solver for thermal radiation has been developed for the Fire Dynamics Simulator code. The solver can be used to compute the transfer of thermal radiation in a mixture of combustion gases, soot particles and liquid droplets. The radiative properties of the gas-soot mixture are computed using a RadCal narrow-band model and spectrally averaged. The three-dimensional field of radiation intensity is solved using a finite volume method for radiation. By the use of an explicit marching scheme, efficient use of look-up tables and relaxation of the temporal accuracy, the computational cost of the radiation solution is reduced below 30% of the total CPU time in engineering applications. If necessary, the accuracy of the solution can be improved by dividing the infrared spectrum into discrete bands corresponding to the emission bands of water and carbon dioxide, and by increasing the number of angular divisions and the temporal frequency. A new model has been developed for the absorption and scattering by liquid droplets. The radiative properties of droplets are computed using a Mie-theory and averaged locally over the spectrum and presumed droplet size distribution. To simplify the scattering computations, the single-droplet phase function is approximated as a sum of forward and isotropic components. The radiation solver has been verified by comparing the results against analytical solutions and validated by comparisons against experimental data from pool fires and experiments of radiation attenuation by water sprays at two different length scales.

Hostikka, Simo. Development of fire simulation models for radiative heat transfer and probabilistic risk assessment [Tulipalon simuloinnissa käytettävän säteilylämmönsiirtomallin ja riskianalyysimenetelmän kehittäminen]. Espoo 2008. VTT Publications 683. 103 s. + liitt. 82. s.

**Keywords** fire simulation, Monte Carlo simulation, probabilistic risk assessment, thermal radiation, verification, validation

# Tiivistelmä

Paloriskien arvioinnissa on olennaista palon seurausten ja leviämismahdollisuuksien analysointi. Tässä työssä on kehitetty tulipalojen numeerisen simuloinnin malleja ja työkaluja. Työn päätavoitteita ovat olleet palosimuloinnin parhaimpien laskentamallien hyödyntäminen todennäköisyyspohjaisessa paloriskien arvioinnissa sekä laskennallisesti tehokkaan säteilylämmönsiirron ratkaisijan kehittäminen Fire Dynamics Simulator -ohjelmaan.

Työn ensimmäisessä osassa on kehitetty insinöörikäyttöön soveltuva, Probabilistic Fire Simulator (PFS) -niminen työkalu paloriskien arviointiin. PFS-työkalulla tulipaloa voidaan tutkia Monte Carlo -menetelmällä, jossa simulointeja toistetaan useita kertoja satunnaisilla syöteparametrien arvoilla, jolloin yksittäisen numeroarvon sijaan tuloksena saadaan tulosten jakauma. Käytännön sovelluksissa tarvitaan numeeriseen virtauslaskentaan perustuvia simulointimenetelmiä, koska simuloitavat tilavuudet ovat suuria ja monimutkaisia ja koska niissä pitää pystyä simuloimaan palon leviämistä. Monte Carlo -menetelmän toteutuksessa on tällöin käytettävä tehtävään sopivia erikoismenetelmiä, koska virtauslaskenta on laskennallisesti raskasta ja aikaa vievää. Tässä työssä kehitetyn Kahden mallin Monte Carlo -menetelmän avulla laskentaa voidaan nopeuttaa yhdistämällä kahden eritasoisen mallin tulokset. Nopeasti ratkaistavan mutta epätarkan mallin tuottamia tuloksia parannetaan hitaammin ratkaistavan mutta tarkemman mallin avulla. Menetelmää on testattu erilaisilla palomallien yhdistelmillä aina analyyttisistä kaavoista virtauslaskentaan asti.

Työn toisessa osassa on kehitetty säteilylämmönsiirron numeerinen ratkaisija Fire Dynamics Simulator -ohjelmaan. Ratkaisija laskee säteilyn etenemistä palokaasuja, nokea ja nestepisaroita sisältävässä väliaineessa. Palokaasujen ja noen muodostaman seoksen säteilyominaisuudet lasketaan keskiarvoistamalla RadCal-kapeakaistamallin tulokset aallonpituuden yli. Lämpösäteilyn eteneminen ratkaistaan säteilylämmönsiirron kontrollitilavuusmenetelmällä. Säteilyratkaisijan vaatima laskenta-aika saadaan alle 30 %:iin kokonaislaskenta-ajasta käyttämällä eksplisiittistä ratkaisumenetelmää ja tehokkaita taulukkohakuja sekä luopumalla ratkaisun aikatarkkuudesta. Tarkkuutta voidaan tarvittaessa parantaa jakamalla tarkasteltava aallonpituusalue veden ja hiilidioksidin tärkeimpiä absorptiokaistoja vastaaviin osiin sekä tihentämällä diskretointia avaruuskulman ja ajan suhteen. Työssä on kehitetty uusi laskentamalli nestepisaroiden ja säteilyn vuorovaikutukselle. Pisaroiden säteilyominaisuudet lasketaan Mie-teorian avulla ja keskiarvoistetaan sekä spektrin että pisarakokojakauman yli. Yksittäisen nestepisaran sirottaman energian vaihefunktiota approksimoidaan eteenpäin siroavien ja isotrooppisten komponenttien summana. Säteilyratkaisijaa on testattu vertaamalla laskettuja tuloksia analyyttisiin ja kokeellisiin tuloksiin.

# Preface

This work has been carried out during 1997–2007 under the auspices of the VTT Technical Research Centre of Finland, and the Building and Fire Research Laboratory of National Institute of Standards and Technology (NIST), USA, where I worked as a guest researcher.

I am grateful to my supervisor, Dr. Olavi Keski-Rahkonen, who originally introduced me to the scientific approach to fire and fire technology. At the age of 12, I had joined Vehkalahti volunteer fire brigade, to which I wish to express my gratitude, but during my studies at Helsinki University of Technology, I already thought that fire, as interesting as it had been, was in my past. With his enthusiasm to for fire dynamics, Dr. Keski-Rahkonen showed that fire might become my profession and the source of challenges for research. Dr. Keski-Rahkonen is my co-author in two of the papers of this thesis.

The favourable and encouraging attitude of Prof. Rolf Stenberg from the Institute of Mathematics at Helsinki University of Technology is greatly acknowledged. I thank Prof. Frederick W. Mowrer and Dr. Stewart Miles for reading the manuscript and suggesting numerous improvements.

I have had the privilege to have a group of wonderful colleagues at two research organizations, VTT and NIST. To these people and especially to the co-authors of the papers, I wish to express my gratitude. The most important of my colleagues and co-authors has been Dr. Kevin McGrattan of NIST. His commitment and self-sacrifice have been essential for our successful co-operation. From the very first moment when I visited NIST and later when my wife, Salla, and I lived in Maryland, I have constantly been overtaken by the hospitality and friendship of the entire McGrattan family.

I wish to thank my wife Salla – the most important person in my life – for the love and encouragement, and our children Helka, Kerkko, Iisak and Atro for sharing my attention during the preparation of this thesis. I also wish to thank my parents Raita and Veikko Hostikka for their endless support and trust.

Finally, I thank my Heavenly Father for everything He has done, and all the victories I have already won.

# List of publications

The dissertation is based on the following publications, which are referred to in the text by Roman numerals I–V:

I Hostikka, S. & Keski-Rahkonen, O. Probabilistic simulation of fire scenarios. Nuclear engineering and design, 2003. Vol. 224, No. 3, pp. 301–311.

II Hostikka, S., Korhonen, T. & Keski-Rahkonen, O. Two-model Monte Carlo simulation of fire scenarios. In: Gottuk, D. & Lattimer, B. (Eds.). Proceedings of the Eighth International Symposium on Fire Safety Science. Beijing, China, 18–23 Sept. 2005. International Association for Fire Safety Science, 2005. Pp. 1241–1252.

III Floyd, J.E., McGrattan, K.B., Hostikka, S. & Baum, H.R. CFD fire simulation using mixture fraction combustion and finite volume radiative heat transfer. Journal of Fire Protection Engineering, 2003. Vol. 13, No. 1, pp. 11–36.

IV Hostikka, S., McGrattan, K.B. & Hamins, A. Numerical modeling of pool fires using LES and finite volume method for radiation. In: Evans, D.D. (Ed.). Proceedings of the Seventh International Symposium on Fire Safety Science. Worcester, MA, 16–21 June 2003. International Association for Fire Safety Science, 2003. Pp. 383–394.

V Hostikka, S. & McGrattan, K. Numerical modeling of radiative heat transfer in water sprays. Fire Safety Journal, 2006. Vol. 41, No. 1, pp. 76–86.

# Author's contribution

Paper I deals with the development of a probabilistic approach and tool for fire simulations. The author implemented the first version of Probabilistic Fire Simulator software, performed the application simulations and did most of the writing. Paper II is an extension of the probabilistic tool to more complicated scenarios. The software was implemented jointly with the co-author, Dr. Timo Korhonen but the model formulation, actual application simulations and most of the writing were made by the author. In papers I–II, the formulation of the general approach and analysis of the results were made jointly by Dr. Olavi Keski-Rahkonen, who supervised the work.

Papers III–V deal with the development of Fire Dynamics Simulator (FDS) computer code. Paper III is a general description of the major development steps that were taken during 2000–2001 when the author worked as a guest researcher at NIST, developing and implementing a new computational model for thermal radiation. In Paper III, the author contributed to the description of Finite Volume Radiation Model. In Paper IV, the author is responsible for the computations, analysis of the results and most of the writing.

Paper V deals with the extension of the radiation model described in Papers III–IV to account for the interaction of thermal radiation and liquid droplets. Water sprays were used as an application. The author is solely responsible for the model development, computations and writing the paper. All the model implementations to FDS code were made in close co-operation with Dr. Kevin McGrattan of NIST.

# Contents

Abstract ..... 3

Tiivistelmä ..... 5

Preface ..... 7

List of publications ..... 8

Author's contribution ..... 9

List of symbols and abbreviations ..... 12

Part I Probabilistic simulation of fires ..... 15

1. Introduction ..... 17

2. Development of Probabilistic Fire Simulator ..... 21
   - 2.1 Monte Carlo simulation of fires ..... 21
   - 2.2 Two-Model Monte Carlo simulations ..... 23
   - 2.3 Probabilistic Fire Simulator ..... 26

3. Results and discussion ..... 27
   - 3.1 Scope ..... 27
   - 3.2 Verification of TMMC ..... 27
   - 3.3 Validation of TMMC ..... 28

Part II Radiative heat transfer solver for FDS fire model ..... 35

4. Introduction ..... 37

5. Fire modelling using Computational Fluid Dynamics ..... 38
   - 5.1 Scope of the review ..... 38
   - 5.2 Physical models ..... 39
     - 5.2.1 Fluid dynamics ..... 39
     - 5.2.2 Combustion ..... 42
     - 5.2.3 Radiation ..... 44
     - 5.2.4 Solid phase heat transfer ..... 48
     - 5.2.5 Flame spread ..... 49

5.2.6 Multiple phases ..... 50
5.3 Numerical implementations ..... 50
5.4 User interfaces ..... 51

6. Development of the radiation solver ..... 53
6.1 Radiative transport equation ..... 53
6.2 Model formulation ..... 54
6.2.1 Spectrally averaged RTE ..... 54
6.2.2 Discretized RTE ..... 58
6.2.3 Spatial and angular discretization ..... 60
6.2.4 Computation of cell face intensities ..... 62
6.2.5 Interaction between liquid sprays and radiation ..... 64

7. Results ..... 70
7.1 Verification of the radiation solver ..... 70
7.2 Radiative fluxes from diffusion flames ..... 72
7.3 Attenuation of radiation in water sprays ..... 74

8. Discussion ..... 81

9. Concluding remarks ..... 83
9.1 Summary ..... 83
9.2 Development of probabilistic fire simulation ..... 83
9.3 Weaknesses of TMMC technique and suggestions for future work ..... 84
9.4 Development of radiation solver for Fire Dynamics Simulator ..... 84
9.5 Weaknesses of the radiation solver and suggestions for future work ..... 86

References ..... 88

List of related publications ..... 103

# List of symbols and abbreviations

| | |
|---|---|
| $A$ | cell face area |
| $B$ | radiative emission term |
| $C$ | cross sectional area (absorption or scattering) |
| $c$ | speed of light |
| $d$ | droplet diameter |
| $e_{\lambda b}$ | Planck's spectral distribution of emissive power |
| $E_3$ | exponential integral function (order 3) |
| $f$ | probability density function |
| $F$ | probability distribution function |
| $g$ | limit state function |
| $I$ | intensity |
| $ijk$ | cell indices |
| $P$ | probability |
| $\dot{\mathbf{q}}''$ | heat flux vector |
| $m$ | cell index |
| $N$ | number of random samples, spectral bands or solid angles, droplet number density |
| $\mathbf{n}$ | cell face normal vector |
| $n$ | number of random variables, spectral band |
| $r$ | droplet radius |
| $\mathbf{s}$ | unit direction vector |
| $T$ | temperature |
| $t$ | time |
| $t_g$ | growth time of the heat release rate |
| $U$ | total combined intensity |
| $V_{ijk}$ | cell volume |
| $\mathbf{x}$ | random vector, position vector |
| $\mathbf{x}_s$ | scaling point |
| $x$ | random variable |

**Greek**

| | |
|---|---|
| $\chi_f$ | forward scattering fraction |
| $\chi_r$ | local radiative fraction |
| $\partial\Omega^l$ | discretized solid angle |
| $\varepsilon$ | surface mean hemispherical emissivity |
| $\Phi$ | scaling function, scattering phase function |
| $\phi$ | joint density function, azimuthal angle |

| | |
|---|---|
| $\kappa$ | absorption coefficient |
| $\lambda$ | wavelength |
| $\Omega$ | random space, solid angle |
| $\theta$ | polar angle |
| $\rho$ | density |
| $\sigma$ | scattering coefficient, Stefan-Boltzmann constant |

**Subscripts**

| | |
|---|---|
| *d* | droplet |
| *m* | mean droplet property |
| $\lambda$ | spectral value |
| *n* | average over spectral band |
| *r* | radiant |
| *x,y,z* | co-ordinate directions |
| *w* | water |

**Abbreviations**

| | |
|---|---|
| CFD | Computational Fluid Dynamics |
| CFL | Courant-Friedrichs-Lewy |
| DNS | Direct Numerical Simulation |
| FDS | Fire Dynamics Simulator |
| EBU | Eddy Break-Up |
| DOM | Discrete Ordinates Methods |
| DT | Discrete Transfer |
| FVM | Finite Volume Method |
| LES | Large Eddy Simulation |
| LHS | Latin Hypercube Sampling |
| MC | Monte Carlo |
| NPP | Nuclear Power Plant |
| PFS | Probabilistic Fire Simulator |
| PRA | Probabilistic Risk Assessment |
| PSA | Probabilistic Safety Assessment |
| RANS | Reynolds-Averaged Navier-Stokes |
| RTE | Radiation Transport Equation |
| SRS | Simple Random Sampling |
| TMMC | Two-Model Monte Carlo |

# Part I
# Probabilistic simulation of fires

# 1. Introduction

The primary purpose of fire safety engineering is to ensure that the risk of fire induced losses for humans, property, environment and the surrounding society associated with the target of the analysis is acceptable by the common standards of the society. Additional objectives may be imposed, for example by economical goals and needs to protect cultural heritage. Fire safety engineering is typically used to design the fire safety measures of new buildings or transportation vehicles. Traditionally, the design is based on a set of requirements for the physical characteristics, such as the dimensions of the fire compartments, classification of structures and width and length of evacuation routes. These requirements are described in the national building codes and are based mainly on experimental findings and lessons learned from past fires. An alternative way, currently applicable in most countries in some form, is the use of the performance-based design, or alternative design as it is called in the ship industry. In a performance-based design method, the effectiveness of the fire safety measures is studied considering the performance of an entire system, not as fulfilment of individual requirements given by the building code. As a result, the apparent safety level of individual components of the system may be higher or lower, but the total risk level should be at least as good as using the traditional way. Definition of the acceptable risk level is still very much an open question in the context of building design. However, an essential part of the design process is the analysis of the risks associated with fires and the assessment of the efficiency of proposed fire safety measures.

The roots of modern risk analysis are in the 19$^{th}$ century, when both probability theory and scientific methods to assess the health effects of hazardous activities were developed [1]. For example, the probability of dying was calculated for insurance purposes. Conceptual development of risk analysis in industrially developed countries started from two directions: (1) with the development of nuclear power plants and concerns about their safety, and (2) with the establishment of governmental institutions for the protection of the environment, health and safety as a response to a rapid environmental degradation [1]. The development of *fire* risk analysis has been considerably slower than on the other fields because fire as a physical phenomenon is extremely difficult to model on a real scale. The complexity of fire modelling results from the multitude of

physical problems and chemical reactions to be solved simultaneously and the wide range of associated time and length scales. A lack of resources for fire research and education may also be a partial explanation for the relatively slow development. Sufficiently accurate computational models for fires have been introduced during the last two or three decades, and the development of computational resources has allowed their use in probabilistic fire risk analysis during just the last few years. The computational models are discussed in detail in the second part of the thesis.

An important field of fire risk analysis is the probabilistic risk assessment (PRA) of nuclear power plants (NPP). The first systematic application of PRA[1] to study the probabilities and consequences of severe reactor accidents in commercial NPPs was made in WASH-1400 [2] ("Rassmussen report"). WASH-1400 was later updated in NUREG-1150 [3]. In PRA, the fire risk analysis is performed in pieces, typically for one room or class of rooms at the time. Individual damage probabilities are not used directly to make judgements on the plant safety, but weighted by the ignition frequencies and used as node probabilities in the event or fault trees, thus contributing to the probability of severe accidents and overall assessment of the safety [4]. Most early attempts of fire PRA were qualitative, since the fire consequences were usually assumed, rather than predicted using some physically realistic models. A PRA guide [5] introduced three methods for fire propagation analysis, with zone model simulations being the most advanced one, and was based on the use of a few selected scenarios, which was a big step compared to the first generation conservative assumptions. A four-phase procedure proposed in [5] is still valid: (Task 1) fire hazard analysis to identify the critical plant areas and fire frequencies, (Task 2) fire propagation analysis, (Task 3) plant and system analysis to estimate the likelihood of fires leading to damage states, and (Task 4) release frequency analysis. However, the procedure still lacked the possibility to be truly quantitative because the choice of fire scenarios was based on expert opinion. In this work, computational tools are developed for the assessment of conditional fire damage probabilities in a way that has a potential to become truly quantitative by covering the distributions of input parameters and using sufficiently detailed fire models. Expert opinions are still needed in the selection of the rooms and targets to be modelled. The

[1] An alternative term is Probabilistic Safety Assessment (PSA).

development work has been part of the Finnish nuclear power plant safety research programmes [6, 7] with a central goal of improving the deterministic and stochastic tools for fire-PRA. During the work, both small additions and total re-interpretations have been made for Tasks 1–3 of the four phase procedure mentioned above [8, 9].

In the analysis of large and complicated targets, both the existing ones and the ones to be designed, the various techniques of fire risk analysis are usually combined. Qualitative and semi-quantitative methods, such as the fire risk index [10], are fast and simple to use and may be sufficient in some cases. Quantitative techniques such as event and fault trees can be used to manage the complex chains of safety measures, and are the fundamental parts of probabilistic fire risk analysis. One problem of using event trees is the static nature of the tree. Early attempts to bring in the time component to event tree analysis were made in the context of fire spreading [11, 12] and recently in the context of structural safety [13]. Expert judgement is always needed to focus the analysis to the most relevant regions and Bayesian techniques can be used to reduce the uncertainty in the probability estimates by utilizing the observed evidence [14]. The risk analysis techniques may be used to compute probabilities of individual pre-defined events or a general relation between the probability and the hazard severity, in which case the results can be conveniently presented as FN-curves [15, 16, 17]. In FN-curves, the probability of an event is plotted against the severity measure of the event, such as number of fatalities. The role of the fire statistics as a source of information for risk analysis has been studied at VTT by Tillander and Keski-Rahkonen [18,19]. The importance of the fire statistics was recently discussed by Sekizawa [20].

The practical technique for the combination of deterministic fire models to the probabilistic treatment of model variables has been the use of Monte Carlo simulation (MC). In MC, the uncertainty or statistical nature of the initial and boundary conditions can be taken into account rigorously by sampling the model variables randomly from their given distributions and computing a large number of model realizations leading to a distribution of all the potential outcomes that could occur under these uncertainties [21]. The term “Monte Carlo” refers to the application of probabilistic thinking in the computation of the probability of a successful outcome of a game of solitaire [22]. A guide for using MC in the quantitative risk analysis has been written by Vose [23]. Examples of the use of

MC simulations in the PSA work are found in the articles of Hofer and his co-authors [24, 25]. In Paper I of this thesis, a similar approach was chosen to compute the component failure probabilities in NPP cable tunnels and electronics rooms. Within the NPP fire safety projects at VTT, the computational tools were implemented in Probabilistic Fire Simulator (PFS) software [26]. For efficiency reasons, MC is often performed using Latin Hypercube Sampling [27, 28] rather than simple random sampling.

In fire safety engineering, MC simulations can be used for at least two purposes: integration over the statistical distributions to deduce the probability, and for propagation of uncertainty [29]. However, Hofer et al. [30, 31] have shown that the separation of these two purposes is not necessary since both sources of randomness can be taken into account within the same single-stage MC. The fast increase of computational resources during the last 10 years has made it possible to use numerical fire models within the MC simulation. In the context of fire safety engineering, Monte Carlo simulations have been used for instance to model the risks to human life due to PCB-contaminated oil fires [32] and building fires [33], to model fires at dwellings [34], assembly halls [35] and office buildings [36] and the probability of fire deaths due to toxic gas inhalations [37]. Computer tools such as CRISP [38, 34, 36] and CESARE-RISK [37, 39] that include the possibility for MC simulations were developed in the 1990s. Notarianni used Monte Carlo simulation and a two-zone fire model to study the role of uncertainty in fire regulations [40]. Some recent applications of Monte Carlo simulations include the following: the computation of the probability of reaching critical temperatures in steel members [41], the introduction of a probabilistic aspect to fire resistance specification for regulatory purposes [42], the identification of the most critical factors in determining the cost-benefit ratio for sprinkler installation in parking buildings [43], as well as the computation of the failure probabilities of fire detection system designs [44] and structural reliability [39]. In the studies mentioned above, fires were typically modelled using simple hand calculation formulas of zone models because the use of more advanced models has been computationally too expensive. In Paper II of this thesis, the Monte Carlo technique has been extended to allow the use of state-of-the art fire models like CFD as a computational tool. Additional examples of the use of the new technique can be found in reference [9].

# 2. Development of Probabilistic Fire Simulator

## 2.1 Monte Carlo simulation of fires

Monte Carlo (MC) simulation is a method of performing "numerical experiments" using random numbers and computers. An introduction to the mathematical aspects of MC simulations can be found in [45]. Several textbook level references can be found on the use of MC simulation in physics, for example see [46], and in risk analysis [21, 23]. Only a short description of the technique is given here, with an emphasis on the specific application to fire safety.

The question set by the PRA process is usually the following: "What is the probability of event $A$ in case of fire?" Examples of target events are the failure of a certain component or system, activation of a heat detector, smoke filling, flashover, extinction of the fire and fire death. The probability of event $A$ is a function of all possible factors that may affect the development of the fire and the systems' reaction to it. The affecting variables, denoted by a vector $\mathbf{X} = (X_1 \; X_2 \; \ldots \; X_n)^T$, are considered random variables, since the exact values of these variables are not known. Instead, they are associated with probability distributions with density functions by $f_i$ and distribution functions by $F_i$. The occurrence of the target event $A$ is indicated by a limit state function $g(t,\mathbf{x})$, which depends on time $t$ and vector $\mathbf{x}$ containing the values of the random variables. As an example of the target event, we consider the loss of some component. The limit state condition is now defined using function $g(t,\mathbf{x})$:

$$\begin{aligned} g(t,\mathbf{x}) &\le 0, \text{ if the component is lost at time } t \\ g(t,\mathbf{x}) &> 0, \text{ if the component is not lost at time } t \end{aligned} \tag{1}$$

The development of fire and the response of the components under consideration are assumed to be fully deterministic processes where the same initial and boundary conditions always lead to the same final state. With this assumption, the probability of event $A$ can now be calculated by the integral

$$P_A(t) = \iint\cdots\int_{\{\mathbf{x}|g(t,\mathbf{x})\le 0\}} \phi_x(\mathbf{x})dx_i \qquad (2)$$

where $\phi_X$ is the joint density function of variables **X**. The assumption of deterministic processes is valid if the epistemic uncertainty of the applied deterministic models is small as compared with the uncertainties caused by the input distributions. In practice, this means that all the relevant processes can be explicitly depicted as mathematical models that are numerically stable and sufficiently accurate. In highly non-linear problems, such as fire spread, these requirements may sometimes be difficult to meet.

In this work, the probability $P_A$ is calculated using Monte Carlo simulations where input variables are sampled randomly from the distributions $F_i$. The usability of the Monte Carlo simulation often depends on the number of random samples $N$ required for a sufficient degree of accuracy. If $N$ is large and $g(t,\mathbf{x})$ is expensive to evaluate, the computational cost of the MC simulation may become very high. For large $N$, the error of the simple random sampling (SRS) decreases as $1/\sqrt{N}$ according to the central limit theorem [47]. The convergence rate of the simulation can be improved by using sampling schemes that have smaller variance than SRS. Examples of more advanced sampling schemes are the use of quasi-random numbers, importance sampling and stratified sampling [45].

The simulations are made using a stratified sampling scheme called Latin Hypercube Sampling (LHS) [27]. In stratified sampling, the random space is divided into a discrete number of intervals in the direction of each random variable. As the number of samples from each interval is the same, the samples are given weights based on the total probability of the intervals. The advantage of the stratification is that the random samples are generated from all the ranges of possible values, thus giving insight into the tails of the probability distributions. In LHS, the $n$-dimensional parameter space is divided into $N^n$ cells. Each random variable is sampled in a fully stratified way and then these samples are attached randomly to produce $N$ samples from $n$ dimensional space. LHS will decrease the variance of the integral in equation (2) relative to the simple random sampling whenever the sample size $N$ is larger than the number of variables $n$ [48]. However, the amount of reduction increases with the degree of additivity in the random quantities on which the function being simulated depends. In fire simulations, the simulation result may often be a strongly

nonlinear function of the input variables. For this reason, we cannot expect that LHS would drastically decrease the variances of the probability integrals. Problems related to LHS with small sample sizes are discussed by Hofer [49] as well as by Pebesma & Heuvelink [50].

## 2.2 Two-Model Monte Carlo simulations

The numerical simulation of the complicated physical processes is always trading between the desired accuracy of the results and the computational time required. Quite often, the same problem can be tackled by many different models with different physical and numerical simplifications. A good example of this is the fire simulation in which zone models provide a fast way to simulate the essential processes of the fire, being inevitably coarse in the physical resolution. As an alternative, computational fluid dynamics (CFD) models have potentially higher physical resolution and can describe more complicated physical phenomena. The time needed for the CFD computation may be several orders of magnitude longer than the time needed for the zone models. A technique is therefore needed which can combine the results of the different models in a computationally efficient way. In this work, we have developed a technique that allows the use of two different models in one Monte Carlo simulation, and is therefore called Two-Model Monte Carlo (TMMC). TMMC is based on the assumption that the ratio of the results given by two models has smooth variations when moving from point to point of the random space. Therefore, if one of the models is presumably more accurate than the other, the ratio calculated at some point of the random space can be used to scale the result of the less accurate model within the neighbourhood of the point. By using a relatively small number of scaling points, the scaling function or surface can be created. The technique can be compared to the use of response surfaces to model the Monte Carlo data [39]. Instead of using the data from the scaling points directly, they are used to improve the accuracy of the actual Monte Carlo. The TMMC model was originally presented in Paper II of the thesis.

We assume that we have two numerical models, A and B, which can calculate the physical quantity $a(\mathbf{x},t)$ depending on a parameter $\mathbf{x}$ and the time $t$. In our analysis, $\mathbf{x}$ is considered to be a random variable from a random space $\Omega$. Model B is more accurate than model A, but the execution time of model B is (much)

longer than model A. The models are used to get two estimates of the time series: $\widetilde{a}^{A}(\mathbf{x}_s,t)$ and $\widetilde{a}^{B}(\mathbf{x}_s,t)$. In TMMC, we assume that at any point **x** of the random space, the accuracy of the model A results can be improved by multiplying them with a scaling function, which is the ratio of model B time series to model A time series at some point $\mathbf{x}_s$ in the vicinity of the current point **x**. The points $\mathbf{x}_s$ are called scaling points.

In the beginning of the simulation, the random space is divided into distinct regions. A scaling function is then calculated for each region

$$\Phi(\mathbf{x}_s,t)=\frac{\widetilde{a}^{A}(\mathbf{x}_s,t)}{\widetilde{a}^{B}(\mathbf{x}_s,t)} \tag{3}$$

where $\mathbf{x}_s$ is the mid-point of the scaling region $\Omega_s$. This process is illustrated in the upper part of Figure 1 showing the two time series corresponding to models A and B, and the scaling function $\Phi(\mathbf{x}_s,t)$. During the Monte Carlo, the result of the model A is multiplied by the scaling function corresponding to the closest scaling point, to get the corrected times series $\widetilde{a}^{AB}(\mathbf{x},t)$

$$\widetilde{a}^{AB}(\mathbf{x}_s,t)=\Phi(\mathbf{x}_s,t)\cdot\widetilde{a}^{A}(\mathbf{x}_s,t),\quad \mathbf{x}\in\Omega_s \tag{4}$$

The correction is illustrated in the lower part of Figure 1 showing again the time series A and B, and the corrected time series AB, which would be the result used within the TMMC. TMMC can provide significant time savings with respect to a full MC using model B because model B is used only in scaling points. The actual MC is still performed using model A. The magnitude of the time saving depends on the number of scaling points to the number of random points ratio.

Quite often, the result of the MC simulation is not the time series itself, but some scalar property derived from the time series. A typical result is the time to reach some critical value. A simplified version of the TMMC technique can be obtained if the scaling is done for scalar numbers directly. Although the scaling would be easier to implement for the scalars than for the whole time series, the simplification has some unwanted properties, which are demonstrated in Paper II of the thesis.

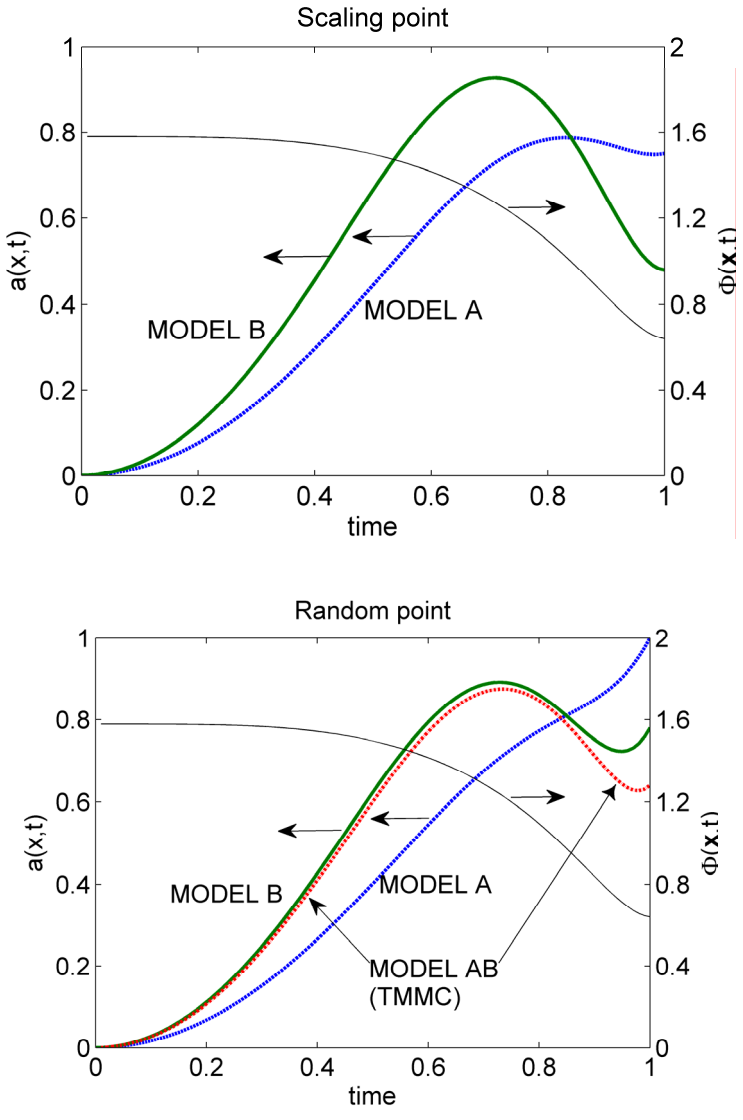


*Figure 1. An example of TMMC scaling. Time series* $\tilde{a}^{A}(\mathbf{x},t)$ *and* $\tilde{a}^{B}(\mathbf{x},t)$ *and scaling function* $\Phi(\mathbf{x}_s,t)$ *at scaling point (upper figure) and random point (lower figure). The lower figure also shows the estimate* $\tilde{a}^{AB}(\mathbf{x},t)$.

For a general function $a(x,t)$, it is not possible to tell how fast the function $\tilde{a}^{AB}(\mathbf{x},t)$ converges towards $\tilde{a}^{B}(\mathbf{x},t)$, when the number of scaling points is increased. However, it is clear that

$$\lim_{N_s \to \infty} \tilde{a}^{AB}(\mathbf{x}_s, t) = \tilde{a}^{B}(\mathbf{x}_s, t) \tag{5}$$

where $N_s$ is the number of scaling points.

## 2.3 Probabilistic Fire Simulator

The techniques described above have been implemented in a Probabilistic Fire Simulator tool (PFS). PFS has been developed at VTT in the projects concerning the fire safety of nuclear power plants [26], but applications are already much wider, covering the performance-based design of large buildings and ships. In addition to the actual Monte Carlo simulations, PFS can be used as an interface for several fire models: Fire Dynamics Simulator, CFAST [51], Ozone [52,53] and OptiMist [54].

PFS tool is implemented as a Microsoft Excel workbook including internal (Visual Basic) and external (Fortran DLL) subroutines for statistics and interfacing with the fire models. The first version of PFS [26] used commercial @Risk package for performing the Monte Carlo simulation and statistical operations, but in later versions, the necessary FORTRAN subroutines have been written for PFS.

# 3. Results and discussion

## 3.1 Scope

The results presented in this section fall into two categories: verification and validation. Verification is performed to ensure that the software has been implemented as planned and works as could be expected based on the provided documentation. Validation in turn deals with the actual accuracy of the software in the intended application. The verification problem is simple and fictitious but the validation problems are designed to be relevant for the software user. Some results from real applications can be found in [9].

## 3.2 Verification of TMMC

To verify the TMMC's capability to capture the cumulative distributions of scalar quantities, the technique is applied to the approximation of analytical function

$$a(x,t) = \min\left[e^{xt} - 1, 0.8 \cdot \left(e^{x} - 1\right)\right], \quad t \in [0,1] \tag{6}$$

The min-function is used to simulate a plateau of the time series reaching a steady state. In model A, the analytical function is approximated by a two term Taylor series expansion. Model B output is the function itself $\tilde{a}^{B}(x,t) = a(x,t)$. The random variable $x$ is distributed uniformly between 1 and 2. The actual outcome of the simulation, denoted by $c(x)$, is the time when $a(x,t)$ reaches a value $a_m = 2$ for the first time. Figure 2 shows the cumulative distributions of $c(x)$. The curve AB, corresponding to TMMC, is very close to the distribution of values derived from the exact function. As shown in Paper II, the scalar scaling would not produce good results in this particular case.

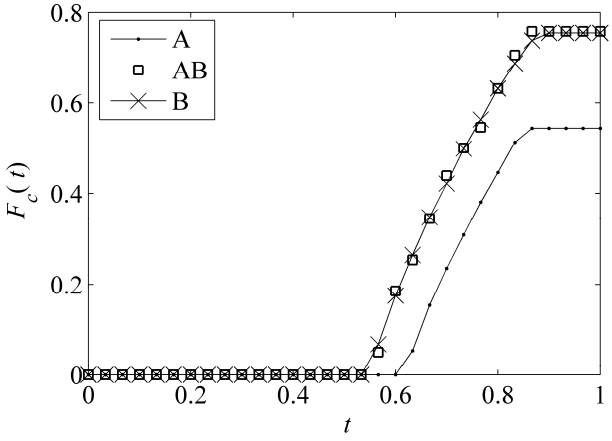


*Figure 2. Cumulative distributions of scalar quantities in the verification example. Curve B corresponds to the exact solution, curve A to its Taylor series approximation and curve AB to the TMMC estimate of the exact solution.*

## 3.3 Validation of TMMC

The possibilities to validate the probabilistic techniques are much more limited than the possibilities to validate the deterministic models, for which experimental data with well-defined boundary conditions can be found. Since the experimental data from a series of hundreds of fire tests is not available, the performance of the probabilistic fire simulation techniques is studied by performing numerical experiments. In the two validation tests, presented originally in Paper II, the reference result is obtained by performing a full MC analysis using the same model that is used as a basis for the scaling functions, i.e. Model B.

In the first validation test, Alpert's ceiling jet model [55] (Model A) and CFAST two-zone model (Model B) were used to predict the ceiling jet temperature under the ceiling of a 10 m × 10 m × 5 m (height) room with a fire in the middle of the floor. The room had one, 2.0 m × 2.0 m door to ambient. We simply assumed that in the current application, CFAST is more accurate than Alpert's model, whether this is true or not in reality. The validity of the applied tools is not relevant for the purpose of TMMC validation because we only want to validate the capability of TMMC to generate a useful correction for one model's

output using the output from another model. The actual model uncertainties become relevant in applications and should be evaluated in relation to the input uncertainties, as discussed in Section 2.1.

The fire heat release rate was of $t^2$-type with a random, uniformly distributed growth time $t_g$. Two scalar results were studied. The scalar result $b(t_g)$ was the ceiling jet temperature at time = 30 s. The scalar result $c(t_g)$ was the time to reach a critical temperature of 100 °C in the ceiling jet. The random space was divided into three sub domains. 1000 samples were calculated using both models. The predicted cumulative distributions of $b(t_g)$ are shown in the left part of Figure 3. At all values of $t_g$, CFAST predicted higher temperatures than Alpert's model. TMMC distribution was very close to the CFAST result, but had small discontinuities at the boundaries of the divisions. The right hand side of Figure 3 shows the cumulative distributions of $c(t_g)$. As can be seen, TMMC scaling very accurately captured the shape of the CFAST distribution.

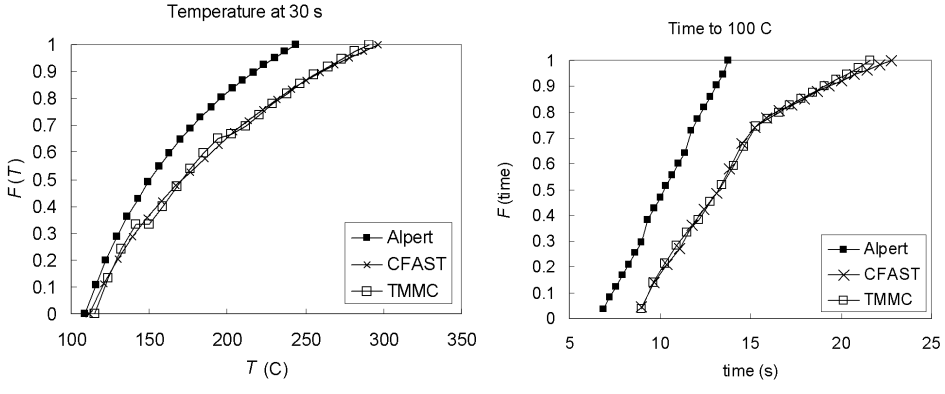


*Figure 3. Distributions of temperature at time = 30 s (left) and time to reach 100 °C (right) in the first validation test.*

The second validation test was the prediction of gas and heat detector temperatures in a room with concrete surfaces and predefined fire. In the test, CFAST two-zone model was used as Model A and FDS as Model B. The fire source was a rectangular burner at the floor level with maximum HRR per unit area of 700 kW/m$^2$. The co-ordinates and surface area of the fire source were random variables. In the beginning, the heat release rate increased proportional to $t^2$ reaching the final value at time $t_g$, which was a uniformly distributed

random variable. A list of the random variables is given in Table 1. The time to reach 200 °C at a certain location under the ceiling and the heat detector activation time were monitored.

*Table 1. Random variables in the second validation test.*

| Variable | Units | Distribution | Min | Max | Mean | Std.dev |
|---|---|---|---|---|---|---|
| BeamHeight $z_B$ | m | Uniform | 0.0 | 0.6 | | |
| GrowthTime $t_g$ | s | Uniform | 60.0 | 180.0 | | |
| Area | $m^2$ | Normal | 0.2 | 1.5 | 0.80 | 0.60 |
| FireX | m | Uniform | 0.0 | 4.0 | | |
| FireY | m | Uniform | 0 | 3.0 | | |

The predicted probability distributions for the time to reach a 200°C gas temperature are shown in Figure 4. As can be seen, the predictions using CFAST and FDS are considerably different: CFAST predicts that the 200°C temperature is reached in only 60% of the fires, but according to FDS the condition is met in 90% of fires. This makes the test very relevant and challenging.

The rank order correlations between the random variables and the time to reach the 200 °C gas temperature are shown in Figure 5. It demonstrates that in the cases where CFAST and FDS lead to different correlations, TMMC can make the necessary correction to the CFAST results.

The effect of the number of TMMC scaling points was studied by using different ways to divide the random space. The number of scaling points was varied from 1 to 32 and the basis for the division was taken from the CFAST simulations, which predicted that the fire surface area, the HRR growth time, and FireX-position were the most important random variables, as shown in Figure 5. The number of scaling points is denoted in the parentheses in Figure 4. For the case with 32 scaling points, a version with two scaling points per random variable (TMMC(32B)) was also tested ($2^5 = 32$).

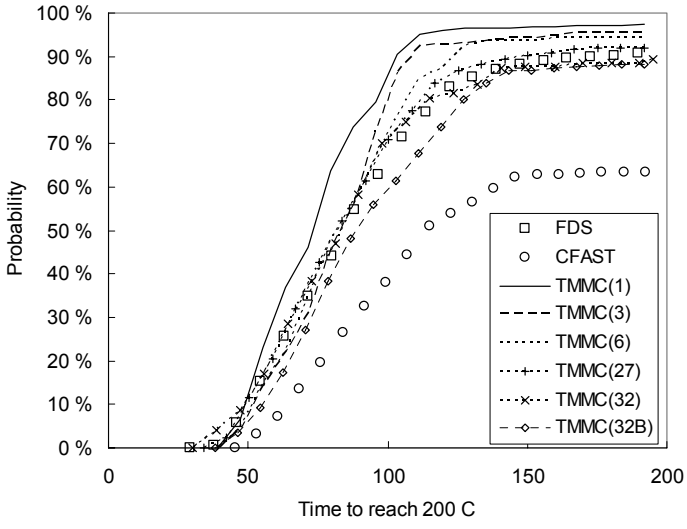


*Figure 4. Predicted probability distributions of time to reach 200 ℃ at gas in the second validation test.*

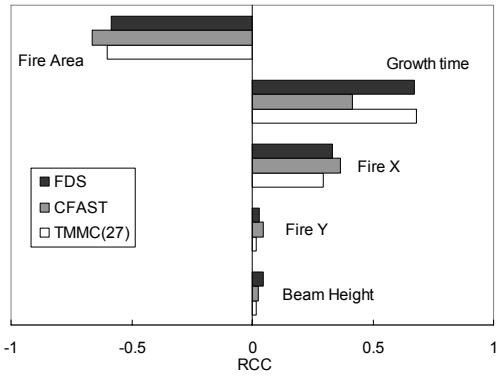


*Figure 5. Rank order correlation coefficients for the time to reach 200℃ gas temperature.*

The division of the random space has a clear effect on the accuracy of the TMMC distribution. If the division is made based on the relative importance of the random variables, the higher number of scaling points generally improves the accuracy. If the scaling points are chosen without any prior information of the importance, the results do not improve as much, as is demonstrated in the case TMMC(32B). In addition, smoothing the transient data was shown to improve the results.

The prediction of the heat detector activation time distribution was not as successful as the time to reach a certain gas temperature. The reason turned out to be the fact that in FDS, the heat detector temperature was not updated after the activation. An artificial limiter was thus applied to the model prediction, while the other model did not have such a limiter. In later versions of FDS, this feature has been changed accordingly, but the actual lesson learned from this exercise is that variables being scaled should rigorously represent the same physical quantity without any artificial limiters. If there is no correlation between the outputs of the two models, it does not make sense to scale one with another. Unfortunately, there is no simple way to identify the cases where this is not the case. The basic requirement for the TMMC applicability is that the relevant phenomena are included in both models at sufficient accuracy. In the validation tests above, both models had the necessary physics to describe the studied variables. Even though the zone and CFD models are mathematically very different, they both are theoretically capable of modelling the gas and heat detector temperatures within the fire room. However, trying to predict the vent mass flow using both ceiling jet correlation and zone model, for instance, would have been unsuccessful. In principle, the correlation between the two models can be ensured by computing a large number of model realizations with both models but in case of computationally expensive models like CFD, this is hardly practical. A good understanding of the behaviour of the physical models is therefore required for the judgement of the applicability of TMMC technique to the problem under consideration. Additionally, special attention should be paid to the choice of model B, since there is an inherent assumption that it is always more accurate than model A.

In the light of the above discussion, an important alternative for the use of totally different models than models A and B is the use of same model but with different numerical discretizations. The dependency of computational cost and accuracy of the CFD codes on the spatial resolution makes them suitable for the TMMC. The use of an FDS model in both phases of TMMC was demonstrated in [56]. Models A and B were FDS models with relatively coarse and fine computational meshes, respectively. When 1000 simulations were performed using model A and 24 simulations using model B, the savings in computation time was roughly a factor of five.

The results presented are special cases and do not prove that TMMC technique always works. However, the experiences so far have been positive, considering the improvement of both probabilities and correlations. This demonstrates the potential value of TMMC for large-scale quantitative fire risk studies in the future.

# Part II
# Radiative heat transfer solver for FDS fire model

# 4. Introduction

The quantitative risk analysis and performance-based design relies greatly on the use of numerical modelling and simulation of both the fire and evacuation processes. The increased size and complexity of the buildings make new demands for the techniques used for simulations. During the last few years, CFD has become the most widely used technique for the simulation of smoke transport and fire spread. The more simple techniques, such as the hand-calculation formulas and two-zone models, still have an important role in engineering because they are faster and simpler to use, but the majority of challenging fire simulations are performed using CFD. A literature review on CFD fire modelling is given in the next section.

Thermal radiation plays a very important role in the development of fires by allowing the gaseous combustion products to cool due to the emitted radiation and by preheating combustible materials ahead of the flame front. This preheating increases the rate of flame spread, often causing ignition of surfaces without direct flame impingement. Solution of the radiation transport equation requires determining radiative properties of the medium over a wide range of infrared frequencies. It is possible to create a radiation transport model that tracks the emission, transport, and absorption at many frequencies of infrared light. However, such an approach is very time consuming and memory intensive. One typical simplification is to assume a grey gas and solve for only one integrated intensity. The presence of condensed phase particles or droplets can block thermal radiation and thus reduce the rate of fire spread. To incorporate the effect of radiation-spray interaction to the model, the radiative properties of the spray must be calculated with the same level of detail as the gas phase, and the scattering effects must be considered.

The Fire Dynamics Simulator (FDS), developed at the National Institute of Standards and Technology (NIST), originally used a simple Monte Carlo ray tracing method for solving the transport of heat by radiation from the combustion region to the surroundings. This model was easy to implement and worked well for small fires. However, the model did not function well for large fires or fires approaching flashover, and a new radiation heat transfer solver was based on the finite volume method for radiation [57], as described in the papers III–V of the thesis.

# 5. Fire modelling using Computational Fluid Dynamics

## 5.1 Scope of the review

The purpose of this section is to review the aspects of the physical and numerical modelling in the present CFD fire models. The emphasis is put on the physical issues such as fluid dynamics, combustion, radiation, solid phase heat transfer, flame spread and two-phase flows. The features of LES and RANS models and the challenges of radiation modelling are discussed in detail. The issues of numerical implementations and user interfaces are shortly discussed. The models designed for some special types of applications, such as explosions or Direct Numerical Simulation of combustion processes are not discussed.

In 2002 SFPE Handbook chapter concerning the CFD Fire Modelling, Cox and Kumar [58] presented the principles, practices and instruction for proper use of CFD in fire applications, from the perspective of Reynolds-averaged Navier-Stokes (RANS) technique. When the chapter was written, it was widely accepted that the proper method for low speed turbulent flow was RANS using an eddy viscosity turbulence model such as the $k$-ε model, SIMPLE pressure correction algorithm [59] or some of its variants, and the various sub-models like Eddy Break-Up [60] for combustion. However, in a few years, due to faster computers and specialized algorithms, Large Eddy Simulation (LES) is now considered by many to be the preferable technique to study fire-driven flows. LES technique is used in Fire Dynamics Simulator (FDS) [61, 62], which was made publicly available in the year 2000. For FDS users, the article of Cox and Kumar provides very little guidance, although there is no fundamental difference between RANS and LES, other than the treatment of time dependence of the Navier-Stokes equations. This example illustrates how rapidly a computational field of engineering may evolve.

The CFD fire models can be classified based on many different criteria, with RANS vs. LES being probably the most widely used. Other possibilities would be the type of radiation model, availability, price, user interface and hardware requirement. All these aspects have been discussed in the review article of Olenick and Carpenter [63].

## 5.2 Physical models

### 5.2.1 Fluid dynamics

The core of any CFD model is its Navier-Stokes solver. The numerical solution of these equations is considered by many to be a "mature" field because it has been practised for over 30 years, but the nature of turbulence is still one of the unsolved problems of physics. All the current solvers are based on the approximations that have effects on the applicability of the solver and the accuracy of the results – also in the fire simulations.

Current, practical CFD fire models fall into one of two major categories: Reynolds-averaged Navier-Stokes (RANS) or Large Eddy Simulation (LES). The difference of these two categories is the nature of the starting equations: In RANS, the Navier-Stokes equations are *time* or *ensemble averaged* before the derivation of the discrete form suitable for programming as a solver algorithm. The solver then finds a *steady state* or *quasi steady state* solution for the equations. Time dependent flows can be solved as long as the time scale of the mean flow is large compared to the time scale of the turbulent fluctuations [64]. In LES, the time averaging is not performed, and the solutions can be considered "accurate" in time, meaning that the variations in the solution correspond to the motions resolvable by the numerical grid. The marching in time takes place using a short time step $\Delta t$, which is usually defined by the following stability criteria

$$\Delta t < \min_{ijk}\left(\Delta x_{ijk} / u_{ijk}\right) \tag{7}$$

where $\Delta x$ and $u$ are the grid cell size and velocity, respectively, and the minimum is found over the whole domain. Equation (7) is called Courant-Friedrichs-Lewy (CFL) condition [65, 66] according to the German mathematicians who invented it in 1928 – well before modern computers. In LES, the filtering is performed in space, although the actual filtering is usually limited to the length scales below the grid cell size.

The difference of the RANS and LES results is depicted in Figure 6 showing the temperature fields of a pool fire flame. While the RANS result shows smooth

variations and looks like a laminar flame, the LES result clearly illustrates the large scale eddies. Both results are correct solutions of the corresponding equations. However, the time accuracy of LES is also essential for the quantitative accuracy of the buoyancy driven flows. As the NIST researches Rehm and Baum have shown [67], the dynamic motions or 'eddies' are responsible for most of the air entrainment into the fire plumes. Since these motions can not be captured by RANS, LES is usually better suited for fire-driven flow. LES typically requires a better spatial resolution than RANS. Examples of RANS-based fire CFD codes are JASMINE, KAMELEON [68], SMARTFIRE [69], SOFIE [70], ISIS [71] and ISIS-3D [72]. Examples of LES codes are the FDS [61, 62]; SMAFS, developed at Lund University [73]; and the LES fire code developed at the City University of Hong Kong [74].

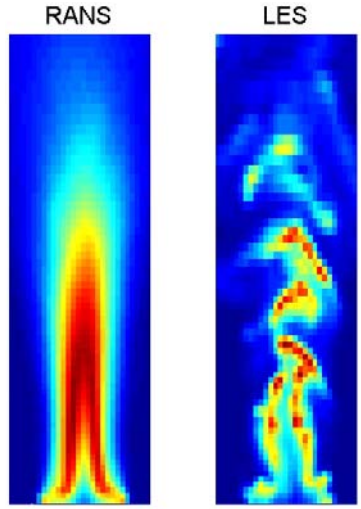


*Figure 6. A comparison of temperature fields in a pool fire flame simulations using RANS and LES.*

There are certain applications, where RANS has a clear advantage over LES. RANS models can take advantage of any a priori knowledge of the mean flow direction by accepting high aspect ratio grid cells. An example of such an application is a flow in a tunnel, where the grid cells can be made long and thin, giving good accuracy in the direction normal to the tunnel walls but saving cells in the direction of the tunnel, where variations are slow. In LES, all the velocity components are present with likelihood of same order, and the cell aspect ratios

must be close to unity. For this reason, the tunnel simulations using LES are computationally expensive. The second type of application where the use of RANS is advantageous is the simulation of long, close to steady state or steady state fires. In such cases, RANS allows fast marching in time using long time steps, while LES is bound by the CFL condition.

Turbulence modelling and time accuracy are closely related. In RANS solvers, the turbulence models are used to describe all the turbulent properties of the flow. A range of different models have been developed. The differences in the models have been mainly related to the assumption of homogenous ($k$-$\varepsilon$, $k$-$\omega$) or inhomogeneous (Reynolds stress models) turbulence and the treatment of boundary layers (Wall functions vs. Small Reynolds Number models). The problems of these models to accurately predict the entrainment of buoyant plumes has been known for long, and is more fundamental than just turbulence closure problem. A review of the turbulence modelling in RANS is given by Kumar [75], and the effect of turbulence models on the CFD simulation of buoyant diffusion flames has been studied by, for example, Liu and Wen [76].

In LES, the role of turbulence models is only to describe the sub-grid scale phenomena that cannot be solved with the computational grid used. In regions of high shear, the sub-grid scale models have a stronger effect on the solution and a lot of research is still needed to find good solutions for handling these flows. Examples of high shear flows in fire simulations are the solid wall boundaries and the interface of the hot and cold flows in doors and windows.

Despite the relatively short history of LES fire modelling, the accuracy of LES technique in fire simulation has been studied extensively. Early validation of FDS predecessor was performed by comparing simulations against salt water experiments [77, 78, 79], fire plumes [80, 81] and room fires [82]. More recently, FDS code has been validated for fire plumes [83] and fires in enclosures in the context of the World Trade Center investigation [84, 85] and the fire model validation project sponsored by the U.S. Nuclear Regulatory Commission [86].

Virtually all CFD fire models assume incompressible flow, which is adequate in typical fire application, but should be kept in mind when dealing with high velocity cases and explosions. Inclusion of the compressibility effects in fire simulations would increase the computational cost considerably. One of the few

compressible fire codes is the Uintah Computational Framework developed at C-SAFE project of the University of Utah [87].

In RANS simulations, the boundary layers have traditionally been handled using the wall functions which assume the logarithmic velocity profile on the wall. In simple applications of the process industry, these functions work well, having the most serious problems in situations involving separation and reattachment. Similar "sub-grid scale wall functions" can be derived for LES, or the effect of the wall can be taken into account in the sub-grid scale model of viscosity [88]. Currently, FDS does not include any wall functions. Only an adjustment of the slip-velocity and simple heat transfer coefficient correlations are used. In their comparison of measured and predicted turbulence statistics, Zhang et al. [89] showed that even with these simple boundary treatments, FDS was able to produce good flows in a room scale. Naturally, new techniques must be studied to improve the accuracy of solid phase heat transfer and flame spread predictions.

### 5.2.2 Combustion

The most important difference between the majority of the CFD applications and the fire CFD is what drives the flow. In typical non-fire CFD, the boundary conditions such as inflow velocity drive the flow. Fire problems, in turn, are always driven by the combustion source terms. The accuracy of the combustion model is therefore essential for the quality of the whole simulation.

Fire science has always been a small field compared to combustion science, which is clearly the closest relative. Through the history of fire CFD, the combustion models have been developed for other combustion problems and directly applied to fire problems. For almost 20 years, the eddy break-up (EBU) or eddy dissipation models were the standard. With the EBU, in its simplest form, the local rate of fuel consumption is calculated as [60]

$$R_{FU} = \overline{\rho}\frac{\varepsilon}{k}\min\left[C_R m_{fu}, \frac{C'_R m_{ox}}{s}\right] \tag{8}$$

where $\varepsilon$ and $k$ are the turbulent diffusivity and energy, respectively; $m_{fu}$ and $m_{ox}$ are the time averaged mass fractions of fuel and oxidant, respectively; $s$ denotes

the stoichiometric oxygen to fuel mass ratio and $C_R$ and $C''_R$ are empirical constants. The form of EBU expression is based mainly on dimensional arguments. Ratio $k/\varepsilon$ is the turbulent time scale. If the turbulence intensity is high, so is the fuel consumption. For the prediction of secondary species, like CO and HCl, and soot, more advanced models based on the laminar flamelets have been used [90].

In LES, it is obvious that the EBU type of model cannot be used because the turbulence quantities are not calculated. The models developed by the combustion scientists for LES are usually based on the use of flamelets and rely on good spatial accuracy where both temperature and concentration fields are well captured in the vicinity of the reaction zone. From this starting point, the range of possible physical models is only limited by the imagination of the engineers or mathematicians and the requirement of computational efficiency. In a typical fire simulation, neither the temperature nor the species concentrations are accurately captured. The robustness can thus only be achieved by simplicity.

In FDS, a relatively simple flame sheet model, presented in Paper III of the thesis, has been used. The local heat release rate is based on the mass loss rate of oxygen that is computed from the mixture fraction diffusion across the flame surface using the following formula:

$$\dot{m}''_{O_2} = -\frac{dY_{O_2}}{dZ}\rho D \nabla Z \cdot \vec{n}\Big|_{Z=Z_f} \tag{9}$$

where $Y_{O2}$ is the oxygen mass fraction, $D$ is the diffusion coefficient and $\vec{n}$ is the flame surface normal. The derivative of the oxygen mass fraction, $dY_{O2}/dZ$, depends only on the assumed chemical reaction. The model has performed very well for most fire scenarios but has had problems capturing some of the more complicated phenomena, such as under-ventilated fires and local ignition and extinction. An extension of the single-scalar mixture fraction model to a two- or three-scalar version has been made in the latest version of FDS [61] in order to capture these effects. The use of laminar flamelet combustion models within FDS have been studied by Yang et al. [91] and Kang & Wen [92]. Unfortunately, the performance or advantage over the simple flame-sheet model in large-scale fire simulation was not demonstrated in these studies. In large-scale calculations, the mixture fraction and temperature fields close to the flame sheet have

overshoots, caused by the second-order transport scheme. It is still unclear how the laminar flamelet models that require both second and first moments of the local mixture fraction field could work in this situation.

### 5.2.3 Radiation

In enclosure fires, radiation may be the dominating mode of heat transfer. For flames burning in an open atmosphere, the radiative fraction of overall heat transfer ranges from less than 0.1 up to 0.4, depending both on the fuel type and the fire diameter [93]. Due to the important role that the radiation plays in fires, all the fire CFD models have a radiation model that solves the radiation transport equation (RTE) [94, 95]

$$\underbrace{\mathbf{s}\cdot\nabla I_\lambda(\mathbf{x},\mathbf{s})}_{\text{rate of change}} = -\underbrace{\left[\kappa_\lambda(\mathbf{x})+\sigma_\lambda(\mathbf{x})\right]I_\lambda(\mathbf{x},\mathbf{s})}_{\text{rate of attenuation}} + \underbrace{\kappa_\lambda(\mathbf{x})I_b(\mathbf{x},\lambda)}_{\text{esmission source}} + \underbrace{\frac{\sigma_\lambda(\mathbf{x})}{4\pi}\int_{4\pi}\Phi(\mathbf{s},\mathbf{s}')I_\lambda(\mathbf{x},\mathbf{s}')d\Omega'}_{\text{in-scattering}} \tag{10}$$

where $\mathbf{s}$ is the unit direction vector; $I_\lambda$ is the intensity at wavelength $\lambda$; $\kappa_\lambda(\mathbf{x})$ and $\sigma_\lambda(\mathbf{x})$ are the local absorption and scattering coefficients at $\lambda$, respectively; $I_b$ is the emissive power of the medium; $\Phi(\mathbf{s},\mathbf{s}')$ is the scattering phase function giving the scattered intensity from direction $\mathbf{s}'$ to $\mathbf{s}$. The terms of the RTE have the following interpretations: The left hand side is the rate of change of the intensity in direction $\mathbf{s}$; the first right hand side term describes the attenuation by absorption and scattering to other directions; the second right hand side term is the emission source term; the last right hand side term is the in-scattering integral, describing how much intensity is gained by scattering from all the other directions to the present direction. The intensity depends on place, direction and wavelength. Typically, the wavelength dependence is removed by first integrating the RTE over the spectrum, and solving RTE for the integrated field.

Like combustion modelling, the development of radiation modelling in fire CFD has consisted mostly of the copying of techniques developed for combustion simulations. However, in fires the radiation modelling may be even more challenging and its role more pronounced than in the pure combustion problems.

A wide range of different radiation models have been used for fire CFD over the years. The models mainly differ from each other in the way how they solve the spatial and angular field of intensity. The simple models like P-1 and six flux models [94] were popular in the early years. In P-1, the diffusion approximation of RTE is adopted, and spherical harmonics are used to describe the intensity. It is best suited for optically thick cases where intensity fields are fairly smooth. The six-flux model in turn is related to the use of Cartesian grid system; the intensity is solved in the six co-ordinate directions. The ray tracing models such as Discrete Transfer (DT) [96] are theoretically good for fires but may become computationally expensive. In DT, RTE is integrated along the imaginary lines of sight, or rays, starting from the boundaries of the domain. The flux models like Discrete Ordinates Methods (DOM) [95] and Finite Volume Method (FVM) [57] are currently the most popular in new codes. In these models, the solid angle is first divided to small control angles or directions, and the flux of intensity for each direction is solved separately in space. DOM and FVM are very similar techniques. In DOM, the angular distributions are defined by generalized $S_N$ and $T_N$ quadratures. In FVM, the polar/azimuthal discretization is code specific but the angular integration is performed exactly. The most general technique is the use of Monte Carlo where the radiative emission and absorption processes are modelled by sending photons with random energy and direction. It is currently beyond the computational resources in most practical simulations, but an important validation tool for the other models. However, MC can be used if the spatial resolution of the simulation is very coarse, in which case the total number of photons does not increase too much. Various modelling approaches for radiative heat transfer in pool fires are compared in [97].

Another feature of RTE that needs modelling is the calculation of the absorption coefficient $\kappa(\mathbf{x},\lambda)$, which depends on the local gas and soot concentrations. In a typical fire CFD, a grey gas is assumed, which means that a single value is used for the whole spectrum. Some aspects of the spectral resolution can be captured by dividing the spectrum to a relatively small number of bands, and solving a separate RTE for each band. In the combustion literature, a large number of wide-band models have been developed to account for the band-structure of the emission spectra of the most important combustion gases. The most accurate results could be obtained by using a narrow-band model, where separate RTEs are solved for hundreds of wavelengths. This is still too expensive for practical

fire CFD. The use of correlated-$k$ [98] and spectral narrow-band and global gas radiation models [99, 100] have been studied at Kingston University.

Next, some of the challenges of radiation modelling are discussed:

i. **Inhomogeneity**: The strong inhomogeneity of the optical properties and temperature field makes the simplest and fastest models like P-1 and six flux models very inaccurate. The presence of large optically thin areas aggravates the ray effect for all the models dealing with discrete directions, especially the ray tracing methods.

ii. **Emission source term**: For spectrally integrated RTE, the emission source term is

$$\kappa I_b = \kappa T^4 \tag{11}$$

where $T$ is the local temperature. Due to the $T^4$-dependence, it is extremely sensitive to errors in temperature. For example, a 15% underestimation of temperature would lead to a source term that is 48% too small. In large-scale simulation, this kind of error in the flame region can rarely be avoided. The problem is typically solved by modelling the emission term either as a linear function of heat release rate (used in FDS) or using precomputed flamelet libraries (e.g. SOFIE).

iii. **Spectral dependence**: Ways to handle the spectral dependence of the radiation are currently being studied to find computationally efficient ways to include both the smooth emission spectrum from soot and solid surfaces, and the sharp peaks of gaseous combustion products.

iv. **Time dependence**: The inherent time dependence of the fires sets strong requirements for the computational efficiency. In RANS codes, the radiation field must be updated within the internal iterations of the time step, but the computational cost can be relaxed by solving RTE only every $N$th iteration. In SOFIE, for example, it is typical to use $N$=10. In FDS, the time accuracy of the radiation field has been relaxed by solving the FVM equations typically every third time step and only part of the directions at the time.

v. **Scattering**: When the beam of radiation meets soot or water droplets, it is scattered to all directions. The scattering has a tremendous effect on the radiation blocking ability of the fine water sprays and smoke. Due to the computational complexity, scattering has often been neglected in fire CFD codes. To accurately simulate the water mist and sprinkler systems, this effect should be taken into account. There are actually two challenges related to the scattering: The first challenge is the computation of the radiative properties, i.e. absorption and scattering coefficients and the scattering phase function. For water droplets, Mie-theory can be used for the calculation of *single droplet* radiative properties. Free subroutines performing these Mie-calculations are available for use in the radiation solvers [101, 102]. The integration over the spectrum and droplet size distribution must be performed in the model. The second challenge is the computation of the scattering integral. The first approximation is to use isotropic scattering, which considerably simplifies the computation. Full integrations using DOM and FVM have been performed in simplified scenarios [103, 104, 105], but not yet in practical fire CFD. In FDS, the scattering integral is approximated by a combination of functions describing isotropic and forward scattering, as explained in Paper V of this thesis and summarized in Section 6.2.5.

vi. **Soot**: In fires, soot is usually the most important source and absorber of radiation. The modelling of soot formation and oxidation processes is therefore important for the accurate prediction of radiation emissions. Detailed models that solve the fields of soot number density and mass fraction have been developed over the years, and implemented also in fire CFD codes such as SOFIE, and more recently in [106] and [107]. In post-flame conditions, the problem is mostly following of the soot produced in the flame zone. Currently, FDS can only follow this "inactive" soot, but an attempt to include more advanced soot modelling was presented by Lautenberger et al. [108]. Unfortunately, the soot formation and oxidation processes are sensitive to the temperature and the same problems appear as in the detailed modelling of combustion.

### 5.2.4 Solid phase heat transfer

The solution of solid phase heat transfer is needed in the analysis of structures response to fires and the simulation of flame spread on solid surfaces. The solution of this conjugate heat transfer problem is typical for fires but rarely found from commercial CFD packages. Over the years, different techniques have been developed to tackle this problem. Since the solid phase heat transfer is a completely separate problem from the fluid dynamics problem, the following techniques are code specific, having no relation to the use of RANS or LES.

i. The simplest technique is to use separate numerical solvers for the fluid and solid phases and to exchange information through the boundary conditions. The use of separate solver allows a flexible gridding inside the solid phase, which is required due to the three orders of magnitude in thermal conductivities. It is also easy to include various physical phenomena like charring and moisture transfer. Quite often, one-dimensional solution of the heat conduction equation on each wall cell is accurate enough. This technique is implemented as an internal subroutine for FDS.

ii. Separate solvers of three-dimensional heat conduction can be linked to the CFD solver, either as an external code (e.g. KAMELEON) or internal subroutine (SOFIE). Specialized algorithms may be needed to model the connection between the gas and solid phases due to the disparity in length and time scales [109]. In the recent ECSC project concerning the CFD modelling of natural fires (*The development and validation of a CFD-based engineering methodology for evaluating thermal action on steel and composite structures, co-ordinated by BRE, UK*), a three-dimensional heat conduction model was developed for SOFIE code. The model allows the simulation of temperature profiles in structural metal elements such as beams and columns. The information between the fluid and solid phases is passed through the boundary conditions, and fine structural gridding can be used. The solver requires a special user interface developed by BRE (UK) and is limited to I-shape structures.

iii. A full coupling of the solid and fluid phases can be achieved by solving only one enthalpy equation, common for both phases. Such an approach was used in SOFIE code [70], but the use of a structured grid system

usually prevented the necessary refinement inside the solids. A fully coupled system is being developed in the C-SAFE project at University of Utah [87]. However, the practical applications of this code have not been demonstrated, probably due to the extremely high computational cost of the solver.

### 5.2.5 Flame spread

The simulation of flame spread is one of the most challenging and most important physical modelling problems in fire CFD. The importance is caused by the need to simulate fire development instead of fire consequences. The challenge comes from the fact that in order to simulate the flame spread process, one must be able to simulate all three sub-processes:

i. The development of far field temperature and radiation. In large fires, the far field radiation dominates the heat transfer.

ii. The flame structure and heat transfer in the region close to the wall. In small fires, the near field flames are responsible for most of the heat transfer to the wall. In a typical fire simulation, this region is totally covered by one or two grid cells, making it impossible to capture the flame structure and temperature distribution. Some kind of sub-grid scale model of this region is needed in fire CFD codes to accurately model the flame spread. The sub-grid scale model might use the ideas of wall functions and boundary layer flame structures [110].

iii. The heat transfer and pyrolysis inside the solid material.

In the context of fire CFD, the flame spread simulation usually means the ability to predict the fire growth starting from a *small initial fire* or ignition point, where all three sub-processes are important but the second sub-process dominates the heat transfer. The fire spread, in turn, means the ignition of solid surfaces in the presence of a relatively *large initial fire* dominating the heat transfer by radiation. In practice, the small and large initial fires should be defined relative to the CFD mesh: A large initial fire spans from 10 to 20 grid cells, for example. Currently, none of fire CFD codes can reliably predict the flame spread, with the exception of some relatively simple cases. The reason is

the inability to capture the near wall phenomena, as explained above. Despite this fact, fire spread simulations are routinely performed.

### 5.2.6 Multiple phases

The transport of water droplets can be simulated with practically all the fire CFD codes. The level of detail may vary, but the basics of the mass and heat transfer can be handled. Monodisperse droplets have traditionally been assumed by the two-phase solvers, but in fires, it is important to include the whole size distribution of droplets, because the different droplet sizes have very different effects in the fire: large droplets transport most of the water mass and have a sufficient momentum to penetrate the buoyant flow. Small droplets in turn block radiation more efficiently than large droplets. The evaporation of droplets is important to include for the simulation of the gas phase suppression effects. Far more difficult than the actual modelling is to find good boundary conditions for water nozzles. Surprisingly little data has been published on the droplet size and velocity distributions of common sprinkler or water mist nozzles. To some extent, the uncertainty of droplet size distributions can be reduced by modelling the secondary droplet breakup mechanism [110], i.e. by trying to predict the stable droplet size of the water jet. Various models for droplet breakup and coalescence were summarized by Madsen [112].

## 5.3 Numerical implementations

The efficiency and robustness of the numerical implementation is often equally or even more important than the sophistication of the physical models. For academic purposes, the implementation of the most elaborate physical models may be justified, but quite often the resulting code is of little use for fire engineering. The requirement of computational efficiency is even more pronounced when CFD is used as a tool of probabilistic analysis, as discussed in Part I of the thesis.

Most fire CFD codes use structured meshes; some of them curvilinear and some Cartesian. The advantage of the Cartesian mesh is the simplicity of the solver, which often leads to fast computing and reduced risk of coding errors. The

obvious weakness is the difficulty of describing complex geometries. To overcome this, methods such as cut-cell method have been developed [113] Naturally, there are cases where the geometry could be much more efficiently described by curved structured or unstructured mesh. Therefore, the comparison of various codes based on some individual property is not justified. The most important question is: "Which code gives the required answer with lowest cost and sufficient reliability?" The cost naturally includes both the price of the software and the required hardware, but also the required working time and learning.

A common way to add some flexibility to the structured and Cartesian solvers is the so-called multi-block technique, where the solution domain is divided to individual blocks having a their own computational grids. The availability of low-cost personal computers and the possibility to build small computer clusters has increased the interest in the parallel processing which is often based on the domain decomposition where each block is associated with its own processor. This parallelisation technique has the following advantages: (1) It is relatively easy to implement, although the efficient communications need careful organisation of the data structures. (2) It can be very efficient when the individual blocks share only a small amount of common information. The natural boundaries of the fire scenario, such as walls and floors, should be used as block boundaries whenever possible. The disadvantages of this technique include: (1) The possibility of instability, especially in LES, if the block boundaries are out of phase. (2) The difficulty of load balancing.

## 5.4 User interfaces

The quality of the user interface has been claimed to be crucial for the reliability and usability of fire CFD codes. From this perspective, it has been quite surprising to see the success of FDS, having originally no user interface at all for input. Lately, such an user interface has become available as a commercial software [114]. Naturally, the availability of a good post processing tool has been crucial for the FDS success. One reason for the emphasis on (graphical) user interfaces may have been the large number of controlling parameters in the RANS codes. These parameters have a strong effect on the convergence of the solver, but are difficult to understand by ordinary users. In engineering applications with complicated geometries and high requirements for efficiency, a

well-designed graphical user interface may help to avoid user errors by giving instant visual feedback. At best, the interface guides the user through the modelling process thus reducing the need to remember the meanings of the input parameters and syntaxes and therefore improving the modelling reliability.

Several challenges are associated with the development of the graphical user interfaces: (1) They must be maintained parallel with the actual solver, and this may be more laborious than the solver development. (2) It may be difficult to select which features of the CFD code should be available in the user interface and which should not. (3) So far, the tools of 3D geometry definition are neither versatile nor easy to use. In most cases, it is faster to write the definition in a simple text file than create the three-dimensional drawing. Tools that use CAD and other building design information may change the situation in the future. Automatic generation of FDS models from a building product model has been studied in [115] and [116].

# 6. Development of the radiation solver

## 6.1 Radiative transport equation

The radiative transport equation (RTE) for spectral intensity $I_\lambda$ passing through a participating medium is [94, 95]

$$\frac{1}{c}\frac{\partial I_\lambda(\mathbf{x},\mathbf{s},t)}{\partial t} + \mathbf{s}\cdot\nabla I_\lambda(\mathbf{x},\mathbf{s},t) = -\left[\kappa_\lambda(\mathbf{x}) + \sigma_\lambda(\mathbf{x})\right] I_\lambda(\mathbf{x},\mathbf{s},t) + B_\lambda(\mathbf{x},t) + \frac{\sigma_\lambda(\mathbf{x})}{4\pi}\int_{4\pi}\Phi(\mathbf{s},\mathbf{s}')I_\lambda(\mathbf{x},\mathbf{s}',t)d\Omega' \tag{12}$$

For most engineering applications, the time derivative can be neglected because of the large magnitude of $c$. If we assume that a local thermodynamic equilibrium is established and that the Kirchoff's law is valid, the emission term $B_\lambda(\mathbf{x},t)$ is related to the Planck function

$$B_\lambda(\mathbf{x},t) = \kappa_\lambda(\mathbf{x}) I_{\lambda b}(T) = \kappa_\lambda(\mathbf{x})\frac{e_{\lambda b}(T)}{\pi} \tag{13}$$

The RTE for absorbing-emitting and scattering medium can now be written as

$$\underbrace{\mathbf{s}\cdot\nabla I_\lambda(\mathbf{x},\mathbf{s})}_{\text{rate of change}} = \underbrace{-\left[\kappa_\lambda(\mathbf{x}) + \sigma_\lambda(\mathbf{x})\right] I_\lambda(\mathbf{x},\mathbf{s})}_{\text{rate of attenuation}} + \underbrace{\kappa_\lambda(\mathbf{x}) I_{\lambda b}(\mathbf{x})}_{\text{esmission source}} + \underbrace{\frac{\sigma_\lambda(\mathbf{x})}{4\pi}\int_{4\pi}\Phi(\mathbf{s},\mathbf{s}')I_\lambda(\mathbf{x},\mathbf{s}')d\Omega'}_{\text{in-scattering}} \tag{14}$$

where the temperature dependence of the Planck function is implicit through the position vector **x**. In a non-scattering case, the RTE simplifies to

$$\mathbf{s}\cdot\nabla I_\lambda(\mathbf{x},\mathbf{s}) = \kappa_\lambda(\mathbf{x})\left[I_{\lambda b}(\mathbf{x}) - I_\lambda(\mathbf{x},\mathbf{s})\right] \tag{15}$$

## 6.2 Model formulation

This section describes the approximations and assumptions that are made during the development of the numerical radiation transport solver in FDS. The general description and applications of the Finite Volume radiation solver were provided in papers III and IV of the thesis. Paper V described the model for radiation-water spray interaction. Section 7 summarizes the results of two verification tests, also available in the FDS (version 5) User's guide [62] and the validation tests originally presented in papers IV and V.

### 6.2.1 Spectrally averaged RTE

In practical fire simulations, the spectral (λ) dependence of thermal radiation cannot be solved accurately. Instead, the radiation spectrum can be divided into a relatively small number of wavelength bands and a separate RTE is derived for each band. For a non-scattering gas, the band specific RTE is

$$\mathbf{s}\cdot\nabla I_n(\mathbf{x},\mathbf{s}) = \kappa_n(\mathbf{x})\left[I_{nb}(\mathbf{x}) - I_n(\mathbf{x},\mathbf{s})\right], \qquad n = 1...N \tag{16}$$

where $I_n$ is the intensity integrated over the band $n$, and $\kappa_n$ is the appropriate mean absorption coefficient within the band. The source term can be written as a fraction of the blackbody radiation

$$I_{nb} = F_n \frac{\sigma T^4}{\pi} \tag{17}$$

where $\sigma$ is the Stefan-Boltzmann constant. $F_n$ is defined as

$$\begin{aligned} F_n = F_{\lambda_{\min}-\lambda_{\max}} &= F_{0-\lambda_{\max}} - F_{0-\lambda_{\min}} = F_{0-\lambda_{\max}T} - F_{0-\lambda_{\min}T} \\ &= \frac{1}{\sigma}\left[\int_0^{\lambda_{\max}T} \frac{e_{\lambda b}(\lambda,T)}{T^5}\,d(\lambda T) - \int_0^{\lambda_{\min}T} \frac{e_{\lambda b}(\lambda,T)}{T^5}\,d(\lambda T)\right] \end{aligned} \tag{18}$$

where $\lambda_{\min}$ and $\lambda_{\max}$ are the lower and upper bounds of the wavelength band, respectively [94]. $F_{0\text{-}\lambda T}$ can be written as an infinite series [117]

$$F_{0-\lambda T} = \frac{15}{\pi^4} \sum_{j=1}^{\infty} \frac{e^{-jz}}{j} \left( z^3 + \frac{3z^2}{j} + \frac{6z}{j^2} + \frac{6}{j^3} \right) \tag{19}$$

where $z = C_2/\lambda T$ and $C_2$ is the Planck's second radiation constant. In FDS, 50 terms are used in the series to compute $F_{0-\lambda T}$. The values of $F_{0-\lambda T}$ are tabulated in the range $0 < \lambda T < 10^5$ μmK with 25 μmK intervals. During the simulation, the values of $F_n$ are found by table-lookup using the band limits and local temperature.

When the intensities corresponding to the bands are known, the total intensity is calculated by summing over all the bands

$$I(\mathbf{x},\mathbf{s}) = \sum_{n=1}^{N} I_n(\mathbf{x},\mathbf{s}) \tag{20}$$

Even with a reasonably small number of bands, solving multiple RTEs is very time consuming. Fortunately, in most large-scale fire scenarios, soot is the most important combustion product controlling the thermal radiation from the fire and hot smoke. As the radiation spectrum of soot is continuous, it is possible to assume that the gas behaves as a grey medium. The spectral dependence is then lumped into one absorption coefficient ($N = 1$) and the source term is given by the blackbody radiation intensity

$$I_b = \frac{\sigma T^4}{\pi} \tag{21}$$

This is the default mode of FDS and appropriate for most problems of fire engineering. In optically thin flames, where the amount of soot is small compared to the amount of $CO_2$ and water, the grey gas assumption may produce significant overpredictions of the emitted radiation. From a series of numerical experiments it has been found that six bands ($N = 6$) are usually enough to improve the accuracy in these cases. The limits of the bands are selected to give an accurate representation of the most important radiation bands of $CO_2$ and water. If the absorption of the fuel is known to be important, separate bands can be reserved for fuel, and the total number of bands is increased to nine ($N = 9$).

For simplicity, the fuel is assumed to be $CH_4$. The limits of the bands are shown in Table 2.[2]

*Table 2. Limits of the wavelength bands in both wave numbers ($\nu$) and wave lengths ($\lambda$).*

| 9 Band Model | 1 | 2 | 3 | 4 | 5 | 6 | 7 | 8 | 9 |
|---|---|---|---|---|---|---|---|---|---|
| Major Species | Soot | $CO_2$ $H_2O$, Soot | $CH_4$ Soot | Soot | $CO_2$ Soot | $H_2O$ | $H_2O$ $CH_4$, Soot | Soot | Soot |
| $\nu$ (1/cm) | 10000 | 3800 | 3400 | 2800 | 2400 | 2174 | 1429 | 1160 | 1000 | 50 |
| $\lambda$ (μm) | 1.00 | 2.63 | 2.94 | 3.57 | 4.17 | 4.70 | 7.00 | 8.62 | 10.0 | 200 |

| 6 Band model | 1 | 2 | 3 | 4 | 5 | 6 |
|---|---|---|---|---|---|---|
| Major Species | Soot | $CO_2$ $H_2O$, Soot | $CH_4$ Soot | $CO_2$ Soot | $H_2O$, $CH_4$, Soot | Soot |

For the calculation of the grey or band-mean absorption coefficients, $\kappa_n$, a narrow-band model, RadCal [118], has been implemented in FDS. At the start of a simulation, the absorption coefficients are tabulated as a function of mixture fraction and temperature. During the simulation, the local absorption coefficient is found by table-lookup.

In calculations of limited spatial resolution, the source term, $I_b$, in the RTE requires special treatment. In the neighbourhood of the flame sheet, both temperatures and absorption coefficient are smeared out over a grid cell and are thus considerably lower than one would expect in a diffusion flame. Because of its fourth-power dependence on the temperature, the source term must be modelled in those grid cells cut by the flame sheet. Elsewhere, there is greater confidence in the computed temperature, and the source term can be computed directly

[2] The presented band structure corresponds to version 5 of FDS [61]. Slightly different band limits were used in the pool fire simulations in Paper II.

$$\kappa I_{nb} = \begin{cases} F_n \kappa \sigma T^4 / \pi & \text{Outside flame zone} \\ F_n \max\left(\chi_r \dot{q}''' / 4\pi, \kappa \sigma T^4 / \pi\right) & \text{Inside flame zone} \end{cases} \tag{22}$$

Here, $\dot{q}'''$ is the chemical heat release rate per unit volume and $\chi_r$ is an empirical estimate of the *local* fraction of that energy emitted as thermal radiation. For a small fire ($D < 1$ m), the local $\chi_r$ is approximately equal to its global counterpart. However, as the fire increases in size, the global value will typically decrease due to the net absorption of the thermal radiation by the increasing smoke mantle.

The boundary condition for the radiation intensity leaving a diffuse wall is given as

$$I_{nw}(\mathbf{s}) = F_n \frac{\varepsilon \sigma T_w^4}{\pi} + \frac{1-\varepsilon}{\pi} \int_{\mathbf{s}'\cdot\mathbf{n}<0} I_{nw}(\mathbf{s}') |\mathbf{s}' \cdot \mathbf{n}| d\mathbf{s}' \tag{23}$$

where $I_w(\mathbf{s})$ is the intensity at the wall, $\varepsilon$ is the mean hemispherical emissivity, and $T_w$ is the wall surface temperature. The walls are assumed to behave as diffuse reflectors when $\varepsilon < 1$.

The radiant heat flux vector is defined as

$$\dot{\mathbf{q}}''(\mathbf{x}) = \int_{4\pi} \mathbf{s}' I(\mathbf{x}, \mathbf{s}') d\mathbf{s}' \tag{24}$$

and the total combined intensity as

$$U(\mathbf{x}) = \sum_{n=1}^{N} \int_{4\pi} I_n(\mathbf{x}, \mathbf{s}') d\mathbf{s}' \tag{25}$$

The radiative loss term in the gas phase energy equation is

$$-\nabla \cdot \dot{\mathbf{q}}_r''(\mathbf{x})(\text{gas}) = \kappa(\mathbf{x})\left[U(\mathbf{x}) - 4\pi I_b(\mathbf{x})\right] \tag{26}$$

In words, the net radiant energy gained by a control volume is the difference between that which is absorbed and that which is emitted.

### 6.2.2 Discretized RTE

The radiative transport equation (16) is solved using techniques similar to those for convective transport in finite volume methods for fluid flow [57], thus the name given to it is the Finite Volume Method (FVM). Note that the procedure outlined below is appropriate for each band of a wide band model, thus the subscript *n* has been removed for clarity.

To obtain the discretized form of the RTE, the unit sphere is divided into a finite number of solid angles. In each grid cell, a discretized equation is derived by integrating equation over the volume of cell *ijk* and the control angle $\partial\Omega^l$, to obtain

$$\int_{\partial\Omega}\int_{V_{ijk}} \mathbf{s}\cdot\nabla I(\mathbf{x}',\mathbf{s}')d\mathbf{x}'d\mathbf{s}' = \int_{\partial\Omega^l}\int_{V_{ijk}} \kappa(\mathbf{x}')\left[I_b(\mathbf{x}') - I(\mathbf{x}',\mathbf{s}')\right]d\mathbf{x}'d\mathbf{s}' \tag{27}$$

The volume integral on the left-hand side is replaced by a surface integral over the cell faces using the divergence theorem. Assuming that the radiation intensity $I(\mathbf{x},\mathbf{s})$ is constant on each of the cell faces, the surface integral can be approximated by a sum over the cell faces. Assuming further that $I(\mathbf{x},\mathbf{s})$ and $\kappa(\mathbf{x})$ are constants within the volume $V_{ijk}$ and over the angle $\partial\Omega^l$ we obtain

$$\sum_{m=1}^{6} A_m I^l_{ijk,m}\int_{\partial\Omega^l}(\mathbf{s}'\cdot\mathbf{n}_m)d\mathbf{s}' = \kappa_{ijk}\left[I_{b,ijk} - I^l_{ijk}\right]V_{ijk}\partial\Omega^l \tag{28}$$

where

| | |
|---|---|
| $I^l_{ijk}$ | is the radiant intensity in direction $\mathbf{s}^l$ in cell *ijk* |
| $I^l_{ijk,m}$ | is the radiant intensity in direction $\mathbf{s}^l$ at face *m* of cell *ijk* |
| $I_{b,ijk}$ | is the radiant source term in the cell *ijk* |
| $\partial\Omega^l$ | is the solid angle centred around the direction vector $\mathbf{s}^l$ |
| $V_{ijk}$ | is the volume of cell *ijk* |
| $A_m$ | is the area of cell face *m* of cell *ijk* |
| $\mathbf{n}_m$ | is the unit normal vector of the cell face *m* of cell *ijk.* |

Note that while the intensity is assumed constant within the angle $\partial\Omega^l$, its direction covers the angle $\partial\Omega^l$ exactly.

In Cartesian coordinates, the normal vectors $\mathbf{n}_m$ are the base vectors of the coordinate system. As a result, the integrals over the solid angle do not depend on the physical coordinate, but the direction only, and can be calculated analytically. Equation (28) can be simplified to

$$a_{ijk}^{l} I_{ijk}^{l} = a_{x}^{l} I_{xu}^{l} + a_{y}^{l} I_{yu}^{l} + a_{z}^{l} I_{zu}^{l} + b_{ijk}^{l} \tag{29}$$

where

$$a_{ijk}^{l} = A_x \left| D_x^l \right| + A_y \left| D_y^l \right| + A_z \left| D_z^l \right| + \kappa_{ijk} V_{ijk} \delta\Omega^l \tag{30}$$

$$\begin{aligned} a_x^l &= A_x \left| D_x^l \right| \\ a_y^l &= A_y \left| D_y^l \right| \\ a_z^l &= A_z \left| D_z^l \right| \end{aligned} \tag{31}$$

$$b_{ijk}^{l} = \kappa_{ijk} I_{b,ijk} V_{ijk} \delta\Omega^l \tag{32}$$

$$\delta\Omega^l = \int_{\Omega^l} d\Omega = \int_{\delta\phi\delta\theta} \int \sin\theta d\theta d\phi \tag{33}$$

$$\begin{aligned} D_x &= \int_{\Omega^l} \left( \mathbf{s}^l \cdot \mathbf{i} \right) d\Omega \\ &= \int_{\delta\phi\delta\theta} \int \left( \mathbf{s}^l \cdot \mathbf{i} \right) \sin\theta d\theta d\phi \\ &= \int_{\delta\phi\delta\theta} \int \cos\phi \sin\theta \sin\theta d\theta d\phi \\ &= \frac{1}{2} \left( \sin\phi^+ - \sin\phi^- \right) \left[ \Delta\theta - \left( \cos\theta^+ \sin\theta^+ - \cos\theta^- \sin\theta^- \right) \right] \end{aligned} \tag{34}$$

$$
\begin{aligned}
D_y &= \int_{\Omega^l} \left(\mathbf{s}^l \cdot \mathbf{j}\right) d\Omega \\
&= \int_{\delta\phi\delta\theta} \int \sin\phi \sin\theta \sin\theta d\theta d\phi \\
&= \frac{1}{2}\left(\cos\phi^- - \cos\phi^+\right)\left[\Delta\theta - \left(\cos\theta^+ \sin\theta^+ - \cos\theta^- \sin\theta^-\right)\right]
\end{aligned}
\tag{35}
$$

$$
\begin{aligned}
D_z &= \int_{\Omega^l} \left(\mathbf{s}^l \cdot \mathbf{k}\right) d\Omega \\
&= \int_{\delta\phi\delta\theta} \int \cos\theta \sin\theta d\theta d\phi \\
&= \frac{1}{2}\Delta\phi\left(\sin^2\theta^+ - \sin^2\theta^-\right)
\end{aligned}
$$

Here **i**, **j** and **k** are the base vectors of the Cartesian coordinate system. $\theta^+$, $\theta^-$, $\phi^+$ and $\phi^-$ are the upper and lower boundaries of the control angle in the polar and azimuthal directions, respectively, and $\Delta\theta = \theta^+ - \theta^-$ and $\Delta\phi = \phi^+ - \phi^-$. The solution method of equation (29) is based on an explicit marching sequence [119]. The marching direction depends on the propagation direction of the radiation intensity. As the marching is done in the "downwind" direction, the "upwind" intensities in all three spatial directions are known, and the intensity $I^l_{ijk}$ can be solved directly from an algebraic equation. This makes the numerical solution of the FVM very fast. Iterations are needed only to account for the reflective boundaries, optically very thick scenarios and scattering. In practice, no iterations are made in FDS because the frequency of radiation solutions is quite high due to the small time step of the LES flow solver, and the time accuracy of the radiative heat fluxes is sufficient for engineering purposes. Some degree of delay between the flow and radiation solutions is accepted.

### 6.2.3 Spatial and angular discretization

The grid used for the RTE solver is the same as for the fluid solver. The rectangular domain is divided into rectangular grid cells. Each cell is assigned indices *i*, *j* and *k*, representing the position of the cell in *x*, *y* and *z* directions, respectively.

The coordinate system used to discretize the solid angle is shown in Figure 7. The discretization of the solid angle is done by dividing first the polar angle, θ, into $N_\theta$ bands, where $N_\theta$ is an even integer. Each θ-band is then divided into $N_\phi(\theta)$ parts in the azimuthal (ϕ) direction. $N_\phi(\theta)$ must be divisible by 4. The numbers $N_\theta$ and $N_\phi(\theta)$ are chosen to give the total number of angles $N_\Omega$ as close to the value defined by the user as possible. $N_\Omega$ is calculated as

$$N_\Omega = \sum_{i=1}^{N_\theta} N_\phi(\theta_i) \tag{36}$$

The distribution of the angles is based on empirical rules that try to produce equal solid angles $\delta\Omega^l = 4\pi/N_\Omega$. The number of θ-bands is

$$N_\theta = 1.17 N_\Omega^{1/2.26} \tag{37}$$

rounded to the nearest even integer. The number of ϕ-angles on each band is

$$N_\phi(\theta_i) = \max\left\{4, \frac{N_\Omega}{2}\left[\cos(\theta_i^-) - \cos(\theta_i^+)\right]\right\} \tag{38}$$

rounded to the nearest integer that is divisible by 4. $\theta^-$ and $\theta^+$ are the lower and upper bounds of the θ-band, respectively. The discretization is symmetric with respect to the planes $x = 0$, $y = 0$, and $z = 0$. This symmetry has three important benefits: First, it avoids the problems caused by the fact that the first-order upwind scheme, used to calculate intensities on the cell boundaries, is more diffusive in non-axial directions than axial. Second, the treatment of the mirror boundaries becomes very simple. Third, it avoids the so-called "overhang" situations, where **s'·i**, **s'·j** or **s'·k** would change sign inside the control angle. These "overhangs" would make the resulting system of linear equations more complicated. In the axially symmetric case, these "overhangs" can not be avoided, and a special treatment, developed by Murthy and Mathur [120], is applied. In these cases, $N_\phi(\theta)$ is kept constant, and the total number of angles is $N_\Omega = N_\theta \times N_\phi$. In addition, the angle of the vertical slice of the cylinder is chosen to be the same as $\Delta\phi$.

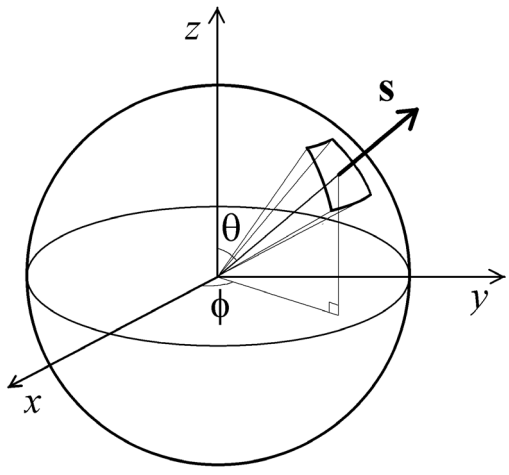


*Figure 7. The discretization of the angular direction in FVM for radiation.*

### 6.2.4 Computation of cell face intensities

To close the system described by equation (29), the cell face intensities $I^l_{ijk,m}$ must be computed. Several alternatives have been proposed, but the FVM does not constrain this choice provided that conservation is rigorously maintained [121]. To illustrate some typical schemes to compute the cell face intensities, let us consider the situation shown in Figure 8. The task is to solve the intensity $I^l$ to the direction $\mathbf{s}^l$ at cell *ijk* when the value of $I^l_{(i-1)jk}$ in the cell (*i*-1)*jk* is known. The intensity at the cell face between (*i*-1)*jk* and *ijk* is $I^l_u$.

If the intensity $I^l_{(i-1)jk}$ is written as a weighted sum of cell face intensities

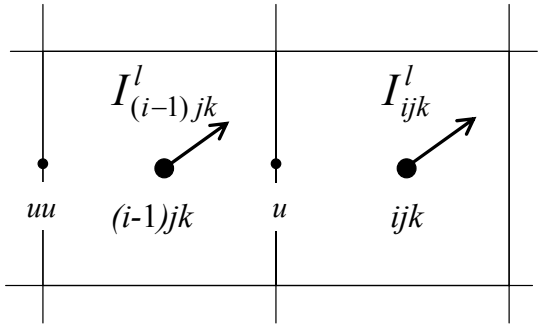


*Figure 8. The notation of cell face intensities.*

$$I^l_{(i-1)jk} = fI^l_u + (1-f)I^l_{uu} \tag{39}$$

we can solve

$$I^l_u = \left[I^l_{(i-1)jk} - (1-f)I^l_{uu}\right]/f \tag{40}$$

The simplest possible approximation is $f = 1$. In the numerical heat transfer literature, the resulting scheme is called the *step scheme*:

$$I^l_u = I^l_{(i-1)jk} \tag{41}$$

The step scheme is first order accurate in space, and is sometimes referred to as the *upwind scheme*. It is very fast to compute, since the cell face intensities are directly taken from the upstream solutions. A scheme of second-order accuracy is obtained by setting $f = 0.5$. The resulting scheme is called *diamond scheme*

$$I^l_u = 2I^l_{(i-1)jk} - I^l_{uu} \tag{42}$$

The diamond scheme is supposed to be more accurate than the step scheme, but like the higher-order schemes in fluid dynamics, it may become unstable in some situations. As a result, the intensities may have positive and negative spikes or unphysical values like $I^l_u < 0$. The diamond scheme requires more memory than the step scheme because the intensities $I^l_{uu}$ must also be stored.

Even higher accuracy can be achieved by the use of exponential schemes where the development of intensity inside the grid cells is computed using the Beer-Lambert law. The *modified exponential scheme* of Chai et al. [122] is formulated as

$$I^l_u = I^l_{(i-1)jk} e^{-\kappa\Delta x} + I_{b,ijk}\left(1 - e^{-\kappa\Delta x}\right) \tag{43}$$

where $\Delta x$ is the distance that the intensity has travelled within cell $(i\text{-}1)jk$. The schemes based on the use of exponential functions may have much higher computing times than the schemes based on simple algebraic operations.

In FDS code, the cell face intensities are computed using the first-order step scheme. The advantage of the lower order accuracy is that the ray effect is actually reduced due to the numerical diffusion. This phenomenon is illustrated in Figure 9 showing the total combined intensity around a methane flame. The step scheme was used in the figure on the left and diamond scheme in the figure on the right. The intensity field of the step scheme is more uniform than the intensity of the diamond scheme, which clearly shows the directions of angular discretization.

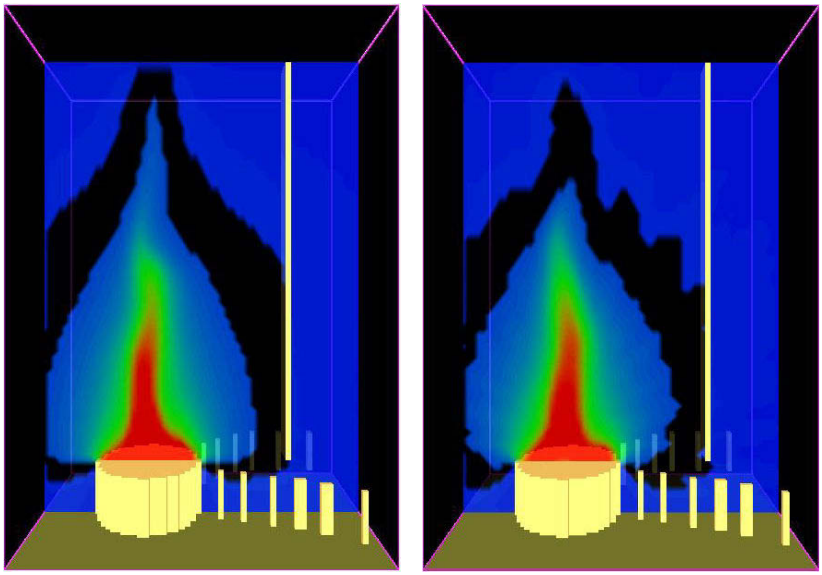

*Figure 9. Effect of intensity interpolation schemes on ray effect. The step scheme is on the left and the diamond scheme is on the right.*

### 6.2.5 Interaction between liquid sprays and radiation

The attenuation of thermal radiation by liquid droplets is an important consideration, especially for water mist systems [123]. Liquid droplets attenuate thermal radiation through a combination of scattering and absorption. The radiation-droplet interaction must therefore be solved for both the accurate prediction of the radiation field and for the droplet energy balance.

The situation of radiation-spray interaction is illustrated in Figure 10. Intensity $I_\lambda(\mathbf{s})$ is entering to a grid cell containing liquid droplets with size distribution

$f(r,\mathbf{x})$. The mass of liquid within the cell is $\rho_d(\mathbf{x})\ V_{ijk}$. Some part of the energy is scattered to an angle $\theta_d$ from the original direction. The scattering is assumed to be axially symmetric around the initial direction.

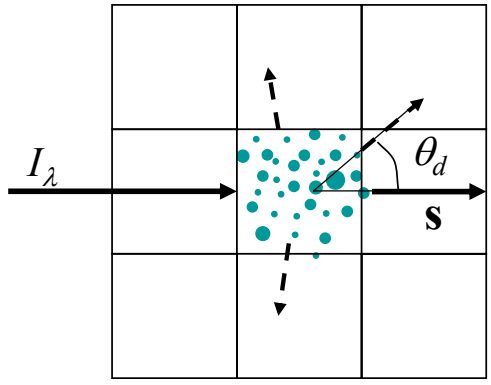


*Figure 10. The radiation-droplet interaction.*

If the gas phase absorption and emission are temporarily neglected for simplicity, the radiative transport equation (14) becomes

$$\mathbf{s}\cdot\nabla I_\lambda(\mathbf{x},\mathbf{s}) = -\left[\kappa_{\lambda,d}(\mathbf{x}) + \sigma_{\lambda,d}(\mathbf{x})\right] I_\lambda(\mathbf{x},\mathbf{s}) + \kappa_{\lambda,d}(\mathbf{x}) I_{b\lambda,d}(\mathbf{x}) + \frac{\sigma_{\lambda,d}(\mathbf{x})}{4\pi}\int_{4\pi}\Phi(\mathbf{s},\mathbf{s}')I_\lambda(\mathbf{x},\mathbf{s}')d\Omega' \tag{44}$$

where $\kappa_{\lambda,d}$ and $\sigma_{\lambda,d}$ are the droplet absorption and scattering coefficients at wavelength $\lambda$, respectively, and $I_{\lambda b,d}$ is the emission term of the droplets. $\Phi(\mathbf{s},\mathbf{s}')$ is a scattering phase function that gives the scattered intensity from direction $\mathbf{s}'$ to $\mathbf{s}$. The local absorption and scattering coefficients are calculated from the local droplet number density $N(\mathbf{x})$ and mean diameter $d_m(\mathbf{x})$ as

$$\kappa_{\lambda,d}(\mathbf{x}) = N(\mathbf{x})\int_{r=0}^{\infty} f(r,d_m(\mathbf{x}))C_a(r,\lambda)dr$$
$$\sigma_{\lambda,d}(\mathbf{x}) = N(\mathbf{x})\int_{r=0}^{\infty} f(r,d_m(\mathbf{x}))C_s(r,\lambda)dr \tag{45}$$

where $r$ is the droplet radius and $C_a$ and $C_s$ are absorption and scattering cross sections, respectively. The droplet number density function $f(r,d_m)$ is assumed to have the same form as the initial droplet size distribution, but a mean diameter depending on the location **x**. For the numerical implementation, the above equations are written in the form

$$\kappa_{\lambda,d}(\mathbf{x}) = A_d(\mathbf{x}) \int_{r=0}^{\infty} \frac{f(r,d_m(\mathbf{x}))C_a(r,\lambda)}{\pi\left[d_m(\mathbf{x})/2\right]^2} dr$$
$$\sigma_{\lambda,d}(\mathbf{x}) = A_d(\mathbf{x}) \int_{r=0}^{\infty} \frac{f(r,d_m(\mathbf{x}))C_d(r,\lambda)}{\pi\left[d_m(\mathbf{x})/2\right]^2} dr \tag{46}$$

where $A_d$ is the total cross sectional area per unit volume of the droplets. $A_d$ is approximated as

$$A_d(\mathbf{x}) \approx \frac{\rho_d(\mathbf{x})}{2\rho_w d_m(\mathbf{x})/3} \tag{47}$$

where $\rho_w$ is the density of liquid water. An accurate computation of the in-scattering integral on the right hand side of equation (44) would be extremely time consuming. It is here approximated by dividing the total $4\pi$ solid angle to a "forward angle" $\delta\Omega^l$ and "ambient angle" $\delta\Omega^* = 4\pi - \delta\Omega^l$ . For compatibility with the FVM solver, $\delta\Omega^l$ is set equal to the control angle given by the angular discretization. However, it is assumed to be symmetric around the centre of the control angle. Within $\delta\Omega^l$ the intensity is $I^l(\mathbf{x},\mathbf{s})$ and elsewhere it is approximated as

$$U_\lambda^*(\mathbf{x}) = \frac{U_\lambda(\mathbf{x}) - \delta\Omega^l I_\lambda(\mathbf{x})}{\delta\Omega^*} \tag{48}$$

where $U_\lambda(\mathbf{x})$ is the combined intensity at wavelength $\lambda$. The in-scattering integral can now be written as

$$\frac{\sigma_{\lambda,d}(\mathbf{x})}{4\pi} \int_{4\pi} \Phi(\mathbf{s},\mathbf{s}') I_\lambda(\mathbf{x},\mathbf{s}') d\Omega' = \sigma_{\lambda,d}(\mathbf{x})\left[\chi_f I_\lambda(\mathbf{x},\mathbf{s}) + (1-\chi_f)U^*(\mathbf{x})\right] \tag{49}$$

where $\chi_f \equiv \chi_f(r,\lambda)$ is a fraction of the total intensity originally within the solid angle $\delta\Omega^l$ that is scattered into the same angle $\delta\Omega^l$. A derivation of the formula for $\chi_f$ in case of two-flux approximation has been presented in Ref. [124]. For an arbitrary solid angle it becomes

$$\chi_f(r,\lambda) = \frac{1}{\delta\Omega^l} \int_0^{\mu^l} \int_0^{\mu^l} \int_{\mu_{d,0}}^{\mu_{d,\pi}} \frac{P_0(\mu_d)}{\left[\left(1-\mu^2\right)\left(1-\mu'^2\right) - \left(\mu_d - \mu\mu'\right)^2\right]^{1/2}} d\mu_d d\mu d\mu' \qquad (50)$$

where $\mu_d = \cos\theta_d$ and $P_0(\mu_d)$ is a single droplet scattering phase function

$$P_0(\mu_d) = \frac{\lambda^2\left(\left|S_1(\mu_d)\right|^2 + \left|S_2(\mu_d)\right|^2\right)}{2C_s(r,\lambda)} \qquad (51)$$

$S_1(\mu_d)$ and $S_2(\mu_d)$ are the two polarized scattering amplitudes, given by Mie-theory. The integration limit $\mu^l$ is a cosine of the polar angle defining the boundary of the symmetric control angle $\delta\Omega^l$

$$\mu^l = \cos(\theta^l) = 1 - \frac{2}{N_\Omega} \qquad (52)$$

The limits of the innermost integral are

$$\begin{aligned} \mu_{d,0} &= \mu\mu^l + \sqrt{1-\mu^2}\sqrt{1-\mu'^2} \\ \mu_{d,\pi} &= \mu\mu^l - \sqrt{1-\mu^2}\sqrt{1-\mu'^2} \end{aligned} \qquad (53)$$

When $\chi_f$ is integrated over the droplet size distribution to get an averaged value, it is multiplied by $C_s(r,\lambda)$. It is therefore $|S_1|^2 + |S_2|^2$, not $P_0(\mu_d)$, that is integrated. Physically, this means that intensities are added, not probabilities [125].

An effective scattering coefficient can now be defined

$$\overline{\sigma}_{\lambda,d}(\mathbf{x}) = \frac{4\pi N(\mathbf{x})}{4\pi - \delta\Omega^l} \int_0^\infty (1-\chi_f) C_s(r,\lambda) dr \qquad (54)$$

and the spray RTE becomes

$$\mathbf{s}\cdot\nabla I_\lambda(\mathbf{x},\mathbf{s}) = -\left[\kappa_{\lambda,d}(\mathbf{x}) + \overline{\sigma}_{\lambda,d}(\mathbf{x})\right] I_\lambda(\mathbf{x},\mathbf{s}) + \kappa_{\lambda,d}(\mathbf{x}) I_{b\lambda,d}(\mathbf{x}) + \frac{\overline{\sigma}_{\lambda,d}(\mathbf{x})}{4\pi} U_\lambda(\mathbf{x}) \tag{55}$$

This equation can be integrated over the spectrum to get the band specific RTEs. The procedure is exactly the same as that used for the gas phase RTE. After the band integrations, the spray RTE for band *n* becomes

$$\mathbf{s}\cdot\nabla I_n(\mathbf{x},\mathbf{s}) = -\left[\kappa_{n,d}(\mathbf{x}) + \overline{\sigma}_{n,d}(\mathbf{x})\right] I_n(\mathbf{x},\mathbf{s}) + \kappa_{n,d}(\mathbf{x}) I_{bn,d}(\mathbf{x}) + \frac{\overline{\sigma}_{n,d}(\mathbf{x})}{4\pi} U_n(\mathbf{x}) \tag{56}$$

where the source function is based on the average droplet temperature within a cell. The droplet contribution to the radiative loss is

$$-\nabla\cdot\dot{\mathbf{q}}''_{\mathrm{r}}(\mathbf{x})(\text{droplets}) = \kappa_d(\mathbf{x})\left[U(\mathbf{x}) - I_{b,d}(\mathbf{x})\right] \tag{57}$$

For each individual droplet, the radiative heating/cooling power is computed as

$$\dot{q}_{\mathrm{r}} = \frac{m_d}{\rho_d(\mathbf{x})}\kappa_d(\mathbf{x})\left[U(\mathbf{x}) - I_{b,d}(\mathbf{x})\right] \tag{58}$$

where $m_d$ is the mass of the droplet and $\rho_{\mathrm{d}}(\mathbf{x})$ is the total density of droplets in the cell.

The absorption and scattering cross sections and the scattering phase functions are calculated using the MieV code developed by Wiscombe [125]. Currently, the spectral data on is only included for water. The values of the imaginary part of the complex refractive index (absorption coefficient) are taken from Ref. [126], and value 1.33 is used for the real part (index of refraction).

Before the actual simulation, both $\kappa_d$ and $\sigma_d$ are averaged over the possible droplet radii and wavelength. A constant "radiation" temperature, $T_{\mathrm{rad}}$, is used in the wavelength averaging. $T_{\mathrm{rad}}$ should be selected to represent a typical radiating

flame temperature. By default, $T_{rad}$ = 1173 K. After the averaging processes, the spray radiative properties are functions of the mean droplet diameter only. The properties are computed for a range of different mean diameters and stored in one-dimensional arrays. During the simulation, the local properties are found by table look-up using the local mean droplet diameter.

# 7. Results

## 7.1 Verification of the radiation solver

The purpose of the computer program verification is to ensure that the program works as intended by the developers and indicated by the program documentation. The verification cases are typically simpler than the actual applications of the program. The verification may have some features of validation, if the verification includes assessment of the accuracy of the results.

The first verification test is the computation of the configuration factors within a rectangular enclosure with one hot wall and other walls maintained at 0 K, shown in Figure 11. The enclosure dimensions are chosen to be that of a cube. The exact values of the configuration factor from plane element *dA* to parallel rectangle *H* are calculated using the analytical solution [94]. Different variations of the case are generated by varying the mesh resolution ($20^3$ and $100^3$ cells) and the number of radiation angles (50, 100, 300, 1000, 2000). A comparison of the exact solutions and FDS predictions at different positions at the diagonal are shown in Figure 12. As can be seen, the FDS predictions converge towards the exact solution when *both* spatial *and* angular resolutions are improved.

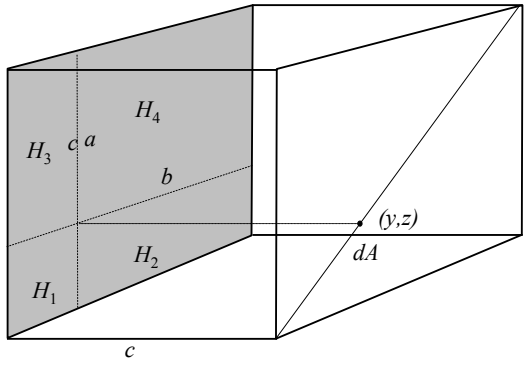


*Figure 11. Radiation verification test for configuration factor computation.*

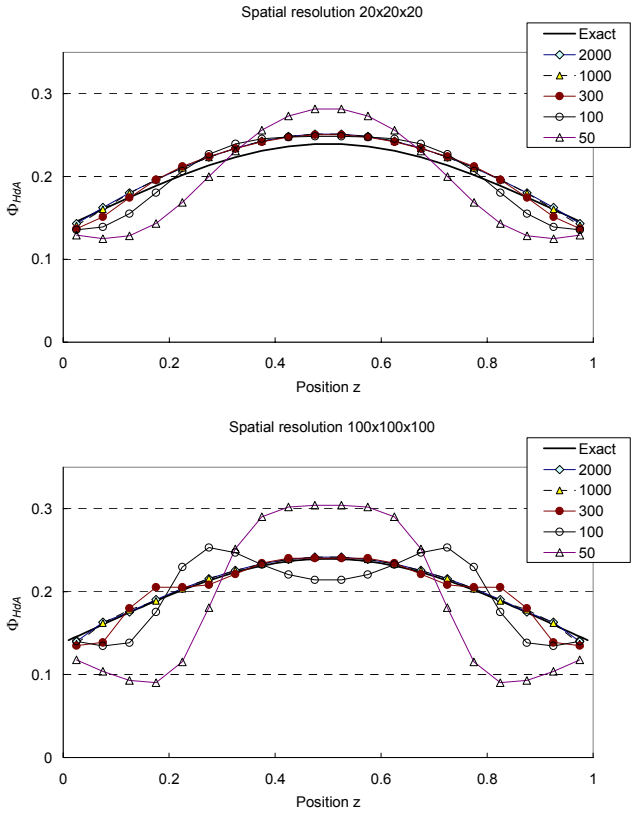


*Figure 12. Comparison of exact configuration factors to FDS predictions with different angular resolutions and two different spatial resolutions. Top: $20 \times 20 \times 20$, bottom: $100 \times 100 \times 100$.*

The second verification test is a three-dimensional computation of the radiative heat flux from a 1.0 m thick homogenous layer of grey and stagnant gas between black infinitely wide walls. The range of optical thicknesses is studied by varying the absorption coefficient $\kappa$. The gas temperatures $T_g$ = 1273.15 K and wall temperatures $T_{w1} = T_{w2} = 0$ K. In a special case with non-absorbing gas ($\kappa = 0$), the temperature of the opposite wall is $T_{w1}$ = 1273.15 K. The exact solution [127] for the heat flux to wall 2 is given by

$$S(\kappa) = \begin{cases} \sigma T_g^4 \left[1 - 2E_3(\kappa L)\right] & \kappa > 0 \\ T_{w1}^4 & \kappa = 0 \end{cases} \tag{59}$$

where $L$ = 1.0 m. The FDS results are computed at two mesh resolutions (I = 20 and I = 150 cells) in the direction over the layer. For the smaller resolution, both one-band and six-band results are included to test the integration of heat fluxes over multiple bands. Two-dimensional versions are also computed (J = 1). The number of radiation angles was 104. The exact values and the FDS predictions are shown in Table 3.

*Table 3. The solutions for the radiative flux from a plane layer.*

| $\kappa$ ($m^{-1}$) | S ($\kappa$) | FDS 3D (I = 20) | | FDS 2D (I = 20) | | FDS 3D (I = 150) |
|---|---|---|---|---|---|---|
| | | 1-band | 6-band | 1-band | 6-band | |
| 0 | 149 | 149 | 148 | 148 | 147 | 149 |
| 0.01 | 2.90 | 2.92 | 2.91 | 2.84 | 2.83 | 2.93 |
| 0.1 | 24.9 | 25.6 | 25.5 | 25.1 | 25.0 | 25.7 |
| 0.5 | 82.9 | 83.1 | 82.8 | 84.4 | 84.1 | 84.0 |
| 1.0 | 116 | 115 | 115 | 118 | 117 | 117 |
| 10.0 | 149 | 149 | 148 | 149 | 148 | 149 |

## 7.2 Radiative fluxes from diffusion flames

The accuracy of the predicted radiative heat fluxes from methane pool flames was studied in Paper IV. Methane and natural gas fires were established in a quiescent environment using circular burners with diameters 0.10 m, 0.38 m and 1.0 m. Radiometers were used to measure the radial and vertical profiles of radiative heat flux outside the flame. A schematic diagram of the set-up is shown in Figure 13 and the experimental approach is reported in Ref. [128]. The radiative flux typically drops off very quickly in the radial direction, whereas in the vertical direction, the flux peaks at a vertical location equal to approximately 50% of the characteristic flame height and then drops to small values above the visible flame tip. The uncertainty (with a coverage factor of two) in the radiative flux measurement is estimated as 10%.

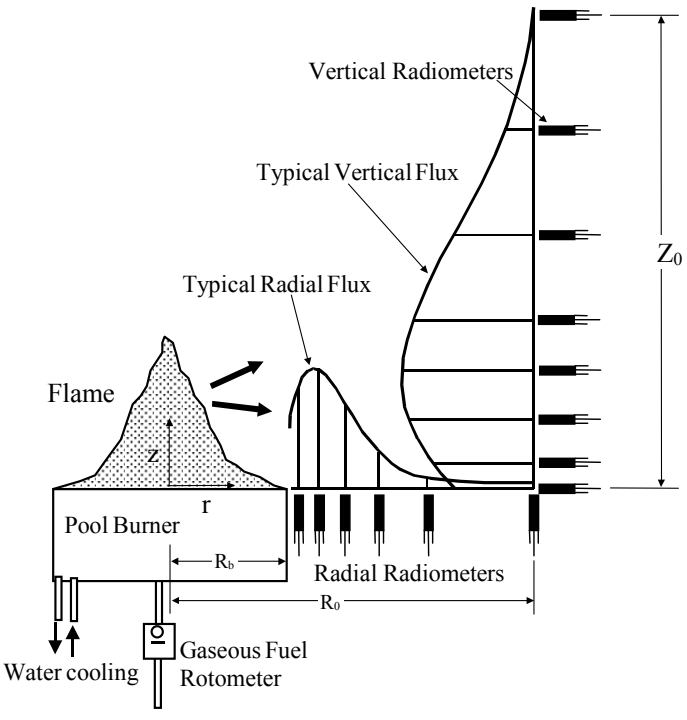


*Figure 13. Experimental set-up for measurement of radiative flux.*

The parameters of the simulated cases are summarized in Table 4, where $D$ is the burner diameter, $R_0$ is the radial position of the vertical row of radiometers, $\dot{m}''_F$ is the mass burning rate per burner area and $\dot{Q}''$ is the rate of heat release per burner area. The size of the simulation domain and the size of the computational grid cell just above the burner surface, $\delta x$, are also shown. The last two columns show the dimensionless heat release rates $Q_D^* = \dot{Q}/(\rho_\infty T_\infty c_p D^2 \sqrt{gD})$ [55] and $Q_{\delta x}^* = \dot{Q}''/(\rho_\infty T_\infty c_p D^2 \sqrt{g\delta x})$ where $\rho_\infty$, $T_\infty$ and $c_p$ are the properties of the ambient air. $Q_D^*$ is the standard dimensionless number, which characterizes the strength of the fire and $Q_{\delta x}^*$ represents the resolution of the current grid, in proportion to the burning rate. A very low value of $Q_{\delta x}^*$ indicates that the position of the flame near the burner surface cannot be resolved. 304 radiation angles were used. A soot conversion factor of 1.0% was assumed for all calculations.

The predictions for the radiative fractions of the heat release rate were systematically higher than the measurements, probably due to the overestimation of the flame temperatures. The measured and predicted radial distributions of

radiative flux are compared in Figure 14. The agreement is very good in general, but the heat flux is highly over estimated in cases B and E. Similar trends can be found in Figure 15, showing the vertical profiles. A few remarks should be made when interpreting the results. First, high radiative fluxes were predicted better than low fluxes, which is good for the applicability in safety relevant scenarios. Second, the 100% errors in radiative heat flux may be caused by as low as 20% error in absolute temperature. The reason for the large error in case B, where the flame should be relatively well resolved, is currently not known.

*Table 4. Summary of the simulated methane / natural gas experiments.*

| Case | Test configuration | | | | Simulated domain | Simulation parameters | | |
|---|---|---|---|---|---|---|---|---|
| | $D$ (m) | $R_0$ (m) | $\dot{m}''_F$ (g/m$^2$/s) | $\dot{Q}''$ (kW/m$^2$) | x × y × z (m$^3$) | $\delta x$ (cm) | $Q_D^*$ | $Q_{\delta x}^*$ |
| A | 0.10 | 0.82 | 1.08 | 53.8 | 0.315 × 0.21 × 0.45 | 0.525 | 0.12 | 0.67 |
| B | 0.10 | 0.82 | 4.80 | 240 | 0.315 × 0.21 × 0.45 | 0.525 | 0.53 | 3.0 |
| C | 0.38 | 0.732 | 5.90 | 295 | 1.26 × 0.84 × 1.80 | 2.1 | 0.34 | 1.8 |
| D | 0.38 | 0.732 | 31.0 | 1550 | 1.26 × 0.84 × 2.20 | 2.1 | 1.8 | 9.6 |
| E | 1.0 | 1.00 | 1.25 | 62.4 | 2.50 × 2.00 × 3.50 | 5.0 | 0.044 | 0.31 |
| F | 1.0 | 0.80 | 4.12 | 206 | 2.50 × 2.00 × 4.50 | 5.0 | 0.14 | 1.05 |

## 7.3 Attenuation of radiation in water sprays

Two validation tests were presented in Paper V. The first validation test is the simulation of an experiment conducted by Murrel et al. [129]. They measured the attenuation of thermal radiation passing through a water spray using a heat flux gauge. The schematics of the system are shown in Figure 16. The radiation was produced by a 1 m × 1 m heat panel at 900°C. Three different nozzles were simulated. Each nozzle was a full-cone type industrial nozzle. The simulations were performed at eight different flow rates for each nozzle.

The initial droplet size distribution was assumed to have the following cumulative distribution for droplet diameter $d$

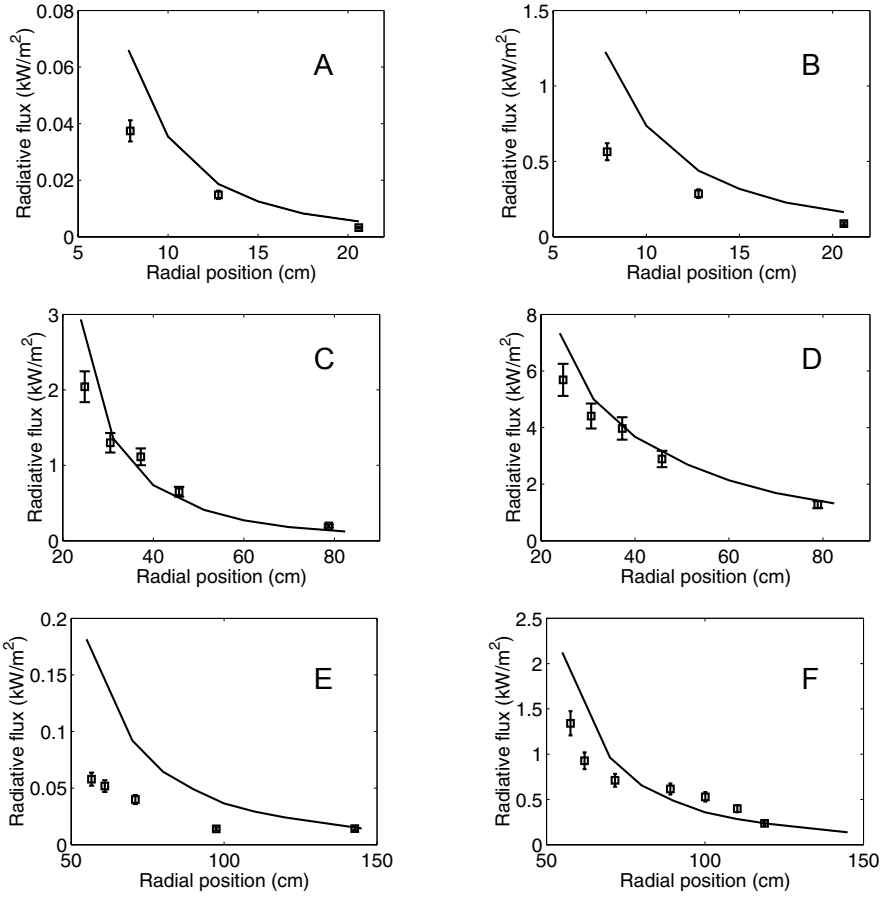


*Figure 14. Comparison of the measured (squares) and predicted (lines) radial heat flux distributions.*

$$F(d)=\begin{cases}\dfrac{1}{\sqrt{2\pi}}\displaystyle\int_0^d \frac{1}{\sigma\tau}\exp\left\{\frac{-\left[\ln\left(\tau/d_m\right)\right]^2}{2\sigma^2}\right\}d\tau & (d\le d_m)\\ 1-\exp\left[-0.693\left(\dfrac{d}{d_m}\right)^{\gamma}\right] & (d>d_m)\end{cases} \tag{60}$$

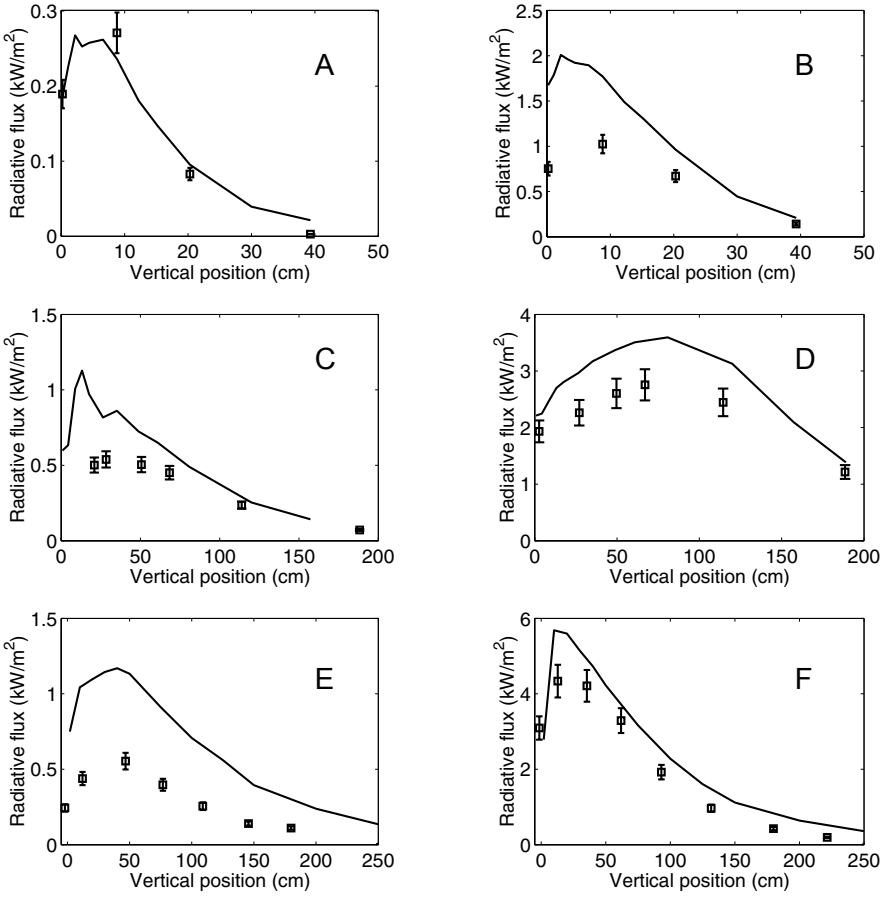


*Figure 15. Comparison of the measured (squares) and predicted (lines) vertical heat flux distributions.*

where $d_m$ is the median droplet diameter, and $\gamma$ and $\sigma$ are empirical constants equal to about 2.4 and 0.6, respectively. In the experiments, Murrel et al. did not measure the droplet diameters in the vicinity of the nozzles, but 0.7 m below the nozzle, i.e. at the height of the heat flux measurement point. The droplet size boundary condition was therefore determined by iterating the initial $d_m$ until the simulated and measured mean diameters at the measurement location were equal, with a few percent tolerance. The iteration was performed for all nozzle-flow rate combinations. The droplet speeds on the inflow boundaries were set equal to the measured vertical velocity component 0.7 m below the nozzle.

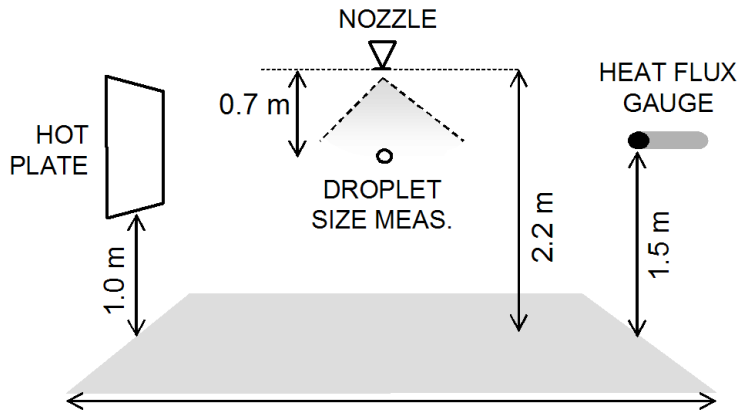


*Figure 16. Schematics of the large-scale attenuation test.*

In the computations, 10 cm grid cells, 1000 control angles, only one spectral band (grey assumption) and no gas phase absorption were used. The measured and predicted attenuation results are compared in Figure 17. Since a good general agreement was found for all three nozzles, and the results of the individual nozzles are well distinct in the flow-rate vs. attenuation space, we can assume that the model can properly take into account both the effect of the water load and the effect of the droplet size distribution. Only the mid-range flow rates of nozzle B and the highest flow rates of nozzle D show sizable discrepancies. These discrepancies are probably caused by a combination of measurement errors and model inaccuracy. The droplet size measurements, in particular, are difficult to conduct in large-scale sprays. The various challenges of spray measurements have been presented by Husted [130]. Some uncertainty is also related to the inverse determination of droplet size boundary conditions for the simulations.

The second validation test for spray-radiation interaction is the experiments of Dembele et al. [131]. They measured the attenuation of a collimated radiation beam passing through a water spray using a Fourier infrared spectrometer. The radiation source was a tungsten filament inside a silica tube. Its emission spectrum was close to that of a blackbody at 1300°C. The spray was produced with one, two or three hydraulic nozzles arranged in a row, and the measurements were made 20 cm below the nozzles at different flow rates. The schematics of the scenario are shown in Figure 18.

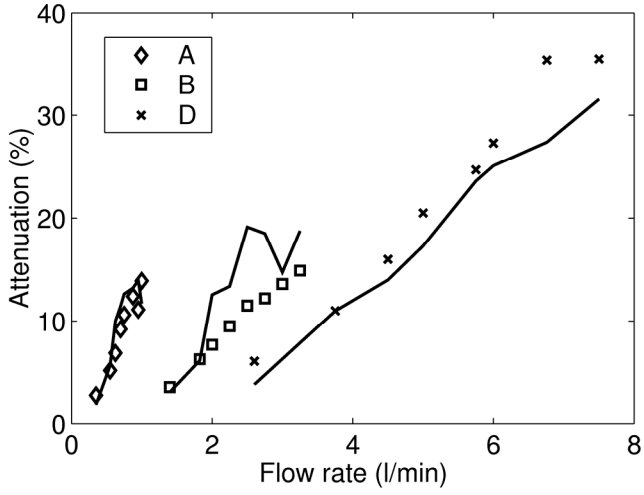


*Figure 17. Results of the large scale attenuation.*

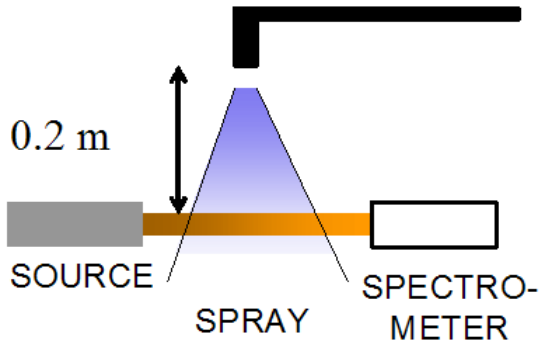


*Figure 18. Schematics of the small-scale attenuation test.*

The simulations were performed at four different flow rates. The droplet size boundary conditions were determined using a procedure similar to the large-scale scenario. The velocity of the droplets at the inflow boundary was found from a simple geometrically based relationship between the flow velocity and distance. Modelling a collimated radiation beam is difficult with FVM due to the symmetric discretization of the unit sphere into solid angles. To alleviate the problem, the radiation source in this exercise was modelled simply as a 4 cm by 4 cm diffuse surface. Despite the strong approximation of the radiation source, the comparison with the measurements is valid on the opposite side of the spray

because the air surrounding the water spray was transparent and non-scattering, but not in the other directions. 2.0 cm grid cells, 1000 radiation angles and six radiation bands were used, but the gas phase absorption was neglected. In this scenario, the independence of the spatial and angular resolutions was very difficult to achieve. For a single-nozzle flow at 0.14 L/min, reducing the cell size from 2.0 cm to 1.0 cm increased the attenuation from 8.3% to 11.4%, with 10.0% being the experimental value. The convergence in angular resolution was difficult to achieve because the radiation source was very small compared to the domain size, and because the ray effect is difficult to avoid in direction of grid axis.

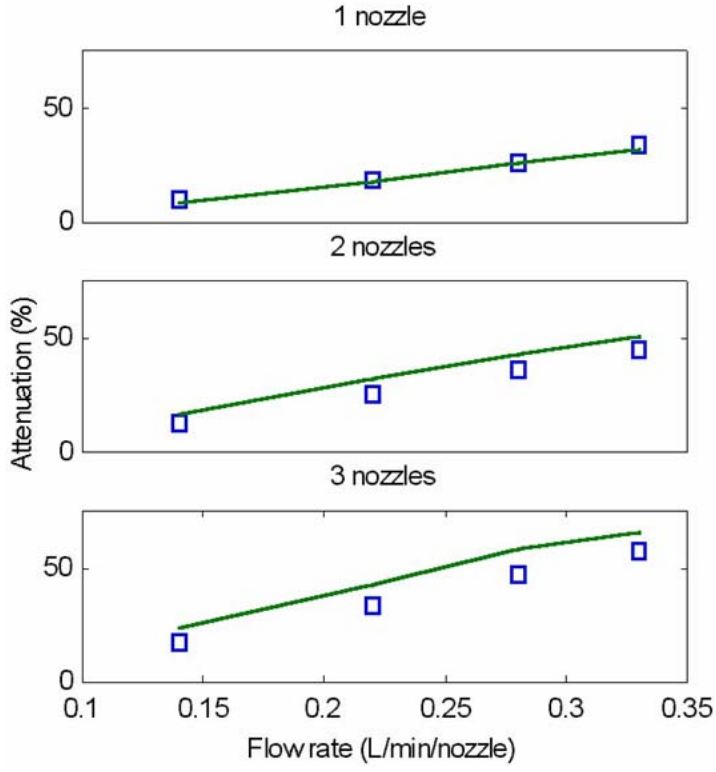


*Figure 19. Comparison of measured (squares) and predicted (lines) attenuation in small-scale tests.*

The measured and simulated attenuation results are compared in Figure 19. In the case of only one nozzle, the agreement is very good, taking into account the unavoidable dependence on the grid and angular resolutions. The root mean-square error between the predicted and measured attenuations is only 1.3%.

When more nozzles are put between the source and the measurement point, the attenuation is clearly over-predicted. The rms errors for two and three nozzles are 6.4 and 8.8%, respectively. One possible reason for the over prediction is the droplet coalescence, which is not taken into account by the model. Coalescence happens as a result of the hydrodynamic interaction between adjacent sprays [131]. This explanation is supported by the finding that while the predicted attenuations with two and three nozzles increase roughly by factors two and three from the values corresponding to the one nozzle, the experimental results increase only by factors of 1.3 and 1.8.

In Paper V, the computed droplet size distributions in different parts of the spray were compared, demonstrating that both the mean diameters and the shapes of the droplet size distributions may vary significantly in different parts of the spray. The same phenomena for hollow cone water mist sprays has been observed experimentally by Husted [130]. During the computation of the mean radiative properties for the spray in this work, the shape of the distribution is fixed to the presumed size probability density function, and only the droplet mean is allowed to vary according to the statistics predicted by the Lagrangian transport model. The importance of this approximation to the radiation solutions is not known, and should be studied in the future.

# 8. Discussion

The applicability of a numerical solver for the intended use depends on the accuracy, computational efficiency and reliability. In this context, the computational efficiency must be measured as a balance between accuracy and computational cost in relation to the rest of the computational framework. Since the intended use of FDS is mainly fire engineering and fire risk analysis, the radiation solver must be efficient and in concordance with the rest of the code to allow *sufficiently* accurate predictions with limited resources. According to Howard Baum, NIST Research Fellow, the CPU consumption of a given numerical routine ought to be commensurate with the particular phenomenon addressed [132]. In a simulation of a typical enclosure fire, where the fraction of heat transfer by radiation is around 30%, the FVM radiation solver consumes less than 30% of the total CPU time. At the same time, the accuracy of the radiation solution is expected to be of the same order with the other phenomena. More accuracy can be achieved by the increased angular, spatial, spectral and temporal resolutions, but at the expense of the increased CPU time. Other requirements, caused by the wide range of uses, are versatility, ease of use and ease of extension.

The presented verification cases demonstrated that in the case of three-dimensional radiation fields, FDS predictions converged towards the exact solutions when *both* spatial *and* angular resolutions were sufficient. In practical simulations, the spatial resolution is usually determined by the flow solution, and the default angular resolution of 104 directions seems to be an appropriate choice. It is important though that the code users are aware of the ray effect and the resulting errors when dealing with heat transfer dominated by far field radiation. The ray effect probably has more importance in code validation, where local radiative fluxes are compared against experiments, than in practical applications.

The validation of the flame radiation computation was performed using diffusion flames ranging from 10 to 100 cm. With few exceptions, the predictions were within 25 % of the measured radiative heat fluxes. Further developments in combustion and radiation source modelling are needed to improve the flame heat fluxes. This is especially true for small heat release rates because the problems appear when the combustion region close to the burning surface is not adequately resolved.

The accuracy of predicting the radiation attenuation by water spray was even better than in the case of flame heat fluxes, demonstrating that the physics of radiation-spray interaction are included with sufficient detail. Aspects of droplet breakup and coalescence should be considered to account for more complicated and dense sprays. Ultimately, the inclusion of secondary droplet breakup could reduce the sensitivity to the droplet size boundary conditions by allowing automatic adjustment of the droplet size according to the flow conditions. However, as pointed out by Madsen [112], the exact mechanisms behind the droplet breakup are still not completely understood. Prediction of the initial atomization processes from the first principles would require very detailed models of the nozzles and relatively complicated models of the two-phase flows, and seems to be beyond the current capabilities of fire simulation.

Due to the challenges of describing the experimental conditions, the angular resolutions and computational costs of the validation simulations were higher than the normal practice in applications. To evaluate the accuracy and cost in situations corresponding to the typical use of the code, a validation study involving real flames and water sprays from sprinklers or water mist nozzles would be needed.

# 9. Concluding remarks

## 9.1 Summary

The objective of this thesis has been to summarize the work of the author in the development of the computational tools for fire risk analysis and fire safety engineering. The work reported in this thesis focused on two particular topics: The first topic was the application of Monte Carlo simulation in the field of fire risk analysis and the development of the necessary tools for performing these simulations using a range of different fire models. The second topic was the development of a numerical solver for the transport of thermal radiation within Fire Dynamics Simulator code. The two topics are linked by the numerous applications of FDS as a deterministic model in fire risk analysis. The efficient and robust radiation solver, developed in the second part of the thesis, will thus benefit the application of the technique developed in the first part.

## 9.2 Development of probabilistic fire simulation

In fire risk analysis, the probabilities of fire consequences are computed using deterministic models for fire phenomena, taking into account the statistical variation or uncertainty of the initial and boundary conditions. The development of the computational resources has allowed the use of Monte Carlo simulation, the most general approach where the space of possible answers is covered in a statistically satisfactory manner. However, the convergence of the Monte Carlo simulation must be accelerated when computationally expensive tools such as CFD are used. The TMMC technique, developed in this work, allows the use of relatively simple and fast models in the collection of the main body of the statistical data, while retaining the physical accuracy by running a small set of simulations with more accurate but slower model and introducing a multi-dimensional scaling function to provide a correction to the main data. The performance of TMMC was validated using simple room fire scenarios, and the use of the FDS code as a deterministic tool of the Monte Carlo simulation was demonstrated.

## 9.3 Weaknesses of TMMC technique and suggestions for future work

The principal weakness of TMMC is a limited knowledge of its theoretical basis. Although it has been seen heuristically to yield good results, and the mechanism is understood, the evidence is not yet sufficient. In the examples presented, the method works well, but there is no general guarantee that the process converges towards the true solution if the fast and slow models differ considerably.

For economy, the accuracy and efficiency of the TMMC technique could be improved by a better numerical treatment of the scaling process. Possible reduction of the number of scaling points should be studied in the future because in some applications, the derivation of the scaling function may form the majority of the computational cost. As demonstrated in the second validation test, all the available a priori information on the relative importance of the random variables should be used to concentrate more scaling points to the most important variables. The application of adaptive sampling techniques to the scaling point placement should be studied in order to reduce the cost in the situations where a priori information is not valid. An example of such a situation is when the inaccuracy of the simple model (Model A) would lead to wrong conclusions on the relative importance of the random variables. Further improvement of the accuracy could be achieved by interpolating the scaling functions between the scaling points to ensure a smoother transition from one scaling region to another.

## 9.4 Development of radiation solver for Fire Dynamics Simulator

During the last few years, CFD fire simulation has become a routine part of fire engineering. This is especially true in the field of design work, where the introduction of a performance-based design concept has created a market for simulation tools that are reliable and accurate enough for the given purpose, and that are fast and relatively easy to use. After its release in 2000, FDS has become the most widely used fire simulation tool in the world. From the code reliability viewpoint, the high number of active users is an advantage, since the wide range of different applications inevitably reveals the errors in the code. The width of

the range also means that some of the applications push the limits of the code in terms of both applicability and validity. On the other hand, the widespread use of CFD may have lured the audience into a sense of complacency with its visually appealing presentation. As a result, CFD may be used or requested when more simple techniques would suffice.

In this work, an FVM-based radiation solver was implemented in FDS. The solver can be used to compute the transport of thermal radiation in a participating medium consisting of combustion gases, soot and water droplets. The goal of the solver implementation was to find a balance between accuracy and computational cost in engineering applications. In the presented verification and validation examples, the accuracy of the predictions was found sufficient for engineering purposes. The highest errors were found in predictions of heat fluxes from weak flames. Computational efficiency was achieved by making three major approximations. First, the use of rectilinear grids in spatial discretization, which is consistent with the rest of the code, increases the computational efficiency by allowing the use of an explicit marching scheme as a method for transport solution and reduces the memory requirement because the geometrical coefficients of the discretized RTE are constants over the whole domain. As a second approximation, the time accuracy of the radiation solution was relaxed by assuming that the numerical time step of the hydrodynamic solver, given by the CFL-condition, is much smaller than the time scale of the global heat transfer processes. The third approximation was the spectral averaging over wide wavelength regions. Additional efficiency was achieved by the extensive use of lookup tables and application of first order accurate scheme for intensities. The high numerical diffusion caused by the first order accuracy was not found to adversely affect the model accuracy.

An important enhancement of the basic radiation solver was the introduction of radiation-spray interactions. Despite the complexity of the physical phenomena, the computational cost of the radiation solution remained in balance with the physical importance. The major approximations were the assumed global similarity of the droplet size distributions and the approximation of scattering phase functions by a sum of isotropic and forward components. Speed of the solution was again achieved by computing the spray radiative properties in advance and storing in lookup tables.

## 9.5 Weaknesses of the radiation solver and suggestions for future work

Some of the model approximations are deeply embedded and improvements in the corresponding code capabilities would be difficult to carry out. The influences of other approximations, however, are more easily controlled by adjusting the model parameters. For example, the extension of the FDS capability with respect to the rectilinearity of the grid would require a complete revision of the radiation solver, whereas an accurate simulation of turbulence-radiation interactions could be implemented simply by adjusting the time interval of the radiation updates. Naturally, higher computational costs should then be expected.

Topics of future work include the generalization of the spectral band structure to allow the use of arbitrary species in the computation of absorption coefficients, generalization of the dispersed phase radiative properties beyond those of water, and allowing the suspensions of other types of particles than liquid droplets. For example, soot is known to both absorb and scatter radiation, but currently only the absorption is taken into account via RadCal. The water spray validation examples demonstrated that the shapes of the droplet size distributions may vary significantly in different parts of the spray. The effect of the global size distribution similarity approximation is currently not known and should be studied in the future by comparing against simulations where the local droplet size distributions are rigorously taken into account in the computation of spray radiative properties. Inclusion of secondary droplet breakup and coalescence processes may be necessary in order to reduce the sensitivity to the droplet size boundary conditions. In addition, a validation of the model using realistic sources of radiation and relevant water spray types should be performed.

In large scale fire simulations, the increase in spatial resolution that would be necessary for a detailed solution of the flame temperature distribution will not be possible for a long time. The modelling of the radiative source term is therefore needed in order to reduce the sensitivity on the unavoidable temperature errors. The current model is based on the assumption of local radiative fraction of heat release, and may be insufficient in fires where the flame optical properties change considerably. An example of such a situation is the transition from a well-ventilated to an under-ventilated enclosure fire. Possible means of

modelling could use the ideas of flamelets, adapted to the practical restrictions of large-scale simulations. A special problem is flame spread on a material, where the process essentially becomes two-dimensional. Application of submodels, similar to the boundary layer theory of Prandtl, might be feasible [133]. Interfacing them to LES codes and addressing the whole problem of wall functions is an issue still to be studied. One practical tool for studying the existence and shape of the flame spread wall functions could be the direct numerical simulation (DNS) of the near wall phenomena. In DNS, all the turbulent length scales are resolved by using very fine spatial resolution and sufficiently accurate numerical schemes. A two-dimensional approximation of DNS may already be possible using the existing tools. DNS can also serve as a detailed tool for experimental design.

# References


1. Molak, V. (ed.) Fundamentals of Risk Analysis and Risk Management. Boca Raton: Lewis Publishers, 1997. 472 p.

2. The Reactor Safety Study – An Assessment of Accident Risks in U.S. Commercial Nuclear Power Plants. Washington, D.C.: U.S. Nuclear Regulatory Commission (USNRC), 1975. WASH-1400 (NUREG-75/014).

3. Severe Accident Risks: An Assessment for Five U.S. Nuclear Power Plants. Washington, D.C.: U.S. Nuclear Regulatory Commission (USNRC), 1991. NUREG-1150.

4. Kaiser, G.D. Overall assessment. In: Green, A.E. (ed.). High Risk Safety Technology. Chichester: Wiley, 1982. Pp. 101–110.

5. PRA Procedures Guide – A Guide to the Performance of Probabilistic Risk Assessment for Nuclear Power Plants. Washington, D.C.: U.S. Nuclear Regulatory Commission (USNRC), 1983. NUREG/CR2300.

6. Keski-Rahkonen, O. Fire safety research (FISRE): FISRE summary report. In: Kyrki-Rajamäki, R. & Puska, E.-K. (eds.). FINNUS The Finnish Research Programme on Nuclear Power Plant Safety 1999–2002. Final Report. Espoo: VTT Processes, 2002. VTT Research Notes 2164. Pp. 197–204.

7. Keski-Rahkonen, O., Mangs, J., Hostikka, S. & Korhonen, T. POTFIS summary report. In: Räty, H. & Puska, E.K. (ed.). SAFIR. The Finnish Research Programme on Nuclear Power Plant Safety 2003–2006. Final Report. Espoo: VTT, 2006. VTT Research Notes 2363. Pp. 335–342.

8. Keski-Rahkonen, O., Mangs, J., Hostikka, S. & Korhonen, T. Quantitative assessment of potential fire spread in nuclear power plant scenarios. In: Post-Conference Seminar III of the 18th International Conference on Structural Mechanics in Reactor Technology (SMIRT 18). 2005. 9th International Seminar on Fire Safety in Nuclear Power Plants and Installations. August 22–24, 2005, Vienna, Austria. CD-ROM.

9. Keski-Rahkonen, O., Mangs, J., Hostikka, S. & Korhonen, T. Quantitative application of Monte Carlo simulation in Fire-PSA. Kerntechnik, 2007. Vol. 72, No. 3, pp. 149–155.

10. Karlsson, B. & Tomasson, B. Repeatability Tests of a Fire Risk Index Method for Multi-Storey Apartment Buildings. In: Gottuk, D.T. & Lattimer, B.Y. (eds.). Proceedings of Eighth International Symposium on Fire Safety Science. Beijing, China, September 18–23, 2005. International Association for Fire Safety Science, 2005. Pp. 901–912.

11. Williamson, R.B. Coupling Deterministic and Stochastic Modeling to Unwanted Fire. Fire Safety Journal, 1981.Vol. 3, pp. 243–259.

12. Ling, W. C. T. & Williamson, R. B. Use of Probabilistic Networks for Analysis of Smoke Spread and the Egress of People in Buildings. In: Grant, C.E. & Pagni, P.J. (Eds.). Proceedings of 1st International Symposium. Fire Safety Science. October 7–11, 1985, Gaithersburg, MD. International Association for Fire Safety Science. Hemisphere Publishing Corp., NY, 1986. Pp. 953–962.

13. Korhonen, T. Hietaniemi, J., Baroudi, D. & Kokkala, M. Time-dependent event-tree method for fire risk analysis: tentative results. In: Evans, D.D. (ed.). Proceedings of the Seventh International Symposium on Fire Safety Science. Worcester, MA, 16–21 June 2003. International Association for Fire Safety Science, 2003. Pp. 321–332.

14. Fontana, M. & Maag, T. Fire Risk Assessment Based on Bayesian Networks. In: Almand, K., Attlan, J.M., D'Hoop, J.M. & Gordon, J. (eds.) Proceedings of 5th International Conference on Performance-Based Codes and Fire Safety Design Methods. October 6–8, 2004, Luxembourg. 2004. Pp. 238–249.

15. Frantzich, H. Risk Analysis and Fire Safety Engineering. Fire Safety Journal, 1998. Vol. 31, No. 4, pp. 313–329.

16. Korhonen, T., Hostikka, S. & Keski-Rahkonen, O. A proposal for the goals and new techniques of modelling pedestrian evacuation in fires. In: Gottuk, D. & Lattimer, B. (eds.). Proceedings of the Eight International Symposium on Fire Safety Science. Beijing, China, 18–23 Sept. 2005. International Association for Fire Safety Science, 2005. Pp. 557–569.

17. Helton, J. C. Treatment of Uncertainty in Performance Assessments for Complex Systems. Risk Analysis, 1994. Vol. 14, No. 4, pp. 483–511.

18. Tillander, K. & Keski-Rahkonen, O. The Ignition Frequency of Structural Fires in Finland 1996–99. In: Evans, D.D. (ed.). Proceedings of the Seventh International Symposium on Fire Safety Science. Worcester, MA, 16–21 June 2003. International Association for Fire Safety Science, 2003. Pp. 1051–1062.

19. Tillander, K. Utilisation of statistics to assess fire risks in buildings. Espoo: VTT Building and Transport, 2004. VTT Publications 537. 224 p. + app. 37 p.

20. Sekizawa, A. Fire Risk Analysis: Its Validity and Potential for Application in Fire Safety. In: Gottuk, D.T. & Lattimer, B.Y. (eds.). Proceedings of Eighth International Symposium on Fire Safety Science. Beijing, China, September 18–23, 2005. International Association for Fire Safety Science, 2005. Pp. 82–100.

21. Vose, D. Monte Carlo Risk Analysis Modeling. In: Molak, V. (ed.). Fundamentals of Risk Analysis and Risk Management. Boca Raton: Lewis Publishers, 1997. 472 p.

22. Metropolis, N. & Ulam, S. The Monte Carlo Method. Journal of the American Statistical Association, 1949. Vol. 44, No. 247, pp. 335–341.

23. Vose, D. Quantitative risk analysis: a guide to Monte Carlo simulation modelling. Chichester, England: Wiley, 1996. 328 p.

24. Hofer, E., Jahn, H. & Krzykacz, B. Uncertainty and sensitivity analysis of an oil and cable fire simulation with the code CRDLOC. In: Apostolakis, G. (ed.) Probabilistic Safety Assessment and Management, Elsevier Science Publishing Co., 1991.

25. Krzykacz, B., Hofer, E. & Kloos, M. A software system for probabilistic uncertainty and sensitivity analysis of results from computer models. In: Proceedings of PSAM II. San Diego, CA, USA, 20–25 March 1994.

26. Hostikka, S., Keski-Rahkonen, O. & Korhonen, T. Probabilistic Fire Simulator. Theory and User's Manual for Version 1.2, Espoo: VTT Building and Transport, 2003. VTT Publications 503, 72 p. + App. 1 p.

27. McKay, M.D., Beckman, R.J. & Conover, W.J. A comparison of three methods for selecting values of input variables in the analysis of output from a computer code. Technometrics, 1979. Vol. 21, No. 2, pp. 239–245.

28. Iman, R.L. & Helton, J.C. Investigation of Uncertainty and Sensitivity Analysis Techniques for Computer Models. Risk Analysis, 1988. Vol. 8, No. 1, pp. 71–90.

29. Magnussion, S.E. Risk Assessment. International Association for Fire Safety Science. In: Hasemi, Y. (ed.) Proceedings of Fifth (5th) International Symposium on Fire Safety Science. March 3–7, 1997, Melbourne, Australia. Boston, MA: International Association for Fire Safety Science, 1997. Pp. 41–58.

30. Hofer, E., Kloos, M., Krzykacz, B., Peschke, J. & Sonnenkalb, M. Methodenentwicklung zur simulativen Behandlung der Stochastik in probabilistischen Sicherheitsanalysen der Stufe 2. Garching: GRSA-2997, Gesellschaft für Anlagen- und Reaktorsicherheit, 2001.

31. Hofer, E, Kloos, M., Krzykacz-Hausmann, B. Peschke, J. & Woltereck, M. An approximate epistemic uncertainty analysis approach in the presence of epistemic and aleatory uncertainties, Reliability Engineering and System Safety, 2002. Vol. 77, pp. 229–238.

32. Eschenroeder, A.Q. & Faeder, E.J. Monte Carlo Analysis of Health Risks From PCB-Contaminated Mineral Oil Transformer Fires. Risk Analysis, 1988. Vol. 8, No. 2, pp. 291–298.

33. Zhao, L. Methodology of Calculating the Risk to People in Building Fires. In: Shields, J. (ed.). Proceedings of 1st International Symposium on Human Behavior in Fire. August 31 – September 2, 1998, Belfast, Northern Ireland. Northern Ireland: University of Ulster, 1998. Pp. 401–410.

34. Fraser-Mitchell, J. Risk Assessment of Factors Related to Fire Protection in Dwellings. In: Hasemi, Y. (ed.) Proceedings of Fifth (5th) International Symposium on Fire Safety Science. March 3–7, 1997, Melbourne,

Australia. Boston, MA: International Association for Fire Safety Science, 1997. Pp. 631–642.

35. Magnusson, S.E., Frantzich, H. & Harada, K. Fire Safety Design Based on Calculations: Uncertainty Analysis and Safety Verification. Fire Safety Journal, 1996. Vol. 27, pp. 305–334.

36. Fraser-Mitchell, J.N. Modelling Human Behavior Within the Fire Risk Assessment Tool "CRISP". In: Shields, J. (ed.). Proceedings of 1st International Symposium on Human Behavior in Fire. August 31 – September 2, 1998, Belfast, Northern Ireland. Northern Ireland: University of Ulster, 1998. Pp. 447–457.

37. Zhao, L. & Beck, V. Definition of Scenarios for the CESARE-RISK Model. In: Hasemi, Y. (ed.) Proceedings of Fifth (5th) International Symposium on Fire Safety Science. March 3–7, 1997, Melbourne, Australia. Boston, MA: International Association for Fire Safety Science, 1997. Pp. 655–666.

38. Phillips, W.G.B. Simulation Models for Fire Risk Assessment. Fire Safety Journal, 1994. Vol. 23, No. 2, pp. 159–169.

39. Hasofer, A.M. & Qu, J. Response Surface Modelling of Monte Carlo Fire Data. Fire Safety Journal, 2002. Vol. 37, No. 8, pp. 772–784.

40. Notarianni, K.A. Role of Uncertainty in Improving Fire Protection Regulation. Pittsburgh, PA: Carnegie-Mellon Univ. 2000. Thesis, 269 p.

41. Hamilton, S.R. & Deierlein, G.G. Probabilistic Methodology for Performance-Based Fire Engineering. In: Almand, K., Attlan, J.M., D'Hoop, J.M. & Gordon, J. (eds.) Proceedings of 5th International Conference on Performance-Based Codes and Fire Safety Design Methods. October 6–8, 2004, Luxembourg. 2004. Pp. 327–341.

42. Kirby, B.R., Newman, G.M., Butterworth, N., Pagan, J. & English, C. Development of a Performance Based Approach to Specifying Fire Resistance for Regulatory Purposes. In: Almand, K., Attlan, J.M., D'Hoop, J.M. & Gordon, J. (eds.) Proceedings of 5th International Conference on Performance-Based Codes and Fire Safety Design Methods. October 6–8, 2004, Luxembourg. 2004. Pp. 183–194.

43. Li, Y. & Spearpoint, M. Cost-Benefit Analysis of Sprinklers for Property Protection in New Zealand Parking Buildings. Journal of Applied Fire Science, 2003–2004. Vol. 12, No. 3, pp. 223–243.

44. Yuen, W.W. & Chow, W.K. Monte Carlo Approach for the Layout Design of Thermal Fire Detection System. Fire Technology, 2005. Vol. 41, No. 2, pp. 93–104.

45. Madras, N. Lectures on Monte Carlo methods. Providence, RI: American Mathematical Society, 2002. 103 p.

46. Landau, D.P. & Binder, K.A guide to Monte Carlo simulations in statistical physics. Cambridge University Press, 2005. 2nd ed. 432 p.

47. Milton, J.S. & Arnold, J.C. Introduction to probability and statistics: principles and applications for engineering and the computing sciences. New York, NY: McGraw-Hill, 1990. 2nd ed. 700 p.

48. Stein, M.L. Large sample properties of simulations using latin hypercube sampling. Technometrics, 1987. Vol. 29, No. 2, pp. 143–151.

49. Hofer, E. Sensitivity analysis in the context of uncertainty analysis for computationally intensive models. Computer Physics Communications, 1999. Vol. 117, pp. 21–34.

50. Pebesma, E.J. & Heuvelink, G.B.M. Latin hypercube sampling of multigaussian random fields. Technometrics, 1999. Vol. 41, No. 4, pp. 303–312.

51. Jones, W.W., Forney, G.P., Peacock, R.D. & Reneke, P.A. Technical Reference for CFAST: An Engineering Tool for Estimating Fire and Smoke Transport. Gaithersburg, MD: National Institute of Standards and Technology, 2000. NIST TN 1431. 190 p.

52. Cadorin, J.-F. & Franssen, J.-M. A tool to design steel elements submitted to compartment fires-OZone V2. Part 1: Pre-and post-flashover compartment fire model. Fire Safety Science, 2003. Vol. 38, No. 5, pp. 395–427.

53. Cadorin, J.-F., Pintea, D., Dotreppe, J.-C. & Franssen, J.-M. A tool to design steel elements submitted to compartment fires-OZone V2. Part 2: Methodology and application. Fire Safety Science, 2003. Vol. 38, No. 5, pp. 429–451.

54. Vaari, J. A transient one-zone computer model for total flooding water mist fire suppression in ventilated enclosures. Fire Safety Journal, 2002. Vol. 37, No. 3, pp. 229–257.

55. Drysdale, D. An Introduction to Fire Dynamics. Chichester: Wiley-Interscience, 1999. Second Edition, 140 p.

56. Hostikka, S. & Keski-Rahkonen, O. Advanced probabilistic simulation of NPP fires. Proceedings of the 18th International Conference on Structural Mechanics in Reactor Technology. SMIRT 18. Beijing, China, August 7–12, 2005. Beijing: Atomic Energy Press, 2005. Pp. 3984–3996.

57. Raithby, G.D. & Chui, E.H. A Finite-Volume Method for Predicting Radiant Heat Transfer in Enclosures with Participating Media. Journal of Heat Transfer, 1990. Vol. 112, No. 2, pp. 415–423.

58. Cox, G. & Kumar, S. Modelling Enclosure Fires Using CFD. In: SFPE Handbook of Fire Protection Engineering. Quincy, MA: Society of Fire Protection Engineers, 2002. 3rd Edition. Pp. 3-194–3-218.

59. Patankar, S.V. & Spalding, D.B.A Calculation Procedure for Heat, Mass and Momentum Transfer in Three-dimensional Parabolic Flows. International Journal for Heat and Mass Transfer, 1972. Vol. 15, pp. 1787–1806.

60. Magnussen B. & Hjertager G.H. On mathematical modelling of turbulent combustion with special emphasis on soot formation and combustion. In: Proceedings of 16th International Symposium on Combustion. The Combustion Institute, 1976. Pp. 719–729.

61. McGrattan, K.B., Hostikka, S., Floyd, J.E., Baum, H. & Rehm, R. Fire Dynamics Simulator (Version 5): Technical Reference Guide. Gaithersburg, MD: National Institute of Standards and Technology, October 2007. NIST Special Publication 1018-5.

62. McGrattan, K.B., Klein, B., Hostikka, S. & Floyd, J.E. Fire Dynamics Simulator (Version 5): User's Guide. Gaithersburg, MD: National Institute of Standards and Technology, October 2007. NIST Special Publication 1019-5.

63. Olenick, S. & Carpenter, D. An Updated International Survey of Computer Models for Fire and Smoke. Journal of Fire Protection Engineering, 2003. Vol. 13, pp. 87–110.

64. Ferziger, J.H. & Perić, M. Computational Methods for Fluid Dynamics. Heidelberg: Springer, 1997. Corrected 2nd printing. 364 p.

65. Courant, R. Friedrichs, K.O. & Lewy, H. Über die partiellen Differential-gleichungen der mathematischen Physik. Mathematische Annalen 100, 1928. Pp. 32–74.

66. Courant, R., Friedrichs, K. & Lewy, H. On the partial difference equations of mathematical physics. IBM Journal, 1967, pp. 215–234. English translation of the 1928 German original paper.

67. Baum, H.R. & Rehm, R.G. Calculations of Three Dimensional Buoyant Plumes in Enclosures. Combustion Science and Technology, 1984. Vol. 40, pp. 55–77.

68. Holen, J., Brostrom, M. & Magnussen, B.F. Finite Difference Calculation of Pool Fires. In: Proceedings of the 23rd Symposium (International) on Combustion, Combustion Institute, 1990. Pp. 1677–1683.

69. Taylor, S., Petridis, M., Knight, B., Ewer, J., Galea, E.R & Patel, M. SMARTFIRE: an integrated computational fluid dynamics code and expert system for fire field modelling. In: Hasemi, Y. (ed.) Proceedings of Fifth (5th) International Symposium on Fire Safety Science. March 3–7, 1997, Melbourne, Australia. Boston, MA: International Association for Fire Safety Science, 1997. Pp. 1285–1296.

70. Welch, S. & Rubini, P. Three-Dimensional Simulation of a Fire-Resistance Furnace. In: Hasemi, Y. (ed.) Proceedings of Fifth (5th) International Symposium on Fire Safety Science. March 3–7, 1997, Melbourne, Australia. Boston, MA: International Association for Fire Safety Science, 1997. Pp. 1009–1020.

71. Suard, S., Audouin, L., Babik, F., Rigollet, L. & Latche, J.C. Verification and Validation of the ISIS CFD Code for Fire Simulation. Workshop on Assessment of Calculation Methods in Fire Safety Engineering, San antonio, TX, USA, 10 April 2006. ISO/TC 92/SC4. 28 p.

72. Greiner, M. & Suo-Anttila, A. Radiation Heat Transfer and Reaction Chemistry Models for Risk Assessment Compatible Fire Simulations. Journal of Fire Protection Engineering, 2006. Vol. 16, No. 2, pp. 79–104.

73. Yan, Z. Large Eddy Simulation of Soot Formation in a Turbulent Diffusion Flame. In: Gottuk, D.T. & Lattimer, B.Y. (eds.). Proceedings of Eighth International Symposium on Fire Safety Science. Beijing, China, September 18–23, 2005. International Association for Fire Safety Science, 2005. Poster abstract.

74. Cheung, A.L.K., Cheung, S.C.P., Yeoh, G.H. & Yuen, R.K.K. Investigation of Pulsating Behaviour of Buoyant Fires by Using Large Eddy Simulation (LES) Approach with Soot and Radiation. In: Gottuk, D.T. & Lattimer, B.Y. (eds.). Proceedings of Eighth International Symposium on Fire Safety Science. Beijing, China, September 18–23, 2005. International Association for Fire Safety Science, 2005. Poster abstract.

75. Kumar, S. Mathematical modelling of Natural Convection in Fire – A State of the Art Review of the Field Modelling of Variable Density Turbulent Flow. Fire and Materials, 1983. Vol. 7, pp. 1–24.

76. Liu, F. & Wen, J.X. The effect of different turbulence models on the CFD simulation of buoyant diffusion flames. Fire Safety Journal, 2002. Vol. 37, No. 2, pp. 125–151.

77. McGrattan, K.B., Rehm, R.G. & Baum, H.R. Fire-Driven Flows in Enclosures. Journal of Computational Physics, 1994. Vol. 110, No. 2, pp. 285–291.

78. Rehm, R.G., McGrattan, K.B., Baum, H.R. & Cassel, K.W. Transport by Gravity Currents in Building Fires. In: Fire Safety Science – Proceedings of the Fifth International Symposium. International Association for Fire Safety Science, 1997. Pp. 391–402.

79. Clement, J.M. & Fleischmann, C.M. Experimental Verification of the Fire Dynamics Simulator Hydrodynamic Model. In: Fire Safety Science – Proceedings of the Seventh International Symposium. International Association for Fire Safety Science, 2002. Pp. 839–862

80. Baum, H.R., McGrattan, K.B. & Rehm, R.G. Three Dimensional Simulations of Fire Plume Dynamics. In: Hasemi, Y. (ed.) Proceedings of Fifth (5th) International Symposium on Fire Safety Science. March 3–7, 1997, Melbourne, Australia. Boston, MA: International Association for Fire Safety Science, 1997. Pp. 511–522.

81. Baum, H.R. & McCaffrey, B.J. Fire Induced Flow Field – Theory and Experiment. In: Proceedings of the Second International Symposium on Fire Safety Science. International Association for Fire Safety Science, 1989. Pp. 129–148.

82. McGrattan, K.B., Baum, H.R. & Rehm, R.G. Large Eddy Simulations of Smoke Movement. Fire Safety Journal, 1998. Vol. 30, pp. 161–178.

83. Ma, T.G. & Quintiere, J.G. Numerical simulation of axi-symmetric fire plumes: accuracy and limitations. Fire Safety Journal, 2003. Vol. 38, No. 5, pp. 467–492.

84. Hamins, A., Maranghides, A., McGrattan, K.B., Johnsson, E., Ohlemiller, T., Donnelly, M., Yang, J., Mulholland, G., Prasad, K., Kukuck, S., Anleitner, R. & McAllister, T. Report on Experiments to Validate Fire Dynamic and Thermal-Structural Models for Use in the World Trade Center Investigation. Gaithersburg, MD: National Institute of Standards and Technology, 2004. NIST Special Publication 1000-B.

85. Hamins, A., Maranghides, A., McGrattan, K.B., Ohlemiller, T. & Anletiner, R. Experiments to Validate Models of Fire Growth and Spread for use in the World Trade Center Investigation. Gaithersburg, MD: National Institute of Standards and Technology, 2004. NIST Special Publication 1000-10E.

86. McGrattan, K.B. Verification and Validation of Selected Fire Models for Nuclear Power Plant Applications. Volume 7. Fire Dynamics Simulator (FDS). Gaithersburg, MD: National Institute of Standards and Technology. Washington, DC: Nuclear Regulatory Commission. Palo Alto, CA: Electric Power Research Institute, 2007. NUREG-1824, EPRI 1011999. Volume 7. 205 p.

87. de St. Germain, J.D., McCorquodale, J., Parker, S.G. & Johnson, C.R. Uintah: A Massively Parallel Problem Solving Environment, Ninth IEEE International Symposium on High Performance and Distributed Computing. IEEE, 2000. Pp. 33–41.

88. Pope, S.B. Ten questions concerning the large-eddy simulation of turbulent flows. New Journal of Physics, 2004. Vol. 6, pp. 1–24.

89. Zhang, W., Hamer, A., Klassen, M., Carpenter, D. & Roby, R. Turbulence statistics in a fire room model by large eddy simulation. Fire Safety Journal, 2002. Vol. 37, No. 8, pp. 721–752.

90. Tuovinen, H., Blomqvist, P. & Saric, F. Modelling of hydrogen cyanide formation in room fires. Fire Safety Journal, 2004. Vol. 39, No. 8, pp. 737–755.

91. Yang, R., Weng, W.G., Fan, W.C. & Wang, Y.S. Subgrid scale laminar flamelet model for partially premixed combustion and its application to backdraft simulation. Fire Safety Journal, 2005. Vol. 40, No. 2, pp. 81–98.

92. Kang, Y. & Wen, J. X. Large Eddy Simulation of a Small Pool Fire. Combustion Science and Technology, 2004. Vol. 176, No. 12, pp. 2193–2223.

93. Beyler, C.L. Fire Hazard Calculations for Large, Open Hydrocarbon Fires. In: SFPE Handbook of Fire Protection Engineering. Quincy, MA: Society of Fire Protection Engineers, 2002. 3rd Edition. Pp. 3-268–3-314.

94. Siegel, R. & Howell, J.R. Thermal Radiation Heat Transfer. New York, NY: Hemisphere Publishing Corporation, 1981. 2nd ed. 862 p.

95. Özisik, M.N. Radiative transfer and interactions with conduction and convection. New York, NY: John Wiley & Sons Inc., 1973. 575 p.

96. Lockwood, F.C. & Shah, N.G. A new radiation solution method for incorporation in general combustion prediction procedures. In: Proceedings of the 18th Symposium (International) on Combustion. Pittsburgh, PA: The Combustion Institute, 1981. pp. 1405–1416.

97. Jensen, K.A., Ripoll, J.-F., Wray, A.A., Joseph, D. & El Hafi, M. On various modeling approaches to radiative heat transfer in pool fires. Combustion and Flame, 2007. Vol. 148, No. 4, pp. 263–279.

98. Dembele, S. & Wen, J.X. Evaluation of a fast correlated-k approach for radiation calculations in combustion systems. Numerical Heat Transfer Part B, 2003. Vol. 44, No. 4, pp. 365–385.

99. Dembele, S., Zhang, J. & Wen, J.X. Assessments of Spectral Narrow Band and Weighted-Sum-of-Gray-Gases Models for Computational Fluid Dynamics Simulations of Pool Fires. Numerical Heat Transfer Part B, 2005. Vol. 48, No. 3, pp. 257–276.

100. Zhang, J., Dembele, S., Karwatzki, J. & Wen, J. X. Effect of Radiation Models on CFD Simulations of Upward Flame Spread. In: Gottuk, D.T. & Lattimer, B.Y. (eds.). Proceedings of Eighth International Symposium on Fire Safety Science. Beijing, China, September 18–23, 2005. International Association for Fire Safety Science, 2005. Pp. 421–432.

101. Wiscombe, W. Mie scattering calculations: Advances in technique and fast, vector-speed computer codes. National Center For Atmospheric Research, 1979 (revised 1996). NCAR Technical Note NCAR/TN-140+STR.

102. Bohren, C.F. & Huffman, D.R. Absorption and scattering of light by small particles. New York, NY: John Wiley & Sons, 1983. 530 p.

103. Berour, N., Lacroix, D., Boulet, P. & Jeandel, G. Radiative and conductive heat transfer in a nongrey semitransparent medium. Application to fire protection curtains. Journal of Quantitative Spectroscopy & Radiative Transfer, 2004. Vol. 86, pp. 9–30.

104. Trivic, D.N., O'Brien, T.J. & Amon, C.H. Modeling the radiation of anisotropically scattering media by coupling Mie theory with Finite volume method. International Journal of Heat and Mass Transfer, 2004. Vol. 47, pp. 5765–5780.

105. Collin, A., Boulet, P., Lacroix, D. & Jeandel, G. On radiative transfer in water spray curtains using the discrete ordinates method. Journal of Quantitative Spectroscopy & Radiative Transfer, 2005. Vol. 92, pp. 85–110.

106. Yeoh, G.H., Yuen, R.K.K., Chueng, S.C.P. & Kwok, W.K. On modelling combustion, radiation and soot processes in compartment fires. Building and Environment, 2003. Vol. 38, No. 6, pp. 771–785.

107. Wen, J.X., Huang, L.Y. & Roberts, J. The effect of microscopic and global radiative heat exchange on the field predictions of compartment fires. Fire Safety Journal, 2001. Vol. 36, No. 3, pp. 205–223.

108. Lautenberger, C.W., de Ris, J.L., Dembsey, N.A., Barnett, J.R. & Baum, H.R. A simplified model for soot formation and oxidation in CFD simulation of non premixed hydrocarbon flames. Fire Safety Journal, 2005. Vol. 40, No. 2, pp. 141–176.

109. Prasad, K.R. & Baum, H.R. Coupled Fire Dynamics and Thermal Response of Complex Building Structures. In: Chen, J.H., Colket, M.D., Barlow, R.S. & Yetter, R.A. (eds.). Proceedings of the 30th Symposium (International) on Combustion. July 25–30, 2004, Chicago, IL. Pittsburgh, PA: Combustion Institute, 2005. Vol. 30. Part 2. Pp. 2255–2262.

110. Atreya, A. & Baum, H.R. Model of Opposed-Flow Flame Spread Over Charring Materials. In: Chen, J.H. & Colket, M. D. (eds.). Proceedings of the 29th Symposium (International) on Combustion. July 21–25, 2002, Sapporo, Japan. Pittsburgh, PA: Combustion Institute, 2002. Vol. 29. Part 1. Pp. 227–236.

111. Kim, S.C. & Ryou, H.S. An experimental and numerical study on fire suppression using a water mist in an enclosure. Building and Environment, 2003. Vol. 38, No. 11, pp. 1309–1316.

112. Madsen, J. Computational and Experimental Study of Sprays from the Breakup of Water Sheets. Denmark: Aalborg University Esbjerg, 2006. PhD Thesis. 260 p.

113. Ingram, D.M., Causon, D.M. & Mingham, C.G. Developments in Cartesian cut cell methods. Mathematics and Computers in Simulation, 2003. Vol. 61, pp. 561–572.

114. Gemeny, D.F., Alex, P.E., Kline, A.J. & Hardeman, B. PyroSim: A Dynamic Graphical User Interface for the Fire Dynamics Simulator and Pathfinder: A Companion Egress Model. INTERFLAM 2007. Proceedings of the 11th International Conference. September 3–5, 2007, London, England. Vol. 2, pp. 1417–1422.

115. Heinisuo, M. & Laasonen, M. Product modeling, part of the fire safety concept in the future for metal structures? In: Advanced research workshop on Fire Computer Modeling. Santander, Spain: University of Cantabria. 2007.

116. Dimyadi, J.A.W., Spearpoint, M. & Amor, R. Generating fire dynamics simulator geometrical input using an IFC-based building information model. Electronic Journal of Information Technology in Construction, 2007. Vol. 12, p. 443.

117. Chang, S.L. & Rhee, K.T. Blackbody radiation functions. International Communications in Heat and Mass Transfer, 1984. Vol. 11, pp. 451–455.

118. Grosshandler, W. RadCal: A Narrow Band Model for Radiation Calculations in a Combustion Environment. Gaithersburg, MD: National Institute of Standards and Technology, 1993. NIST Technical Note TN 1402.

119. Kim, S.H. & Huh, K.Y. Assessment of The Finite-Volume Method and The Discrete Ordinate Method for Radiative Heat Transfer In a Three-Dimensional Rectangular Enclosure. Numerical Heat Transfer, Part B, 1999. Vol. 35, pp. 85–112.

120. Murthy, J.Y. & Mathur, S.R. Radiative Heat Transfer in Axisymmetric Geometries Using an Unstructured Finite-Volume Method. Numerical Heat Transfer, Part B, 1998. Vol. 33, pp. 397–416.

121. Raithby, G.D. Discussion of the Finite-Volume Method for Radiation, and its Application Using 3D Unstructured Meshes. Numerical Heat Transfer, Part B, 1999. Vol. 35, pp. 389–405.

122. Chai, J.C., Lee, H.S. & Patankar, S.V. Finite Volume Method for Radiation Heat Transfer. Journal of Thermophysics and Heat Transfer, 1994. Vol. 8, No. 3, pp. 419–425.

123. Ravigururajan, T. & Beltran, M. A Model for Attenuation of Fire Radiation Through Water Droplets. Fire Safety Journal, 1989. Vol. 15, pp. 171–181.

124. Yang, W., Parker, T., Ladouceur, H.D. & Kee, R.J. The Interaction of Thermal Radiation and Water Mist in Fire Suppression. Fire Safety Journal, 2004. Vol. 39, pp. 41–66.

125. Wiscombe, W.J. Improved Mie Scattering Algorithms. Applied Optics, 1980. Vol. 19, No. 9, pp. 1505–1509.

126. Hale, G.M. & Querry, M.R. Optical constants of water in the 200 nm to 200 mum wavelength region. Applied Optics, 1973. Vol. 12, No. 3, pp. 555–563.

127. Zel'dovich, Y.B. & Raizer, Y.P. Physics of shock waves and high-temperature hydrodynamic phenomena. New York, NY: Dover Publications, 2002. Translated from the Russian and then edited by W.D. Hayes and R.F. Probstein.

128. Hamins, A., Klassen, M., Gore, J. & Kashiwagi, T. Estimate of Flame Radiance via a Single Location Measurement in Liquid Pool Fires. Combustion and Flame, 1991. Vol. 86, pp. 223–228.

129. Murrel, J.V., Crowhurst, D. & Rock, P. Experimental study of the thermal radiation attenuation of sprays from selected hydraulic nozzles. In: Proceedings of Halon options technical working conference. The University of New Mexico, Albuquerque, 1995. pp. 369–378.

130. Husted, B.P. Experimental measurements of water mist systems and implications for modelling in CFD. Lund, Sweden: Lund University, 2007. Doctoral Thesis. 124 p. + app.

131. Dembele, S., Wen, J.X. & Sacadura, J.-F. Experimental study of water sprays for the attenuation of fire thermal radiation. Journal of Heat Transfer, 2001. Vol. 123, pp. 534–543.

132. McGrattan, K. B. Fire Modeling: Where Are We? Where Are We Going? In: Gottuk, D.T. & Lattimer, B.Y. (eds.). Proceedings of Eighth International Symposium on Fire Safety Science. Beijing, China, September 18–23, 2005. International Association for Fire Safety Science, 2005. Pp. 53–68.

133. Schlichting, H. Boundary Layer Theory, New York, NY: McGraw-Hill, 1987. 7th reissued ed. 817 p.

# List of related publications


1. Hostikka, S., Baum, H. & McGrattan, K. Large eddy simulation of the cone calorimeter. Proceedings of the 2nd Joint Meeting of the US Sections of the Combustion Institute. Oakland, CA, 25–28 March 2001. Western States Section of the Combustion Institute, 2001.

2. Hostikka, S. & McGrattan, K. Large eddy simulation of wood combustion. INTERFLAM 2001. Proceedings of the 9th International Conference. Edinburgh, GB, 17–19 Sept. 2001. Vol. 1, pp. 755–765.

3. McGrattan, K.B., Floyd, J.E., Forney, G.P., Baum, H.R. & Hostikka, S. Improved radiation and combustion routines for a large eddy simulation fire model. Fire Safety Science. Proceedings of the seventh international symposium. Worcester, MA, 16–21 June 2003. Evans, D.D. (ed.). International Association for Fire Safety Science, 2003, pp. 827–838.

4. Hostikka, S., Keski-Rahkonen, O. & Korhonen, T. Probabilistic Fire Simulator. Theory and User's Manual for Version 1.2, VTT Building and Transport. VTT Publications 503, 2003. 72 p. + app. 1 p.

5. Hietaniemi, J., Hostikka, S. & Korhonen, T. Probabilistic Fire Simulation, Proc. of the 5th Int'l Conference on Performance-Based Codes and Fire Safety Design Methods, Society of Fire Protection Engineers, 2004, pp. 280–291.

6. Hostikka, S. & Keski-Rahkonen, O. Advanced probabilistic simulation of NPP fires. Proceedings of the 18th International Conference on Structural Mechanics in Reactor Technology. SMIRT 18. Beijing, China, August 7–12, 2005. Atomic Energy Press. Beijing (2005), 3984–3996.

7. Keski-Rahkonen, O., Mangs, J., Hostikka, S. & Korhonen, T. Quantitative application of Monte Carlo simulation in Fire-PSA. Kerntechnik, Vol. 72, 3, 2007, pp. 149–155.

8. Heikkinen, J., Hostikka, S., Shemeikka, J. & Kauppinen, T. Prediction of Draught and Surface Temperatures in a Living Room Using CFD. Roomvent 2007, 10th International Conference on Air Distribution in Rooms, Helsinki, Finland, 13–15 June 2007. Finvac ry, 2007.

PAPER I

# Probabilistic simulation of fire scenarios

In: Nuclear Engineering and Design 2003.
Vol. 224, No. 3, pp. 301–311.

Available online at www.sciencedirect.com
SCIENCE DIRECT®
Nuclear Engineering and Design 224 (2003) 301–311
Nuclear Engineering and Design
www.elsevier.com/locate/nucengdes

# Probabilistic simulation of fire scenarios

Simo Hostikka*, Olavi Keski-Rahkonen

*VTT Building and Transport, PO Box 1803, FIN-02044 VTT, Finland*

Received 15 November 2002; received in revised form 26 March 2003; accepted 29 March 2003

**Abstract**

A risk analysis tool is developed for computation of the distributions of fire model output variables. The tool, called Probabilistic Fire Simulator (PFS), combines Monte Carlo simulation and CFAST, a two-zone fire model. In this work, the tool is used to estimate the failure probability of redundant cables in a cable tunnel fire, and the failure and smoke filling probabilities in an electronics room during an electronics cabinet fire. Sensitivity of the output variables to the input variables is calculated in terms of the rank order correlations. The use of the rank order correlations allows the user to identify both modelling parameters and actual facility properties that have the most influence on the results. Various steps of the simulation process, i.e. data collection, generation of the input distributions, modelling assumptions, definition of the output variables and the actual simulation, are described.


## 1. Introduction

### *1.1. Setting the problem*

Traditionally, the deterministic fire models have been used to estimate the consequences of the fire with some given set of input variables. Presuming the model is principally valid for the given problem, the uncertainty of the prediction depends on, how the uncertainties in input values are transferred through the system described by the model. As the systems are usually non-linear and rather complicated, the classical analytic methods of estimation of random error propagation are of little use. The possible uncertainty or distribution of the input variables can be taken into account by manually varying the inputs within allowable and rather narrow limits. This is mathematically a fairly well-posed problem, and a rough range of error can be established for the target function by carrying out a fairly small number of such calculations.

If more complete information of the error distribution is needed, Monte Carlo techniques should be used. In Monte Carlo, a large number of samples is randomly chosen from the input space and mapped through the system into the target distribution. In demanding error analyses this has been a standard technique for some time.

The problem is somewhat different when fire models are used for estimation of target fire safety. To enlighten the difference, we consider two examples. In Example 1, the scenario is taken as the author's office. While writing this paper, the computer might catch fire. The target question is: what is the probability that the fire spreads outside the room of origin, i.e. outside the author's office?

While this target question might be interesting individually, a more relevant question for the fire safety of our office building would be (Example 2): given a fire breaks out in an office, what is the probability it spreads outside the room of origin? Since various

* Corresponding author. Tel.: +358-9-456-4839; fax: +358-9-456-4815.
*E-mail address:* simo.bostikka@vtt.fi (S. Hostikka).

0029-5493/$ – see front matter © 2003 Elsevier Science B.V. All rights reserved.
doi:10.1016/S0029-5493(03)00106-7

**Nomenclature**

| | |
|---|---|
| $A_{\text{fuel}}$ | area of the fuel surface inside the electronics cabinet |
| $A_{\text{e}}$ | area of the cabinet exhaust opening |
| $A_{\text{i}}$ | area of the cabinet inflow opening |
| $F_i$ | probability distribution function of variable $i$ |
| $f_i$ | probability density function of variable $i$ |
| $g$ | limit state function |
| $H_{\text{v}}$ | height between the cabinet openings |
| $n$ | number of random variables |
| $P_{\text{A}}$ | probability of event A |
| $P_{\text{ign}}$ | probability of ignition |
| $\dot{Q}$ | rate of heat release (RHR) |
| $\dot{Q}''_{\text{fuel}}$ | rate of heat release per fuel area |
| $\boldsymbol{X}$ | vector of random variables |
| $x$ | random variable |
| $t$ | time |
| $t_{\text{g}}$ | RHR growth time |
| $t_{\text{d}}$ | starting time of the RHR decay phase |
| $z$ | height |
| $z_{\text{target}}$ | height of the target component |
| $z_{\text{source}}$ | height of the fire source |

*Greek letters*

| | |
|---|---|
| $\chi$ | combustion efficiency |
| $\phi_x$ | joint probability density function |
| $\tau$ | RHR decay time |

rooms do not differ considerably from each other, a deterministic room fire model could be used as well for the both cases. Since in Example 2, the room of ignition could be any of the rooms in the building, an averaging over the rooms is needed to answer the final question. For Example 1, we assess only one room, for Example 2, some 100 rooms need to be assessed. To find an answer to Example 2, we have to take averages over the whole set of these 100 rooms forming our office building.

### *1.2. Goal of the paper*

The goal of this study is to develop a calculation tool for Example 2 in the form of a probabilistic fire simulation. A specific task is the prediction of the failure probabilities of specified items in fires. If the size of the set to be assessed grows, individual assessment of each scenario becomes uneconomic. Describing variables of the set to be assessed as distributions a risk analysis model can be developed using the Monte Carlo simulation. Formally, deterministic calculations are the same for Examples 1 and 2. Backed by some experience we believe, that input distributions are generally much narrower for Example 1 than for Example 2. Typically, for Example 1, an input variable is normally distributed, whereas for Example 2, the same variable has lognormal or other skewed distribution. While using this approach, we presume further, that the epistemic uncertainty of the applied deterministic model is small as compared with the uncertainties caused by input distributions. When this is not the case, Monte Carlo is not the way to handle the problem. Instead, the modelling must be improved. We have already built this possibility in our tool: starting economically from correlations for simple cases, we can change to a zone model, and ultimately go to computational fluid dynamics.

Commercial Monte Carlo simulation software @RISK[1] is used for the random sampling and post processing. A two-zone model CFAST (Peacock et al., 1993) is used to model smoke spreading and gas temperature during the fire. The risk analysis software and CFAST are combined in a spreadsheet computing environment. The tool, called Probabilistic Fire Simulator (PFS), is intended to be fully general and applicable to any fire scenario amenable to deterministic numerical simulation. The main outcome of the new tool is the automatic generation of the distributions of the selected result variables, for example, component failure time. The sensitivity of the output variables to the input variables can be calculated in terms of the rank order correlations. The use of the rank order correlations allows the user to simultaneously identify both the modelling parameters and the actual facility properties that have the most influence on the results. Typically, the simulation process consists of the data collection, generation of the input distributions, modelling and assumptions, definition of the output variables and the actual Monte Carlo simulation.

The validity of the models used is not discussed here. We do not compare our results with experiments

[1] @RISK is a product of Palisade Corporation, Newfield, NY.

either, because the results from some 1000 random experiments are not available for any real fire scenario. There is only one potential source on such data: fire statistics. Even the best statistical data would not contain information detailed enough for comparison with deterministic calculations. In the future, we are going to enlarge the input database, and improve the fire models for the calculation of true scenarios allowing comparison with fire statistics directly. So far it is too early to say whether this goal is realistic. Meanwhile, we concentrate on the collection of good statistical data for input distributions, and use deterministic fire models, which are well evaluated.

Two example scenarios are studied here: a fire in a nuclear power plant cable tunnel and a fire in an electronics room. The cable tunnel fire was studied experimentally by Mangs and Keski-Rahkonen (1997) and theoretically by Keski-Rahkonen and Hostikka (1999). These studies showed that the CFAST two-zone model can be used to predict the thermal environment of a cable tunnel fire, at least in its early stages. Here, the effects of the input variables, like tunnel geometry and fire source properties, are studied by choosing them randomly. The input distributions are based on the statistics collected from the power plant.

The electronics room fire was previously studied by Eerikäinen and Huhtanen (1991). They used computational fluid dynamics to predict the thermal environment inside the room, when one electronics cabinet is burning. The same scenario is studied here using the two-zone model. The fire source is selected randomly based on the collected distribution of different cabinet types.

## 2. Monte Carlo simulation

The question set by the probabilistic safety assessment process is usually: "What is the probability that a certain component or system is lost during a fire?" This probability is a function of all possible factors that may affect on the development of the fire and the systems reaction to it. This question has not been dealt with exactly for fire in this form, but similar systems in other fields have been studied extensively (Spiegel, 1980; Vose, 1996). Here we adapt this general theory for our specific fire problem.

Let us denote the group of affecting variables by a vector $\boldsymbol{X} = (X_1, X_2, \ldots, X_n)^{\mathrm{T}}$ and the corresponding density functions by $f_i$ and distribution functions by $F_i$. The occurrence of the target event A is indicated by a limit state function $g(t, \boldsymbol{x})$, which depends on time $t$ and vector $\boldsymbol{x}$ containing the values of the random variables. As an example of the target event, we consider the loss of some component. The limit state condition is now defined using function $g(t, \boldsymbol{x})$:

$$\begin{aligned} &g(t, \boldsymbol{x}) \leq 0, \text{ if the component is lost at time } t \\ &g(t, \boldsymbol{x}) > 0, \text{ if the component is not lost at time } t \end{aligned} \tag{1}$$

Other possible target events are, for example, heat detector activation and smoke filling. The development of fire and the response of the components under consideration are assumed to be fully deterministic processes where the same initial and boundary conditions always lead to the same final state. With this assumption, the probability of event A can now be calculated by the integral

$$P_{\mathrm{A}}(t) = \iint_{\{\boldsymbol{x} | g(t,\boldsymbol{x}) \leq 0\}} \cdots \int \phi_x(\boldsymbol{x}) \, \mathrm{d}x_i \tag{2}$$

where $\phi_x$ is the joint density function of variables $\boldsymbol{X}$. Generally, variables $\boldsymbol{X}$ are dependent, and $\phi_x(\boldsymbol{x}) \neq \prod_{i=1}^{n} f_i(x_i)$.

In this work, the probability $P_{\mathrm{A}}$ is calculated using Monte Carlo simulations where input variables are sampled randomly from the distributions $F_i$. If $g(t, \boldsymbol{x})$ is expensive to evaluate, a stratified sampling technique should be used. In Latin Hypercube sampling (LHS) the $n$-dimensional parameter space is divided into $N^n$ cells (McKay et al., 1979). Each random variable is sampled in fully stratified way and then these samples are attached randomly to produce $N$ samples from $n$ dimensional space. The advantage of this approach is that the random samples are generated from all the ranges of possible values, thus giving insight into the tails of the probability distributions. A procedure for obtaining a Latin Hypercube sample for multiple, spatially correlated variables is given by Stein (1987). He showed that LHS will decrease the variance of the resulting integral relative to the simple random sampling whenever the sample size $N$ is larger than the number of variables $n$. However, the amount of reduction increases with the degree of additivity in the random quantities on which the function being simulated depends. In fire simulations, the simulation

result may often be a strongly non-linear function of the input variables. For this reason, we cannot expect that LHS would drastically decrease the variances of the probability integrals. Problems related to LHS with small sample sizes are discussed by Hofer (1999) as well as by Pebesma and Heuvelink (1999).

The sensitivity of the output $y$ to the different input variables $x$ is studied by calculating the Spearman's rank-order correlation coefficients (RCC). A value's "rank" is determined by its position within the min–max range of possible values for the variable. RCC is then calculated as

$$\mathrm{RCC} = 1 - \frac{6\sum d^2}{m(m^2-1)} \tag{3}$$

where $d$ is the difference between ranks of corresponding $x$ and $y$, and $m$ is the number of data pairs. RCC is independent of the distribution of the initial variable. The significance of the RCC values should be studied with the methods of statistical testing. In case of small datasets, the actual values of RCC should be interpreted with caution due to the possible spurious correlations inside the input data (Hofer, 1999).

## 3. Fire modelling

The transport of heat and smoke is simulated using a multi-room two-zone model CFAST (Peacock et al., 1993). It assumes two uniform layers, hot and cold, in each room of the building and solves the heat and mass balance equations for each room. A PFS worksheet is used to generate the input data for CFAST. The user may combine any experimental information or functions to the fire model input. The most important source term in the simulation is the rate of heat release (RHR). The RHR can be defined using analytical curves, like $t^2$-curve (Heskestad and Delichatsios, 1977; NFPA, 1985), or specific experimental curves.

Typical results of the fire simulation are gas temperatures, smoke layer position and temperature of some solid object like cable. Usually, the actual target function is the time when some event takes place. Some examples of the target functions are smoke filling time, flash over time and component failure time. In this work, the most important target function is the cable failure time. An analytical, time dependent solution of the axially symmetric heat transfer equation is used to calculate the cable core and surface temperatures. The boundary condition is the gas temperature, given by CFAST. The analytical solution is relatively easy to implement, but the actual calculation may be time consuming, because the solution involves the roots of a non-linear equation and long convolution sums. These operations are made faster by pre-computing and tabulating the roots in advance, and by re-arranging the convolution sums to a form, where only current, and previous time step values are needed. The accuracy of the model has been validated by comparing against 1-D finite element solutions of the same problem. The failure of the cable is assumed, when it reaches some predefined failure temperature, which may be chosen randomly to consider the uncertainty of the method.

## 4. Results and discussion

### 4.1. Cable tunnel fire scenario

A fire in the cable tunnel of a nuclear power plant is simulated to find out the failure probability of cables located in the same tunnel with the fire. The fire ignites in a cable tray and the fire gases heat up a redundant cable, located on the opposite side of the same tunnel. The effect of a screen that divides the tunnel between the source and target is also studied. The distribution of the heat detector activation times is also calculated. A plan view of the physical geometry and the corresponding CFAST model are outlined in Fig. 1. A vertical cut of the tunnel is shown in Fig. 2. The tunnel is divided into five virtual rooms to allow horizontal variations in layer properties. The fire source is located in ROOM 1 and the target cable in ROOM 3, just on the opposite side of the screen. The length of the screen does not cover the whole tunnel, and therefore it is possible that smoke flows around the screen to the target. It is also possible, that smoke flows below the screen. In the end of the tunnel is a door to the ambient. The RHR from the fire source is modelled using an analytical $t^2$-type curve

$$\dot{Q}(t)\,(\mathrm{kW}) = \min\left\{\dot{Q}_{\max},\ 1000\left(\frac{t}{t_g}\right)^2\right\} \tag{4}$$

where $t$ is time, $t_g$ is the RHR growth time and $\dot{Q}_{\max}$ is the maximum RHR, that depends on the tunnel size.

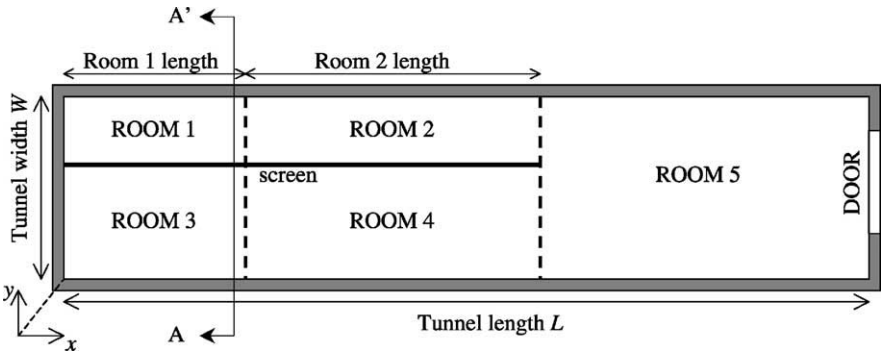


Fig. 1. A plan view of the cable tunnel model.

$t_g$ is treated as a normally distributed random variable with mean of 1000 s and standard deviation of 300 s.

Two different versions of the screen are studied. First, the screen is assumed to exist, with the lower edge below the 50% of the tunnel height. In the second scenario, the screen is removed by setting the lower edge very close to the ceiling, retaining the virtual room structure of the model. The dimensions of the tunnel and the cable tray locations are taken from the measured distributions of the power plant. About 50 tunnel cross sections have been studied to generate the distributions. The distribution of the cable diameter is based on the measurements in seven tunnel cross sections, containing 815 cables. A complete list of the random variables is given in Table 1. Fictitious, but typical values are assumed for the heat detector properties. Detector Response Time Index (RTI) determines the thermal inertia of the detector. While most of the variables are true physical properties and dimensions, the lengths of the virtual rooms are purely associated to the numerical model. It is desirable that these variables are less important than the true physical variables.

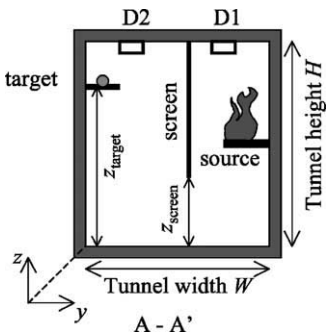


Fig. 2. A vertical cut A–A′ of the cable tunnel model. D1 and D2 denote heat detectors 1 and 2, respectively.

Three output variables are considered:

1. Failure time of the target cable.
2. Activation time of the first heat detector (D1), located in the room of fire origin.
3. Activation time of the second heat detector (D2), located in the room of target cable.

The Monte Carlo simulations were performed for both scenarios to generate the distributions of the output variables, and to find out the importance of each input variable. The convergence of the simulations was ensured by monitoring the values of the 10, 20, . . . , 90% fractiles, mean values and standard deviations of the output variable distributions. The convergence was assumed, when the values changed less than 1.5% in 50 iterations. About 1000 iterations were needed to reach the convergence. The simulations took typically about 1 day on a 1.7 GHz Pentium Xeon processor.

The distributions of the target failure times are shown in Fig. 3. The overall failure probabilities cannot be derived from the simulations because the distributions do not reach their final values during the total simulation time of 2400 s. However, the existence of the screen is found to dramatically decrease the failure probability of the redundant cable.

The distributions of the activation times of fire detectors D1 and D2 are shown in Figs. 4 and 5, respectively. The activation time distributions of detector D1 are very narrow. For D2, the distributions are wider than for D1, and the existence of the screen decreases the activation probability from 1.0 to 0.8.

Table 1
A list of random variables used in the cable tunnel fire scenario

| Variable | Distribution | Mean | S.D. | Min | Max | Units |
|---|---|---|---|---|---|---|
| RHR growth time $t_g$ | Normal | 1000 | 300 | 0 | 3000 | s |
| Source height $z_{source}/H$ | Uniform | | | 0 | 0.7 | |
| Ambient temperature | Normal | 20 | 3.0 | | | °C |
| Tunnel height $H$ | Measured | | | 1 | 8 | m |
| Tunnel width $W_{tunnel}$ | Measured | | | 1.5 | 6.5 | m |
| ROOM 1 length | Uniform | | | 2 | 5 | m |
| ROOM 2 length | Uniform | | | 5 | 10 | m |
| Tunnel length $L$ | Uniform | | | 30 | 100 | m |
| Door height $z_{door}/H$ | Uniform | | | 0.1 | 1.0 | |
| Door width $W_{door}/W_{tunnel}$ | Uniform | | | 0.01 | 1.0 | |
| Screen edge height $z_{screen}/H$ | Uniform | | | 0/0.95 | 0.5/1.0 | |
| Dimensionless cable height $z_{target}/H$ | Measured | | | 0.34 | 1 | |
| Cable radius | Measured | | | 9 | 81 | mm |
| Critical cable temperature | Normal | 200 | 20 | | | °C |
| Cable conductivity | Normal | 0.16 | 0.05 | 0.1 | 0.5 | W/km |
| Cable density | Normal | 1400 | 200 | 1000 | 2000 | kg/m$^3$ |
| Detector activation temperature | Normal | 57 | 3 | | | °C |
| Detector RTI | Normal | 50 | 10 | 40 | 60 | (m/s)$^{1/2}$ |
| Ventilation time constant | Uniform | | | 0.5 | 10 | h |
| Concrete density | Uniform | | | 1500 | 3000 | kg/m$^3$ |

The probability that the fire is detected before the target failure is studied in Fig. 6 by plotting the failure times of both scenarios against the corresponding detection times. In all cases, the detection takes place before the failure. However, this does not tell about the probability of the fire extinction because the sprinkler reliability and suppression processes are not considered.

The sensitivity of the target failure time for the various input variables is studied by calculating the rank order correlations. A graphical presentation of the rank order correlation coefficients is shown in Fig. 7. For clarity, only the values corresponding to the situation without a screen are shown. The three most important variables are the RHR growth time, assumed cable failure temperature and the cable radius. As the distributions of the first two variables do not have a solid physical background, this result can be used to direct the future research. In addition, the length of the virtual fire room has a strong correlation

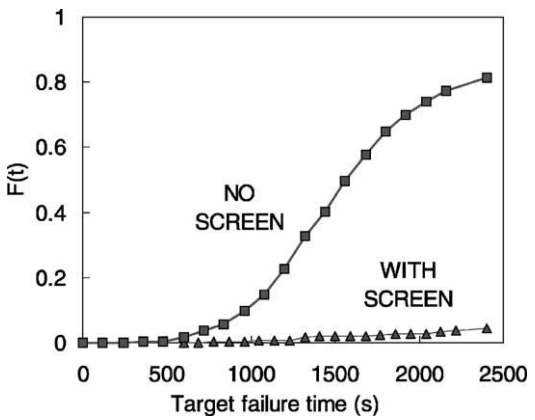


Fig. 3. The distributions of the target cable failure time.

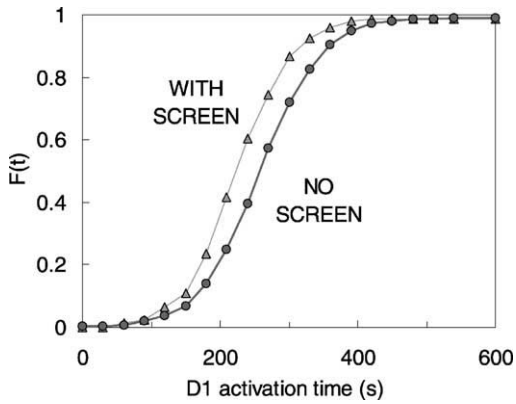


Fig. 4. The distributions of the heat detector D1 activation times. D1 is located inside the fire room (ROOM 1).

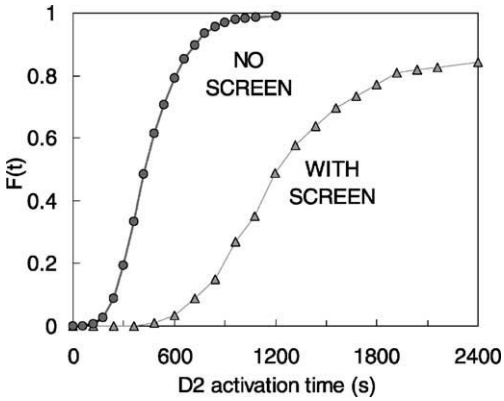


Fig. 5. The distributions of the heat detector D2 activation times. D2 is located inside the target room (ROOM 3).

with the failure time. In the scenario where screen is present, the height of the lower edge of the screen has strong negative correlation with the failure time. It is therefore recommended, that the screen, when present, should reach as low as possible to prevent smoke from flowing under the screen. The correlations with absolute value less than about 0.2 are not significant.

### 4.2. Electronics room fire scenario

As a second example, a fire of an electronics cabinet inside the electronics room is studied. In their previous study of the similar fire, Eerikäinen and Huhtanen (1991) found that a fire of a single cabinet does not cause direct threat to the other cabinets, in terms of the

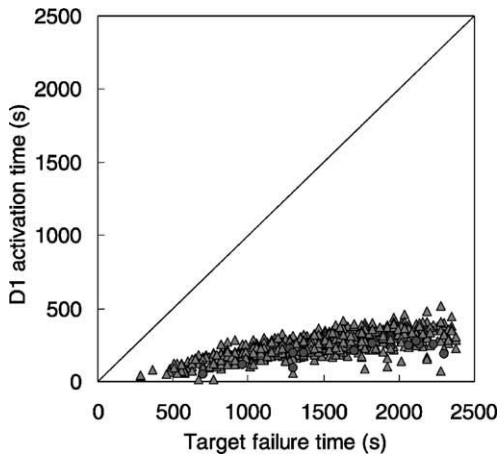


Fig. 6. Comparison of D1 activation times vs. target failure times ($N = 954$).

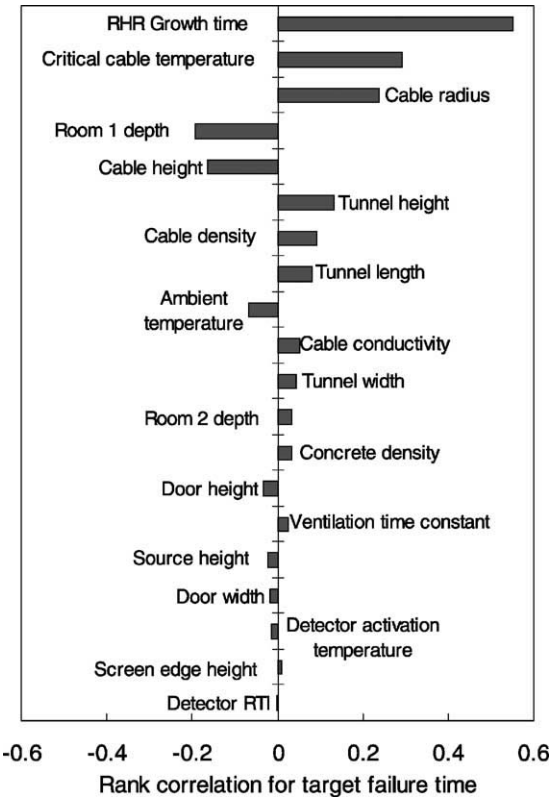


Fig. 7. The sensitivity of the target failure time to the input variables in the cable tunnel scenario.

gas temperature. However, the spreading of the fire, conductive heating of the components in the neighbour cabinets and the effect of smoke on the electronic components may cause failures in the other cabinets of the fire room. Therefore, the probability that the room is filled with smoke during a fire must be considered in addition to the temperature increase.

The fire room is 18.5 m long, 12.1 m wide and 3.0 m high electronics room, containing about 100 electronics cabinets in 12 rows. The geometry is outlined in Fig. 8. The room has mechanical ventilation with a nominal flow rate (1.11 $m^3$/s) and some additional leakages to the ambient. Both the ventilation flow rate and the leakage area are taken to be random variables. Separate cooling devices and smoke circulation through the ventilation system are not taken into account, nor is the heat transfer to the room boundaries. The omission of the cooling devices is known to change the predicted gas temperature sig-

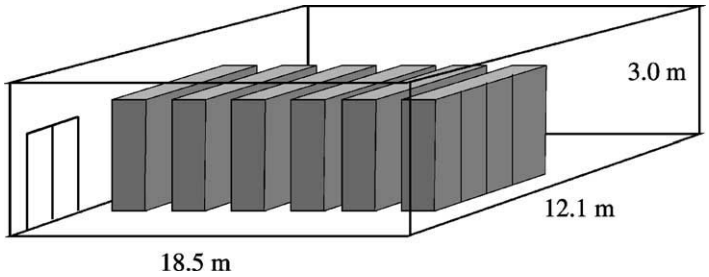


Fig. 8. An outline of the electronics room fire scenario.

nificantly. The results should therefore be considered as indicative only.

The starting point of the simulation is the collection of the physical data on the electronic cabinets. The geometrical properties and fuel content of 98 cabinets were measured. Based on the collected information, the cabinets were grouped into seven groups, shown in Table 2. The second column shows the number of cabinets in each group. $P_{\text{ign}}$ is the probability, that the ignition takes place in the particular group, calculated based on the amount of electronic devices (circuit boards and relays) inside the cabinets. Most differences are found in the fuel surface area $A_{\text{fuel}}$ and fire load. As these properties have an effect on the heat release rate curve, they are chosen to be distinctive properties like the vent properties.

The RHR is calculated using a cabinet model of Keski-Rahkonen and Mangs (2003), that assumes that the heat release rate during the fully developed cabinet fire is determined by the ventilation openings in the upper and lower parts of the cabinet. The maximum RHR is given by

$$\dot{Q}_{\text{max,vent}}\,(\text{kW}) = 7400\chi\sqrt{\frac{H_{\text{v}}}{(2.3/A_{\text{e}}^2)+(1/A_{\text{i}}^2)}} \qquad (5)$$

where $\chi$ is combustion efficiency factor, $H_{\text{v}}$ is the height between the openings and $A_{\text{e}}$ and $A_{\text{i}}$ are the areas of the exhaust and inflow openings, respectively. During the fire, the cabinet doors may open due to the thermal effects. In this case, the heat release rate is not ventilation but fuel controlled, and the maximum RHR becomes

$$\dot{Q}_{\text{max,fuel}} = \dot{Q}''_{\text{fuel}} \times A_{\text{fuel}} \qquad (6)$$

where $\dot{Q}''_{\text{fuel}}$ is the nominal heat release rate per unit surface of fuel, a random variable in the simulation, and $A_{\text{fuel}}$ is the free fuel area. A door opening indicator is used to select which equation is used to calculate the maximum RHR. The probability of the door-opening event during the fire is assumed to be 0.50. A $t^2$-type RHR curve with an exponential decay rate is used.

$$\dot{Q}(t)\,(\text{kW}) = \min\left\{1000\left(\frac{t}{t_{\text{g}}}\right)^2,\ \dot{Q}_{\text{max}},\ \dot{Q}_{\text{max}}\exp\left(-\frac{t-t_{\text{d}}}{\tau}\right)\right\} \qquad (7)$$

where $\dot{Q}_{\text{max}}$ is either $\dot{Q}_{\text{max,vent}}$ or $\dot{Q}_{\text{max,fuel}}$, depending on the value of the door opening indicator. The

Table 2
Grouping of the electronic cabinets

| Cabinet group | Number of cabinets | $P_{\text{ign}}$ | $H_{\text{cabinet}}$ (m) | $H_{\text{v}}$ (m) | $A_{\text{e}}$ (m$^2$) | $A_{\text{i}}$ (m$^2$) | $\dot{Q}_{\text{max,vent}}$ (kW) | $A_{\text{fuel}}$ (m$^2$) | Fire load (MJ) |
|---|---|---|---|---|---|---|---|---|---|
| HA | 42 | 0.53 | 2.33 | 1.96 | 0.126 | 0.121 | 425.8 | 5.35 | 1520 |
| 2HA | 9 | 0.18 | 2.36 | 1.97 | 0.129 | 0.110 | 419.5 | 8.54 | 2700 |
| 2HD | 1 | 0.02 | 2.36 | 1.97 | 0.129 | 0.110 | 419.5 | 7.76 | 2000 |
| JB | 14 | 0.08 | 2.36 | 1.97 | 0.129 | 0.110 | 419.5 | 2.49 | 800 |
| JK2 | 3 | 0.05 | 2.20 | 2.05 | 0.015 | 0.068 | 63.8 | 7.37 | 1200 |
| JM | 17 | 0.13 | 2.36 | 1.97 | 0.129 | 0.110 | 419.5 | 3.22 | 800 |
| P | 5 | 0.01 | 2.19 | 1.89 | 0.215 | 0.126 | 574.4 | 0.64 | 100 |

The symbols are explained in the text.

Table 3
A list of random variables used in the electronics room fire scenario

| | Distribution type | Mean | S.D. | Min | Max | Units |
|---|---|---|---|---|---|---|
| RHR growth time $t_g$ | Uniform | | | 750 | 2000 | s |
| Door opening indicator | Discrete | | | 0 | 1 | |
| RHR decay time $\tau$ | Uniform | 800 | 1400 | 800 | 1400 | s |
| Cabinet type | Measured | | | 1 | 7 | |
| RHR per unit area $\dot{Q}''_{fuel}$ | Normal | 150 | 40 | 50 | 300 | kW/m$^2$ |
| Detector RTI | Normal | 80 | 10 | 50 | 100 | (m/s)$^{1/2}$ |
| Detector activation temperature | Normal | 57 | 5 | 40 | 100 | °C |
| Critical target temperature | Normal | 80 | 10 | 50 | 200 | °C |
| Target radius | Uniform | | | 1 | 5 | mm |
| Leakage area | Uniform | | | 0 | 3 | m$^2$ |
| Virtual source height $z_f/H_{cabinet}$ | Uniform | | | 0 | 0.5 | |
| Ventilation flow rate | Normal | 1.11 | 0.2 | 0.5 | 2 | m$^3$/s |

growth and decay time constants, $t_g$ and $\tau$, are random variables in the simulation. The parameters of their distributions are taken from the experimental works of Mangs and Keski-Rahkonen (1994, 1996). The decay phase starts ($t = t_d$) when 70% of the fire load is used.

It is very difficult to apply the zone-type fire model to the cabinet fire, because the actual source term for the room is the smoke plume flowing out of the cabinet. A reasonable representation of the smoke flow can be found if the base of the "virtual" fire source is placed close to one-half of the cabinet height. Then the mass flow of free smoke plume at the height of the cabinet ceiling is roughly equal to the vent flow. Now, the height of the virtual fire source is considered as a random variable. A list of the random variables is given in Table 3.

Four output variables are considered

1. Failure time of the target cable. The cable is located 0.5 m below the height of the cabinet, therefore simulating a device inside a similar cabinet.
2. Smoke filling time: time when the smoke layer reaches the height 2.0 m.
3. Smoke filling time: time when the smoke layer reaches the height 1.5 m.
4. Smoke filling time: time when the smoke layer reaches the height 1.0 m.

The effect of the observation height is studied by observing the smoke filling at three different heights. The convergence was ensured in the same manner, as in the previous example. Seven hundred iterations were needed for convergence this time. The simulation took about 4 h on a 2.0 GHz Xeon processor.

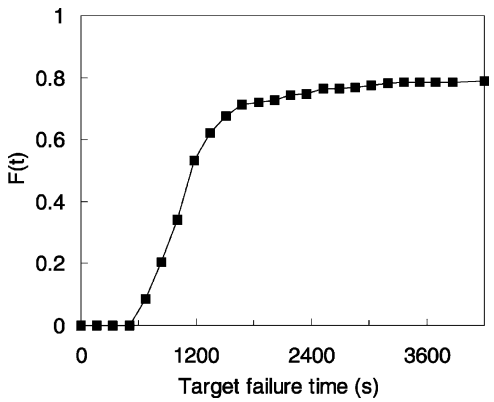


Fig. 9. The distribution of the target failure time.

The distribution of the target failure times is shown in Fig. 9. Target failures start after 500 s, after which the failure probability increases to 0.8. Higher failure probability would be found inside the neighbouring cabinets with a direct contact to the burning cabinet, and in the ceiling jet of the fire gases. These results are inconsistent with the previous findings of Eerikäinen and Huhtanen (1991), who concluded, based on the CFD simulations, that the mean gas temperatures in the room do not become high enough for component failures. The most obvious reason for the inconsistency is the difference in the simulation times. The overall simulated period employed here was 7200 s, while Eerikäinen and Huhtanen stopped their simulation after 600 s. At this point, our failure probability is still very small. Other possible reasons for the inconsistency are the omission of the cooling devices

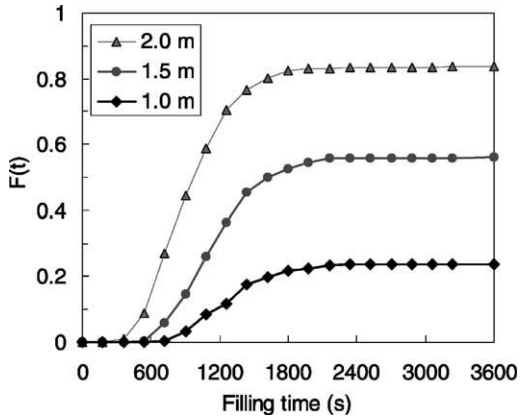


Fig. 10. The distributions of the smoke filling time.

and the variation of the RHR curve, which may cause very severe conditions in some simulations.

The distributions of the smoke filling times are shown in Fig. 10. The smoke layer reaches the height of the electronic cabinets from 500 to 1800 s after the ignition. The overall probability of getting inside the smoke layer drops from 0.8 to 0.2, when the observation height is reduced from 2.0 to 1.0 m.

The sensitivity of the failure time to the input variables is shown in Fig. 11. The height of the virtual fire source has the strongest effect on the failure time. This is very unfortunate, because in this particular application it is a numerical parameter. Other important variables are the door opening indicator, RHR growth time and the ventilation flow rate. The reliable locking of the cabinet doors is the most important physical variable that can be directly affected by engineering decisions.

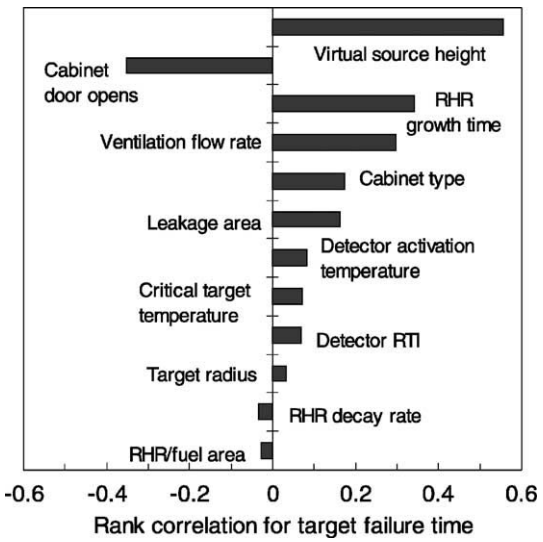


Fig. 11. The sensitivity of the target failure time to the input variables in the electronics room scenario.

## 5. Summary

Probabilistic Fire Simulator is a tool for Monte Carlo simulations of fire scenarios. The tool is implemented as a worksheet computing tool, using commercial @RISK package for Monte Carlo part. The fire is modelled using two-zone model CFAST. The Monte Carlo simulations can provide the distributions of the output variables and their sensitivities to the input variables. Typical outputs are for example the times of component failure, fire detection and flashover. The tool can also be used as a worksheet interface to CFAST. Extension to the other fire models is possible.

The presented example cases demonstrate the use of the tool. Best available information on the input distributions was used in the cable tunnel scenario, which can therefore be considered as a realistic representation of the problem. The results of the tunnel scenario show that the heat detector gives an alarm before the loss of the redundant cables, with a very high probability. However, the detector reliability was not considered. According to the sensitivity measures, the most important parameters for the safety of the redundant cables are (i) the growth rate of the fire, (ii) the screen providing a physical separation of the burning and target cable trays, (iii) the critical temperature of the cable material and (iv) the radius (mass) of the cable. Unfortunately, the failure time is also sensitive to the length of the virtual room of fire origin, which is a purely numerical parameter. This phenomenon should be studied more carefully in the future.

The second example considered an electronic cabinet fire inside an electronics room. The procedure of data collection, model development and actual simulation were described to demonstrate the use of the model in practical applications. The data collection and analysis was found to be the most time consuming part of the process. The various ways to enhance this kind of analysis are therefore needed. The simulation results showed that during a fire of a single cabinet,

the thermal environment inside the room might cause a failure of an electronic component, with a probability of 0.8. The inconsistency with the earlier studies can be explained with the longer simulation time and the variation of the RHR curve. Due to the strong effect of opening the cabinet door on the RHR curve, a reliable locking of the cabinet doors is the most important physical variable that can be directly affected by engineering decisions.

## Acknowledgements

The contribution of Dr. Timo Korhonen from VTT during the data collection is greatly appreciated. This study has been financed by the Finnish Centre for Radiation and Nuclear Safety, the Ministry of Trade and Industry, IVO Power Engineering Ltd. (now Fortum) and TeollisuudenVoima Oy.

## References

Eerikäinen, L., Huhtanen, R., 1991. Ydinvoimalaitoksen huonetilapalo, Loviisa 1:n valvomorakennuksen huonetilan palon numeerinen tarkastelu (Room fire in a Nuclear Power Plant, Numerical Study of the Room Fire in a Control Building of Loviisa 1 Power Plant). Finnish Centre for Radiation and Nuclear Safety, Helsinki. Report STUK-YTO-TR 30, 59 pp. + App. 26 pp.

Hofer, E., 1999. Sensitivity analysis in the context of uncertainty analysis for computationally intensive models. Comp. Phys. Commun. 117, 21–34.

Heskestad, G., Delichatsios, M.A., 1977. Environments of Fire Detectors. Phase 1. Effect of Fire Size, Ceiling Height and Materials. Vol. 2. Analysis. NBS GCR 77-95, National Bureau of Standards. Gaithersburg, MD, 129 pp.

Keski-Rahkonen, O., Hostikka, S., 1999. Theory versus experiment—did you forget design of experiment and data reduction? Structural Mechanics in Reactor Technology 15, Post Conference Seminar No. 6, Fire Safety in Nuclear Power Plants and Installations. Munich-Garching, Germany, September 6–7, 21 pp.

Keski-Rahkonen, O., Mangs, J., 2003. Quantitative determination of source terms from fires in electronic cabinets: maximum rate of heat release, minimum rate of heat release needed for flashover, and effluent yields from incomplete combustion. Fire Safety J., submitted for publication

Mangs, J., Keski-Rahkonen, O., 1994. Full scale fire experiments on electronic cabinets. Espoo, Technical Research Centre of Finland. VTT Publications 186, 50 pp. + App. 37 pp.

Mangs, J., Keski-Rahkonen, O., 1996. Full scale fire experiments on electronic cabinets II. Espoo, Technical Research Centre of Finland. VTT Publications 269, 48 pp. + App. 6 pp.

Mangs, J., Keski-Rahkonen, O., 1997. Full-scale fire experiments on vertical and horizontal cable trays. Technical Research Centre of Finland, Espoo. VTT Publications 324, 58 pp. + App. 44 pp.

McKay, M.D., Beckman, R.J., Conover, W.J., 1979. A comparison of three methods for selecting values of input variables in the analysis of output from a computer code. Technometrics 21 (2), 239–245.

NFPA, 1985. NFPA 204M, Guide for Smoke and Heat Venting, National Fire Protection Association, Quincy, MA.

Peacock, R.D., Forney, G.P., Reneke, P., Portier, R., Jones, W.W., 1993. CFAST, the Consolidated Model of Fire Growth and Smoke Transport. Gaithersburg, National Institute of Standards and Technology, NIST Technical Note 1299. 118 pp. + App. 116 pp.

Pebesma, E.J., Heuvelink, G.B.M., 1999. Latin hypercube sampling of multigaussian random fields. Technometrics 41 (4), 303–312.

Spiegel, M.R., 1980. Theory and Problems of Probability and Statistics, SI ed. McGraw-Hill, New York, 372 pp.

Stein, M.L., 1987. Large sample properties of simulations using latin hypercube sampling. Technometrics 29 (2), 143–151.

Vose, D., 1996. Quantitative risk analysis: a guide to Monte Carlo simulation modelling. Wiley, Chichester, England, 328 pp.

PAPER II

# Two-model Monte Carlo simulation of fire scenarios

In: Gottuk, D. & Lattimer, B. (Eds.). Proceedings of the Eighth International Symposium on Fire Safety Science. Beijing, China, 18–23 Sept. 2005. International Association for Fire Safety Science, 2005. Pp. 1241–1253.

# Two-model Monte Carlo Simulation of Fire Scenarios

SIMO HOSTIKKA, TIMO KORHONEN, and OLAVI KESKI-RAHKONEN
VTT Technical Research Centre of Finland
P.O. Box 1803
FI-02044 VTT, Finland

**ABSTRACT**

A risk analysis tool called Probabilistic Fire Simulator (PFS) is developed for the computation of the distributions of fire model output variables and the sensitivities of the output variables to the inputs. PFS performs a Monte Carlo simulation using different fire models, including CFAST two-zone model and FDS fluid dynamics model. In this work, a new technique is developed for the use of two different fire models in the same Monte Carlo simulation. The two-model Monte Carlo technique provides a computationally effective means to improve the accuracy of the fast but inaccurate models, using the results of the more accurate but computationally more demanding models. The technique is tested in three scenarios: approximation of an analytical function, calculation of a ceiling jet temperature and a simulation of a simple room fire.

**KEYWORDS:** fire modelling, Monte Carlo simulation, risk assessment

## INTRODUCTION

The numerical simulation of fires is widely used in the fire safety design and the risk analysis of large targets like shopping centres and industrial facilities. The uncertainty or the distribution of the predictions is of major interest in both applications. Presuming the model is principally valid for the given problem; the uncertainty of the prediction depends on, how the uncertainties of the input values are transferred through the system described by the model. In practically all applications, some uncertainty is related to the input values of the simulation. This uncertainty may be caused by the lack on information on the actual conditions, or by the fact that the simulation should actually represent a variety of different scenarios. Traditionally, the uncertainty has been taken into account by manually varying the input values. If more complete information of the output distribution is needed, Monte Carlo techniques should be used. This applies specially to fire problems, where many of the input distributions are skewed, of the class of lognormal distributions. In Monte Carlo, a large number of samples is randomly chosen from the input space and mapped through the system into the target distribution. Although Monte Carlo as a technique is almost sixty years old [1], its use in fire simulations has been prohibitively expensive. With modern computers, the situation has changed, and the tools described here have already been applied to engineering problems.

The numerical simulation of the complicated physical processes is always trading between the desired accuracy of the results and the computational time required. Quite often, the same problem can be tackled by many different models with different physical and numerical simplifications. A good example of this is the fire simulation, where zone models provide a fast way to simulate the essential processes of the fire, being inevitably coarse in the physical resolution. As an alternative, computational fluid dynamics (CFD) models have higher physical resolution and can describe more complicated physical

FIRE SAFETY SCIENCE–PROCEEDINGS OF THE EIGHTH INTERNATIONAL SYMPOSIUM, pp. 1241-1252

processes. On the other hand, the time needed for the computation may be longer with several orders of magnitude. A technique is therefore needed, which can combine the results of the different models in a computationally effective way. A new technique, based on an intuitive approach, is proposed here. The technique allows the use of two different models in one Monte Carlo simulation, and is therefore called two-model Monte Carlo (TMMC). The technique is based on the assumption that the ratio of the results given by two models has smooth variations when moving from point to point of the random space. Therefore, if one of the models is presumably more accurate than the other, the ratio calculated at some point of the random space can be used to scale the result of the less accurate model within the neighbourhood of the point. The method is first presented in one dimensional problem, and extended later to general case.

In the previous research projects concerning the fire safety of Finnish nuclear power plants, a Monte Carlo tool called Probabilistic Fire Simulator (PFS) was developed [2]. The tool has been applied to fires in a cable tunnel and an electronics room. The tool allows the simulation of fire scenarios using various fire models, including two-zone model CFAST [3] and Fire Dynamics Simulator (FDS) [4]. The main outcomes of the tool are the distributions of the selected result variables, for example component failure time, and the sensitivities of the output variables to the input variables, in terms of the rank order correlations. The use of the rank order correlations allows the user to simultaneously identify both the modelling parameters and the actual physical properties that have the most influence on the results. The PFS tool has been implemented as a Microsoft Excel workbook with additional function libraries for the generation of random numbers and input and output of the external fire models. In the current work, the TMMC method is tested in three scenarios: approximation of an analytical test function, prediction of the ceiling jet temperature and a simple one room environment, where the CFAST results are scaled with the FDS results, and then compared against benchmark result, obtained by performing a full Monte Carlo with FDS. The validity of the used models is not discussed here. We do not compare our results with experiments either, because the results from some 1000 random experiments are not available for any real fire scenario.

## MONTE CARLO SIMULATION

### General

During the probabilistic safety assessment, one typically needs to estimate the probability that a certain component or system is damaged during a fire. This probability is a function of all possible factors affecting the development of the fire and the systems reaction to it. The occurrence of the target event is indicated by a limit state function, $g(t,\mathbf{x})$, which depends on time $t$ and a vector of random variables $\mathbf{x}$. As an example of the target event, we consider the damage of a component. The limit state condition is now defined using the function $g(t,\mathbf{x})$:

$$\begin{aligned} &g(t,\mathbf{x}) \le 0, \text{ if the component is damaged at time } t \\ &g(t,\mathbf{x}) > 0, \text{ if the component is not damaged at time } t \end{aligned} \quad (1)$$

Other possible target events are, for example, heat detector activation and smoke filling. The development of a fire and the response of the components under consideration are assumed to be fully deterministic processes where the same initial and boundary conditions always lead to the same final state. With this assumption, the probability of an event at time $t$ can now be calculated by the integral

$$P(t) = \underset{\{\mathbf{x}|g(t,\mathbf{x})\leq 0\}}{\int\int\cdots\int} \phi_x(\mathbf{x})dx_i \tag{2}$$

where $\phi_x$ is the joint density function of the random variables. In this work, the probability $P(t)$ is calculated using Monte Carlo simulation where input variables are sampled randomly from the given distributions. Latin Hypercube sampling [5] is used to generate samples from all ranges of the possible values, thus giving insight into the tails of the probability distributions.

The sensitivity of the output $y$ to the different input variables $x$ is studied by calculating the Spearman's rank order correlation coefficients (RCC). A value's "rank" is determined by its position within the min-max range of possible values for the variable. RCC is then calculated as

$$\mathrm{RCC} = 1 - \frac{6\sum d^2}{m(m^2-1)} \tag{3}$$

where $d$ is the difference between ranks of the corresponding $x$ and $y$, and $m$ is the number of data pairs. RCC is independent of the distribution of the initial variable. The significance of the RCC values is studied with the methods of statistical testing. In small data sets, the actual values of RCC should be interpreted with caution due to the possible spurious correlations inside the input data [6].

**Two-model Monte Carlo (TMMC)**

We assume that we have two numerical models A and B, which can calculate physical quantity $a(x,t)$ depending on a parameter $x$ and the time $t$. In our analysis, $x$ is considered to be a random variable from a random space $\Omega$. The model B is more accurate than the model A, but the execution time of model B is longer than model A. The models are used to get two estimates of the time series: $\tilde{a}^A(x,t)$ and $\tilde{a}^B(x,t)$. The developed two-model Monte Carlo (TMMC) technique is based on the assumption that the results of the model A, at any point $x$ of the random space, can be corrected by multiplying them with scaling function, which is the ratio of model B time series to model A time series at some point $x_s$ in the vicinity of the current point $x$. The points $x_s$ are called scaling points.

In the beginning of the simulation, the random space is divided into distinct regions. Scaling function is then calculated for each region

$$\Phi(\mathbf{x}_s,t) = \frac{\tilde{a}^B(\mathbf{x}_s,t)}{\tilde{a}^A(\mathbf{x}_s,t)} \tag{4}$$

where $\mathbf{x}_s$ is the mid-point of the scaling region $\Omega_s$. During the Monte Carlo, the result of the model A is multiplied by the scaling function corresponding to the closest scaling point, to get the corrected times series $\tilde{a}^{AB}(\mathbf{x},t)$

$$\tilde{a}^{AB}(\mathbf{x},t) = \Phi(\mathbf{x}_s,t)\cdot\tilde{a}^{A}(\mathbf{x},t), \quad \mathbf{x}\in\Omega_s \tag{5}$$

For a general function $a(x,t)$, it is not possible to tell how fast the function $\tilde{a}^{AB}(\mathbf{x},t)$ converges towards $\tilde{a}^{B}(\mathbf{x},t)$, when the number of scaling points is increased. However, it is clear that $\tilde{a}^{AB}(\mathbf{x},t)=\tilde{a}^{B}(\mathbf{x},t)$, when the number of scaling points goes to infinity. In this work, the performance of TMMC is studied in terms of practical examples.

The result of the Monte Carlo simulation is usually not the time series itself, but some scalar property derived from the time series. A typical result is the time to reach some critical value. A simplified version of the TMMC technique can be obtained, if the scaling is done for scalar numbers directly. Although the scaling would be easier to implement for the scalars than for the whole time series, the simplification has some bad properties, which are demonstrated below.

## RESULTS AND DISCUSSION

### Approximation of Analytical Function

The two models approximate function

$$a(x,t) = \min\left[e^{xt}-1, 0.8\cdot\left(e^{x}-1\right)\right], \quad t\in[0,1] \tag{6}$$

The min-function was used to simulate a plateau of the time series reaching a steady state. In the model A, the analytical function was approximated by a two term Taylor series expansion. Model B output was $\tilde{a}^{B}(x,t)=a(x,t)$. The random variable $x$ was distributed uniformly between 1 and 2. The actual outcome of the simulation, denoted by $c(x)$, was the time when $a(x,t) = a_m = 2$ for the first time.

Figure 1 shows 100 realisations of the scalar result $c(x)$ as a function of random variable $x$. The time series scaling was used in the left side and scalar scaling on the right. At all values of $x$, model A gave higher values of $c(x)$ than model B. However, the monitoring value $a_m$ was not reached at all values of $x$, corresponding to a situation where the overall probability of the event is smaller than one. As a result, the scalar scaling could not be performed adequately, since there was no data to scale in the region $1.25 < x < 1.45$. The cumulative distributions of the 1000 realisations of $c(x)$ are shown in Fig. 2. In the regions, where the model A results do exist ($x > 1.45$), the scalar scaling worked very well, but the tail of the distribution was not corrected at all. As the number of scaling points was increased, the errors of the time series scaling converged towards zero but for the scalar scaling, the errors did not converge at all. The result shows that the time series scaling should be used if there is a possibility that the event under consideration does not take place during the simulation period.

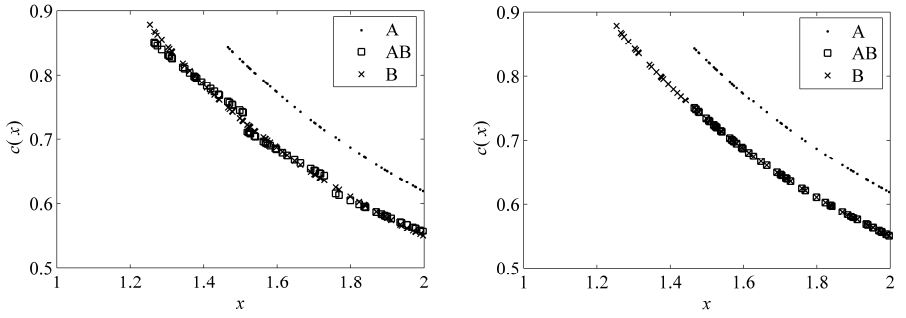


Fig. 1. Realisations of function $c(x)$ in the first example. Time series scaling on the left and scalar scaling on the right. AB is the TMMC result.

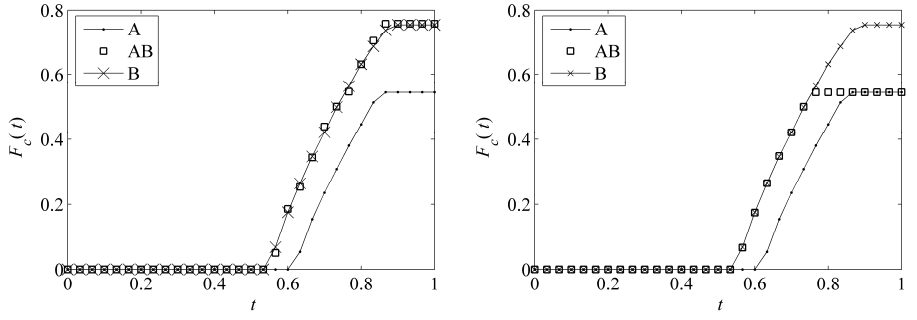


Fig. 2. Model predictions for the cumulative distribution of $c(x)$ in the first example. Time series scaling on the left and scalar scaling on the right. AB is the TMMC result.

**Ceiling Jet Temperature**

Two models were used to predict the ceiling jet temperature under the ceiling of a 10 m × 10 m × 5 m (height) room with a fire in the middle of the floor. The room had one, 2.0 m × 2.0 m door to ambient. The fire heat release rate was of $t^2$-type with a random, uniformly distributed growth time $t_g$. Two scalar results were studied. The scalar result $b(t_g)$ was the ceiling jet temperature at time = 30 s. The scalar result $c(t_g)$ was the time to reach a critical temperature of 100 °C in the ceiling jet.

Alpert's ceiling jet model [7] was used as Model A and two-zone model CFAST as Model B. We simply assumed that CFAST is more accurate than Alpert's model, whether this is true or not in reality. The random space was divided into three subdomains. 1000 samples were calculated using both models. The predicted cumulative distributions of $b(t_g)$ are shown in the left part of Fig. 3. At all values of $t_g$, CFAST predicted higher temperatures than Alpert's model. TMMC distribution was very close to the CFAST result, but had small discontinuities at the boundaries of the divisions. The right hand side of Fig. 3 shows the cumulative distributions of $c(t_g)$. As can be seen, TMMC scaling very accurately captured the shape of the CFAST distribution.

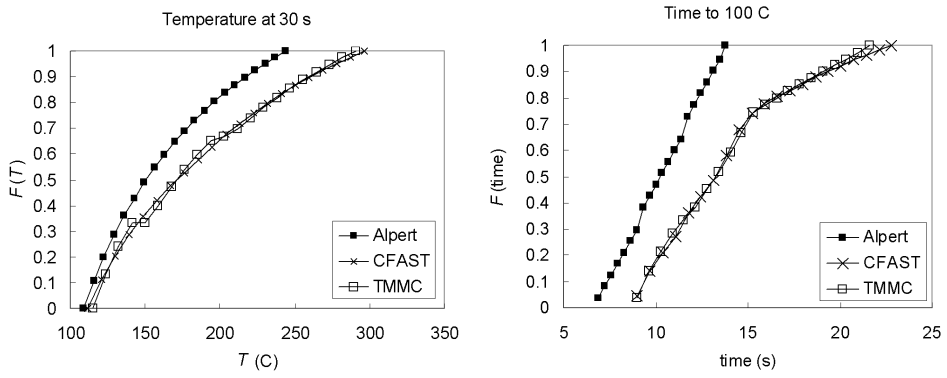


Fig. 3. Distributions of temperature at time = 30 s (left) and time to reach 100 °C (right).

In this example, TMMC was able to accurately reproduce the results as a full CFAST Monte Carlo, within a fraction of time required for the full CFAST Monte Carlo. Assuming that the execution times for of Alpert's model and CFAST are one and 10 CPU seconds, respectively, and that the scaling overhead time is very small, the TMMC simulation time would be 1030 seconds in total. For comparison, the full CFAST Monte Carlo would take 10,000 seconds (2.8 hours).

**Simple Room Fire**

The purpose of this example was to provide a more realistic test for the TMMC technique. CFAST and FDS models were used for the fire modelling. For the evaluation of the TMMC results, a full Monte Carlo using FDS model was needed. Therefore, the size of the room was chosen very small in order to keep the simulation times short. The room was 4.0 m deep, 3.0 m wide and 3.0 m high, having a 1.0 m wide and 2.1 m high door to ambient. All the room boundaries were concrete and there was a concrete beam under the ceiling, 1.5 m from the back wall. The height of the beam was a random variable, ranging from zero to 0.6 m. A schematic picture of the room is shown in Fig. 4.

The fire source was a rectangular burner at the floor level. The co-ordinates and surface area of the fire source were random variables. The maximum value of the HRR per unit area was fixed to 700 kW/m$^2$. In the beginning, the heat release rate increased proportional to $t^2$ reaching the final value at time $t_g$, which was a uniformly distributed random variable. A list of the random variables is given in Table 1. The target functions were the gas temperature and heat detector activation time under the ceiling, left from the concrete beam. For gas temperature, the time to reach 200 °C was monitored.

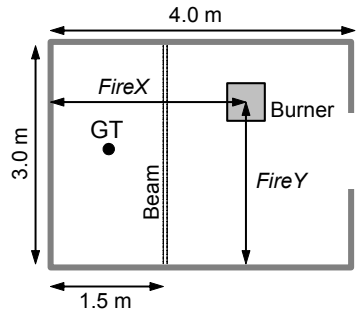


Fig. 4. The geometry of the room fire scenario. GT shows the location of the heat detector and the gas temperature measurement point 5 cm under the ceiling.

CFAST was used as the model A and FDS as the model B. The absolute accuracy of these codes is not discussed here. It was simply assumed, that the FDS results were more accurate than the CFAST results. In CFAST, two virtual rooms were used by splitting the room at the beam location. In FDS, a constant grid cell size of 0.10 m was used. Before the actual TMMC application, simulations using only CFAST and only FDS were carried out. With 1000 realisations with both models, the final distributions were well converged. The maximum difference between the cumulative distributions after 500 iterations and 1000 iterations was 0.015 (1.5 %). The difference was smallest in the tails of the distributions, being order of 0.001 (0.1 %).

Table 1. A list of random variables in the room fire example.

| **Variable** | **Units** | **Distribution** | **Min** | **Max** | **Mean** | **Std.dev** |
|---|---|---|---|---|---|---|
| BeamHeight $z_B$ | m | Uniform | 0.0 | 0.6 | | |
| GrowthTime $t_g$ | s | Uniform | 60.0 | 180.0 | | |
| Area | $m^2$ | Normal | 0.2 | 1.5 | 0.80 | 0.60 |
| FireX | m | Uniform | 0.0 | 4.0 | | |
| FireY | m | Uniform | 0.0 | 3.0 | | |

The effect of the number of TMMC scaling points was studied by using different ways to divide the random space. The number of scaling points varied from one to 32. A summary of the different versions is given in Table 2. The basis for the division was taken from the CFAST simulations, which predicted that the fire surface area, the HRR growth time, and FireX-position were the most important random variables. Due to the division to the virtual rooms, FireX variable was especially interesting as the results had a clear discontinuity at FireX = 1.5 m. Therefore, more divisions were used for FireX than for other variables in some of the cases.

Table 2. A summary of scaling divisions in different TMMC versions.

| Name | $N_{tot}$ | $N(z_B)$ | $N(t_g)$ | $N$(Area) | $N$(FireX) | $N$(FireY) |
|---|---|---|---|---|---|---|
| TMMC(1) | 1 | 1 | 1 | 1 | 1 | 1 |
| TMMC(3) | 3 | 1 | 1 | 1 | 3 | 1 |
| TMMC(6) | 6 | 1 | 2 | 1 | 3 | 1 |
| TMMC(27) | 27 | 1 | 3 | 3 | 3 | 1 |
| TMMC(32) | 32 | 1 | 4 | 4 | 2 | 1 |
| TMMC(32B) | 32 | 2 | 2 | 2 | 2 | 2 |

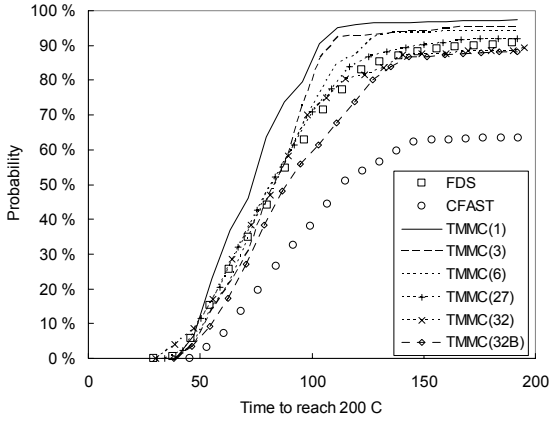


Fig. 5. Predicted probability distributions of time to reach 200 °C.

A comparison of predicted probability distributions for the time when the gas temperature reached 200 °C is shown in Fig. 5. The large difference in the distributions of CFAST and FDS codes made this a challenging problem for the TMMC scaling. The overall probability was 63.5 % according to CFAST, while the FDS results lead to a final probability of 90.7 %. Unfortunately, the simulation time was slightly too short for FDS distribution to reach a fully converged value. Therefore, an uncertainty of 1 % percentage unit is associated with the final probability given by FDS.

The division of the random space had a clear effect on the accuracy of the TMMC distribution. If the division was made based on the information of the relative importance of the random variables, the higher number of scaling points generally improved the accuracy. However, if the scaling points were chosen without any prior information of the importance, the results did not improve as much as one might have expected, as was shown in the case TMMC(32B). In addition, the smoothness of the transient data affected the quality of the results. This is demonstrated in Fig. 6 showing the errors in the final probability in two cases. In the upper curve, the FDS data was not smoothed before the calculation of the scaling function $\Phi(\mathbf{x}_s, t)$ and in the lower curve a 5-point running average was taken. The original FDS data was saved with 2.0 second intervals. In the case of 32 scaling points, the filtered FDS data, which mostly works better, gave higher error than the unfiltered. The reason for this is currently not known.

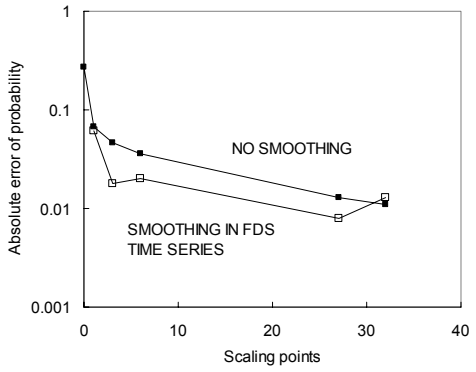


Fig. 6. The error of final probability as a function of number of scaling points.

The dependence of the TMMC accuracy on the final probability was studied by varying the critical gas temperature from 150 °C to 500 °C. Fig. 7 shows the predicted final probabilities as a function of the probability given by FDS. The lowest probabilities correspond to the highest values of the critical gas temperature. The correct result is at the diagonal. The TMMC probabilities corresponding to 6, 27 and 32 scaling points are very close to the diagonal but the uniform distribution of scaling points (case 32B) results in clearly lower probabilities. An important observation of the figure is that, while CFAST did not observe the highest temperatures at all, after the scaling these highest temperatures are found, leading to non-zero probabilities in the low left corner of the figure. The accuracy of the smallest probabilities is sensitive to the smoothing of the FDS data. Here, the FDS results were obtained from the "raw" data without any smoothing, but five point smoothing was used before the computation of the scaling functions.

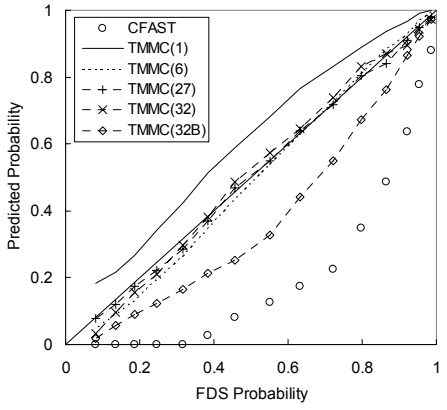


Fig. 7. The effect of the final probability on the TMMC accuracy.

TMMC scaling also improves the predicted sensitivity measures. Fig. 8 shows the predicted rank order correlation coefficients between the time to reach 200 °C temperature and the random variables. For most variables, all the three methods, CFAST, FDS and TMMC, gave very similar coefficients. However, for the HRR growth time,

CFAST gave much lower RCC than FDS, but the TMMC result was very close to FDS result. The case with 27 scaling points was used.

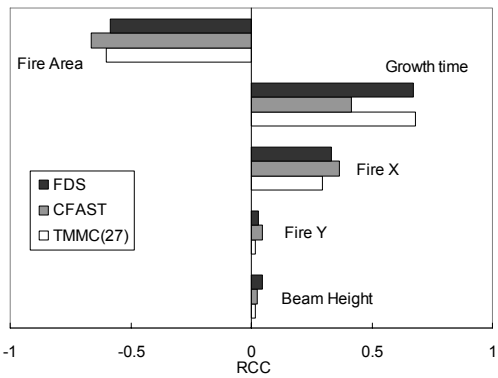


Fig. 8. Rank order correlation coefficients for the gas temperature reaching time.

For the prediction of the heat detector activation time, the TMMC method was not as successful as for the time to reach a certain gas temperature. The predicted probability distributions are shown in Fig. 9. As before, the increased number of scaling points improved the results, but all the TMMC curves fall on the original CFAST curve at high values of activation time. The reason for this turned out to be the fact that, in FDS the detector temperature was not updated after the detector activation. To be compatible with FDS, the CFAST results were also limited to the detection temperature after the detection, although CFAST actually did update the detector temperature. This limiting process forced all the scaling functions to unity in the end of the time period, which is clearly seen in Fig. 9. The conclusion is that for the TMMC method to work, the time series should not have unphysical limitations, which prevent the calculation of realistic scaling functions.

This example demonstrates that the models A and B must always represent the same physical problem, at least quantitatively. If there is no correlation between the outputs of the two models, it does not make sense to scale one with another. Unfortunately, there is no simple way to identify the cases, where this is not the case, without plotting a large number of results to the same figure, like in Fig. 1. This, in turn, would require a large number of simulation runs. A good understanding of the behaviour of the physical models is therefore required for the judgement of the applicability of TMMC technique to the problem under consideration. Additionally, a special attention should be paid to the choice of the model B, since there is an inherent assumption that it is always more accurate than model A.

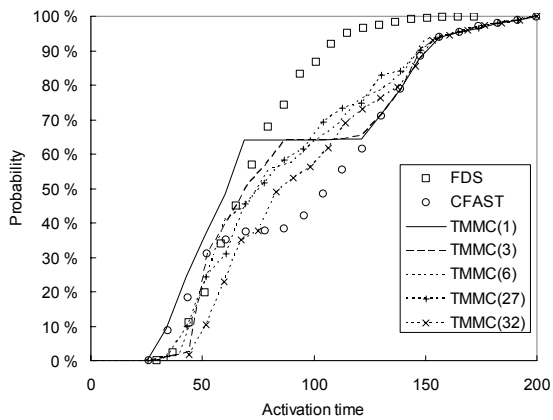


Fig. 9. Predicted probability distributions of the heat detector activation time.

## CONCLUSIONS

Probabilistic Fire Simulator is a tool for Monte Carlo simulations of fire scenarios. The tool is implemented as a worksheet computing tool, and can be used as user interface for various fire models. The Monte Carlo simulations can provide the distributions of the output variables and their sensitivities to the input variables. Typical outputs are for example the times of component failure, fire detection, and flashover.

A new technique was developed that can be used to improve the accuracy of the Monte Carlo simulation. Two-model Monte Carlo is a computationally affordable technique to utilize advanced simulation techniques like CFD in the probabilistic safety assessment of large systems. In practical applications, the results of the simple but defective simulation models can be corrected by scaling them with the results achieved from an order of few tens of simulations with the more advanced model. A good accuracy can be achieved if the existing information on the relative importance of the random variables is used to efficiently place the scaling points. If such information is not available, or is not reliable, the random space must be divided uniformly in all dimensions, and the number of required scaling points may become very high. A special care must be taken to ensure that the physical time series, that are used to calculate the scaling functions, have no artificial and unphysical limitations. Such limitations may prevent the convergence of the TMMC distributions towards the correct results.

The new model has already found applications in the computation of the fire induced damage probabilities in large and complicated compartments like the switchgear rooms of the nuclear power plants. In these applications, we have demonstrated that an alternative for the use of two different computer codes is the modelling of the same scenario with one code but two different discretizations. The role of the TMMC scaling can then be seen as an utilisation of the posteriori error information. In the projects currently going on, the TMMC simulations are performed using FDS at two different grids.

As the experimental results from some 1000 experiments are not available for any real fire scenario, the only possible means to validate the probabilistic simulation technique is

the use of the fire statistics or long series of small or medium scale laboratory experiments. The future work will include the collection of quantitative fire loss statistics and an attempt to reproduce the statistics using Monte Carlo simulation.

**ACKNOWLEDGEMENTS**

This study has been financed by the Finnish Centre for Radiation and Nuclear Safety, the Ministry of Trade and Industry, Fortum Engineering Ltd. and TeollisuudenVoima Oy.

**REFERENCES**

[1] Metropolis, N. and Ulam, S., "The Monte Carlo Method," *Journal of the American Statistical Association*, 44 (1949) 247, pp.335-341.

[2] Hostikka, S. and Keski-Rahkonen, O., "Probabilistic Simulation of Fire Scenarios," *Nuclear engineering and design*, 224 (2003) 3, pp. 301-311.

[3] Jones, W.W., Forney, G.P., Peacock, R.D., and Reneke, P.A. "Technical Reference for CFAST: An Engineering Tool for Estimating Fire and Smoke Transport," National Institute of Standards and Technology NIST TN 1431, Gaithersburg, MD, 2000, 190 p.

[4] McGrattan, K.B., Baum, H.R., Rehm, R.G., Hamins, A., Forney, G.P, Floyd, J.E, Hostikka, S., and Prasad, K., "Fire Dynamics Simulator (Version 3) – Technical Reference Guide," National Institute of Standards and Technology, Gaithersburg, MD, 2002, 46 p. NISTIR 6783, 2002 Ed.

[5] McKay, M.D., Beckman, R.J., and Conover, W.J., "A Comparison of Three Methods for Selecting Values of Input Variables in the Analysis of Output from a Computer Code," *Technometrics*, 21(2) (1979), pp. 239-245.

[6] Hofer, E., "Sensitivity Analysis in the Context of Uncertainty Analysis for Computationally Intensive Models," *Computer Physics Communications* 117 (1999), pp. 1-34.

[7] Drysdale, D. *An Introduction to Fire Dynamics*. Wiley-Interscience, Chichester, 1999. Second Edition, p. 140.

PAPER III

# CFD fire simulation using mixture fraction combustion and finite volume radiative heat transfer

In: Journal of Fire Protection Engineering 2003.
Vol. 13, No. 1, pp. 11–36.

# CFD Fire Simulation Using Mixture Fraction Combustion and Finite Volume Radiative Heat Transfer

J. E. FLOYD[1,*], K. B. MCGRATTAN[2], S. HOSTIKKA[3] AND H. R. BAUM[2]

[1]*Hughes Associates, Inc., 3610 Commerce Dr., Suite 817, Baltimore, MD 21227-1652, USA*

[2]*Building and Fire Research Laboratory, National Institute of Standards and Technology, 100 Bureau Drive Stop 8640, Gaithersburg, MD 20899-8640, USA*

[3]*VTT Building and Transport, Espoo, Finland*

**ABSTRACT:** A computational fluid dynamics (CFD) model of fire and smoke transport is described. Combustion is represented by means of a single conserved scalar known as the mixture fraction. Radiation transport is approximated in the gray gas limit. The algorithms have been incorporated in the Fire Dynamics Simulator (FDS), a computer program maintained by the National Institute of Standards and Technology. Sample calculations are presented demonstrating the performance of the new algorithms, especially as compared to earlier versions of the model.

**KEY WORDS:** mixture fraction, computational fluid dynamics, fire simulation, radiation heat transfer.

## INTRODUCTION

THE SIMULATION OF fires using computational fluid dynamics (CFD) is challenging due to the need to resolve length scales ranging from those characteristic of the combustion processes to those characteristic of the mass and energy transport throughout an entire building. The width of a diffusion flame is on the order of a millimeter; the eddies associated with the

*Author to whom correspondence should be addressed. E-mail: jfloyd@haifire.com



1042-3915/03/01 0011–26 $10.00/0 DOI: 10.1177/104239103031494

entrainment of air into a fire are of the order of centimeters; and the flow fields generated by a fire span an entire building. While it is possible to create a combustion model that tracks the significant species required to calculate the heat release rate, it is too expensive to construct a grid fine enough to resolve individual flame sheets except in cases where the domain is very small. For example, consider a small compartment 1 m on a side. If the combustion length scale is assumed to be 1 mm and the hydrodynamic scale 1 cm, this compartment would require one billion computational cells at the combustion length scale and one million cells at the hydrodynamic scale. Few computers exist that can do a calculation with a billion cells. Even if current desktop computers could handle the calculation, it would take 10,000 times as long to perform a billion node transient calculation as compared to a million node calculation. A method, therefore, is needed to model the combustion chemistry in a manner that can be used at the length scales of the resolvable flow field.

The Fire Dynamics Simulator (FDS) [1,2], developed at the National Institute of Standards and Technology (NIST), originally used Lagrangian particles to represent burning fuel gases, hereafter referred to as the ''particle method''. Each particle was assigned a user-prescribed energy content and release rate. While this method was computationally simple and inexpensive, it lacked the necessary physics to describe underventilated fire scenarios. The severest restriction of the model was that each particle required a user-prescribed fuel burn-out time, which has been characterized for well-ventilated fires but not for under-ventilated fires. A second restriction was that the fuel transport was purely convective, neglecting the small-scale diffusive processes near the flame. A third restriction was that the model did not account for the effect of oxygen depletion on the burning rate, a very important consideration for underventilated fire scenarios.

To better model realistic fire scenarios, a better combustion model was needed; but one that was consistent with the relatively large length and time scales afforded by typical computing platforms. The fast chemistry assumption inherent in the particle method could be maintained, but better transport phenomena were needed. A natural candidate for the job was the mixture fraction approach. The transport equations for the major gas species can be combined into a single equation for a conserved scalar known as the mixture fraction [3]. This quantity is defined as the fraction of the fluid mass that originates as fuel and, from it, mass fractions for all other species can be derived based on semiempirical state relationships. Typically, a mixture fraction-based combustion model assumes that the reaction is taking place on an infinitely thin flame sheet where both the fuel and oxygen concentrations go to zero. However, since we wish to avoid the expense of

resolving the flow field at length scales fine enough to capture the actual flame sheet location, the traditional mixture fraction-based model is modified to allow for a reaction zone of finite thickness. These modifications preserve the original chemical equation for the combustion process as well as provide a framework for the inclusion of minor combustion species.

In addition to an improved treatment of the combustion processes, it was necessary to improve the radiation transport algorithm to handle phenomena such as flashover. Solution of the radiation transport equation requires determining emission, transport, and absorption properties over a wide range of infrared frequencies. Plus, the instantaneous nature of radiation transport requires that every computational cell have knowledge of the conditions in every other cell. As with the combustion model, it is possible to create a radiation transport model that tracks the emission, transport, and absorption of many frequencies of infrared light. However, such an approach is very time consuming and memory intensive. One typical simplification is to assume a gray gas and solve for only one frequency. This method still requires some form of coupling of every grid cell to every other grid cell to properly solve for attenuation. In the original version of FDS, a simple Monte-Carlo ray tracing method was used. This model was easy to implement and worked well for small fires. However, as with the particle method, this radiation model did not function well for underventilated scenarios. Thus, a finite volume radiation model [4] was added to FDS.

In the present paper, the mixture fraction-based combustion model and the finite volume radiation heat transfer model are described. Comparisons between the new and old algorithms will be performed for a variety of test cases, demonstrating the improvements added by the new routines. These test cases include a simple fire plume, a small compartment fire, and a full-scale multi-compartment fire.

## IMPROVEMENTS TO FDS

### Mixture Fraction Combustion Model

The Fire Dynamics Simulator solves the ''low Mach number'' form of the Navier–Stokes equations [5] for a multiple species fluid. These equations are obtained by filtering out pressure waves from the Navier–Stokes equations, resulting in a set of conservation equations valid for low-speed, buoyancy driven flow. These equations allow for large variations in density but not pressure. These equations are discretized in space using second order central differences and in time using an explicit, second order, predictor–corrector scheme.

For very small-scale fires, such as a small diffusion flame burner, it is feasible to create a simulation capable of being run on a modestly powered computing platform that is detailed enough in both length scales and time scales to directly capture the combustion processes. However, for the large-scale problems of interest to the fire safety community, this is not feasible. A typical compartment fire involves length scales of meters and time scales of minutes. To create a simulation of a typical compartment fire at the resolution of a Bunsen burner could be done with an extremely powerful supercomputer; however, this would be of little practical use. Instead we must approximate the combustion process in both space and time.

One simple method of coupling the combustion process with the flow field is to track three species: fuel, oxygen, and nitrogen. Since the time scales of the convective processes are much longer than the time scales of the combustion processes, infinite reaction rate chemistry can be assumed. Note, however, that this method requires solving for three species and that more species would be required to handle combustion products.

The observation can be made, however, that to track both fuel and oxygen when assuming an infinite reaction rate is redundant if the local temperature is not considered. Since neither fuel nor oxygen can coexist under those assumptions, if fuel is present there can be no oxygen and vice-versa. Thus, the above method could be simplified further by replacing all the species with a single conserved scalar that represents the amount of fuel or oxygen present in any given location.

One scalar parameter that can be used to represent the local concentration of fuel or oxygen is the mixture fraction. If $Y_{O_2}^{\infty}$ is defined as the ambient oxygen mass fraction and $Y_F^I$ the fuel mass fraction in the fuel stream, then the mixture fraction, $Z$, is defined as [6]:

$$Z = \frac{sY_F - (Y_{O_2} - Y_{O_2}^{\infty})}{sY_F^I + Y_{O_2}^{\infty}}; \qquad s = \frac{\nu_{O_2} w_{O_2}}{\nu_F w_F} \tag{1}$$

What the mixture fraction represents in Equation (1) can be seen in Equations (2) and (3). Equation (2) below gives the chemical reaction for the combustion of a generic hydrocarbon fuel.

$$C_x H_y + \left(x + \frac{y}{4}\right)(O_2 + 3.76N_2) \rightarrow xCO_2 + \frac{y}{2}H_2O + \left(x + \frac{y}{4}\right)3.76N_2 \tag{2}$$

In a simulation of the combustion of such a fuel, at any point in the computational domain, the ideal stoichiometric conditions shown in Equation (2) will not be present as either fuel or oxygen will be in excess. The reaction for this is shown in Equation (3) below where $\zeta$ is a multiplier

of the oxygen term to account for the relative amounts of fuel and oxygen and it varies from 0 to $\infty$.

$$C_xH_y + \xi\left(x+\frac{y}{4}\right)(O_2 + 3.76N_2) \rightarrow \text{Max}[0, 1-\xi]C_xH_y + \text{Min}[1,\xi]xCO_2 + \text{Min}[1,\xi]\frac{y}{2}H_2O + \text{Max}[0,\xi-1]\left(x+\frac{y}{4}\right)O_2 + \xi\left(x+\frac{y}{4}\right)3.76N_2 \quad (3)$$

The two terms on the left hand side will yield the mixture fraction if the definition in Equation (1) is applied. However, since the mixture fraction assumes infinitely fast chemistry, what is present in the computational domain is the right hand side of Equation (3). Thus the mixture fraction at all points in the computational domain, in essence represents a 'post-combustion' value, i.e., only products are present at any location in the computational domain.

Using Equation (1), the mass fractions of the products in Equation (3) can be plotted as a function of $Z$. As $\zeta$ varies from $\infty$ to 0, $Z$ will vary from 0 to 1, and a series of state relationships for the species can be expressed in terms of the mixture fraction. In this manner, the mixture fraction can be used to represent many species in the simulation. It is important to note that minor species such as carbon monoxide or soot (smoke) can be included in the mixture fraction state relationships if their production can be defined in terms of the mixture fraction. For example, if the molar production of soot, which can be assumed to be carbon, and CO is assumed to be proportional to the molar production of $CO_2$ where $\chi_S$ and $\chi_{CO}$ are the respective molar production ratios, then Equation (4) results; this is the manner in which FDS v2 accounts for CO and soot formation. If the fuel is assumed to be propane and $\chi_S$ and $\chi_{CO}$ are defined respectively as 0.15 and 0.1, chosen purely for purposes of illustration, the corresponding state relations are shown in Figure 1. However, FDS is not truly predicting CO or soot formation as in fact CO and soot production is a much more complex phenomena that can be modeled by the mixture fraction as implemented.

$$C_xH_y + \xi\left(\frac{x(1+\frac{1}{2}\chi_{CO})}{1+\chi_S+\chi_{CO}} + \frac{y}{4}\right)(O_2 + 3.76N_2) \rightarrow \text{Max}[0,1-\xi]C_xH_y + \text{Min}[1,\xi]\left(\frac{x}{1+\chi_S+\chi_{CO}}\right)CO_2 + \text{Min}[1,\xi]\frac{y}{2}H_2O + \text{Min}[1,\xi]\left(\frac{x\chi_{CO}}{1+\chi_S+\chi_{CO}}\right)CO + \text{Min}[1,\xi]\left(\frac{x\chi_S}{1+\chi_S+\chi_{CO}}\right)C + \text{Max}[0,\xi-1]\left(x+\frac{y}{4}\right)O_2 + \xi\left(x+\frac{y}{4}\right)3.76N_2 \quad (4)$$

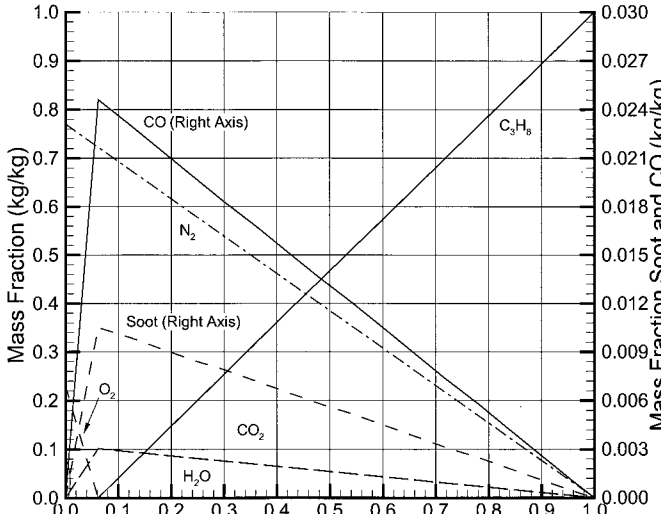


***Figure 1.*** *Mixture fraction state relationships for propane assuming constant production of soot and CO at 0.15 mol Soot/mol $CO_2$ and 0.10 mol CO/mol $CO_2$.*

With this representation, the flame sheet is defined to exist at the point where both fuel and oxygen disappear as products. The mixture fraction corresponding to this point is designated $Z_F$ and this point is equivalent to the reaction shown in Equation (2). This region is a two-dimensional surface and, for larger-scale simulations, is difficult to resolve. To implement the mixture fraction, an expression for the local heat release rate as a function of the mixture fraction must be developed.

This is done rather simply. Combustion of fuel consumes oxygen. Since the mixture fraction yields information about the local oxygen concentration, we need only determine an expression for the oxygen consumption rate based on the mixture fraction. Then, using the heat of combustion yields the local heat release rate. Consider the following two transport equations for the conserved scalar $Z$ and for oxygen:

$$\rho \frac{DZ}{Dt} = \nabla \times \rho D \nabla Z \tag{5}$$

$$\rho \frac{DO_2}{Dt} = \nabla \times \rho D \nabla Y_{O_2} + \dot{m}'''_{O_2} \tag{6}$$

The derivatives for oxygen in Equation (6) are expressed in terms of mixture fraction using the chain rule, diffusion is assumed constant with

respect to species, and Equation (5) is multiplied by $dY_{O_2}/dZ$.

$$\rho \frac{dY_{O_2}}{dZ}\frac{DZ}{Dt} = \frac{dY_{O_2}}{dZ}\nabla \times \rho D \nabla Z \tag{7}$$

$$\rho \frac{dY_{O_2}}{dZ}\frac{DZ}{Dt} = \nabla \times \rho D \frac{dY_{O_2}}{dZ}\nabla Z + \dot{m}'''_{O_2} \tag{8}$$

Equation (7) is subtracted from Equation (8).

$$-\dot{m}'''_{O_2} = \nabla \times \rho D \frac{dY_{O_2}}{dZ}\nabla Z - \frac{dY_{O_2}}{dZ}\nabla \times \rho D \nabla Z \tag{9}$$

At first glance, Equation (9) appears to be rather complex. However, its meaning can be understood simply. It can be seen in Figure 1 that $dY_{O2}/dZ$ at any point in the computational domain is either zero or a constant depending on which side of $Z_F$ one is located. If the computational domain is divided into the two regions of $Z \leq Z_F$ and $Z > Z_F$, then Equation (9) can be integrated over these two regions while applying the divergence theorem. Since the $dY_{O2}/dZ$ term will be zero in the region $Z > Z_F$, this region can be ignored. The end result is the mass loss rate of oxygen as a function of the mixture fraction diffusion across the flame surface as shown below:

$$\dot{m}''_{O_2} = -\frac{dY_{O_2}}{dZ}\rho D \nabla Z \times \hat{n}|_{Z=Z_F} \tag{10}$$

Since oxygen is a function of only the mixture fraction, this is equivalent to saying that the global heat release rate is a function of the oxygen gradient across the flame sheet. In fact, due to the diffusion constant in the expression and the assumption of infinite reaction rates, Equation (10) states that the heat release rate is due solely to the diffusion of oxygen across the flame, which is given by the hydrodynamic solver. Since we do not know a priori the location and orientation of the flame sheet, only Equation (9) is useful for a numerical scheme. However, to save computational time, Equation (9) needs only be evaluated at the cell interfaces where one cell is greater than $Z_F$ and one cell is less than $Z_F$.

**Finite Volume Radiation Model**

FDS v1 computes radiative fluxes with a Monte-Carlo style ray-tracing from the burning particles to the walls. The model neglects gas-to-gas interactions and wall-to-wall interactions, and, thus, performs poorly for compartment scenarios with very hot gas layers or surfaces as would occur

in a compartment approaching flashover. The original ray-tracing radiation model was changed to a Finite Volume Method [4]. This method is derived from the radiative transport equation (RTE) for a nonscattering gray gas [7].

$$\hat{s} \times \nabla I(\hat{x}, \hat{s}) = \kappa(\hat{x})[I_b(\hat{x}, \hat{s}) - I(\hat{x}, \hat{s})] \tag{11}$$

$I(\hat{x},\hat{s})$ is the radiation intensity, $I_b(\hat{x},\hat{s})$ is the blackbody radiation intensity, $\kappa(\hat{x})$ is the absorption coefficient, and $\hat{s}$ is the unit normal direction vector. Implementing this equation in a large eddy simulation requires determining how to specify the absorption coefficient, $\kappa$, and how to create the source term, $I_b(\hat{x},\hat{s})$. For the length scales of interest to the fire research community, the specification of both terms in a computationally simple manner is nontrivial.

The source term is typically given by the Stefan–Boltzman law [7]:

$$I_b(\hat{x}, \hat{s}) = \frac{\sigma T(\hat{x})^4}{\pi} \tag{12}$$

Where $T(\hat{x})$ is the local temperature and $\sigma$ is the Stefan–Boltzman constant. Since the cell temperature represents the average temperature over the entire volume of the cell, in the case of a computational cell without combustion, the cell temperature is a reliable indicator of the radiative emission. However, in the case of a cell with combustion occurring, where the average temperature is not necessarily the flame temperature, this may not hold true. For most computations, the volume of a grid cell is much larger than the volume within the cell where combustion would actually be taking place. With the fourth power dependence on temperature, this will result in greatly under predicting the source term in cells with combustion. Thus, the source term will need to be corrected in these cells. One manner of correcting the source term is to simply add a fraction of the cell's heat release, for example a typical value of 35% [8] for a coarse grid, to the source term. FDS v2 uses a simple rule to adjust the source term. If the calculated emission from a combusting cell is less than a user specified fraction of the local heat release rate, with a default of 35%, that calculated term is replaced with the user specified fraction.

$\kappa(\hat{x})$ is a function of the local concentrations of absorbing species ($CO_2$, CO, $H_2O$, Soot, and fuel), the local temperature, and a pathlength over which the radiation travels [9]. The species concentrations can be obtained from the mixture fraction and the temperature can be obtained from the hydrodynamics solver. There is no simple way, however, to evaluate the pathlength. In reality, this would involve determining, for each grid cell, the

potential travel distance through the computational domain for all possible directions of travel, a computationally expensive process. Instead a pathlength is assumed at the onset of a simulation based on the overall size of the computational domain. Then an array of values of $\kappa$ is created as a function of temperature and mixture fraction by using RADCAL with the assumed pathlength [10]. $\kappa(\hat{x})$ is then found by table lookup.

To solve the RTE, the finite volume method first divides all possible direction vectors, $\hat{s}$, into a number of spherical angles, typically around 100, which results in one RTE for each angle grouping. The RTE is then integrated over each cell, with cell indices of $i$, $j$, and $k$, resulting in the following equation:

$$\sum_{m=1}^{6} A_m I_m^L \int_{\Omega^L} \hat{s} \times \hat{n}_m \, d\Omega = \kappa_{ijk} \left( I_{b,ijk} - I_{ijk}^L \right) V_{ijk} \, d\Omega^L \tag{13}$$

This RTE is solved for each grid cell and for each angle. For each angle, $L$, the upwind direction is determined and the appropriate boundary condition used to determine the upwind flux. For example, if the current angle were a vector pointing downward to the right and to the back of the domain, the upwind direction would be the upper, front, left corner. The flux into the domain from the three cells bounding that corner would be used for the boundary condition. The downwind fluxes are then determined by marching through the domain in the downwind direction. The net radiant intensity is found by summing over all angle groupings. To save computational time, only a subset of the angle groupings is updated at each time step, typically about every fifth angle.

## COMPARISONS OF FDS V1 TO FDS V2

The new version of FDS with the mixture fraction combustion and finite volume radiation model has been tested with a variety of fire scenarios. A few are shown here and compared with version 1 with its Lagrangian particle model and ray-tracing model.

### Pool Fire

Simulations of a 0.2 m diameter pool fire were performed for three different fire sizes: 15, 30, and 60 kW. The cell size over the burner was 0.024 m, the burner was defined in FDS as a square, and the default FDS fuel chemistry for propane was used. This grid size was chosen to meet the requirements of the flow solver, which requires that the grid be of the order

of 10% of the plume length scale [5]. The 60 kW plume was also simulated using a denser grid with a grid size of 0.013 m. Once a steady-state was reached, time averages were taken of the centerline temperatures and vertical velocities. These were compared with temperatures and velocities calculated using McCaffrey's correlation [8].

Figure 2 illustrates the major advantage that arises from the use of the mixture fraction as opposed to the Lagrangian particle model. Since the Lagrangian particles are transported solely by the velocity field, and since the normal velocity at a surface is essentially zero, it takes the particles time to move away from the burner. As a result, a large fraction of the particle's heat is emitted incorrectly near the burner surface. The requirement that combustion occurs on the $Z_F$ surface results in the heat being released towards the edge of the plume where the oxygen is located. In contrast, the Lagrangian particles, which move towards the center of the plume due to the radial entrainment velocity, release their heat towards the plume center.

Figures 3 and 4 display respectively the centerline temperature and velocity predictions of the 30 kW simulation versus McCaffrey's correlation. FDS results are shown time-averaged over a period of approximately 30 s. The results of the other simulations were similar and are omitted for brevity. Far-field temperature predictions for both methods are the same and agree

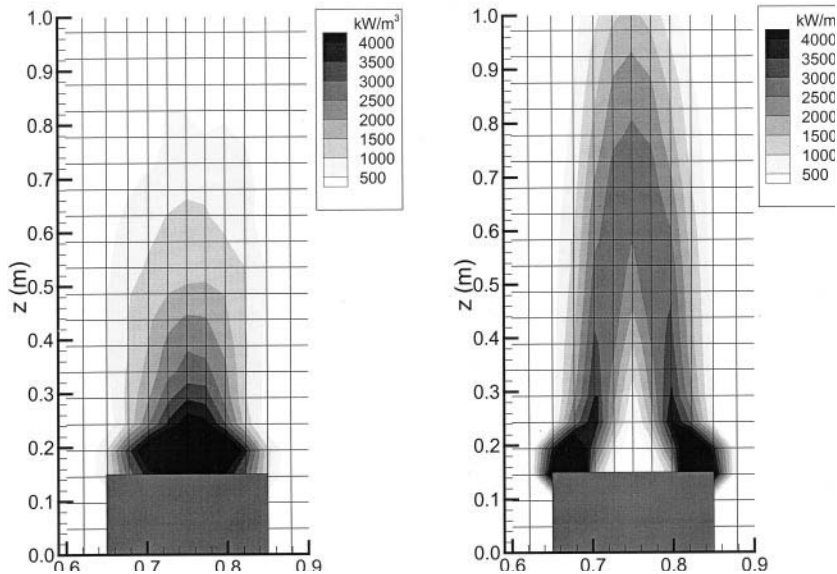


***Figure 2.*** *Comparison of heat release rate contours for FDS v1 (Left) and FDS v2 (Right) for a 0.2 m square burner, 60 kW pool fire.*

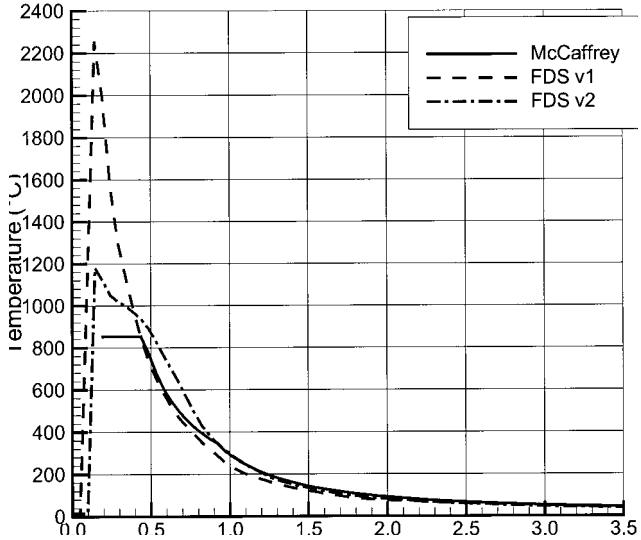


***Figure 3.*** *Centerline temperature profile for a 30 kW pool fire: FDS v1, FDS v2, and McCaffrey's correlations.*

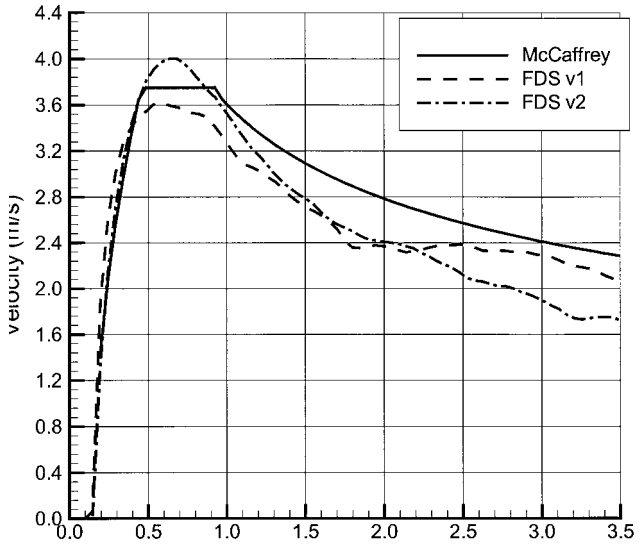


***Figure 4.*** *Centerline velocity profile for a 30 kW pool fire: FDS v1, FDS v2, and McCaffrey's correlations.*

with McCaffrey's correlation. This is to be expected since buoyancy forces drive the far field calculation, which depends more upon the total heat release rate rather than its spatial distribution. Temperatures for the mixture fraction method are significantly better in the near field. The temperature plots clearly show the improvement in the geometric distribution of the heat release. Velocity predictions show a small improvement relative to McCaffrey's correlation for the mixture fraction model. The mixture fraction method better captures the near-field velocity profile as the heat release is occurring in a more realistic distribution. Thus, the near-field buoyancy forces are being better simulated with the mixture fraction model than with the Lagrangian particle method. The far field velocities are slightly worse with the mixture fraction, the reason for which is not clear. However, since the particle method does not show a smoothly decreasing centerline velocity, the mixture fraction version while not matching the end magnitude as close as the particle method, is matching the trend correctly.

## NIST-BFRL 40% Reduced Scale Enclosure (RSE)

A recent investigation at NIST attempted to determine the measurement uncertainties in the use of bare-bead and aspirated thermocouples for compartment fires [12]. As part of this investigation, natural gas and hexane fires were set inside of a 40% scale compartment based on a standard compartment in ISO-9705. A 400 kW natural gas fire was selected from this investigation for simulation with FDS. The compartment and the measurement locations chosen for simulation are shown in Figure 5. The gas burner was located in the center of the compartment with its top 0.15 m above the floor. For the simulations, the grid size was 0.04 m and the computational domain was extended beyond the doorway by one third of the compartment's length. The simulation results are compared with data collected during the 400 kW test.

Figures 6 and 7 show predicted versus measured temperatures for the two aspirated thermocouples (TC) located at 0.24 m and 0.80 m inside the front of the compartment. These were the only aspirated TCs located inside the compartment. A few observations are made from these figures:

1. At the start of the fire, both models show much faster temperature increases than measured during the test. This is probably due in part to numerical diffusion of heat, since a relatively coarse grid was used.
2. For the upper TC, the particle method over predicts the temperature increase by 60% at this location whereas the new model over predicts the measured value by 20%. The over prediction by the particle method is primarily a result of the radiation model, which does not calculate

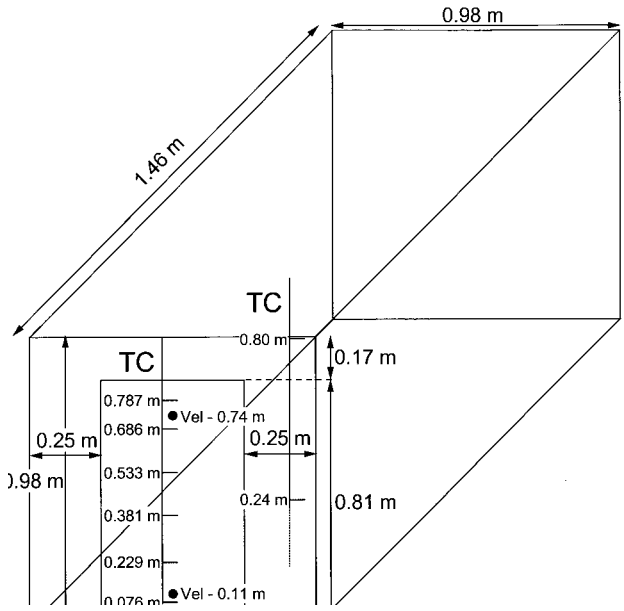


***Figure 5.*** *NIST 40% reduced scale enclosure showing dimensions and locations of instrumentation.*

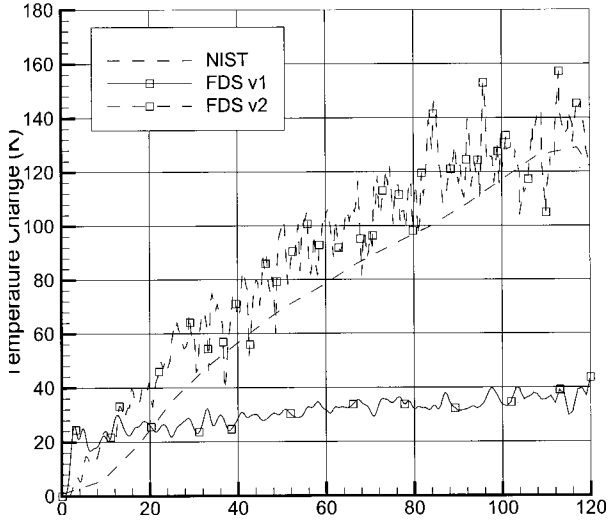


***Figure 6.*** *FDS v1 and FDS v2 predictions for NIST 40% RSE lower layer temperature (front corner at 0.24 m above the floor) for a 400 kW fire. Plotted as temperature change from ambient.*

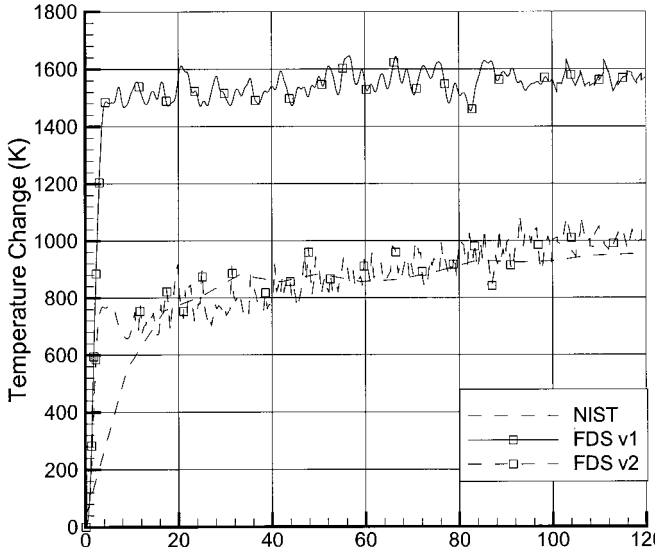


***Figure 7.*** *FDS v1 and FDS v2 predictions for NIST 40% RSE upper layer temperature (front corner at 0.80 m above the floor) for a 400 kW fire. Plotted as temperature change from ambient.*

radiative transfer from the ceiling layer to the floor. The over prediction of the new model has two possible contributions. One, is that too much heat is being released inside the compartment. This could result from an underprediction of the flame lengths due to the grid resolution enhancing mixing, and it also results from the assumption of complete combustion which is not the case for a 400 kW fire in a compartment of that size. During the actual test, a significant portion of the heat release was outside the compartment, whereas FDS did not predict as large a flame surface. Two, the new models may be under predicting the wall and radiative losses from the hot gas.

3. For the lower TC, after 40 s, the particle method predictions lie well below the measured data whereas FDS v2 predictions agree well with the measurements over this time period. These results are primarily due to the different radiation models.

Figures 8 and 9 plot the predicted and measured velocities in the doorway. The measurements were made by bi-directional probes. In the lower layer, the particle method under predicts the velocity by 15% whereas the mixture fraction model over predicts the measured data by 40%. In the upper layer, it is observed that both FDS versions under predict the velocity at this

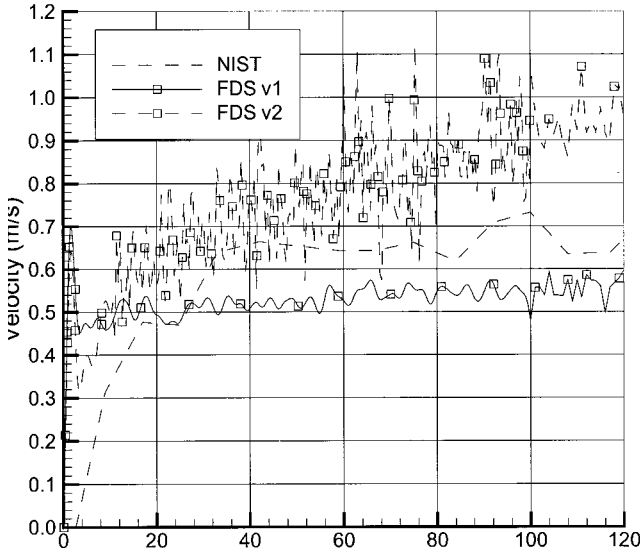


***Figure 8.*** *FDS v1 and FDS v2 predictions for NIST 40% RSE lower layer doorway centerline velocity (0.1 m above the floor) for a 400 kW fire.*

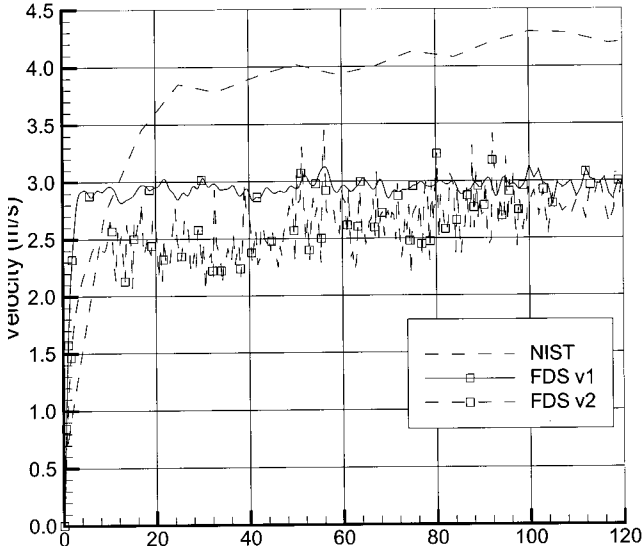


***Figure 9.*** *FDS v1 and FDS v2 predictions for NIST 40% RSE upper layer doorway centerline velocity (0.07 m below the top of the doorway) for a 400 kW fire.*

location by 31% for the particle method and by 35% for the mixture fraction. Again, it is observed that both versions of FDS show a faster initial transient. This discrepancy has two possible contributions. The first may be that the nodding results in smearing the doorway massflow profile resulting in lower velocities at the measurement location. The second is that FDS may be predicting a slightly different shape for the velocity profile which would result in a difference between the experiment and the simulation. Without further resolution in the data, the exact cause of the discrepancy cannot be identified.

The final graphical comparisons for this scenario are Figures 10 and 11, which depict the temperature and velocity profiles in the doorway at 120 s. The temperature profile results clearly show that the mixture fraction predictions are closer to the observed temperature profile than the particle method. Both versions predict a somewhat larger upper layer than indicated by the data which could be due to the grid resolution. The velocity profiles show both versions predicting similar profiles, though the mixture fraction method predicts a slightly smaller lower layer. The pointwise prediction errors look more reasonable when the entire profile is considered.

Lastly, species predictions made by the mixture fraction method are compared to values measured in the top center of the door in the vicinity of the uppermost thermocouple. $CO_2$ and $O_2$ concentrations measured during

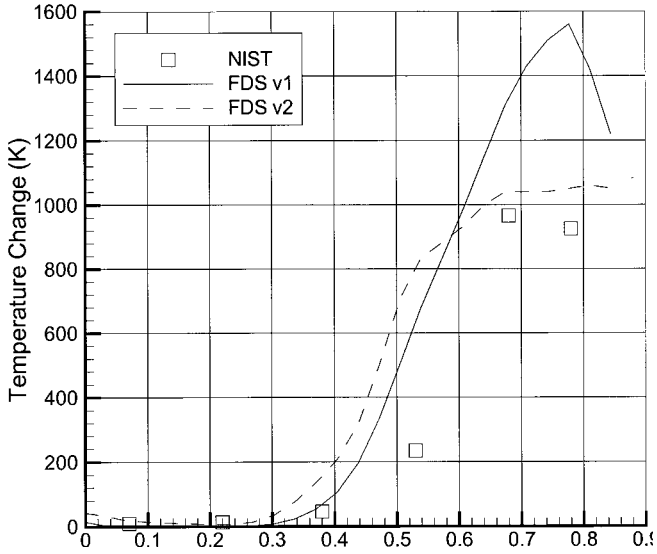


***Figure 10.*** *FDS v1 and FDS v2 predictions for NIST 40% RSE doorway centerline temperature profile for a 400 kW fire at 120 s. Plotted as temperature change from ambient.*

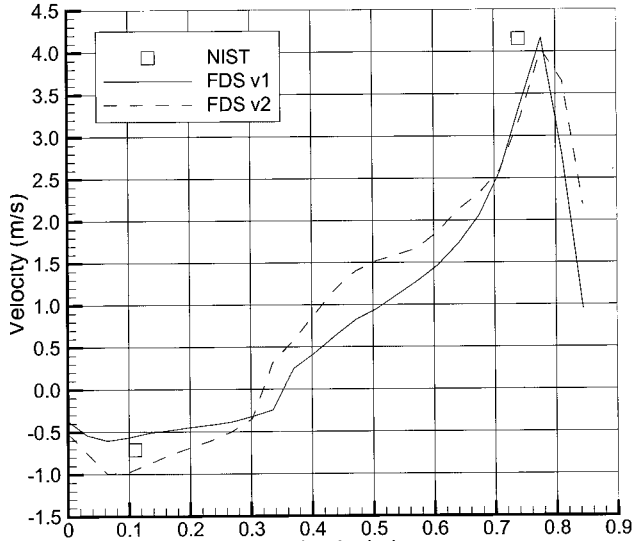


***Figure 11.*** *FDS v1 and FDS v2 predictions for NIST 40% RSE doorway centerline velocity profile for a 400 kW fire at 120 s.*

the test were 8.7 and 0.2%, respectively. FDS predicted respectively 9.0 and 0.0%. These values indicate that FDS with mixture fraction is capable of making good predictions of major species concentrations. However, they also indicate a weakness of the current mixture fraction implementation. There were flames out the doorway during this test, indicating the presence of yet unreacted fuel and oxygen. The mixture fraction model as implemented assumes infinitely fast chemistry and precludes the simultaneous presence of fuel and oxygen. Thus, combustion inefficiencies that occur during underventilated fires are not completely captured. See comment discussion of Figures 6 and 7.

**HDR Propane Fire Test**

The HDR test facility was the containment building from a decommissioned nuclear reactor in Germany. The facility was a cylinder 20 m in diameter and 50 m in height and was topped by a 10 m radius hemispherical dome. The facility had eight levels and over 60 compartments. Multiple vertical flowpaths were present in the form of two axially located sets of equipment hatches, two staircases, and an elevator shaft. The total free air volume in the facility was 11,000 $m^3$ of which the dome contained 4800 $m^3$ [13]. The facility was used for a number of studies of different types of

containment building threats including earthquakes, blowdowns, plane crashes, and fires. The fire study consisted of seven test groups using different fuels in different locations [14].

The test simulated in this paper is test T51.23, a 1 MW propane fire test performed in 1986 on the 4th level of the facility in a series of specially constructed compartments [14,15], see Figure 12, which were lined with fire brick to prevent damage to the facility. Hatches on the 4th level were open to the levels above to provide an exhaust path to the dome for combustion products. For this test, five propane gas burners located near the outer wall of the facility were fed propane premixed with 10% excess air. The facility was instrumented with numerous velocity sensors (Pitot tubes) and thermocouples. The thermocouples were not aspirated, thus, significant errors can be expected in the temperature measurements made in the lower portion of the fire room.

The FDS simulation of this fire included the fire room and the curved hallway leading to the open hatch to the 5th level. The resulting geometry yielded a computational domain 11.2 m x 9.6 m × 4.6 m in dimension. This region was mapped to a finite differenced volume of 108 cells × 96 cells × 54 cells for a total of 560,000 nodes. The resulting geometry is shown in Figure 13. Since the mixture fraction model precludes a true premixed fuel–air mixture, two sets of five burners were defined for the simulation. One set of burners, located at the actual burner locations for the test, fed fuel, and the other set, located just above the actual burners, fed air. The FDS

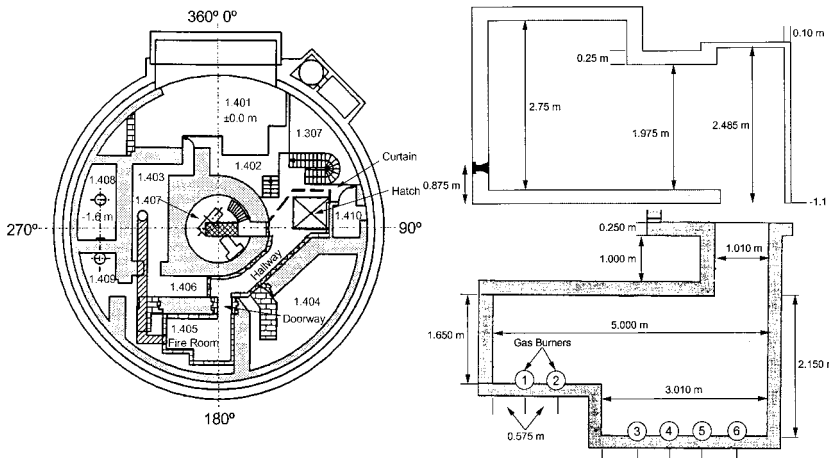


***Figure 12.*** *HDR propane fire test layout.*

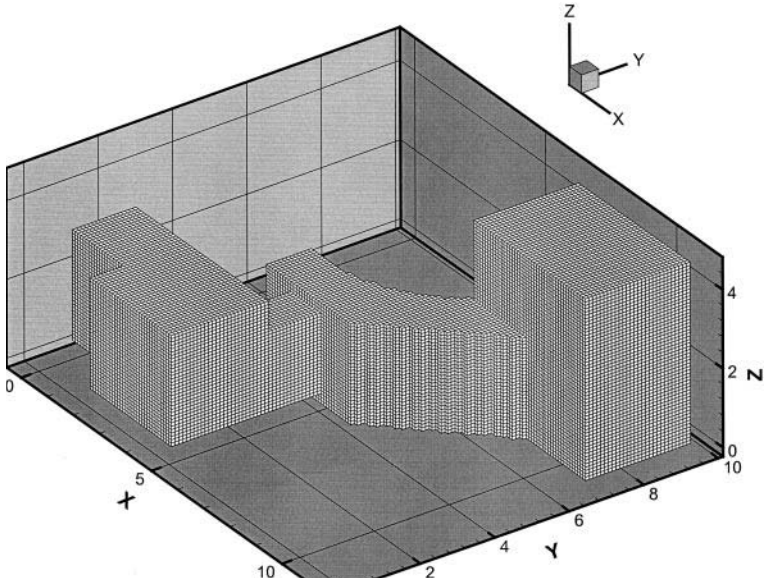


***Figure 13.*** *FDS grid for the HDR propane fire test.*

simulations were run for 10 min of real time. An extensive description of the input model for this simulation can be found in Reference [15].

The first two comparisons of FDS results to HDR data, Figures 14 and 15, show the temperature rise in the fire room near the doorway at elevations 0.15 m above the floor and 0.2 m below the ceiling. Combined, these figures show the tremendous improvement in predictive capabilities for large compartment fires. The particle method, with its simple radiation model, precludes the hot upper layer from radiating heat to the floor. This results in over predicting the upper layer temperature by a factor of two and not predicting any noticeable change in the lower layer temperature. The mixture fraction version of FDS, with its improved radiation model, does much better at predicting the upper layer to lower layer heat transfer. It now under predicts the upper layer temperatures by less than 5% and predicts a temperature rise in the lower layer indicating that the floor is heating up and convecting heat to the incoming gas in the lower layer. As the thermocouples in the fire room have a direct line of site to the gas burners, they indicate a measured temperature higher than the actual gas temperature. For the upper layer, this is not likely to be a large error percentage, but it will be for the lower layer. Thus, with the mixture fraction and finite volume radiation, FDS is likely performing better than indicated by these plots. Both versions of FDS show a much faster initial transient,

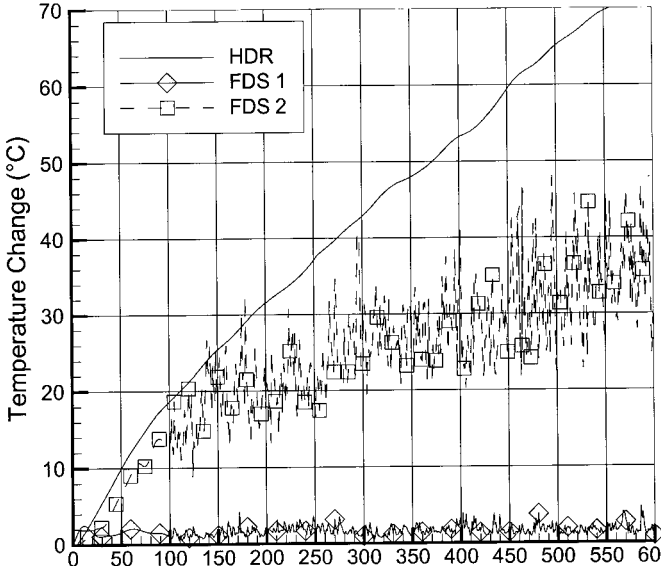


***Figure 14.*** *FDS v1 and FDS v2 predictions for HDR fire room temperature rise 0.15 m above the floor near the doorway. Plotted as temperature change from ambient.*

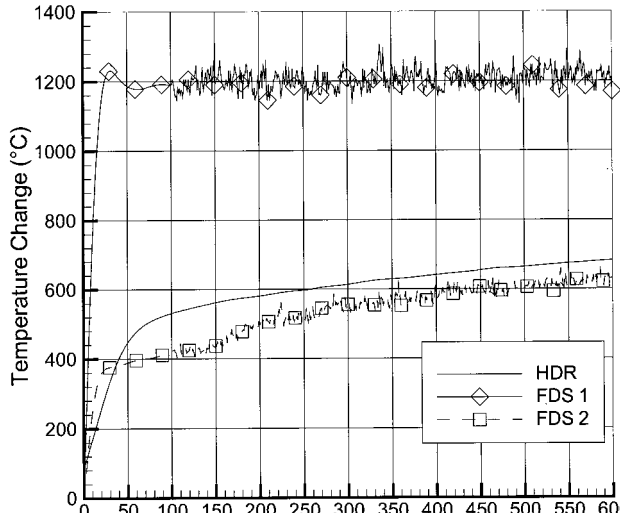


***Figure 15.*** *FDS v1 and FDS v2 predictions for HDR fire room temperature rise 0.2 m below the ceiling near the doorway. Plotted as temperature change from ambient.*

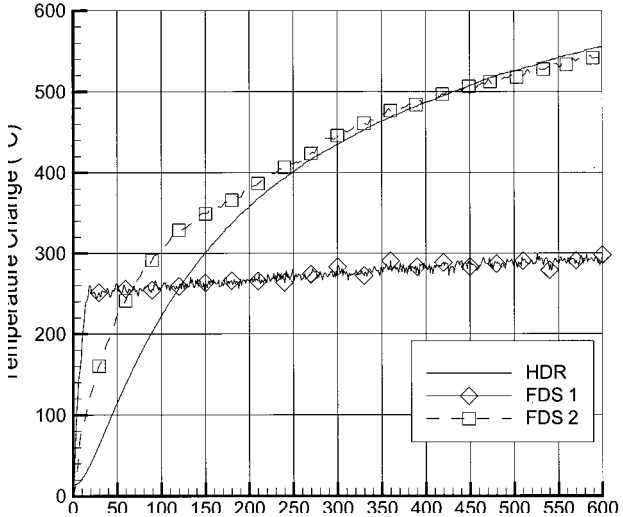


***Figure 16.*** *FDS v1 and FDS v2 predictions for HDR fire room wall temperature rise 0.6 m below the ceiling opposite burner #3 near the midpoint elevation of the fire room.*

however, the particle method quickly reaches steady state, whereas after 200 s, the mixture fraction method matches the rate of temperature rise seen in the data.

The next figure, Figure 16, depicts the wall temperature change opposite Burner #3 at 0.6 m below the ceiling in the upper layer of the fire room. This figure illustrates well the improvements made in modeling wall heat transfer. As in the previous two figures, the particle method shows a much faster initial transient than seen in the data. However, even though the gas temperatures are over predicted by a factor of two, the wall temperatures are under predicted by a factor of two. Again, this is primarily a result of the radiation model. The mixture fraction version on the other hand shows an initial transient that is closer, though still too fast, to that seen in the data, and at 600 s is predicting a surface temperature that is only 3% less than the measured data. This improvement in surface temperature prediction greatly improves the ability of FDS to predict thermal damage potential and the possible ignition of objects distant from the fire, which is critical in predicting the onset of flashover.

The last figure, Figure 17, shows the upper layer temperature change in the hallway 0.23 m below the ceiling approximately halfway between the fire room doorway and the region beneath the maintenance hatch to the facility's 5th level. Again it is observed that both versions show too fast of an initial transient. However, the particle method reaches a steady state

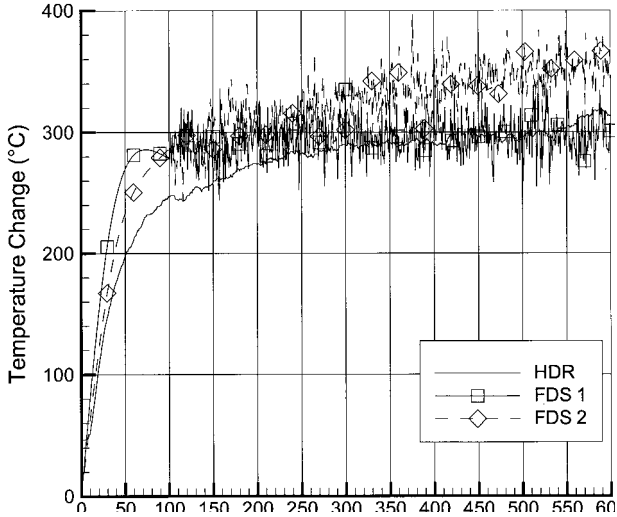


***Figure 17.*** *FDS v1 and FDS v2 predictions for HDR hallway upper layer temperature rise 0.23 m below the ceiling midway between fire room and hatch to 5th level.*

temperature change approximately 15% lower than the mixture fraction version. This is surprising since the initial temperature change of the upper layer in the fire room was a factor of two higher. This would suggest that the heat transfer to the hallway ceiling is being greatly over predicted by the particle method. The mixture fraction version, which over predicts the hallway temperature rise by 12%, is slightly under predicting the heat transfer to the ceiling, a result which is similar to that seen in the fire room wall temperature. Since radiation heat transfer plays a much smaller role in the hallway due to the lower temperatures, the improvements seen in this location are likely the result of modifications to the convective heat transfer model in FDS [1].

The final HDR comparisons are for a set of gas sensors located in the centerline of the doorway, 0.16 m below the doorway soffit. Four sensors were placed here, $CO_2$, CO, unburned hydrocarbons, and $O_2$. Only the $CO_2$ and $O_2$ sensors generated useable data for this test. At 10 min, the sensors indicated respective concentrations of 8.0 and 11.5% whereas mixture fraction predictions were 7.2 and 7.7%. For this simulation, the mixture fraction is still predicting well the $CO_2$ concentration at this point, but is over predicting the oxygen consumption at this point. It is not clear why this is the case, though it may result from the actual test using premixed air and fuel which cannot be directly simulated with the mixture fraction concept as implemented.

## CONCLUSIONS

A new combustion model and a new radiation model have been added to FDS v1 as part of a series of enhancements to create a new version of FDS, which has been released as v2. The new combustion model is a mixture fraction model modified to work on the coarse grids usually used in simulating compartment fires. This model adds the ability to track major combustion species with only a small added computational cost. The mixture fraction model may also be extended to include minor species once appropriate data concerning state relationships for compartment fires can be developed. The new radiation model allows FDS to model gas–gas and gas–surface radiation heat transfer, which was not possible in the original model.

To test the new version of FDS and to compare it with the previous release, two sets of simulations were done. The first set was a simulation of three different pool fires. Since this set involved nonventilation controlled fires that do not form hot gas layers, the results are a good comparison of predictive changes caused solely by the combustion model. The second set involved two compartment fires including a 400 kW fire in the NIST 40% Reduced Scale Enclosure, which was ventilation controlled and a 1 MW fire in the HDR test facility, which was not ventilation controlled.

The plume tests clearly indicate two things. First, since both versions predict nearly the same results in the far-field, it is clear that the changes made to add the mixture fraction and finite volume radiation models, did not adversely affect the hydrodynamics solution. Second, the results illustrate well a major advantage of the mixture fraction model. Since the mixture fraction model preserves the single step chemical reaction and has the fuel as a gas rather than solid particles, the volume where combustion takes place is more realistic. With the Lagrangian particle method, combustion occurs too close to burner surface and the burner's centerline. This is not realistic, as that region in reality will contain little oxygen to support combustion. The mixture fraction model, however, has the combustion occurring near the edge of the burner. It still has numerical artifacts, which can be seen in the region of intense combustion at the burner's edge where the coarseness of the grid results in overly high mixture fraction gradients at that location.

The compartment fire simulations also show that the new version of FDS is an improvement over the particle method. Temperature predictions, especially the lower layer temperatures, are greatly improved with the new version. This is mostly a result of the new radiation model. However, there are also some minor benefits from the mixture fraction model which does account for the small changes in total moles of gas that result from combusting a hydrocarbon, which has a slight impact on the mass flow

predictions, which in turn impacts the temperature predictions. The mixture fraction also managed to reasonably predict major species concentrations exiting the compartment. This represents a major improvement over FDS v1, which did not have this capability.

The compartment simulations indicate that further improvements could be made to the mixture fraction model. The comparison of gas concentrations in the doorway, notably the complete lack of oxygen, and the comparison of the FDS results with visual observations indicate that the combusting surface in the mixture fraction model is too small. That is, too much combustion is taking place inside the compartment. An extension of the mixture fraction model to account for combustion inefficiencies during underventilated fires might improve the prediction of the flame surface, which in turn should lead to lower upper layer temperatures. The inclusion of a reaction progress parameter would also allow for a better simulation of premixed fuels.

In conclusion, the mixture fraction combustion model and finite volume method radiation solver were successfully implemented in FDS. These improvements result in markedly improved predictive capabilities for the cases tested. However, these are not the only benefits. The mixture fraction, as a single species, through its state relationships, see Figure 1, contains information about combustion products. It is hoped that the current idealized combustion can be expanded to more realistically include minor species such as soot and CO, e.g., by creating a two-parameter mixture fraction that includes a reaction progress variable as opposed to merely specifying a fixed $CO/CO_2$ production ratio. The new radiation model, which includes gas-to-surface and surface-to-surface radiation heat transfer enables FDS to begin making plausible predictions of object ignition times for flashover prediction. While further development could improve both models, the mixture fraction combustion model and the finite volume radiation transport model are a significant improvement over the Lagrangian particle model and the ray-tracing model.

## NOMENCLATURE

| | |
|---|---|
| $D\phi/Dt$ | substantial or material derivative of $\phi$ |
| $ijk$ | cell indices |
| $I$ | radiation intensity ($W/m^2$) |
| $I_b$ | radiation source term ($W/m^2$) |
| $\dot{m}_i'''$ | production rate of change of species $i$ per unit volume ($kg/s\,m^3$) |
| $\dot{m}_i''$ | production rate of change of species i per unit area ($kg/s\,m^2$) |
| $\hat{n}$ | normal vector |

| | |
|---|---|
| $s$ | oxygen mass to fuel mass ratio for stoichiometry (kg $O_2$/kg fuel) |
| $\hat{s}$ | path vector |
| $t$ | time ($s$) |
| $T$ | temperature ($K$) |
| $\hat{x}$ | position vector ($m$) |
| $V$ | volume ($m^3$) |
| $Z$ | mixture fraction |
| $Z_F$ | stoichiometric value of the mixture fraction |
| $Y_i$ | mass fraction (kg species $i$/kg gas) |
| $w_i$ | molecular weight of species $i$ (g/mol) |
| $\chi_i$ | yield of species $i$ (moles species i/moles fuel burned) |
| $\kappa$ | absorptivity (1/m) |
| $\nu_i$ | stoichiometric coefficient of species $i$ (moles) |
| $\rho$ | density (kg/m$^3$) |
| $\sigma$ | Stefan–Boltzman constant (W/m$^2$ K$^4$) |
| $\zeta$ | ratio of supplied air to stoichiometrically required air (moles air supplied/moles required) |

## REFERENCES


1. McGrattan, K. et al., *Fire Dynamics Simulator* (*Version 2*) – *Technical Reference Guide, NISTIR 6783, National Institute of Standards and Technology*, Gaithersburg, MD, 2001.
2. McGrattan, K. and Forney, G., *Fire Dynamics Simulator* (*Version 2*) – *User's Manual, NISTIR 6784, National Institute of Standards and Technology*, Gaithersburg, MD, 2001.
3. Kuo, K., *Principles of Combustion*, New York, NY, John Wiley and Sons, 1986.
4. Raithby, G. and Chui, E., "A Finite-Volume Method for Predicting Radiant Heat Transfer in Enclosures with Participating Media", *Journal of Heat Transfer*, Vol. 112, 1990, pp. 415–423.
5. Rehm, R. and Baum, H., "The Equations of Motion for Thermally Driven, Buoyant Flows", *Journal of Research of the NBS*, Vol. 83, 1978, pp. 297–308.
6. Mahalingam, S. et al., "Analysis and Numerical Simulation of a Nonpremixed Flame in a Corner", *Combustion and Flame*, Vol. 118, 1999, pp. 221–232.
7. Siegel, R. and Howell, J.R. *Thermal Radiation Heat Transfer*, 3rd Edn., Philadelphia, PA, Hemisphere Publishing Corp., 1992.
8. Karlsson, B. and Quintiere, J., *Enclosure Fire Dynamics*, Boca Raton, FL, CRC Press, 2000.
9. Mulholland, G. and Choi, M. Measurement of the Mass Specific Extinction Coefficient for Acetylene and Ethene Smoke Using the Large Agglomerate Optics Facility, 27th Symposium on Combustion, The Combustion Institute, 1998, pp. 1515–1522.
10. Grosshandler, W., RADCAL: A Narrow-Band Mode for Radiation Calculations in a Combustion Environment, NIST Technical Note 1402, National Institute of Standards and Technology, Gaithersburg, MD, 1993.
11. Baum, H. et al., "Three Dimensional Simulations of Fire Plume Dynamics", In: *Proceedings of the 5th International IAFSS Symposium*, Fire Safety Science, 1997, pp. 511–522.
12. Blevins, L., "Behavior of Bare and Aspirated Thermocouples in Compartment Fires, HTD99–280", In: *Proceedings of the ASME National Heat Transfer Conference*, Albuquerque, NM, 1999.

13. Schall, M. and Valencia, L., *Data Compilation of the HDR Containment for Input Data Processing for Pre-Test Calculations*, PHDR Working Report 3.143/79, Project HDR Nuclear Center, Karlsruhe, Germany, 1982.
14. Floyd, J., *Evaluation of the Predictive Capabilities of Current Computational Methods for Fire Simulation in Enclosures Using the HDR T51 and T52 Tests with a Focus on Performance-Based Fire Codes*, Ph.D. Dissertation, University of Maryland, College Park, MD, 2000.
15. Floyd, J., *Comparison of CFAST and FDS for Fire Simulation with the HDR T51 and T52 Tests, NISTIR-6866*, National Institute of Standards and Technology, Gaithersburg, MD, 2002.

PAPER IV

# Numerical modeling of pool fires using LES and finite volume method for radiation

In: Evans, D.D. (Ed.). Proceedings of the Seventh International Symposium on Fire Safety Science. Worcester, MA, 16–21 June 2003. International Association for Fire Safety Science, 2003. Pp. 383–394.

# Numerical Modeling of Pool Fires Using LES and Finite Volume Method for Radiation

SIMO HOSTIKKA
VTT Building and Transport, Espoo, Finland
simo.hostikka@vtt.fi

KEVIN B. McGRATTAN and ANTHONY HAMINS
Building and Fire Research Laboratory
National Institute of Standards and Technology
Gaithersburg, Maryland, USA

**ABSTRACT**

The thermal environment in small and moderate-scale pool flames is studied by Large Eddy Simulation and the Finite Volume Method for radiative transport. The spectral dependence of the local absorption coefficient is represented using a simple wide band model. The predicted radiative heat fluxes from methane/natural gas flames as well as methanol pool burning rates and flame temperatures are compared with measurements. The model can qualitatively predict the pool size dependence of the burning rate, but the accuracy of the radiation predictions is strongly affected by even small errors in prediction of the gas phase temperature.

**KEYWORDS:** Large Eddy Simulation, radiation modeling, pool flames, radiative fraction, burning rate

## INTRODUCTION

Use of computational fluid dynamics (CFD) for fire modeling has increased dramatically during the last few years, mainly due to the increased computational power and the development of fire specific computer codes. Most models have used Reynolds-averaged Navier-Stokes solvers combined with turbulence models and relatively simple combustion models. On the other hand, highly complex combustion models with detailed solution of gas phase flows have been presented by the combustion research community for many years. The exchange of information and experiences between the fire and combustion communities has been rare, mainly due to the very different physical length scales over which the models are applied.

The objective of the paper is to explore the application of a Large Eddy Simulation (LES) technique to pool flames, which are typical source terms in the fire safety engineering. LES technique is used to model pool flames characterized by a physical scale that lies between combustion research and compartment fire research. Combustion is modeled using a mixture fraction approach, which assumes that the reaction takes place in a flame sheet that moves with the three dimensional turbulent flow. The focus of the paper is in the modeling of the transport of thermal radiation using a Finite Volume Method combined with a simple wide band model for the spectral dependence of the local

absorption coefficient. The model is used to predict the radiation from methane/natural gas flames for burner diameters between 10 cm and 100 cm. Another application tested by the models is the prediction of the burning rate of circular methanol pools, ranging from 1 cm to 100 cm diameter. The time averaged flame temperatures are compared with measurements in the case of the 30 cm methanol pool. Measurements of distribution of radiative heat flux, the fuel mass burning rate, and the gas-phase temperature are described here in detail.

## MODEL DESCRIPTION

### Hydrodynamic model

The fluid flow is modeled by solving the conservation equations for mass, mixture fraction, momentum and energy in a low Mach number form. The details of the model have been described previously [1,2] and will not be repeated here. A full description can be found in Ref. [3]. The effect of the flow field turbulence is modeled using LES, in which the large scale eddies are computed directly and the sub-grid scale dissipative processes are modeled. An explicit, second-order accurate scheme is used for the time integration.

### Combustion model

The combustion model is based on the assumption that the combustion is mixing-controlled. This implies that all species of interest can be described in terms of the mixture fraction $Z$, a conserved scalar variable. Heat from the reaction of fuel and oxygen is released along an infinitely thin sheet where $Z$ takes on its stoichiometric value as determined by the solution of the transport equation for $Z$. The heat release rate per unit area of flame surface is

$$\dot{q}_C'' = \Delta H_O \left. \frac{dY_O}{dZ} \right|_{z<z_f} (\rho D) \nabla Z \cdot \mathbf{n} \qquad (1)$$

where $\Delta H_O$ is the energy released per unit mass of oxygen consumed, being almost constant for a wide range of fuels [4], and $\mathbf{n}$ is the unit normal facing outward from the fuel [5]. Note that both $dY_O/dZ$ and $\nabla Z \cdot \mathbf{n}$ are negative. Expressing the heat release rate in terms of the oxygen consumption is very useful because the chemical composition of the fuel is not well characterized in compartment fires.

### Thermal radiation model

The Radiative Transport Equation (RTE) for a non-scattering gas is

$$\mathbf{s} \cdot \nabla I_\lambda(\mathbf{x},\mathbf{s}) = \kappa_\lambda(\mathbf{x}) \left[ I_b(\mathbf{x}) - I_\lambda(\mathbf{x},\mathbf{s}) \right] \qquad (2)$$

where $I_\lambda(\mathbf{x},\mathbf{s})$ is the radiation intensity at wavelength $\lambda$, $I_b(\mathbf{x})$ is the source term given by the Planck function, $\mathbf{s}$ is the unit normal direction vector and $\kappa_\lambda(\mathrm{x})$ is the spectral absorption coefficient. In practical simulations, the spectral dependence cannot be solved accurately. Instead, a simple wide band model is developed by dividing the radiation spectrum into a relatively small number of bands. The band specific RTE's are

$$\mathbf{s}\cdot\nabla I_n(\mathbf{x},\mathbf{s}) = \kappa_n(\mathbf{x})\left[I_{b,n}(\mathbf{x}) - I_n(\mathbf{x},\mathbf{s})\right], \quad n = 1...N \tag{3}$$

where $I_n$ is the intensity integrated over the band $n$ and $\kappa_n$ is the appropriate mean absorption coefficient. The source term can be written as a fraction of the blackbody radiation

$$I_{b,n}(\mathbf{x}) = F_n(\lambda_{\min}, \lambda_{\max})\sigma T(\mathbf{x})^4 \tag{4}$$

where $\lambda_{\min}$ and $\lambda_{\max}$ are the limits of the band and $\sigma$ is the Stefan-Boltzmann constant. The calculation of factors $F_n$ is explained, for example, in Ref. [6]. A narrow-band model RADCAL [7] is combined with the radiation solver for the calculation of the band mean absorption coefficients $\kappa_n$. When the intensities corresponding to the bands are known, the total intensity is calculated by summation $I(\mathbf{x},\mathbf{s}) = \Sigma I_n$.

Even with a reasonably small number of bands, the solution of the RTE's is very time consuming. Fortunately, in most large-scale fire scenarios soot is the most important combustion product affecting thermal radiation. As the radiation spectrum of soot is continuous, it is possible to assume that the gas behaves as a gray medium. The spectral dependence is then lumped into one effective absorption coefficient ($N$=1) and the source term is given by the blackbody radiation intensity. For the computation of the effective absorption coefficients with RADCAL, a path length must be defined. Here, it is calculated as $0.1\times3.6\times L_xL_xL_x/(L_xL_y+L_xL_z+L_yL_z)$ which is one tenth of the mean beam length of the computational domain, with dimensions $L_x$, $L_y$ and $L_z$. In case of the wide band model, the Planck mean absorption coefficients are used as band mean coefficients. The limits of the bands are selected to give an accurate representation of the most important radiation bands of $CO_2$ and water. The absorption coefficients are tabulated as a function of mixture fraction and temperature. During the simulation, the local absorption coefficient is found by a look-up table.

To retain computational simplicity and applicability to the different length scales, the soot formation and oxidation processes are not modeled. Instead, the soot concentration is obtained by assuming a certain conversion factor (yield) of soot. The local soot concentration is based on the value of mixture fraction alone. This is not a very good approximation in general, as the soot chemistry depends on the scale of the problem. However, it is consistent with the relatively simple combustion model adopted. A state relation between soot and mixture fraction is created, and the effect of soot is taken into account during the tabulation of absorption coefficients.

Numerical experiments found that six bands are usually enough ($N$=6) for fire applications. If the absorption of the fuel is known to be important, separate bands should be reserved for the fuel, and the total number of bands is ten ($N$=10). For simplicity, the fuel is assumed to be $CH_4$. The limits of the bands are shown in Table 1 below. High temperature spectral information is not currently available for methanol, but the difference between its values and those of methane are expected to be relatively insignificant for the purpose of this investigation.

Equation (3) is solved using techniques similar to those for convective transport in finite volume methods for fluid flow [8], thus its name is the Finite Volume Method (FVM). To

obtain the discretized form of the RTE, the unit sphere is divided into a finite number of solid angles. The distribution of angles is based on empirical rules that try to produce equal solid angles $\delta\Omega^l = 4\pi/N_\Omega$, where $N_\Omega$ is the total number of control angles. In each grid cell a discretized equation is derived by integrating Eq. (3) over the cell volume $V_{ijk}$ and the control angle $\delta\Omega_l$, to obtain

$$\int_{V_{ijk}} \int_{\partial\Omega^l} \mathbf{s} \cdot \nabla I_n^l \, d\Omega dV = \int_{V_{ijk}} \int_{\partial\Omega^l} \kappa_n(\mathbf{x}) \left[ I_{b,n}(\mathbf{x}) - I_n^l(\mathbf{x}, \mathbf{s}) \right] d\Omega dV \tag{5}$$

The volume integral on the left hand side is replaced by a surface integral over the cell faces using the divergence theorem. Assuming that the radiation intensity is constant on each of the cell faces, the surface integral can be approximated by a sum over the cell faces. The cell face intensity is calculated from the neighboring cells using the so called "step scheme" which is equivalent to a first order upwind scheme. The numerical diffusion caused by the low order scheme is actually used to smooth out the intensity field. Therefore, FVM suffers from the ray effects to a smaller extent than the more commonly used ray tracing approaches. The solution method of the resulting system is based on an explicit marching sequence [9], in which the marching direction depends on the propagation direction of the radiation intensity, and no iterations are needed.

Table 1. - Limits of the spectral bands. $\nu$ and $\lambda$ are the wave number and wavelength.

| Model version | Bands | | | | | | | | | | |
|---|---|---|---|---|---|---|---|---|---|---|---|
| 6 band model | 1 | 2 | 3 | | | 4 | 5 | | | 6 | |
| major species | soot | $CO_2$ $H_2O$ | soot | | | $CO_2$ | soot | | | soot | |
| limits | | | | | | | | | | | |
| ν (1/cm) | 10000 | 3800 | 3450 | 3200 | 2800 | 2400 | 2080 | 1400 | 1200 | 1000 | 50 |
| λ (μm) | 1.00 | 2.63 | 2.90 | 3.13 | 3.57 | 4.17 | 4.81 | 7.14 | 8.33 | 10.0 | 200.0 |
| 10 band model | 1 | 2 | 3 | 4 | 5 | 6 | 7 | 8 | 9 | 10 | |
| major species | soot | $CO_2$ $H_2O$ | soot | $CH_4$ | soot | $CO_2$ | soot | $CH_4$ | soot | soot | |

**Pyrolysis model for liquid fuels**

The rate at which liquid fuel evaporates when burning is a function of the liquid temperature and the concentration of fuel vapor above the pool surface. Equilibrium is reached when the partial pressure of the fuel vapor above the surface obtains equilibrium as determined by the Clausius-Clapeyron expression

$$p_{cc} = p_0 \exp\left[ \frac{\Delta H_v M_f}{R} \left( \frac{1}{T_s} - \frac{1}{T_b} \right) \right] \tag{6}$$

where $\Delta H_v$ is the heat of vaporization, $M_f$ is the molecular weight, $R$ is the universal gas constant, $T_s$ is the surface temperature, and $T_b$ is the boiling temperature of the fuel. For simplicity, the liquid fuel itself is treated like a thermally-thick solid for computing heat conduction into the pool. There is no consideration of convection within the liquid pool.

## EXPERIMENTAL METHOD

Methane, natural gas, and methanol fires were established in a quiescent environment using six different circular burners. A water-cooled, porous sintered-bronze 0.38 m burner and 1.0 m and 0.10 m water-cooled sand burners were used for the gaseous fuels. The liquid fuel burners were 0.10 m, 0.30 m, and 1.0 m diameter. The sand burners had a 3 mm (outer diameter) copper water-cooling tube positioned 1 cm below the sand in the form of a loosely wound spiral. In addition, a copper water cooling tube was wrapped around the outside of the burner. The rate of gaseous fuel delivery was controlled using calibrated rotometers. The mass flow of the gaseous fuels was determined using a dry test meter and a stopwatch to measure the volume per unit time of fuel delivered to the burner and a thermocouple measurement of the ambient temperature. For the liquid fuel fires, the fuel was stored in a reservoir and gravity-fed to the burner at a controlled rate such that the fuel was maintained ½ cm below the rim of the burner. The mass delivery of liquid fuel was measured using a calibrated load-cell positioned under the fuel reservoir. Steady state burning conditions were established before measurements were initiated. A warm-up period of approximately 10 min was required for the experiments involving methanol and approximately 3 min for the gaseous fuels. The combined expanded measurement uncertainty for the burning rate was estimated as 4 % for the gaseous fuels and 10 % for methanol (as determined from the load cell measurements). All uncertainties are reported with a coverage factor of two, which is equal to two times the value of the standard deviation [10]. The experimental apparatus and method are described in more detail in Refs. [11] and [12], respectively.

Calibrated radiometers were used to measure the radiative flux along a cylindrical control surface surrounding the fire. Approximately 12 water-cooled (2.5 cm diameter) wide-angle ($150^o$ view) radiometers were positioned in two rows. The first row was positioned on a vertical axis several burner diameters away from the fire. These radiometers were all oriented radially facing the fire. The second row was oriented facing up and positioned along a radius on the plane aligned with the burner surface. A schematic diagram of the set-up is shown in Fig. 1 and the experimental approach is reported in Ref. [12]. The gauges were calibrated using a secondary standard in the BFRL/NIST Radiometer Calibration Facility [13]. The measured signal was averaged for a 90 s period. The radiated power emitted by the fire was determined by integrating the measured spatial distributions of radiant flux. The radiative flux typically drops off very quickly in the radial direction, whereas in the vertical direction, the flux peaks at a vertical location equal to approximately 50% of the characteristic flame height and then drops to small values above the visible flame tip. The uncertainty (with a coverage factor of two) in the radiative flux measurement is estimated as 10 %. The radiative heat loss fraction ($\chi_R$) was determined by dividing the measured radiant power by the idealized measured fire heat release rate. The uncertainty in the value of $\chi_R$ (with a coverage factor of two) is estimated as 11 % for the gaseous fuels and 14 % for methanol. Temperature measurements were conducted using fine (75 μm) platinum/rhodium thermocouples and the results were corrected for radiative losses. The absolute magnitude of the uncertainty in the temperature is a function of the flame position; it typically was 5 % to 10 % (with a coverage factor of two).

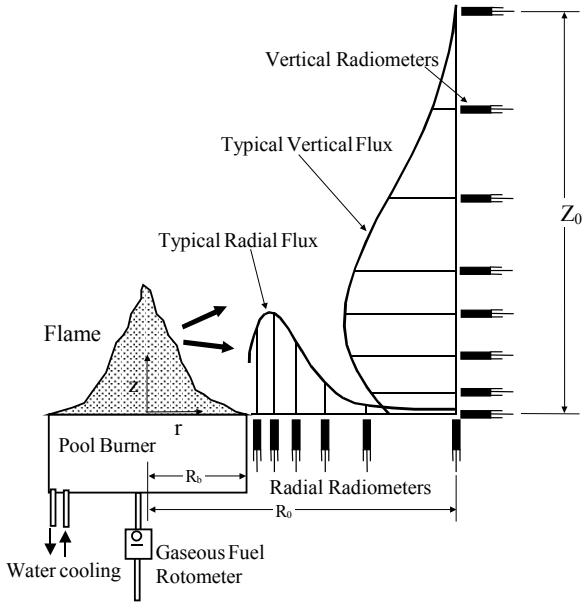


Fig. 1. - A schematic diagram of the set-up used to measure the radiative fraction.

## RESULTS AND DISCUSSION

The model was used to predict the radiative heat flux from the methane / natural gas pool flames above the circular burners. The selected cases are summarized in Table 2, where $D$ is the burner diameter, $R_0$ is the radial position of the vertical row of radiometers, $\dot{m}''_F$ is the mass burning rate per burner area and $\dot{Q}''$ is the rate of heat release per burner area. The size of the simulation domain and the size of the computational grid cell just above the burner surface, $\delta x$, are also shown. The last two columns show the dimensionless heat release rates $Q_D^* = \dot{Q}/(\rho_\infty T_\infty c_p D^2 \sqrt{gD})$ and $Q_{\delta x}^* = (\dot{Q}/A)/(\rho_\infty T_\infty c_p D^2 \sqrt{g\delta x})$ where $\dot{Q}$ is the heat release rate, $A$ is the burner area and $\rho_\infty$, $T_\infty$ and $c_p$ are the properties of the ambient air. $Q_D^*$ is the standard dimensionless number, which characterizes the strength of the fire and $Q_{\delta x}^*$ represents the resolution of the current grid, in proportion to the burning rate. A very low value of $Q_{\delta x}^*$ indicates that the position of the flame near the burner surface cannot be resolved.

Table 2. - Summary of the simulated methane burner experiments.

| Case | Test configuration | | | | Simulated domain | Simulation parameters | | |
|---|---|---|---|---|---|---|---|---|
| | $D$ (m) | $R_0$ (m) | $\dot{m}''_F$ (g/m$^2$/s) | $\dot{Q}''$ (kW/m$^2$) | x × y × z (m$^3$) | $\delta x$ (cm) | $Q_D^*$ | $Q_{\delta x}^*$ |
| A | 0.10 | 0.82 | 1.08 | 53.8 | 0.315 × 0.21 × 0.45 | 0.525 | 0.12 | 0.67 |
| B | 0.10 | 0.82 | 4.80 | 240 | 0.315 × 0.21 × 0.45 | 0.525 | 0.53 | 3.0 |
| C | 0.38 | 0.732 | 5.90 | 295 | 1.26 × 0.84 × 1.80 | 2.1 | 0.34 | 1.8 |
| D | 0.38 | 0.732 | 31.0 | 1550 | 1.26 × 0.84 × 2.20 | 2.1 | 1.8 | 9.6 |
| E | 1.0 | 1.00 | 1.25 | 62.4 | 2.50 × 2.00 × 3.50 | 5.0 | 0.044 | 0.31 |
| F | 1.0 | 0.80 | 4.12 | 206 | 2.50 × 2.00 × 4.50 | 5.0 | 0.14 | 1.05 |

For simplicity, both methane and natural gas flames were modeled as methane flames. The gas burners were modeled as a fuel inflow boundary, with surface temperature corresponding to the measured values. The vertical and top boundaries of the domain were open. The heat flux gauges were modeled as solid obstacles with a constant surface temperature of +20 °C. The size of the domain was selected such that the distance between the vertical boundaries and burner edge was at least one burner radius in the horizontal direction and eight burner radii in the vertical direction. The results were found insensitive to the distance of the vertical boundaries. The length of the domain was larger in *x*-direction than in *y*-direction, to allow the definition of the heat flux gauges. Cartesian, non-uniform grid was stretched in the vertical direction to have the smallest cell size just above the burner. The simulation of the steady state burning was run until the time averages for the predicted heat fluxes converged. The grid dependence of the predicted heat fluxes was studied by varying the grid size. Decreasing the cell size about 20 % changed the results less than 20 % and further reduction of the cell size to 50 % of the original caused only minor changes. A large number (304) of control angles were used for the radiation solver to ensure accuracy of the solution. The results were found insensitive to the temporal accuracy of the radiation solver.

A soot conversion factor of 1.0 % was assumed for all calculations. The resulting volume fractions inside the flame ranged from 0.05 to 0.12 ppm. The sensitivity of the predicted heat fluxes to the assumed conversion factor was studied for case D. Changing the conversion factor to 2.0 % increased the heat fluxes 10 % to 15 %, and correspondingly, setting it to zero decreased them by 15 % to 20 %.

For each case described in Table 2, the radiative fraction of the heat release was calculated based on the predicted radiometer readings, using the same method, as in the interpretation of the experimental results. The measured and predicted radiative fractions are compared in Table 3. The predictions are systematically higher than the measurements. The accuracy of the spectral dependence (6 band, 10 band or gray gas) does not have a strong effect on the results. The most probable reason for the high radiative fractions is the overestimation of the flame temperatures. Predicted peak temperatures in the fluctuating flames were over 2100 °C, which is close to the adiabatic flame temperature. The observed peak mean temperatures were 1300 °C (A), 1700 °C (B), 1600°C (C), 1100 °C (D), 800 °C (D) and 1400 °C (E). As can be seen, the temperatures are not systematically low or high, but in all cases the highest temperatures were found in the first computational cell above the burner.

Table 3. - Comparison of the measured and predicted radiative fractions for the methane/natural gas pool flames.

| Case | $D$ | $\dot{Q}''$ | $\chi_R$ Experiment | $\chi_R$ Model | | | |
|---|---|---|---|---|---|---|---|
| | (m) | (kW/m$^2$) | | 6 band | 6 band, fine grid | 10 band | gray gas |
| A | 0.10 | 53.8 | 0.10 | 0.11 | 0.13 | 0.13 | 0.12 |
| B | 0.10 | 240 | 0.16 | 0.22 | 0.21 | 0.20 | 0.22 |
| C | 0.38 | 295 | 0.15 | 0.19 | 0.24 | 0.19 | 0.20 |
| D | 0.38 | 1550 | 0.19 | 0.21 | 0.23 | 0.21 | 0.24 |
| E | 1.0 | 62.4 | 0.08 | 0.21 | 0.21 | 0.21 | 0.20 |
| F | 1.0 | 206 | 0.16 | 0.19 | 0.20 | 0.18 | 0.20 |

The measured and predicted radial distributions of radiative flux are compared in Fig. 2. The agreement is very good in general, but the heat flux is highly over estimated in two of the cases: the higher burning rate of the 10 cm burner (case B) and the lower burning rate of the 100 cm burner (case E). Similar trends can be found in Fig. 3, showing the vertical profiles. As the main application of the model is the simulation of compartment fires, it is encouraging to see that the high radiative fluxes have been predicted better than low fluxes. A few remarks should be made, when interpreting the results: First, the 100 % errors in radiative heat flux may be caused by as low as 20 % error in absolute temperature. Second, the lowest radiative fluxes here are of the same order of magnitude as the background radiation, and therefore very sensitive to the small errors in the boundary conditions and gas temperatures. Also, some errors are possible in the modeling of the heat flux gauges. For example, the view angle of the simulated gauges is always 180 °, while the experimental gauges had a view angle of 150°.

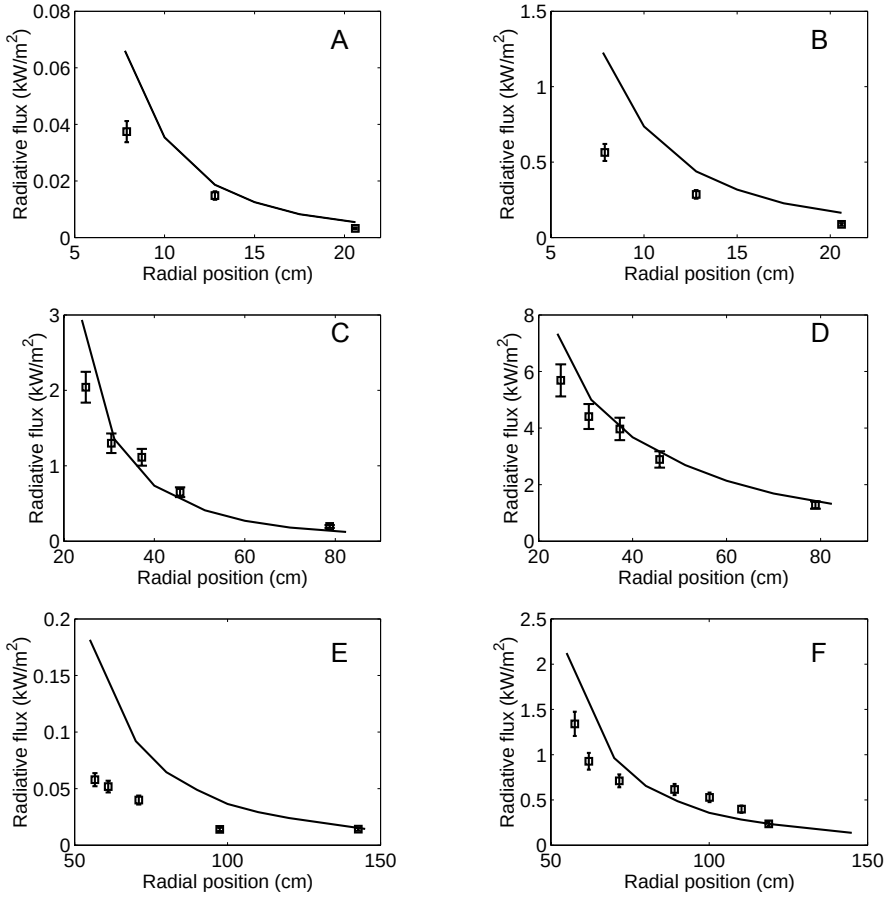


Fig. 2. - Comparison of the measured (squares) and predicted (lines) radial heat flux distributions outside the methane flames.

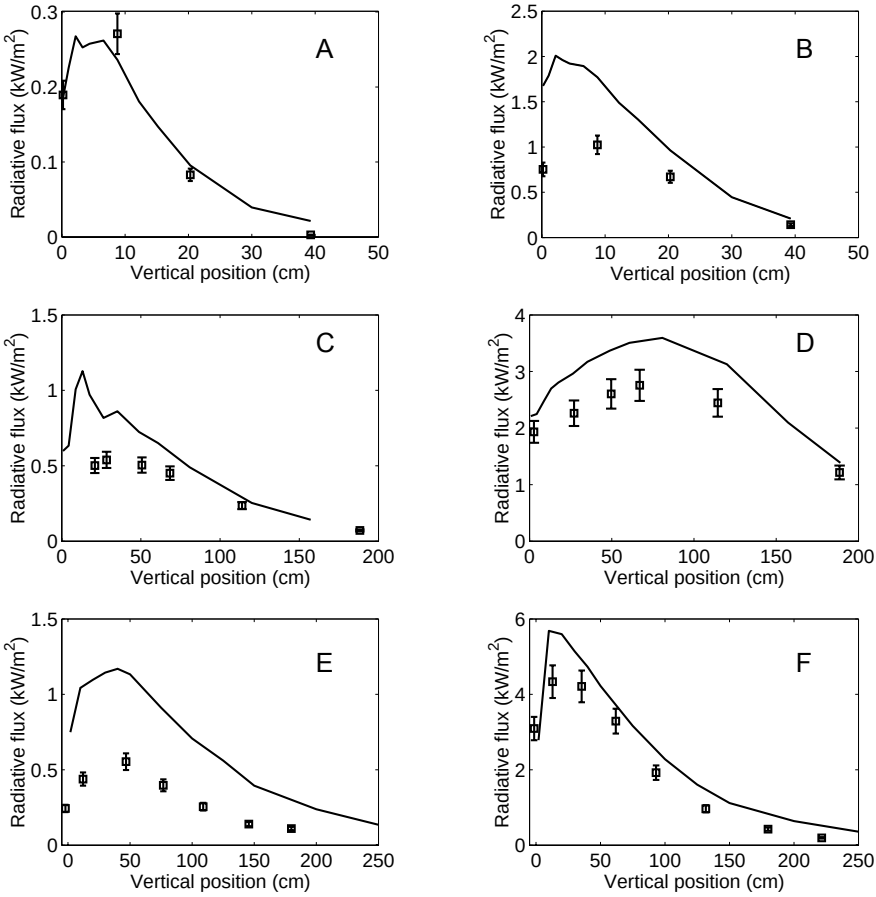


Fig. 3. - Comparison of the measured (squares) and predicted (lines) vertical heat flux distributions outside the methane flames.

Simulations of the methanol pool fires were carried out for four pool diameters: 1.0 cm, 10 cm, 30 cm and 100 cm. The computational grid was $50 \times 50 \times 100$ in all cases. 100 control angles and 6 bands were used for the radiation. A zero soot conversion factor was assumed. The burning rate of the pool was predicted using the pyrolysis model. Fig. 4 shows the instantaneous simulated flame shapes for the four cases. The amount of turbulence increases with diameter. The 1.0 cm flame is laminar and symmetric, but the 10 cm flame already contains asymmetric shapes due to the weak turbulence. The 30 cm and 100 cm flames have a substantial amount of fine structure. The measured burning rates and the corresponding predicted burning rates are given in Table 4. Table 4 also show the average values of the predicted radiative and convective heat fluxes on the pool surface. The convective heat transfer dominates at small diameters and radiation becomes more important at large diameters. The predicted burning rate of the smallest pool is lower than the experimental value and the other three predictions are 37 % to 100 % higher than measured. These errors are larger than the experimental uncertainty and, therefore, significant. The same conclusion can be done, if we compare with the regression rate data presented, for example in [14]. However, it should be recalled that

no account of convection in the liquid pool has been taken, plus the convective heat transfer from the gas to the pool surface is not well resolved.

Fig. 5 shows a comparison of the measured (circles) and predicted (solid line) radial profiles of the mean temperatures above the 30 cm methanol pool. The effect of the burning rate on the temperatures was studied by repeating the simulation at a fixed burning rate, 14 g/m$^2$/s. The corresponding calculated temperature profiles are shown with dashed lines. The comparisons are shown at three heights above the pool: 3.0 cm, 30 cm and 60 cm. Close to the pool surface, at a height of 3.0 cm, the location of the predicted flame structure is too close to the pool edge. At the predicted burning rate, the temperatures near the center of the pool are much lower than the measured and fixed burning rate predictions. Higher above the pool surface, the calculated high burning rate is linked to the calculated temperatures, which are too high. It seems that the high temperatures in and above the flame zone are not the reason for the high burning rates, but a consequence. Possible sources of error are the lack of the liquid phase convection and the fact, that simple empirical correlations of convective heat transfer are being used to calculate the heat fluxes due to the flames touching down into the first grid cell above the liquid surface. Very high, moving spots of convective heat transfer were found to traverse the pool surface. This is also observed experimentally and remains a significant modeling challenge.

Table 4. - Summary of the methanol pool fire burning rates and predicted average heat fluxes to the pool surface.

| Pool diameter (cm) | Measured burning rate (g/m$^2$/s) | Predicted burning rate (g/m$^2$/s) | Predicted heat fluxes (kW/m$^2$) | |
|---|---|---|---|---|
| | | | radiative | convective |
| 1.0 | 59 (Corlett and Fu [15]) | 32 | 5.7 | 175.5 |
| 10 | 16 | 22 | 18.7 | 27.3 |
| 30 | 13 | 28 | 35.4 | 25.9 |
| 100 | 15 | 33 | 56.1 | 25.7 |

The prediction of the liquid pool burning rate, starting from first principles, is an extremely challenging task. Individual numerical and physical errors are difficult to separate due to the strong coupling between the pool burning rate, gas phase heat release, gas temperatures and gas to solid heat transfer. Further validation should be carried out by trying to separate the different sources of errors. In addition, the entrainment rate of fresh air has a strong effect on the flame shape and temperatures. Comparison with experimentally measured velocities is therefore needed.

## CONCLUSIONS

Large eddy simulations of turbulent diffusion flames have been carried out with several fire sizes and boundary conditions. Transport of thermal radiation was solved using the Finite Volume Method for radiation, combined with a simple wide band model for the spectral dependence of the absorption coefficient. The applications included the prediction of the radiative heat flux distributions outside the methane/natural gas flames, and the prediction of the methanol pool burning rates and flame temperatures. The model is capable of capturing the dynamical differences of flames ranging from the small burner to the scale close to the compartment fires.

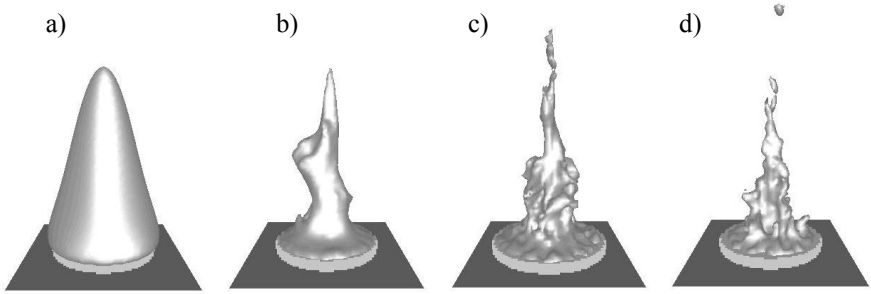


Fig. 4. - Instantaneous flame shapes of the simulated methanol pool fires.
The diameters of the pools are a) 1.0 cm, b) 10 cm, c) 30 cm and d) 100 cm.

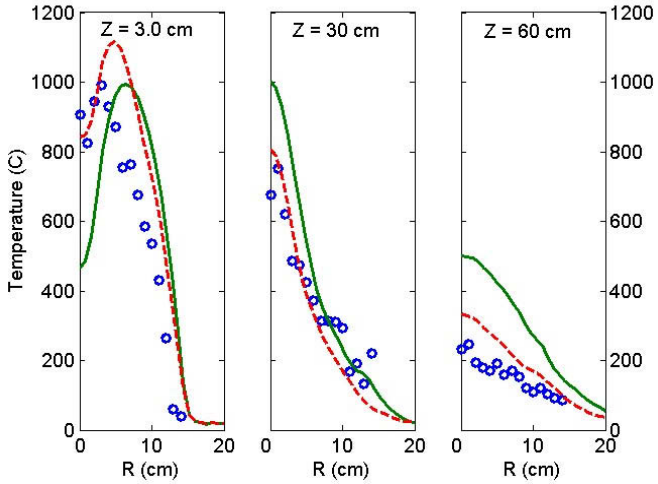


Fig. 5. - Comparison of the measured (circles) and predicted temperatures in the 30 cm methanol pool flame. The simulated temperatures are shown for both the predicted (solid lines) and the prescribed (dashed lines) burning rates.

Based on the shown applications we can conclude, that the current model is able to provide correct qualitative dependence between the pool size and burning rate, but more work is needed to improve the quantitative accuracy. The predicted radiative fractions of the methane/natural gas flames were shown to be systematically on the high side, probably due to the high temperatures close to the burner surface. However, the most accurate predictions of the heat flux distributions were found, where the heat fluxes were highest. This makes the model relevant for the fire safety engineering purposes. However, the physical resolution in the current applications was much better than what one can afford in the typical compartment fire simulations. The robustness of the current models must therefore be studied to ensure the predictive capability of the model in the compartment fires.

More detailed comparisons with measurements are needed to separate the individual sources of errors. The methods of calculating the band mean absorption coefficients should be studied more carefully. Also, the performance of the current combustion model is a subject of critical examination.

**ACKNOWLEDGEMENTS**

The authors would like to thank Dr. Howard Baum of NIST for his guidance and Dr. Jason Floyd of NIST for his contribution to the model development.

**REFERENCES**

1. McGrattan, K.B., Baum, H.R., and Rehm, R.G. "Large Eddy Simulations of Smoke Movement," *Fire Safety Journal*, 30:161–178, 1998.
2. Rehm, R.G. and Baum, H.R. "The Equations of Motion for Thermally Driven, Buoyant Flows," *Journal of Research of the NBS*, 83:297–308, 1978.
3. McGrattan, K.B., Baum, H.R., Rehm, R.G., Hamins, A., Forney, G.P., Floyd, J.E. and Hostikka, S.. "Fire Dynamics Simulator (Version 2) – Technical Reference Guide," National Institute of Standards and Technology Report NISTIR 6783, 2001.
4. Huggett, C. "Estimation of the Rate of Heat Release by Means of Oxygen Consumption Measurements," *Fire and Materials*, 4:61–65, 1980.
5. Floyd, J.E., Baum, H.R., and McGrattan, K.B. "A Mixture Fraction Combustion Model for Fire Simulation Using CFD," Proceedings of the International Conference on Engineered Fire Protection Design, Society of Fire Protection Engineers, 2001, 279-290.
6. Siegel, R. and Howell, J.R. *Thermal Radiation Heat Transfer,* Hemisphere Publishing Corp., Philadelphia, 3rd edition, 1992.
7. Grosshandler, W.L. "RADCAL: A Narrow-Band Model for Radiation Calculations in a Combustion Environment," National Institute of Standards and Technology. NIST Technical Note 1402, 1993.
8. Raithby, G.D. and Chui, E.H. "A Finite-Volume Method for Predicting Radiant Heat Transfer in Enclosures with Participating Media," *Journal of Heat Transfer*, 112(2):415–423, 1990.
9. Kim, S.H. and Huh, K.Y. "Assessment of The Finite-Volume Method and The Discrete Ordinate Method for Radiative Heat Transfer In a Three-Dimensional Rectangular Enclosure," *Numerical Heat Transfer, Part* B, 35:85–112, 1999.
10. International Organization of Standardization, *Guide to the Expression of Uncertainty in Measurement*, Geneve, Switzerland, 1993.
11. Hamins, A., Konishi, K., Borthwick, P. and Kashiwagi, T. "Global Properties of Gaseous Pool Fires", Proceedings of the Twenty-Sixth Sym. on Combust., 1996, 1429-1436.
12. Hamins, A., Klassen, M., Gore, J., and Kashiwagi, T. "Estimate of Flame Radiance via a Single Location Measurement in Liquid Pool Fires," *Combustion and Flame*, 86:223-228, 1991.
13. Pitts, W.M., Lawson, J.R., and Shields, J.R.. Report of Test FR 4014, "NIST/BFRL Calibration System for Heat-Flux Gages", August 6, 2001.
14. Drysdale, D., *An Introduction to Fire Dynamics* (2nd ed), John Wiley and Sons, Chichester, 1999, p. 163.
15. Corlett, R.C. and Fu, T.M., "Some Recent Experiments with Pool Fires," *Pyrodynamics,* 4:253-269, 1966.

PAPER V

# Numerical modeling of radiative heat transfer in water sprays

In: Fire Safety Journal 2006. Vol. 41, No. 1, pp. 76–86.

Available online at www.sciencedirect.com
SCIENCE DIRECT®
Fire Safety Journal 41 (2006) 76–86
FIRE SAFETY JOURNAL
www.elsevier.com/locate/firesaf

# Numerical modeling of radiative heat transfer in water sprays

Simo Hostikka[a,*], Kevin McGrattan[b]

[a]VTT Building and Transport, Technical Research Centre of Finland, FI-02044 VTT, Finland
[b]Building and Fire Research Laboratory, National Institute of Standards and Technology, Gaithersburg, MD 20899, USA

Received 28 February 2005; received in revised form 10 August 2005; accepted 1 September 2005
Available online 21 November 2005

**Abstract**

A numerical method is developed for the transport of polychromatic radiation in polydisperse sprays. The method is implemented within a wide-band radiation solver using the Finite Volume Method. Mie theory is used to compute the absorption and scattering characteristics of the water droplets. The solver is designed to be computationally effective because the simulations of fire scenarios are inherently time-dependent and the radiative transport equation must be solved many times. The model is compared with two sets of experimental data, and a discussion of the results is presented.


*Keywords:* Water sprays; Radiation model; Scattering calculation; Lagrangian droplets

## 1. Introduction

Thermal radiation plays a very important role in the development of fires by preheating combustible materials ahead of the flame front. This preheating increases the rate of flame spread, often causing ignition of surfaces without direct flame impingement. Water-based fire suppression systems, like sprinklers and water mist, can reduce the rate of fire spread by blocking thermal radiation. Also, fire fighters use water spray to protect themselves from thermal radiation during assaults on burning buildings.

Water droplets attenuate radiation by absorption and scattering. The relative importance of these mechanisms depends on the droplet size and the wavelength of the radiation. For the fire protection performance of the spray, the geometrical dimensions and water density of the spray are also important. To simulate the radiation transfer in water sprays, one needs to calculate both the transport of energy and the optical properties of the spray. The simplest technique to calculate the transport of energy is to use Lambert–Beer law which assumes that the droplets are totally absorbing or the scattering can be excluded. Ravigururajan and Beltran [1] used Lambert–Beer law for the transport and simple correlations for the optical properties of the droplets to find the optimum droplet size for the attenuation of fire radiation. Since the assumption of pure absorption is not valid in most practical problems, more advanced schemes such as two-flux model [3–6], six-flux model [7] and discrete ordinates method (DOM) or finite volume method (FVM) [8–13] have been developed. Mie theory is typically used for the calculation of the optical properties [2]. It is generally valid for spherical and isolated droplets. An early investigation of the efficiency of large water droplets in the protection from heat radiation was given by Thomas [3]. He derived the expressions for the radiation transmissivity through the droplet cloud using a two-flux model and the geometric optics. Coppalle et al. [4] used a two-flux model and simple approximations of the droplet optical properties allowing for a fast computation of the radiation flux through a layer of water mist. Log [5] used the method of Coppalle et al. to calculate the attenuation of radiation in polydisperse water sprays by assuming that the attenuation effects of the droplet size groups are additive by nature. Yang et al. [6] used Mie theory for the calculation of the absorption and scattering coefficients and scattering phase functions of the water droplets. The spectrally resolved optical properties of water droplets were incorporated into the two-flux model. The model was used to predict the radiation penetration of a monodisperse water mist at different wavelengths.

*Corresponding author. Tel.: +358 20 722 4839; fax: +358 20 722 4815.

0379-7112/$ - see front matter © 2005 Elsevier Ltd. All rights reserved.
doi:10.1016/j.firesaf.2005.09.003

**Nomenclature**

| | |
|---|---|
| $d$ | droplet diameter, m |
| $f$ | normalized droplet number density function |
| $I$ | total intensity, $\mathrm{Wm^{-2}\,sr^{-1}}$ |
| $I_\lambda$ | monocromatic intensity, $\mathrm{Wm^{-3}\,sr^{-1}}$ |
| $r$ | droplet radius, m |
| $\mathbf{s}$ | direction vector |
| $\mathbf{x}$ | position vector |
| $U$ | combined total intensity, $\mathrm{Wm^{-2}}$ |

*Greek symbols*

| | |
|---|---|
| $\Omega$ | solid angle, sr |
| $\Phi$ | scattering phase function |
| $\chi_f$ | fraction of forward scattering |
| $\phi$ | azimuthal angle |
| $\lambda$ | wavelength, m |
| $\kappa$ | absorption coefficient, $\mathrm{m^{-1}}$ |
| $\sigma$ | scattering coefficient, $\mathrm{m^{-1}}$ |
| $\theta$ | polar angle |

*Subscripts*

| | |
|---|---|
| $b$ | blackbody |
| $m$ | mean |
| $n$ | band-specific |

Keramida et al. [7] used a six-flux model to predict the attenuation in polydisperse water mist. Contributions of different droplet sizes were taken into account by summing the coefficients of a monodisperse spray over the local droplet size distribution. Berour et al. [8] used Mie theory and DOM to investigate the performance of water curtains in fire protection. By stationary simulations of both mono- and polydisperse water sprays in two-dimensional geometry, they studied the effects of droplet size and water curtain thickness on the transmittance and energy balance of the water curtain. Jinbo et al. [9] studied the effect of isotropic scattering approximation on the radiative heat fluxes and temperatures in stationary two-dimensional rectangular media. By comparing the FVM results against benchmark solutions, they concluded that the anisotropic scattering has stronger effect on the relative error of heat flux than the temperature profiles inside the media. Trivic et al. [10] coupled the Mie theory with FVM and studied the radiative transport in monodisperse particle clouds in two dimensions. Similar coupling was made for DOM by Colling et al. [11]. They divided the radiation spectrum to 43–367 bands and solved the RTE for each band in a two-dimensional domain to investigate the performance of water curtains. The use of gray assumption for radiation in monodisperse particle clouds was studied by Consalvi et al. [12]. They also coupled the Mie theory with FVM, and found that the gray model provided correct results for an optical thickness less than 2. The reduction of false scattering was studied in one-dimensional, anisotropically scattering media by Liu et al. [13]. The false scattering appears in the numerical approximation of the in-scattering integral in DOM and FVM methods.

All of the above models have features that limit their applicability on practical fire simulations. Although the one and two-dimensional geometries provide good environment for generation of general rules, like those for water curtains, the practical fire scenarios are always three-dimensional. The same applies for stationary models; the simulations of fire scenarios are inherently time-dependent, and the radiation transport equation must be solved thousands of times for a given scenario. In addition, the coupling of the Mie theory and radiation transport scheme should simultaneously consider the whole spectrum of thermal radiation and distribution of different droplet sizes. The real challenge of the fire model development is to consider these requirements while retaining the computational efficiency. Since radiation typically accounts for about one-third of the energy transport in fires, convection making up the rest, it is logical to require that the computational cost of the radiation solution should not exceed roughly one-third of the overall cost of the calculation.

In this work, a wide-band radiation solver using FVM is implemented within a large eddy simulation fire model. Mie theory is used to compute the radiative properties of the water droplets. The radiative properties of the spray are then computed by averaging the properties of individual droplets over the spectrum and the droplet size distribution. For the fast computation, the spray radiative properties are pre-computed and tabulated as functions of the mean droplet diameter. A simple approximation of the scattering integral is developed to account for the anisotropic scattering.

## 2. Model description

### 2.1. Large eddy simulation fire model

The radiation solver and the droplet algorithms described in this paper have been incorporated into fire dynamics simulator (FDS), a computational fluid dynamics (CFD) model of fire-driven fluid flow. The software is developed at the National Institute of Standards and Technology in co-operation with VTT (Finland). The model solves numerically a form of the Navier–Stokes equations appropriate for low-speed, thermally-driven flow with an emphasis on smoke and heat transport from fires. FDS uses a large eddy simulation (LES) model for turbulence. Unlike most Reynolds-averaged Navier stokes

(RANS) solvers, the LES model solves the time scales of the turbulent eddies and therefore requires the small time steps bound by the CFL (Courant, Freidrichs, Lewy) condition. A full description of the model is given in Ref. [14].

### 2.2. Water droplets

The water spray is modelled as a Eulerian–Lagrangian system, where the gas phase is solved using a Eulerian method and the liquid phase is tracked as numerous Lagrangian particles with mass, momentum and temperature. The Eulerian–Lagrangian approach is currently used in most multidimensional spray simulations because it is simple to implement and computationally efficient [15]. Each droplet, or "parcel", represents a large number of actual droplets. For the statistical representation of the spray, the properties of the parcels are randomly chosen from the given droplet size and velocity distributions. The initial droplet size distribution is expressed in terms of its cumulative volume fraction (CVF), a function that relates the fraction of the water volume (mass) transported by droplets less than a given diameter. The CVF is here represented by a combination of log-normal and Rosin–Rammler distributions [16]

$$F(d)=\begin{cases}\dfrac{1}{\sqrt{2\pi}}\displaystyle\int_0^d \frac{1}{\sigma\, d'}\, \mathrm{e}^{-\frac{[\ln(d'/d_\mathrm{m})]^2}{2\sigma^2}}\, dd' & (d\leqslant d_\mathrm{m}),\\ 1-\mathrm{e}^{-0.693\left(\frac{d}{d_\mathrm{m}}\right)^\gamma} & (d_\mathrm{m}<d),\end{cases} \tag{1}$$

where $d_\mathrm{m}$ is the median droplet diameter, and $\gamma$ and $\sigma$ are empirical constants equal to about 2.4 and 0.6, respectively. A stratified sampling technique is used for the sampling of the droplets to avoid tracking too many of the numerous tiny droplets and too few of the less numerous larger droplets. In this technique, the range of droplet diameters is divided into a discrete number of intervals. The number of samples from each interval is the same, but the droplets are given weights based on the total volume of the interval. In this work, five intervals are used.

### 2.3. Wide band model for radiation

The attenuation of radiation is a well-known feature of water (and other) sprays. The attenuation is caused by absorption by the droplets and scattering. The radiation-droplet interaction must therefore be solved for both the accurate prediction of the radiation field and the droplet energy balance. The radiative transport equation (RTE) for spectral intensity $I_\lambda$ passing through an absorbing/emitting and scattering medium is

$$\mathbf{s}\cdot\nabla I_\lambda(\mathbf{x},\mathbf{s}) = -[\kappa_\lambda(\mathbf{x})+\sigma_\lambda(\mathbf{x})]I_\lambda(\mathbf{x},\mathbf{s})+\kappa_\lambda(\mathbf{x})I_b(\mathbf{x},\lambda) + \frac{\sigma_\lambda(\mathbf{x})}{4\pi}\int_{4\pi}\Phi(\mathbf{s},\mathbf{s}')I_\lambda(\mathbf{x},\mathbf{s}')\,\mathrm{d}\Omega', \tag{2}$$

where $I_\mathrm{b}$ is the blackbody source function and $\Phi(\mathbf{s},\mathbf{s}')$ is the scattering phase function giving the scattered intensity from direction $\mathbf{s}'$ to $\mathbf{s}$. Although the emission of water droplets is usually much smaller than the absorption, it is included in the model for consistency and energy conservation. The gas phase absorption and emission are here neglected for simplicity but included in the computations. The computation of the gas phase radiative properties is explained in Ref. [17].

In practical simulations the spectral dependence cannot be solved accurately. Instead, the radiation spectrum is divided into a relatively small number of bands, and a separate RTE is derived for each band by integrating Eq. (2) over the band. The band specific RTEs are

$$\mathbf{s}\cdot\nabla I_n(\mathbf{x},\mathbf{s}) = -[\kappa_n(\mathbf{x})+\sigma_n(\mathbf{x})]I_n(\mathbf{x},\mathbf{s})+\kappa_n(\mathbf{x})I_{\mathrm{b},n}(\mathbf{x}) + \frac{\sigma_n(\mathbf{x})}{4\pi}\int_{4\pi}\Phi(\mathbf{s},\mathbf{s}')I_n(\mathbf{x},\mathbf{s}')\,\mathrm{d}\Omega', \tag{3}$$

where $\kappa_n$ is the mean absorption coefficient inside the band. The source term can be written as a fraction of the blackbody radiation

$$I_{\mathrm{b},n}=F_n(\lambda_\mathrm{min},\lambda_\mathrm{max})\sigma T_i^4/\pi, \tag{4}$$

where $\sigma$ is the Stefan–Boltzmann constant and $\lambda_\mathrm{min}$ and $\lambda_\mathrm{max}$ are the limits of the $n$'th band. The calculation of factors $F_n$ is explained in Ref. [2]. When the integrated intensities corresponding to the bands are known, the total intensity and combined total intensity are calculated by summing over all the bands

$$I(\mathbf{x},\mathbf{s})=\sum_{n=1}^{N_\mathrm{b}} I_n(\mathbf{x},\mathbf{s}), \tag{5}$$

$$U(\mathbf{x})=\sum_{n=1}^{N_\mathrm{b}} U_n(\mathbf{x})=\sum_{n=1}^{N_\mathrm{b}}\int_{4\pi} I_n(\mathbf{x},\mathbf{s})\,\mathrm{d}\Omega. \tag{6}$$

To include the most important absorption bands of water and $CO_2$, the most important gaseous species in fire simulations, six radiation bands are used. The limits of the bands are shown in Table 1. Even with a reasonably small number of bands, the solution of $N_\mathrm{b}$ RTEs is very time consuming. Fortunately, in most large-scale fire scenarios soot is the most important combustion product controlling the thermal radiation from the fire and hot smoke. As the radiation spectrum of soot is continuous, a gray gas behaviour can be assumed ($N_\mathrm{b}=1$).

### 2.4. Averaging over the droplet size distribution

The local absorption and scattering coefficients are functions of the local droplet size distribution:

$$\kappa_\lambda(\mathbf{x})=\int_0^\infty N(r,\mathbf{x})\,C_\mathrm{a}(r,\lambda)\,\mathrm{d}r,$$
$$\sigma_\lambda(\mathbf{x})=\int_0^\infty N(r,\mathbf{x})\,C_\mathrm{s}(r,\lambda)\,\mathrm{d}r, \tag{7}$$

where $N(r,\mathbf{x})$ is the number of droplets having radius between $r$ and $r+\delta r$ at position $\mathbf{x}$. The absorption and scattering cross sections, $C_\mathrm{a}$ and $C_\mathrm{s}$, are calculated using Mie theory. In practical simulations, it is impossible to perform these integrations at each position at every time

Table 1
Limits of the spectral bands for a 6-band model.

| Band | 1 | 2 | 3 | 4 | 5 | 6 |
|---|---|---|---|---|---|---|
| Major Species | Soot | $CO_2$ $H_2O$, Soot | Soot | $CO_2$ Soot | $H_2O$, Soot | Soot |
| $\nu$ (1/cm) | 10000 | 3800 | 3400 | 2400 | 2174 | 1000 | 50 |
| $\lambda$ ($\mu$m) | 1.00 | 2.63 | 2.94 | 4.17 | 4.70 | 10.0 | 200 |

step. Instead, we assume that the local droplet number density function has the same functional form regardless of position, with only the mean diameter varying from point to point. The local size distribution can now be expressed by

$$N(r,\mathbf{x}) = N'(\mathbf{x}) f(r, d_m(\mathbf{x})) \tag{8}$$

and the local absorption and scattering coefficients can be determined by averaging over the initial droplet size distribution function

$$\kappa_\lambda(\mathbf{x}) = N'(\mathbf{x}) \int_0^\infty f(r, d_m(\mathbf{x}))\, C_a(r,\lambda)\, dr,$$
$$\sigma_\lambda(\mathbf{x}) = N'(\mathbf{x}) \int_0^\infty f(r, d_m(\mathbf{x}))\, C_s(r,\lambda)\, dr. \tag{9}$$

For the numerical implementation, it is useful to write the above equation in the form

$$\kappa_\lambda(\mathbf{x}) = A_d(\mathbf{x}) \int_0^\infty \frac{f(r, d_m(\mathbf{x}))\, C_a(r,\lambda)}{\pi (d_m(\mathbf{x})/2)^2}\, dr,$$
$$\sigma_\lambda(\mathbf{x}) = A_d(\mathbf{x}) \int_0^\infty \frac{f(r, d_m(\mathbf{x}))\, C_s(r,\lambda)}{\pi (d_m(\mathbf{x})/2)^2}\, dr, \tag{10}$$

where $A_d$ is the total cross sectional area of the droplets per unit volume. We approximate $A_d(\mathbf{x}) \approx \rho_d(\mathbf{x}) / [2\rho_w d_m(\mathbf{x})/3]$, where $\rho_w$ is the density of water and $\rho_d(\mathbf{x})$ is the water mass per unit volume, which is provided by the droplet tracking algorithm. The integrals of Eq. (10) can be calculated in advance and stored in tables for different values of $d_m$.

The absorption and scattering cross sections and the scattering phase function are calculated using the "MieV" algorithm developed by Wiscombe [18]. The optical properties of water are taken from Ref. [19]. Mie theory is generally valid for homogenous isotropic spherical objects embedded in a homogenous, isotropic, dielectric and infinite medium. As the current work considers relatively low speed droplets in air, most of the above assumptions are valid. The interference between the droplets can be neglected when the center to center spacing is more than about 3 diameters. In terms of mean diameter and average spacing the interference condition is

$$d_m(\mathbf{x}) \sqrt[3]{N'(\mathbf{x})} < \frac{1}{3}. \tag{11}$$

### 2.5. Approximation of the scattering integral

An accurate computation of the in-scattering integral on the right-hand side of Eq. (2) would be extremely time consuming. It is here approximated by dividing the total $4\pi$ solid angle into a "forward angle" $\delta\Omega^l$ and the corresponding "ambient angle" $\delta\Omega^* = 4\pi - \delta\Omega^l$. For compatibility with the FVM solver, the forward angle is set equal to the control angle resulting from the angular discretization. However, the forward angle is assumed to be symmetric about the center of the corresponding control angle. Within the forward angle $\delta\Omega^l$, the intensity is $I_\lambda(\mathbf{x},\mathbf{s})$. Within the ambient angle, it is approximated as

$$U^*_\lambda(\mathbf{x}) = \frac{U_\lambda(\mathbf{x}) - \delta\Omega^l I_\lambda(\mathbf{x},\mathbf{s})}{\delta\Omega^*} \tag{12}$$

where $U_\lambda(\mathbf{x})$ is the combined spectral intensity at wavelength $\lambda$. The in-scattering integral can now be approximated as

$$\frac{\sigma_\lambda(\mathbf{x})}{4\pi} \int_{4\pi} \Phi(\mathbf{s},\mathbf{s}') I_\lambda(\mathbf{x},\mathbf{s}')\, d\Omega' = \sigma_\lambda(\mathbf{x})[\chi_f I_\lambda(\mathbf{x},\mathbf{s}) + (1-\chi_f) U^*_\lambda(\mathbf{x})], \tag{13}$$

where $\chi_f = \chi_f(r,\lambda)$ is a fraction of incoming intensity originally within solid angle $\delta\Omega^l$ that is scattered into the same angle $\delta\Omega^l$. An effective scattering coefficient is now defined as

$$\bar\sigma_\lambda(\mathbf{x}) = \frac{4\pi A_d(\mathbf{x})}{4\pi - \delta\Omega^l} \int_0^\infty f(r, d_m(\mathbf{x}))\left[1 - \chi_f(r,\lambda)\right] \frac{C_s(r,\lambda)}{\pi d_m(\mathbf{x})^2/4}\, dr. \tag{14}$$

By using the above definition of $\bar\sigma_\lambda(\mathbf{x})$ and integrating the RTE over the spectrum we get a band-specific RTE

$$\mathbf{s}\cdot\nabla I_n(\mathbf{x},\mathbf{s}) = -[\kappa_n(\mathbf{x}) + \bar\sigma_n(\mathbf{x})] I_n(\mathbf{x},\mathbf{s}) + \kappa_n(\mathbf{x}) I_{b,n}(\mathbf{x}) + \frac{\bar\sigma_n(\mathbf{x})}{4\pi} U_n(\mathbf{x}), \tag{15}$$

where the source function is based on the average droplet temperature within a cell.

During the simulation, the local values of $\kappa_n$ and $\bar\sigma_n$ are interpolated from one-dimensional tables using $d_m(\mathbf{x})$. A Planck spectrum, used in the wavelength averaging, is calculated using some appropriate value for temperature. This "radiation temperature" $T_{rad}$ should be selected to represent the temperature of a radiating flame.

A formula for $\chi_f$ was previously derived by Yang et al. [6].

$$\chi_f(r,\lambda) = \frac{1}{\delta\Omega^l} \int_0^{\mu_x} \int_0^{\mu_x} \int_{\mu_{d,0}}^{\mu_{d,\pi}} \times \frac{P_0(\theta_d)}{\left[(1-\mu^2)(1-\mu'^2) - (\mu_d - \mu\mu')^2\right]}\, d\mu_d d\mu d\mu', \tag{16}$$

where $\mu_d$ is a cosine of the scattering angle $\theta_d$ and $P_0(\theta_d)$ is a single droplet scattering phase function

$$P_0(\theta_d) = \frac{\lambda^2\left(|S_1(\theta_d)|^2 + |S_2(\theta_d)|^2\right)}{2C_s(r,\lambda)} \tag{17}$$

and $S_1(\theta_d)$ and $S_2(\theta_d)$ are the scattering amplitudes, given by Mie theory. When $\chi_f$ is integrated over the droplet size distribution in Eq. (14), it is multiplied by $C_s(r,\lambda)$. It is therefore $|S_1|^2 + |S_2|^2$, not $P_0(\theta_d)$, that is integrated. Some examples of phase function $P_0(\theta_d)$ are shown in Fig. 1, at different values of droplet size parameter $X \equiv 2\pi r/\lambda$. At small values of $X$ the phase function is almost constant over the scattering angle, and at high values the (large droplets, small wavelength) the energy is scattered close to the forward direction.

The integration limit $\mu_x$ is the cosine of the polar angle defining the boundary of the symmetric control angle $\delta\Omega^l$

$$\mu_x = \cos(\theta^l) = 1 - \frac{2}{N_\Omega}, \tag{18}$$

where $N_\Omega$ is the total number of control angles. The limits of the innermost integral are

$$\mu_{d,0} = \mu\mu' + \sqrt{1-\mu^2}\sqrt{1-\mu'^2},$$
$$\mu_{d,\pi} = \mu\mu' - \sqrt{1-\mu^2}\sqrt{1-\mu'^2}. \tag{19}$$

One weakness of the modeling approach is that a higher $N_\Omega$ does not always imply better accuracy, because less and less radiation is scattered into the forward control angle. That is, the direction information of the scattered energy at angles $\theta > \theta^l$ is lost, and the energy is divided evenly over the ambient angle $\delta\Omega^*$.

### 2.6. Numerical solution of RTE

The radiative transport (3) is solved using the finite volume method (FVM) for radiation [20]. The intensities on the cell boundaries are calculated using a first order upwind scheme. The solution method of the discretized RTE is based on an explicit marching sequence [21], where the physical space is swept in the propagation direction of the intensity and the intensities can be solved explicitly from an algebraic equation. Iterations are needed only to account for the reflective boundaries and scattering. However, this is seldom necessary in practice, because of the small time step needed by the fluid flow solver.

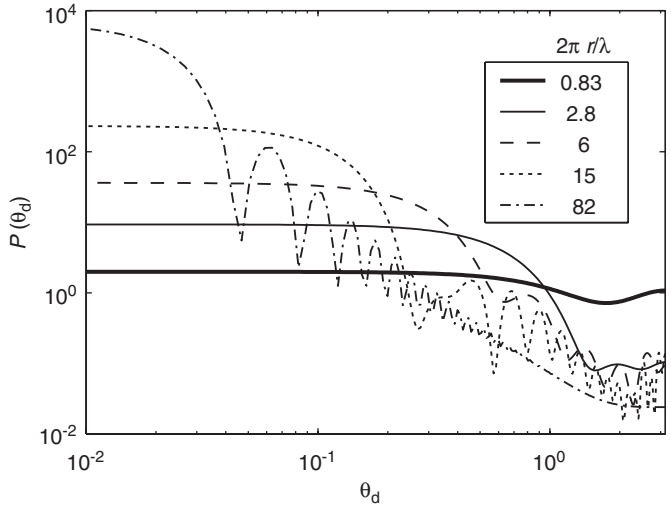


Fig. 1. Normalized unpolarized phase function of a single droplet.

The spatial discretization for the RTE solver is the same as for the fluid solver. The distribution of the angles is based on empirical rules that attempt to produce equal control angles $\delta\Omega^l = 4\pi/N_\Omega$, where $N_\Omega$ is the number given by the user. The polar angle, $\theta$, is first divided into $N_\theta$ bands, where $N_\theta$ is an even integer. Each $\theta$-band is then divided into $N_\phi(\theta)$ parts in the azimuthal ($\phi$) direction. $N_\phi(\theta)$ must be divisible by 4. The number of $\theta$-bands is

$$N_\theta = 1.17\ N_\Omega^{1/2.26} \tag{20}$$

rounded to the nearest even integer. The number of $\phi$-angles on each band is

$$N_\phi(\theta) = \max\{4, 0.5\,N_\Omega\,[\cos(\theta^-) - \cos(\theta^+)]\} \tag{21}$$

rounded to the nearest integer divisible by 4. $\theta^-$ and $\theta^+$ are the lower and upper bounds of the $\theta$-band, respectively. Finally, the exact $N_\Omega$ is calculated as

$$N_\Omega = \sum_{i=1}^{N_\theta} N_\phi(\theta_i). \tag{22}$$

The angular discretization is symmetric with respect to the planes $x = 0$, $y = 0$, and $z = 0$. This symmetry has three important benefits: first, it avoids the problems caused by the fact that a first order upwind scheme is more diffusive in non-axial directions. Second, the treatment of symmetric boundaries becomes very simple. Third, it avoids so-called "overhang" situations, where the sign of the intensity direction vector components is changed inside the control angle. These "overhangs" can make the system of linear equations more complicated.

Computational cost is always an issue in time-dependent simulations, especially in simulations that are bound by the CFL condition. To reduce the cost of the radiation solution, the radiation solver is typically not called at every time step of the hydrodynamic solver. For time steps where the radiation is not being updated, only the radiative loss term must be updated to maintain the time accuracy of the energy equation. More savings can be achieved by updating only a fraction of the control angles for a given call to the radiation solver. The effect of this kind of cost reduction is demonstrated in Fig. 2. The upper figure shows the time development of the combined total intensity $U$ inside a hydrocarbon pool flame in some arbitrary units. Fig. 2(b) shows similar results inside a water spray with external radiation source. Local gas temperature and droplet diameter are shown for reference. As can be seen, the cost reduction has a slight time-averaging effect. These cost–saving measures should not be applied when the exact

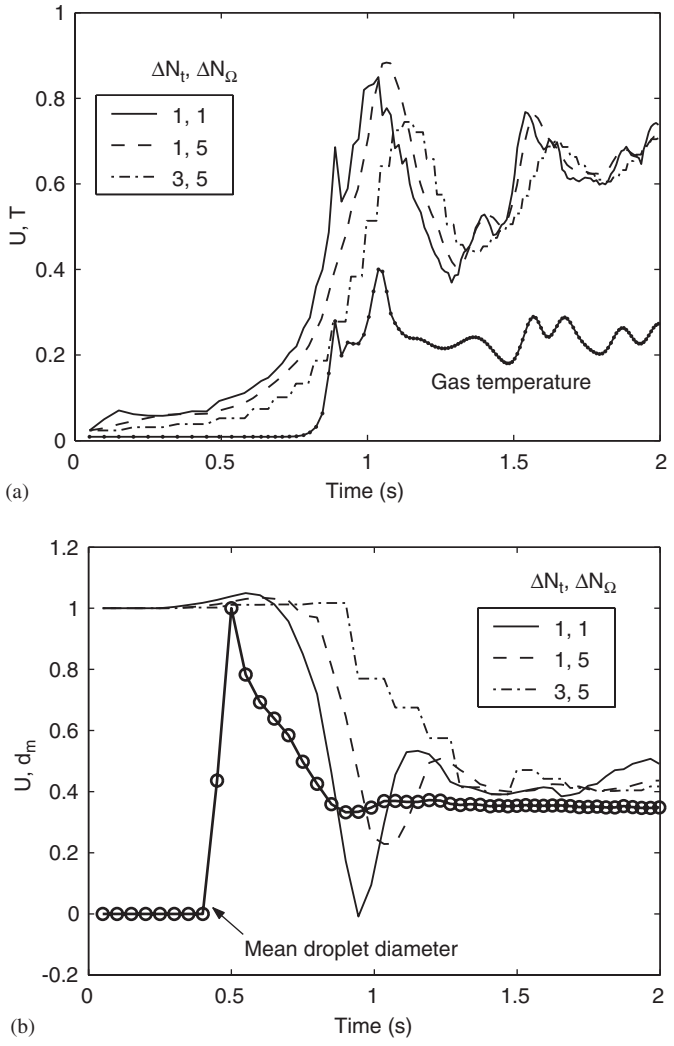


Fig. 2. The effect of the temporal and angular increments on the combined intensity in (a) pool flame and (b) water spray. The units are arbitrary. The radiation solver is called every $\Delta N_t$ time steps of the hydrodynamic solver and every $\Delta N_\Omega$ control angles are updated per call.

time dependence of the turbulence-radiation interaction is needed. Numerical experiments have shown that for practical fire simulations, calling the radiation every 3 time steps and updating 1 out of 5 control angles per call gives acceptable results.

## 3. Results and discussion

### 3.1. Large-scale experiment

The first validation test is the simulation of experiment conducted by Murrel et al. [22]. They measured the attenuation of thermal radiation passing through a water spray using a heat flux gauge. The schematics of the system are shown in Fig. 3. The radiation was produced by a heat panel, one meter square, at 900 °C. The horizontal distance from the radiation panel to the spray nozzle was 2 m and to the measurement point 4 m. The nozzles were positioned at a height 0.24 m above the panel upper edge. The heat flux gauge was positioned at the line passing through the center of the panel. The attenuation of radiation was defined as $(q_0 - q_s)/q_0$, where $q_0$ is the initial radiative heat flux, measured without a spray, and $q_s$ is the heat flux measured during the spray operation. The purpose of the simulation is to compare the measured and simulated attenuation of radiation at different flow conditions.

The computational domain was 4 m wide, 2 m deep and 3 m high. The vertical and top boundaries were open, and the bottom of the domain was a solid floor. The nozzle was positioned horizontally in the center of the domain at height 2.24 m. Three different nozzles were simulated. Each nozzle was a full-cone type industrial nozzle. The simulations were performed at eight different flow rates.

In the experiments, Murrel et al. [22] did not measure the mean droplet diameters in the vicinity of the nozzles, but 0.7 m below the nozzle, i.e. at the height of the heat flux measurement point. The droplet size boundary condition $d_m$ (BC) was therefore determined by iterating $d_m$ (BC) until the simulated and measured mean diameters at the measurement location were equal, with a few percent tolerance. The iteration was performed for all nozzle-flow rate combinations. The initial droplet size distribution was assumed to have the functional form of Eq. (1). The measured and corresponding BC mean diameters are listed in Table 2. For nozzle D, the measured mean droplet diameter increased with increasing pipe pressure $\Delta p$ between 1 and 3 bar, and then dropped sharply between 5 and 6 bar. The experimental results defy a commonly used scaling relation for water droplets, which states that $d_m \propto \Delta p^{-1/3}$ [23,24]. The measured mean diameters (shown in parentheses) were therefore replaced by values that follow the trend found for nozzles A and B. For the parameters $\gamma$ and $\sigma$ controlling the width of the droplet size distribution, the default values 2.43 and 0.6 were used. Numerical experiments showed that attenuation results are relatively insensitive to the small variations of $\gamma$ and $\sigma$. The droplet velocities on the inflow boundaries were set equal to the measured vertical velocity component 0.7 m below the nozzle. At the chosen flow rates, the interference

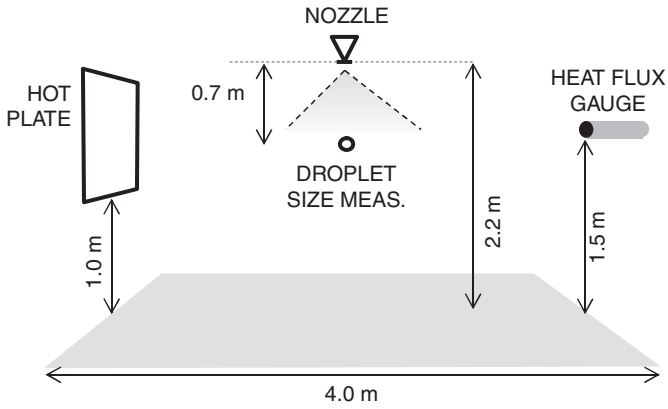


Fig. 3. Schematics of the experiment of Murrel et al. [22].

Table 2
Boundary conditions of the A, B and D nozzles

| | Nozzle A | | | Nozzle B | | | Nozzle D | | |
|---|---|---|---|---|---|---|---|---|---|
| $\Delta p$ (bar) | Flow (L/min) | $d_m$ (exp.) (μm) | $d_m$ (BC) (μm) | Flow (L/min) | $d_m$ (exp.) (μm) | $d_m$ (BC) (μm) | Flow (L/min) | $d_m$ (exp.) (μm) | $d_m$ (BC) (μm) |
| 1 | 0.350 | 268 | 353 | 1.40 | 392 | 552 | 2.60 | 691 | 768 |
| 2 | 0.550 | 175 | 190 | 1.83 | 266 | 398 | 3.75 | 327 (753) | 420 |
| 3 | 0.625 | 110 | 110 | 2.00 | 167 | 212 | 4.50 | 276 (794) | 377 |
| 4 | 0.700 | 104 | 104 | 2.25 | 162 | 209 | 5.00 | 235 (638) | 295 |
| 5 | 0.750 | 102 | 102 | 2.50 | 115 | 120 | 5.75 | 200 (550) | 236 |
| 6 | 0.875 | 102 | 102 | 2.75 | 126 | 140 | 6.00 | 182 | 225 |
| 7 | 0.950 | 93 | 93 | 3.00 | 156 | 212 | 6.75 | 178 | 219 |
| 8 | 1.00 | 126 | 126 | 3.25 | 148 | 186 | 7.50 | 160 | 185 |

Four of the nozzle D measurements (shown in parentheses) were assumed erroneous and replaced by values having the same trend as nozzles A and B.

condition (Eq. (11)) was satisfied in all parts of the computational domain.

The sensitivity to the numerical and other parameters was first studied. For angular discretization $N_\Omega = 1000$ was found to be high enough, as can be seen in Fig. 4(a). The figure shows the change of combined total intensity $U$ from its initial value $U_0$ on the line passing through the spray from the heat panel ($x = -2$ m) to the heat flux measurement point ($x = 2$ m). The spray nozzle D and pressure of 4 bar were used for the tests. On the left-hand side of the spray $U$ first increases due to the scattering from the spray. Strong attenuation is then seen at a distance of 0.4 m inside the spray. The results are independent of the size of the grid cells, as shown in Fig. 4(b), where the attenuation at the different flow rates of nozzle D is plotted for 10 and 5 cm grid cells. The same figure also shows that the use of multiple radiation bands and gas phase absorption do not change the attenuation results considerably. For the calculation of the final results, the following numerical parameters were used: 10 cm grid cells, 1000 control angles, only one spectral band (gray assumption) and no gas phase absorption. For each case, 15 s of real time was simulated and the attenuation results were time averaged over the last 10 s. The simulation of 15 s required about 160 s on a single 3.0 GHz processor of a personal computer. Without the cost-saving measures of the radiation solver, i.e. if all the radiation directions were solved at every time step, the required CPU time was about 1380 s.

The measured and predicted attenuation results for all three nozzles and flow rates are compared in Fig. 5. Since a good general agreement was found for all three nozzles, and the results of the individual nozzles are well distinct in the flow-rate vs. attenuation space, we can assume that the model can properly take into account both the effect of the water load and the effect of the droplet size distribution. Only the mid-range flow rates of nozzle B and the highest flow rates of nozzle D show sizable discrepancies. These discrepancies are probably caused by a combination of measurement errors and model inaccuracy. The droplet size measurements, in particular, are difficult to conduct in large scale sprays. Some uncertainty is also related to the simulation boundary conditions of the droplet size.

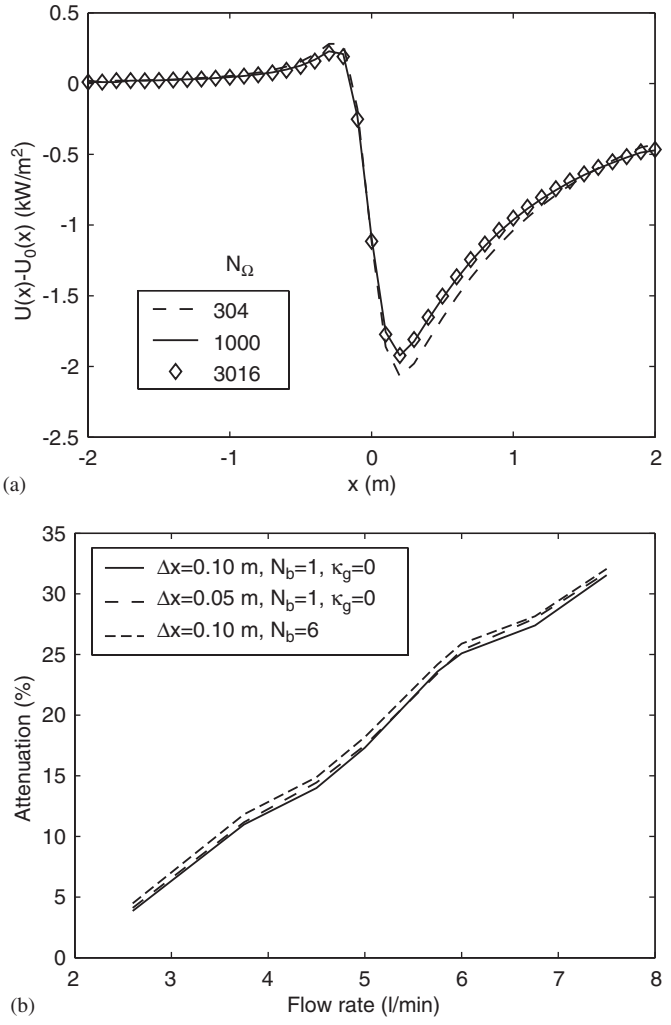


Fig. 4. (a) The effect of the angular discretization on change of combined intensity. (b) The effect of grid cell size, $N_\Omega$ and gas phase absorption on the attenuation at the measurement point.

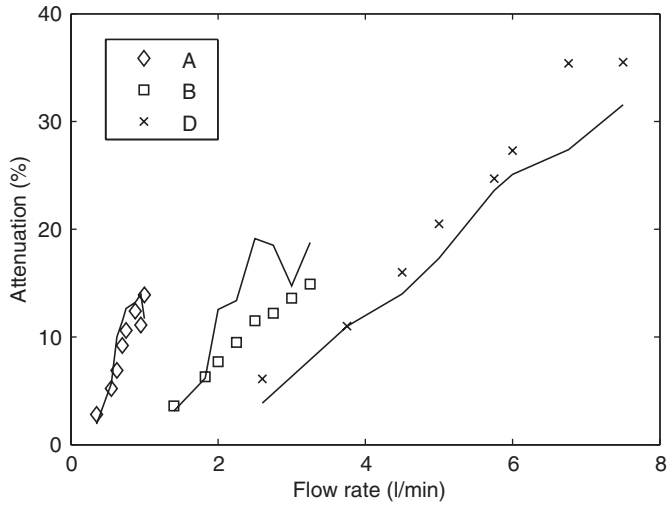


Fig. 5. Comparison of measured and predicted attenuation of thermal radiation at spray nozzles A, B and D, and different flow rates. Lines represent simulation results.

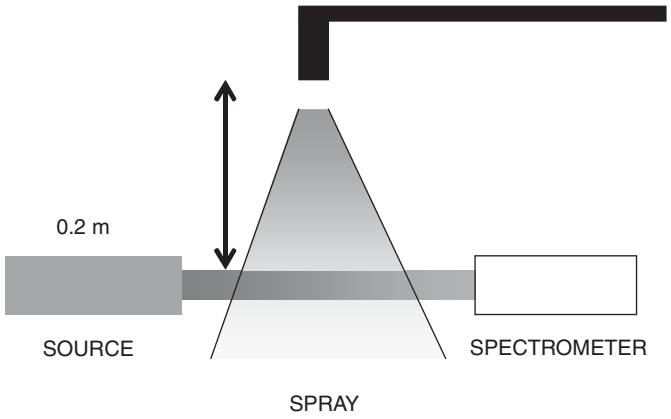


Fig. 6. Schematics of the experiment of Dembele et al. [25].

### 3.2. Small-scale experiment

In the second validation exercise, the experiments of Dembele et al. [25] were simulated. They measured the attenuation of a collimated radiation beam passing through a water spray using a Fourier infrared spectrometer. The radiation source was a tungsten filament inside a silica tube. Its emission spectrum was close to that of a blackbody at 1300 °C. The spray was produced with 1, 2 or 3 hydraulic nozzles arranged in a row, and the measurements were made 20 cm below the nozzles at different flow rates. The schematics of the scenario are shown in Fig. 6. Again, only total intensity data are compared and the spectral information available in the experiment is not used.

The simulations were performed at four different flow rates. The computational domain was a 40 cm cube with open, constant-pressure boundaries. The nozzles were placed 5 cm below the top of the computational domain, and the radiation source was located 20 cm below the nozzles. A numerical grid of $20 \times 20 \times 20$ cells was used for the flow solver and 1000 angles for FVM. Six radiation bands were used, but the gas phase absorption was neglected. At each flow rate, at least 15 s of constant flow was simulated to get a converged time-averaged value for the attenuation. The uncertainty of the time-averaging process is less than 10% for the attenuation results. A simulation of 15 s with 6 bands took about 320 s on a single 3.0 GHz CPU. With only one band, the computation time would drop down to 90 s.

Modeling a collimated radiation beam is difficult with the current implementation of FVM due to the symmetric discretization of the unit sphere into solid angles. To alleviate the problem, the radiation source in this exercise was modeled simply as a 4 cm by 4 cm rectangular surface, radiating in all directions. Because the air surrounding the water spray was cool, practically transparent to radiation, and did not contain any scattering particles, it did not contribute to the predicted intensity field behind the spray. Therefore, the comparison with the measurements is valid on the opposite side of the spray, but not in the other directions.

Dembele et al. measured the droplet size distribution 20 cm below the nozzle for each flow rate. The droplet size boundary conditions were determined using a procedure similar to the large scale scenario. Again, the droplet size distribution function Eq. (1) was assumed, with default values for the width parameters $\gamma$ and $\sigma$. The measured and corresponding mean diameter boundary conditions are given in Table 3. For this exercise, the velocity of the droplets at the inflow boundary was found from a simple geometrically-based relationship between the flow velocity and distance. The cone angle of the nozzle was measured from the illustrations of Ref. [25], and set to 130°.

An example of the time-averaged spray pattern at a flow rate of 0.22 L/min is shown in Fig. 7. The contours of the droplet mean diameter $d_m$ are shown in the vertical plane cutting through the nozzle. The initial conical shape of the spray is very soon squeezed to a vertical column by the entraining air. The core of the spray contains smaller droplets than the edge because the larger droplets have higher momentum and are not as easily entrained as the smaller droplets. This suggests that the droplet size measurement just below the nozzle does not necessarily represent the size distribution of the whole spray.

In the radiation model, we approximate the local droplet size distributions by the initial functional form. The validity of this approximation is demonstrated in Fig. 8. The droplet diameters were sampled from two locations of a simulated water spray. The number densities of the sampled distributions are shown as vertical bars. The mass-weighted mean diameters were calculated from the sampled distributions, and corresponding theoretical density functions (Eq. (1)) were drawn on the figure. As can be seen, the approximation holds well within the core of the spray, but fails near the edge of the spray. Fortunately, the core area

Table 3
Boundary conditions of the TG03 spray droplets

| Flow rate (L/min/nozzle) | $d_m$ (exp.) (μm) | $d_m$ (BC) (μm) | Velocity (BC) (m/s) |
|---|---|---|---|
| 0.14 | 187 | 264 | 0.33 |
| 0.22 | 135 | 187 | 0.51 |
| 0.28 | 115 | 155 | 0.65 |
| 0.33 | 104 | 140 | 0.75 |

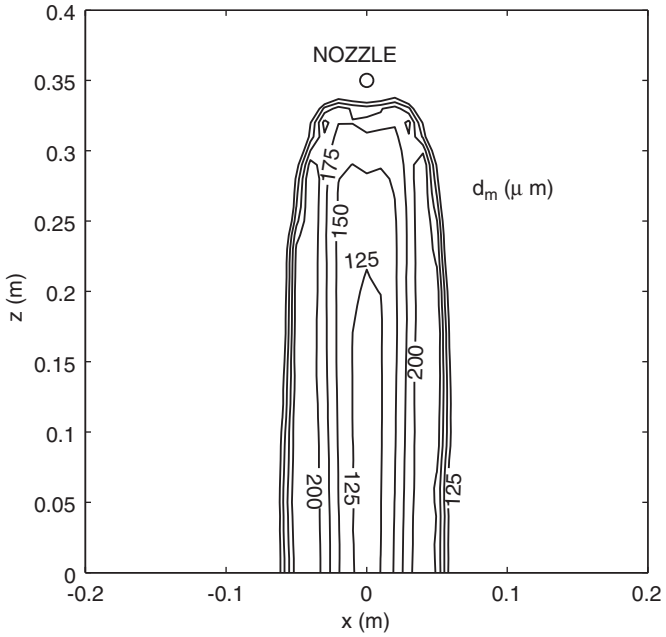


Fig. 7. Contours of the time averaged droplet mean diameter field at 0.22 L/min flow rate. The co-ordinates correspond to the computational domain used.

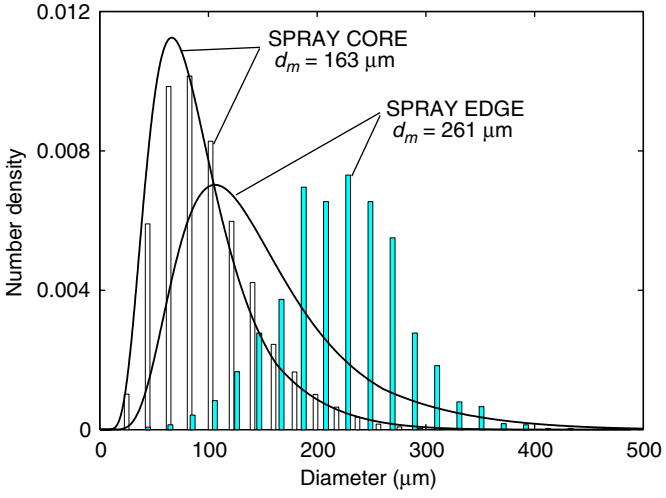


Fig. 8. Theoretical and sampled size distributions in the core and close to the edge of the spray. Lines are the assumed probability density functions and bars are the sample histograms from the simulation.

is much more important for the radiation attenuation because the number density is higher there than at the edge. The approximation may also fail if the spray penetrates a hot environment, because the evaporation rate depends on the droplet radius, and probably affects the shape of the size distribution.

In this scenario, the independence of the spatial and angular resolutions is very difficult to achieve. The effect of the spatial resolution was studied by reducing the cell size from 2.0 cm to 1.0 cm. As a result, the attenuation in the case of one nozzle at 0.14 L/min flow rate changed from 8.3% to 11.4%, with 10.0% being the experimental value. Unfortunately, the 1 cm grid cells could not be used for the all cases due to the strong increase of computational cost. The effect of angular resolution is studied in Fig. 9 by plotting the combined total intensity $U(\mathbf{x})$ at the horizontal line passing through the center of the radiation source at different values of $N_\Omega$. Fig. 9(a) shows that $U(\mathbf{x}) \approx 450\,\mathrm{kW/m^2}$ close to the source and $U(\mathbf{x}) \approx 10\,\mathrm{kW/m^2}$ in the spray region. For $N_\Omega \geqslant 1000$, the absolute value seems well converged but the change of the field from the initial state in Fig. 9(b) shows no convergence even at $N_\Omega = 3000$.

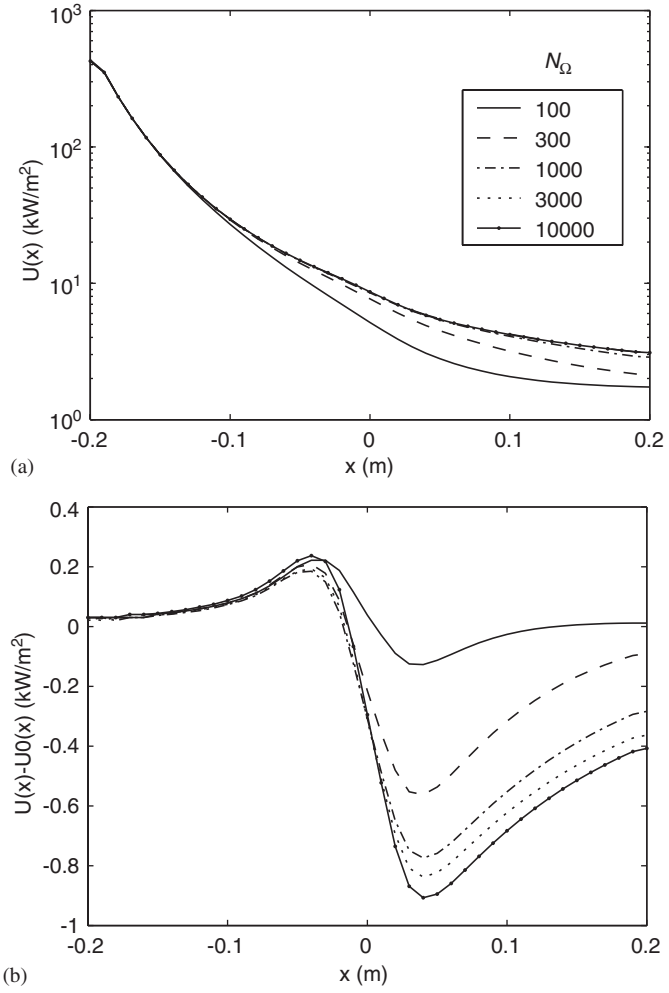


Fig. 9. The effect of the angular accuracy on (a) combined total intensity $U$ and (b) the change of $U$.

Table 4
Results of the TG03 spray simulation

| Flow rate (L/min/nozzle) | Attenuation (%) 1 nozzle | | 2 nozzles | | 3 nozzles | |
|---|---|---|---|---|---|---|
| | Measured | Predicted | Measured | Predicted | Measured | Predicted |
| 0.14 | 10.0 | 8.3 | 12.3 | 16.5 | 17.3 | 23.5 |
| 0.22 | 18.6 | 18.0 | 25.2 | 32.4 | 34.0 | 43.0 |
| 0.28 | 26.4 | 26.3 | 35.9 | 43.3 | 46.8 | 58.1 |
| 0.33 | 33.8 | 32.1 | 44.9 | 51.0 | 57.3 | 65.4 |

There are two reasons why the results are sensitive to the angular resolution. First, the radiation source is very small compared to the overall size of the domain. When 2 cm grid cells are used, the radiation source is spanned by only four cells. The second reason is that the radiation is monitored at the line perpendicular to the source plane. Despite the smoothing effect of the numerical diffusion typical of a first-order solution scheme, the ray effect is practically unavoidable for this direction because the solid angles used in the FVM solver do not overlap with the domain axis. As a result, a large number of solid angles may be needed to reach converged results at the axis perpendicular to the small source. Neither of the above reasons is directly related to the scattering solver, but to the applied angular discretization and FVM schemes. However, at this point one should remember that the numerical method to calculate the forward scattering fraction $\chi_f$ is not fully consistent with the angular discretization, i.e. the accuracy is not consistently improved when the number of control angles is increased. Therefore, the final results are given for $N_\Omega = 1000$. In addition to the above, the spectral resolution (use of multiband model) was also found to be important, especially in the case of low flow rate (optically thin case). Since the difficulties associated with the grid and angular dependence are much related to the small radiation source, rarely found in fire simulations, the results should provide valuable information on the capability of the model to capture the underlying physical processes.

Finally, the measured and simulated attenuation results are compared in Table 4. In the case of only one nozzle, the agreement is very good, taking into account the unavoided dependence on the grid and angular resolutions. The root-mean-square error between the predicted and measured attenuations is only 1.3%-units. When more nozzles are put between the source and the measurement point, the attenuation is clearly over-predicted. The root-mean-square errors for two and three nozzles are 6.4 and 8.8%-units, respectively. One possible reason for the over-prediction is the droplet coalescence, which is not taken into account by the model. Coalescence happens as a result of the hydrodynamic interaction between adjacent sprays [25]. This explanation is supported by the finding that while the predicted attenuations with two and three nozzles increase roughly by factors two and three from the values corresponding to the one nozzle, the experimental results increase only by factors 1.3 and 1.8.

## 4. Conclusions

A numerical model of radiation transport in polydisperse water spray has been described. The turbulent fluid flow is modeled using a low Mach number large eddy simulation and liquid droplets are tracked using a Lagrangian approach. A finite volume method for radiation transport is extended for the droplet absorption and scattering.

In transient engineering applications, the computational efficiency is of equal importance to the accuracy of the physical models. Because of the limitations in computational speed, only a small sample of the droplet population can be explicitly tracked, leading to inaccuracies in the droplet size statistics needed for the absorption and scattering routines. Stratified sampling techniques can be used to improve the accuracy of the sampled distributions. In the radiation solver, the approximation of the incoming intensity by combined intensity $U$ and the efficient use of look-up tables allow the reasonably accurate solution of the droplet scattering with only a small additional cost.

The simulations of two validation scenarios showed that the current model can predict the attenuation of thermal radiation in water sprays when the hydrodynamic interaction between the droplets is weak. Modeling of interacting sprays would require an implementation of the droplet coalescence model, increasing the cost of the entire flow calculation.

## Acknowledgements

The authors wish to acknowledge Dr. Jukka Vaari from VTT, and Dr. Howard Baum and Dr. John Widmann from NIST for the fruitful discussions and advice.

## References

[1] Ravigururajan TS, Beltran MR. A model for attenuation of fire radiation through water droplets. Fire Safety J 1989;15:171–81.
[2] Siegel R, Howell JR. Thermal radiation heat transfer, third ed. Philadelphia: Hemisphere Publishing Corp; 1992.
[3] Thomas PH. Absorption and scattering of radiation by water sprays of large drops. Brit J Appl Phys 1952;3:385–93.

[4] Coppalle A, Nedelka D, Bauer B. Fire protection: water curtains. Fire Safety J 1993;20:241–55.
[5] Log T. Radiant heat attenuation in fine water sprays. In: Interflam 96, Seventh international fire science and engineering conference, Interscience Communications; 1996, p. 425–34.
[6] Yang W, Parker T, Ladouceur HD, Kee RJ. The interaction of thermal radiation and water mist in fire suppression. Fire Safety J 2004;39:41–66.
[7] Keramida EP, Karayannis AN, Boudouvis AG, Markatos NC. Numerical modeling of radiant heat attenuation through water mist. Combust Sci Technol 2000;159:351–71.
[8] Berour N, Lacroix D, Boulet P, Jeandel G. Radiative and conductive heat transfer in a nongrey semitransparent medium. Application to fire protection curtains. J Quant Spectrosc Radiat Transfer 2004;86: 9–30.
[9] Jinbo H, Liming R, Heping T. Effect of anisontropic scattering on radiative heat transfer in two-dimensional rectangular media. J Quantit Spectrosc Radiat Transfer 2003;78:151–61.
[10] Trivic DN, O'Brien TJ, Amon CH. Modeling the radiation of anisotropically scattering media by coupling Mie theory with finite volume method. Int J Heat Mass Transfer 2004;47:5765–80.
[11] Collin A, Boulet P, Lacroix D, Jeandel G. On radiative transfer in water spray curtains using the discrete ordinates method. J Quantit Spectrosc Radiat Transfer 2005;92:85–110.
[12] Consalvi JL, Porterie B, Loraud JC. On the use of gray assumption for modeling thermal radiation through water sprays. Numer Heat Transfer, Part A 2003;44:505–19.
[13] Liu LH, Ruan LM, Tan HP. On the discrete ordinates method for radiative heat transfer in anisotropically scattering media. Int J Heat Mass Transfer 2002;45:3259–62.
[14] McGrattan KB, Baum HR, Rehm RG, Forney GP, Floyd JE, Prasad K, Hostikka S. Fire dynamics simulator (Version 3), Technical Reference Guide, Technical Report NISTIR 6783, 2002 edition. National Institute of Standards and Technology, Gaithersburg, Maryland, November 2002.
[15] Are S, Hou S, Schmidt DP. Second-order spatial accuracy in Lagrangian–Eulerian Spray Calculations. Numer Heat Transfer, Part B 2005;48:25–44.
[16] Chan TS. Measurements of water density and droplet size distributions of selected ESFR sprinklers. J Fire Prot Eng 1994;6(2):79–87.
[17] Hostikka S, McGrattan KB, Hamins A. Numerical modeling of pool fires using LES and finite volume method for radiation, In: Fire safety science—proceedings of the seventh international symposium. International Association for Fire Safety Science; 2003, p. 383–94.
[18] Wiscombe W. Mie scattering calculations: advances in technique and fast, vector-speed computer codes, NCAR Technical Note NCAR/TN-140+STR, National Center For Atmospheric Research, 1979 (revised 1996).
[19] Hale GM, Querry MR. Optical constants of water in the 200 nm to 200 μm wavelength region. Appl Opt 1973;12:555–63.
[20] Raithby GD, Chui EH. A finite-volume method for predicting radiant heat transfer in enclosures with participating media. J Heat Transfer 1990;112(2):415–23.
[21] Kim SH, Huh KY. Assessment of the finite-volume method and the discrete ordinate method for radiative heat transfer in a three-dimensional rectangular enclosure. Numer Heat Transfer, Part B 1999;35:85–112.
[22] Murrel JV, Crowhurst D, Rock P. Experimental study of the thermal radiation attenuation of sprays from selected hydraulic nozzles. In: Proceedings of Halon options technical working conference. The University of New Mexico: Albuquerque; 1995. p. 369–78.
[23] You H. Investigation of spray patterns of selected sprinklers with the FMRC drop size measuring system. In: Fire safety science—proceedings of the first international symposium. International Association for Fire Safety Science; 1986. p. 1165–76.
[24] Widmann JF. Phase Doppler interferometry measurements in water sprays produced by residential fire sprinklers. Fire Safety J 2001;36(6):545–67.
[25] Dembele S, Wen JX, Sacadura J-F. Experimental study of water sprays for the attenuation of fire thermal radiation. J Heat Transfer 2001;123:534–43.

Series title, number and
report code of publication

VTT Publications 683
VTT-PUBS-683

Author(s)
Hostikka, Simo

Title

# Development of fire simulation models for radiative heat transfer and probabilistic risk assessment

Abstract

In the first part of the work, an engineering tool for probabilistic fire risk assessment has been developed. The tool can be used to perform Monte Carlo simulations of fires and is called Probabilistic Fire Simulator (PFS). In practical applications, advanced simulation techniques based on computational fluid dynamics (CFD) are needed. Due to the high computational cost associated with CFD-based fire simulation, specialized algorithms are needed to allow the use of CFD in Monte Carlo simulation. By the use of the Two-Model Monte Carlo (TMMC) technique, developed in this work, the computational cost can be reduced significantly by combining the results of two different models. The developed technique has been verified and validated by using different combinations of fire models, ranging from analytical formulas to CFD.

In the second part of the work, a numerical solver for thermal radiation has been developed for the Fire Dynamics Simulator code. The solver can be used to compute the transfer of thermal radiation in a mixture of combustion gases, soot and liquid droplets. A new model has been developed for the absorption and scattering by liquid droplets. The radiative properties of droplets are computed using a Mie-theory and averaged locally over the spectrum and presumed droplet size distribution. To simplify the scattering computations, the single-droplet phase function is approximated as a sum of forward and isotropic components. The radiation solver has been verified by comparing the results against analytical solutions and validated by comparisons against experimental data from pool fires and experiments of radiation attenuation by water sprays at two different length scales.

ISBN
978-951-38-7099-7 (soft back ed.)
978-951-38-7100-0 (URL: http://www.vtt.fi/publications/index.jsp)

| Series title and ISSN | Project number |
|---|---|
| VTT Publications<br>1235-0621 (soft back ed.)<br>1455-0849 (URL: http://www.vtt.fi/publications/index.jsp) | |

| Date | Language | Pages |
|---|---|---|
| May 2008 | English, Finnish abstr. | 103 p. + app. 82 p. |

| Keywords | Publisher |
|---|---|
| fire simulation, Monte Carlo simulation, probabilistic risk assessment, thermal radiation, verification, validation | VTT Technical Research Centre of Finland<br>P.O. Box 1000, FI-02044 VTT, Finland<br>Phone internat. +358 20 722 4520<br>Fax +358 20 722 4374 |

Julkaisun sarja, numero ja raporttikoodi

VTT Publications 683
VTT-PUBS-683

Tekijä(t)
Hostikka, Simo

Nimeke

# Tulipalon simuloinnissa käytettävän säteilylämmönsiirto-mallin ja riskianalyysimenetelmän kehittäminen

Tiivistelmä

Paloriskien arvioinnissa on olennaista palon seurausten ja leviämismahdollisuuksien analysointi. Tässä työssä on kehitetty tulipalojen numeerisen simuloinnin malleja ja työkaluja. Työn päätavoitteita ovat olleet palosimuloinnin parhaimpien laskentamallien hyödyntäminen todennäköisyyspohjaisessa paloriskien arvioinnissa sekä laskennallisesti tehokkaan säteilylämmönsiirron ratkaisijan kehittäminen Fire Dynamics Simulator -ohjelmaan.

Työn ensimmäisessä osassa on kehitetty insinöörikäyttöön soveltuva, Probabilistic Fire Simulator (PFS) -niminen työkalu paloriskien arviointiin. PFS-työkalulla tulipaloa voidaan tutkia Monte Carlo -menetelmällä, jossa simulointeja toistetaan useita kertoja satunnaisilla syöteparametrien arvoilla, jolloin yksittäisen numeroarvon sijaan tuloksena saadaan tulosten jakauma. Käytännön sovelluksissa tarvitaan numeeriseen virtauslaskentaan perustuvia simulointimenetelmiä, koska simuloitavat tilavuudet ovat suuria ja monimutkaisia ja koska niissä pitää pystyä simuloimaan palon leviämistä. Monte Carlo -menetelmän toteutuksessa on tällöin käytettävä tehtävään sopivia erikoismenetelmiä, koska virtauslaskenta on laskennallisesti raskasta ja aikaa vievää. Tässä työssä kehitetyn Kahden mallin Monte Carlo -menetelmän avulla laskentaa voidaan nopeuttaa yhdistämällä kahden eritasoisen mallin tulokset. Nopeasti ratkaistavan mutta epätarkan mallin tuottamia tuloksia parannetaan hitaammin ratkaistavan mutta tarkemman mallin avulla. Menetelmää on testattu erilaisilla palomallien yhdistelmillä aina analyyttisistä kaavoista virtauslaskentaan asti.

Työn toisessa osassa on kehitetty säteilylämmönsiirron numeerinen ratkaisija Fire Dynamics Simulator -ohjelmaan. Ratkaisija laskee säteilyn etenemistä palokaasuja, nokea ja nestepisaroita sisältävässä väliaineessa. Palokaasujen ja noen muodostaman seoksen säteilyominaisuudet lasketaan keskiarvoistamalla RadCal-kapeakaistamallin tulokset aallonpituuden yli. Lämpösäteilyn eteneminen ratkaistaan säteilylämmönsiirron kontrollitilavuusmenetelmällä. Säteilyratkaisijan vaatima laskenta-aika saadaan alle 30 %:iin kokonaislaskenta-ajasta käyttämällä eksplisiittistä ratkaisumenetelmää ja tehokkaita taulukkohakuja sekä luopumalla ratkaisun aikatarkkuudesta. Tarkkuutta voidaan tarvittaessa parantaa jakamalla tarkasteltava aallonpituusalue veden ja hiilidioksidin tärkeimpiä absorptiokaistoja vastaaviin osiin sekä tihentämällä diskretointia avaruuskulman ja ajan suhteen. Työssä on kehitetty uusi laskenta-malli nestepisaroiden ja säteilyn vuorovaikutukselle. Pisaroiden säteilyominaisuudet lasketaan Mie-teorian avulla ja keskiarvoistetaan sekä spektrin että pisarakokojakauman yli. Yksittäisen nestepisaran sirottaman energian vaihe-funktiota approksimoidaan eteenpäin siroavien ja isotrooppisten komponenttien summana. Säteilyratkaisijaa on testattu vertaamalla laskettuja tuloksia analyyttisiin ja kokeellisiin tuloksiin.

ISBN
978-951-38-7099-7 (nid.)
978-951-38-7100-0 (URL: http://www.vtt.fi/publications/index.jsp)

| Avainnimeke ja ISSN | Projektinumero |
|---|---|
| VTT Publications<br>1235-0621 (nid.)<br>1455-0849 (URL: http://www.vtt.fi/publications/index.jsp) | |

| Julkaisuaika | Kieli | Sivuja |
|---|---|---|
| Toukokuu 2008 | Englanti, suom. tiiv. | 103 s. + liitt. 82 s. |

| Avainsanat | Julkaisija |
|---|---|
| fire simulation, Monte Carlo simulation, probabilistic risk assessment, thermal radiation, verification, validation | VTT<br>PL 1000, 02044 VTT<br>Puh. 020 722 4520<br>Faksi 020 722 4374 |

An essential part of fire risk assessment is the analysis of fire hazards and fire propagation. In this work, models and tools for two different aspects of numerical fire simulation have been developed. In the first part of the work, an engineering tool for probabilistic fire risk assessment has been developed. The tool can be used to perform Monte Carlo simulations of fires and is called Probabilistic Fire Simulator (PFS). By the use of the Two-Model Monte Carlo (TMMC) technique, developed in this work, the computational cost of the simulation can be reduced significantly by combining the results of two different models.

In the second part of the work, a numerical solver for thermal radiation has been developed for the Fire Dynamics Simulator code. The solver can be used to compute the transfer of thermal radiation in a mixture of combustion gases, soot and liquid droplets. A new model has been developed for the absorption and scattering by liquid droplets. The radiation solver has been verified by comparing the results against analytical solutions and validated by comparisons against experimental data from pool fires and experiments of radiation attenuation by water sprays at two different length scales.

Julkaisu on saatavana
VTT
PL 1000
02044 VTT
Puh. 020 722 4520
http://www.vtt.fi

Publikationen distribueras av
VTT
PB 1000
02044 VTT
Tel. 020 722 4520
http://www.vtt.fi

This publication is available from
VTT
P.O. Box 1000
FI-02044 VTT, Finland
Phone internat. + 358 20 722 4520
http://www.vtt.fi

ISBN 978-951-38-7099-7 (soft back ed.)
ISSN 1235-0621 (soft back ed.)

ISBN 978-951-38-7100-0 (URL: http://www.vtt.fi/publications/index.jsp)
ISSN 1455-0849 (URL: http://www.vtt.fi/publications/index.jsp)